The Formation of Metal Nanoparticle-Carbon Nanotube Composite Materials for the Non-enzymatic Detection of Glucose

David Branagan B.Sc. (Hons)

Department of Chemistry

National University of Ireland Maynooth

October 2014

Thesis Submitted to the National University of Ireland in Fulfilment of the Requirements for the Degree of Doctor of Philosophy

Supervisor: Professor Carmel B. Breslin

Head of Department: Doctor John Stephens

Table of Contents

Declaration

I hereby certify that this thesis, which I now submit for assessment on the programme of study leading to the award of PhD, has not been submitted, in whole or part, to any other university for any degree, and is, except where otherwise stated the original work of the author.

Signed:_____ Date:_____

Dedication

Dedicated to my family, with love

Acknowledgements

Firstly, I would like to thank my supervisor, Professor Carmel B. Breslin, for her excellent supervision and support throughout my PhD. Thank you for all of your advice, help and patience throughout my time at Maynooth. Without your supervision and guidance this PhD would not have been possible.

I wish to say a special thank you to Doctor Denise Rooney for her invaluable guidance, knowledge, encouragement, patience and for her very informative feedback. I would like to acknowledge Kildare County Council for covering my fees for the duration of my PhD. If it was not for this help, I may not be where I am now. Thanks to all of my friends in the Chemistry Department, both students and staff, who have always lent a helping hand and made my time at Maynooth so enjoyable. A special thanks to the electrochemistry crew, Karen, Orla, Emer, Lynn, Catherine, Sam, Paul, Conor and Joey for your constant help and advice. I really hope I didn't forget any names! I also wish to thank Doctor John Colleran who supervised me in the electrochem lab during my 4th year research project. Your enthusiasm and knowledge gave me a taste for the area. Thank you to all of the academic staff and technicians who always went above and beyond. To Noel, Ken, Ria, Barbara, Maryanne D and Maryanne R, Ollie, Anne and Orla. A big thank you to the delightful office gals, Donna and Carol, for our wonderful gossiping sessions, chats, laughs and for all of your help during my PhD. Also, I would like to express my gratitude to Doctor Anne Shanahan for enabling me to undertake Raman spectroscopy at the FOCUS Institute, DIT, and to Doctor Wynette Redington of UL for all of your XRD work.

Okay before I forget, I must also say a special thanks to my dear friend Doctor Laura O'Toole. Laura and I grew up together and coincidentally followed each other to the Chemistry Department to carry out our PhDs. Oh wait, we now also work in the same company! Guess she can't get away from me that easily. Also, to Professor John Lowry, Professor Dermot Diamond and Doctor Tom Naughton, for allowing me to have the best possible viva experience. Your patience and calmness sincerely helped to put my nerves at ease and thank you all for your generous and very constructive feedback.

Last, but by no means least, I have to thank my family. To mam and dad, thank you for your unconditional love and encouragement, for teaching me how to stand on my own two feet and for always making sure I have a roof over my head and food in my belly. Thank you to my sisters Laura and Stephanie for our late night conversations and the company when I used to arrive home at such crazy hours. To all my family in Brazil, Mônica, Carlos, Karina e todos os demais. Mesmo estando longe, sinto vocês por perto. Vejo-os em breve! To the ever growing Mr. Plant for always keeping me company in the lab, even though you never talk. Soon you will reach the roof and I'm not sure what I'll do with you then! And finally, to my husband Khayam, thank you for always being there for me, for putting up with my constant 'PhD talk' over the past three years, for always believing in me and for sticking with me through my ups and downs. You're the best!

Abstract

Nano composite materials consisting of gold nanoparticles (AuNPs) and functionalised multiwalled carbon nanotubes (fMWCNTs) were initially prepared using simple synthetic reduction methods, involving the chemical agents sodium borohydride and trisodium citrate. These composites were named fMWCNT-$Au_{nano}(NaBH_4)$ and fMWCNT-Au_{nano}(TriSodCit). AuNPs of a face-centred cubic structure were successfully formed on the sidewalls of the fMWCNTs. The fMWCNT-$Au_{nano}(NaBH_4)$ composite had an Au loading of 2.0% wt. and contained AuNPs with a mode diameter of 7.5 nm. The fMWCNT-Au_{nano}(TriSodCit) composite had an Au loading of 5.0% wt. and contained AuNPs with a mode diameter of 23 nm. These composites were used to form films on glassy carbon and screen printed electrodes for the non-enzymatic electrochemical detection of glucose in PBS buffer at physiological pH. Electrochemical pre-treatments in sodium hydroxide and sulfuric acid provided films with improved sensitivity. These films were combined with a Nafion® membrane to improve selectivity towards glucose in the presence of commonly occurring interferants.

The fMWCNT-$Au_{nano}(NaBH_4)$ composite was also combined with palladium nanoparticles (PdNPs) to form a composite named fMWCNT-$Au_{nano}/Pd_{nano.}$ This bi-metallic composite was formed using a potentiostatic electrodeposition of Pd onto the surface of pre-existing fMWCNT-$Au_{nano}(NaBH_4)$ films. These PdNPs had a mode diameter of 95 nm and the Pd loading was close to 3.0%. This composite film was used for the electrochemical detection of glucose, whereby it facilitated its oxidation at more negative potentials in comparison to the fMWCNT-Au_{nano} composites.

Interference studies were carried out using chemical species commonly present in the blood; ascorbic acid, uric acid, fructose, galactose, serum albumins, chloride and acetaminophen. The severity of interference varied at each electrode and it was shown that Nafion® reduced the level of interference. Sensor reusability and shelf-life studies were also carried out using the composite modified films. These films provided accurate glucose detection over twelve successive uses, although they were not deemed to be suitable for storage.

The materials were characterised using TEM, SEM, EDX, AAS, XRD, EIS, UV-Vis and Raman spectroscopy. An electrochemical characterisation also showed that a

significant electroactive area of Au was present in the fMWCNT-Au_{nano}($NaBH_4$) and fMWCNT-Au_{nano}(TriSodCit) composite when cast onto an electrode surface.
Overall these composite materials show good initial promise for use as non-enzymatic glucose sensors based on these preliminary studies.

Chapter 1

Introduction and Literature Review

1.1 Carbon Nanotubes

1.1.1 What are Carbon Nanotubes?

Carbon nanotubes (CNTs) are cylindrical allotropes of carbon that possess valuable thermal [1, 2], mechanical [3, 4] and electrical properties [2, 5]. Although their formation was initially reported in 1976 by Oberlin and co-workers [6], they were brought to the attention of the wider scientific community in 1991 by Iijima [7]. CNTs of various sizes have been produced and some have even been developed with length-to-diameter ratios close to 132,000,000:1, which is impressively larger than that obtained for any other material [8].

1.1.2 Structures and Properties of Carbon Nanotubes

CNTs typically exist as either singlewalled nanotubes (SWNTs) or multiwalled nanotubes (MWNTs) [9]. Both of these types of CNTs are composed of graphene which is a material consisting solely of carbon in a one atom thick polycyclic aromatic layer [9]. SWCNTs are the smallest CNTs in diameter and consist of a single graphene sheet rolled into a cylindrical form. MWCNTs are larger and consist of two or more rolled layers of graphene [9]. Most SWCNTs have a diameter between 1 and 3 nm with exceptionally larger lengths [10] and MWNTs can have diameters ranging in size from 5 to 100 nm and lengths in the micrometer region [11]. Visual representations of these CNTs are displayed in Figure 1.1, taken from work by Choudhary and Gupta [12].

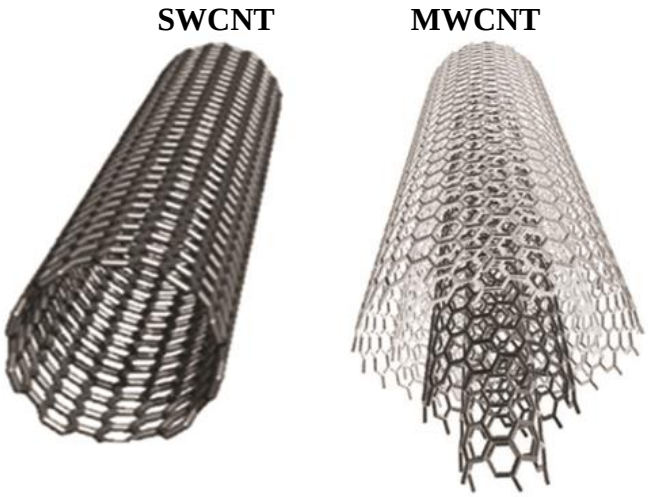

Figure 1.1: Representations of singlewalled and multiwalled carbon nanotubes [12].

CNTs exhibit impressive properties such as high tensile strength [3, 4], electrical [2, 5] and thermal conductivity [1, 2] and possess modifiable surfaces [13]. This makes them attractive and potential candidates in many applications including fuel cells [14], energy storage [15], sensors [16], transistors [17] and in nanoelectronic devices [18]. CNTs are one of the strongest materials in nature. The bonding in CNTs is sp^2, as each carbon atom is bonded to three neighbours, which is the same as in graphite. This type of bonding gives the CNTs their unique strength. It has been shown that CNT axial strength is even harder than the sp^3 bonds found in diamond [19]. Studies by Yu *et al.* on the tensile strengths of MWCNTs, found that this strength can range from 11 - 63 GPa and the Young's modulus is in the order of 270 - 950 GPa [3]. The electrical conductivity of CNTs is associated with the sp^2 bonding between the carbon atoms. This bonding leaves an extra valence electron in the P_z orbital to hybridise with the other P_z orbitals thereby forming a delocalised π bond [5]. The nature of the graphene wrapping, chirality, can determine whether the CNTs exhibit metallic or semiconducting properties [5].

1.1.3 Synthesis of Carbon Nanotubes

Techniques including arc discharge and laser ablation were at first used to produce CNTs, although these syntheses use high temperatures and are now typically replaced

by lower temperature chemical vapour deposition (CVD) [20]. The use of arc discharge to produce CNTs was accidentally discovered in 1991 in work by Iijima who's aim was actually to produce fullerenes [7]. Iijima referred to these CNTs as 'needle-like' tubes.

The various conditions used in arc discharge synthesis are reported in work by Ando and Zhao and in references therein [21]. In a typical synthesis, two graphite electrodes, an anode and cathode, are aligned vertically in a low pressure vacuum chamber separated by a distance of 1 - 2 nm. Ambient gas is then injected into the vacuum chamber and a DC arc discharge is applied to the graphite electrodes. This results in carbon from the anode being deposited on the surface of the cathode in the form of MWCNTs with other carbon nanoparticles including SWCNTs and fullerenes. A purification step involving infrared radiation and high temperatures can then be used for separation of the MWCNTs. Gasses used in these syntheses include hydrogen, helium, argon, methane and acetylene, of which acetylene and hydrogen are considered to be the best as they are reported to produce long fibrous MWCNTs.

As mentioned previously, chemical vapour deposition (CVD) is commonly used to produce CNTs. CVD is advantageous as it allows precise control of the CNT orientation, alignment, length, diameter and purity [20]. CVD results in higher yields and better purity of MWCNTs in comparison to arc discharge and laser ablation. These MWCNTs produced may have inferior crystallinity, in comparison to the crystallinity of SWCNTs grown by this method [22]. In CVD setup, a hydrocarbon vapour, including benzene, acetylene or carbon monoxide, is passed through a reactor tube for a period of time, typically between 15 - 20 min, and at temperatures between 600 – 1200 ^{0}C, in the presence of a catalyst. The resulting CNTs form on the surface of the catalyst and can be collected upon cooling. Commonly used catalyst materials include Fe, Co or Ni nanoparticles which are useful due to the high solubility of carbon in these materials and their high melting points [22].

The use of laser ablation for the mass production of CNTs was first reported in 1996 in work by Smalley and coworkers [23]. This method does not favour the production of MWCNTs, although is very useful for producing SWCNTs and can result in samples with up to 90% purity [24]. In a typically setup, a laser beam is focused onto a composite

consisting of graphite and a metal, including Co, Cu, Nb, Ni or various combinations, while under a high temperature of around 1200 ^{0}C and in the presence of an inert gas, such as Ar. As the laser is scanned across the surface of the composite, its surface is then vapourised and deposited onto a collector in the form of CNTs. Impurities may include amorphous carbon and the catalysts used [24].

1.2 Metal Nanoparticles

1.2.1 What are Nanoparticles?

Nanoparticles are particles ranging in size from 1 and 100 nm that can be composed of various metals or materials [25]. They can be produced and stabilised in solutions known as colloids [26] or on specific surfaces or materials, thereby forming composite materials [27-29]. These nanoparticles possess interesting properties that neither mirror their constituent bulk substances or small molecules [30] and due to their unusual properties they are used in various applications from biomedicine [25] to electronics [31, 32]. The use of nanoparticles dates back to the Roman times, during which Au nanoparticles (AuNPs) in the colloidal form were used in glass staining for decorative purposes [33].

1.2.2 Structures, Properties and Applications of Metal Nanoparticles

Metal nanoparticles are commonly produced from gold (Au) [34-36], silver (Ag) [37-39], copper (Cu) [40-42], palladium (Pd) [29, 43, 44] and iron oxide (Fe_2O_3) [45-47] and can exist in many shapes, including cylindrical and hexagonal nanorods [37, 48, 49], nanospheres [37, 39, 50], nanotriangles [38], oval shaped nanoparticles [51], and nanoboxes and nanocages [52]. Nanoparticles are typically considered to be under 100 nm in size and it is these dimensions that allow them to possess their interesting properties and advantages over their bulk counterparts [53]. When under 10 nm in diameter they can be closer to the size of small molecules than the bulk metal, although their physical properties neither resemble those of bulk metal or those of molecules [30].

In recent years, many areas have embraced the use of nanomaterials due to their use in various useful applications. One such use is in catalysis, in which metal

nanoparticles can be used as heterogeneous catalysts for various kinds of chemical reactions. This is due to their large surface-area-to-volume ratios [54]. Metal nanoparticles can be used in gas sensors, which is again due to their large surface areas [55-57]. An example of this can be seen in studies by Zhang *et al.* [55] in which monodisperse Cu_2O and CuO nanospheres formed in three-dimensional patterns are used for sensing of alcohol, gasoline and hydrogen sulfide gas. In these sensors, the presence of the charged oxygen adsorbed on the copper oxides is presumed to react with the gas, which leads to a change in the surface charge layer and an increase in Cu_2O and CuO resistance and ultimately the detection of the gas.

Metal nanoparticles can also be used in drug delivery systems for anti-tumour therapies [45, 58, 59]. Work by Chertok *et al.* [58] investigated the possibility of using Fe_3O_4 nanoparticles for targeted brain tumour drug delivery. This was undertaken on rats harboring orthotopic 9L-gliosarcomas and the magnetic nature of the Fe_3O_4 nanoparticles allowed their delivery to be monitored using MRI. They found that a 5-fold increase in the total tumour exposure occurred in the presence of the Fe_3O_4 nanoparticles.

In several recent works, it has been shown that silver nanoparticles (AgNPs) can possess anti-microbial properties [60-63]. Work by Vijayakumar *et al.* [60] involving the use of AgNPs synthesised through a green chemistry route using plant extracts, showed that these AgNPs can possess anti-bacterial properties against s*taphylococcus aureus*, *Bacillus subtilis*, *Escherichia coli*, and *Proteus subtilis*. This research was carried out on bacterial cell cultures on agar plates and the resulting zones of inhibition were measured. The exact anti-microbial mechanisms were not known exactly but it was suggested that the AgNPs may interact with the bacterial membranes and cause permeability and degradation, thereby resulting in cell death.

Meanwhile AuNPs, have also attracted substantial interest because of their unique optical and electrical properties, as discussed in recent works [64-66] as well as large active surface areas and excellent catalytic properties [67, 68] which originate from their small sizes and high surface-area-to-volume ratios [68]. AuNPs can be used in a variety of applications including assays for pesticides [69], as SERS-active tags for cellular spectral detection [70] and for the colourimetric detection of DNA, small molecules,

proteins, and ions [71]. They can also be used for the colourimetric detection of Cr^{3+} [72], in various electrochemical sensors for the detection of oxygen [73, 74], nitrobenzene [75] and glucose [76, 77], in drug delivery [78] and in anti-tumour therapies [78]. An example of the use of AuNPs in colourimetric detection of the heavy metal chromium can be seen in work by Zhao *et al.* [72]. In this work, it was discovered that the selective detection of Cr^{3+} was possible even with the coexistence of other transition metal species, including Zn^{2+}, Ni^{2+}, Co^{2+}, Cu^{2+}, Mn^{2+} and Pb^{2+}. This was possible by examining the change in the wine-red colour of the AuNP colloid solution and the surface plasmon resonance peak of the AuNPs at 520 nm during UV-Vis spectroscopy upon the addition of Cr^{3+}. The additions of Cr^{3+} caused a change in colour from wine-red to blue, which indicated that an aggregation of the AuNPs was occurring and a new absorption band appeared at 630 nm. This process was only observed upon the addition of Cr^{3+}. AuNPs have the ability to resonate at their plasmon wavelengths in the visible spectrum due to their ability to sustain oscillation of electrons known as surface plasmons at their surface, this allows them to be active during UV-Vis spectroscopy [79].

The application of AuNPs in non-enzymatic glucose sensing is reported in recent work by Chang *et al.* [77]. Their work involved the formation of AuNPs ranging from 4 nm to 40 nm in size on glassy carbon (GC) electrodes using the reducing agents, sodium borohydride and trisodium citrate. These modified GC electrodes provided high surface area and sensitive films for the non-enzymatic oxidation of glucose in alkaline solution.

Similarly to the works mentioned previously involving AuNPs, palladium nanoparticles (PdNPs) have also been used in colourimetric detections of chemical species [80] and in non-enzymatic glucose sensors [81]. Lan *et al.* [80], reports the use of PdNPs for the colourimetric detection of the amino acid sarcosine, which is produced in high concentrations in patients with prostatic carcinomas. Work by Chen *et al.* [81], reports the formation of PdNPs supported on CNTs and their applications in non-enzymatic glucose detection in alkaline media.

1.2.3 Synthesis of Metal Nanoparticles

Metal nanoparticles are typically produced using a "bottom-up" method in which the reduction of metal salts is undertaken via chemical, electrochemical or decomposition pathways [26]. During these syntheses, a variety of stabilisers, typically named "capping agents", including, ligands, polymers, and surfactants, are used to control the growth of the nanoparticles formed and to prevent their agglomeration [26]. The most conventional method for the synthesis of spherical AuNPs was pioneered in 1951 by Turkevich *et al.* [82] and was later refined in 1973 by Frens *et al.* [83]. This method produces monodisperse AuNPs in the form of a ruby-red colloid via the chemical reduction of an Au(111) chloride ($HAuCl_4$) salt using sodium citrate as the reducing agent. Shown in Scheme 1.1, is a schematic representation of citrate stabilised AuNPs produced by the Frens method, taken from Ghosh *et al.* [84]. An example of the ruby-red colloid formed using this method and its development during the synthesis is shown in Figure 1.2. This image was taken from Kumar *et al.* [85].

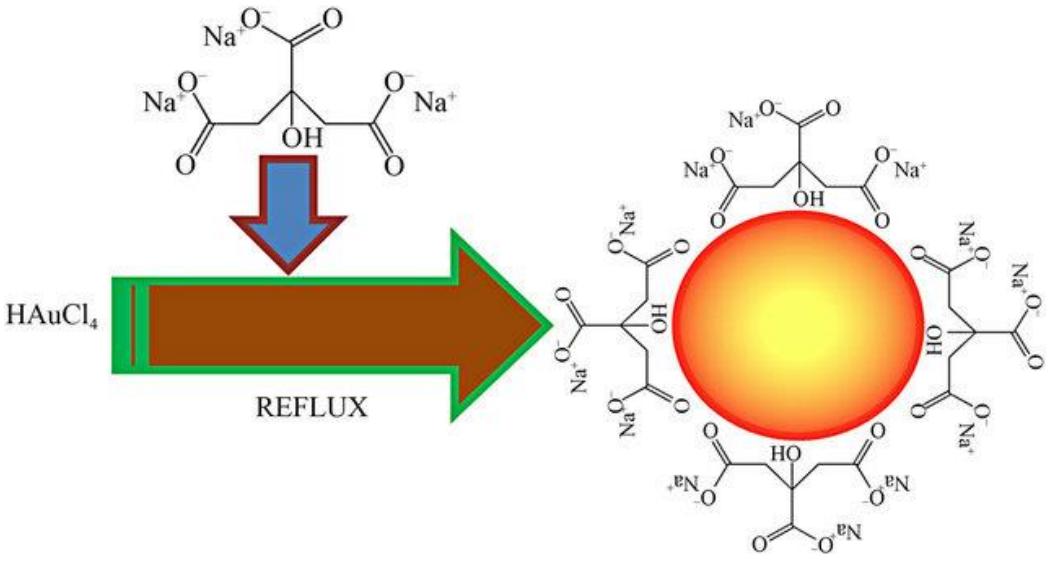

Scheme 1.1: Representation of citrate stabilised AuNPs produced by the Frens method, taken from Ghosh *et al.* [84].

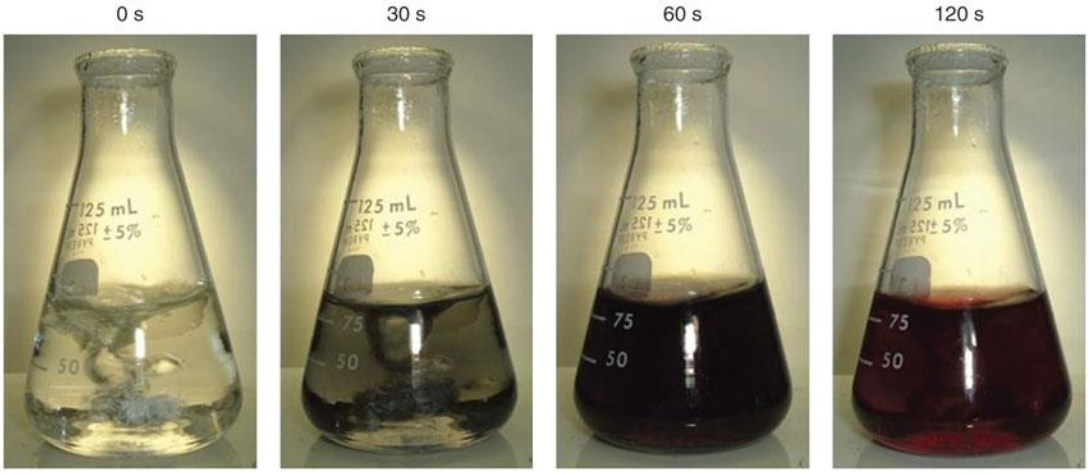

Figure 1.2: Ruby-Red colloid and AuNPs produced using the Frens method, taken from Kumar *et al.* [85].

The mechanisms involved during nanoparticle formation is described in an article by Zhou *et al.* [26] and in the references therein. One of the most common methods to produce metal nanoparticles uses the chemical reduction of transition metal salts, using reducing agents such as trisodium citrate and sodium borohydride, in the presence of stabilising and capping agents. These reactions generate colloidal solutions of zerovalent nanoparticles in either aqueous or organic solutions. The initial step in the production of these nanoparticles is the formation of zerovalent metal atoms from the metal salt, known as "seed" nuclei, followed by growth, and agglomeration to form larger nanoparticles. To stabilise these newly synthesised nanoparticles and to stop their agglomeration, is it necessary to use protecting agents. These protecting agents may exert their effects by electrostatic stabilisation, in which an electrical double layer causes a repulsion effect between the nanoparticles or by steric stabilisation, in which large organic molecules act as bulky protective agents on the metal surface. Protecting agents include, polymers, solvents such as THF, THF/MeOH, long-chain alcohols, organometallics and surfactants. Typically, hydrophilic agents are used in aqueous colloidal solutions and hydrophobic agents in organic colloidal solutions. Many of these substances can also be regarded as capping agents, which both prevent the nanoparticles from aggregating and can control their size.

Other than the conventional methods for nanoparticle generation mentioned previously, other methods can be employed, including syntheses using ultrasonication [86, 87], electrodeposition [27, 88-90] and electroless deposition [91]. In recent work by Kumar *et al.* [86], the synthesis of AgNPs using ultrasonication is reported. AgNPs ranging from 23 nm to 97 nm were produced and starch was used both as a stabilising and capping agent. This synthesis is considered a green synthesis due to the use of the naturally available starch and its efficiency. Another efficient route is by electrodeposition. An example of this can be seen in work by Spain *et al.* [88] in which AuNPs were electrosynthesised on top of a PEDOT conducting polymer film from an $HAuCl_4$ solution, made in 0.1 M KCl, by applying a fixed potential of -0.273 V vs. AgCl. This synthesis took only 3 min to complete and the resulting composite possessed a high surface of AuNPs. Other than mono-elemental nanoparticles, various poly-metallic alloy nanoparticles can be produced using electrodeposition [27, 89, 90, 92]. Recent work by Xu *et al.* [27], reports the electrosynthesis of tri-metallic AuPdCu nanoparticles formed on MWCNT films. This was completed using a mixture of Au, Pd and Cu salts in a Na_2SO_4 electrolyte and by applying a potential of -0.20 V vs. SCE for 200 s. This created nanoparticles of around 80 nm in size.

1.3 Carbon Nanotube-Metal Nanoparticle Composite Materials

1.3.1 What are Composite Materials?

Composites are materials produced using two or more materials of different properties to form a new material with characteristics different from the individual comprising materials which are better than the individual components [93].

1.3.2 Structures, Properties and Applications of Composite Materials

Composite materials are commonly produced using CNTs [27, 42, 94-96], graphene [88, 97, 98], various metal nanoparticles including AuNPs [97, 98], PdNPs [81, 99], CuNPs [42, 96] , PtNPs [100], bi-metallics [27, 89] and polymers [94, 95]. As mentioned, the formation of a composite material produces a material with characteristics different from the individual components comprising the materials and the material is better than the individual components [93]. CNTs are frequently used in composite materials due to the varied

qualities they can provide including improved strength and electrical conductivity, improved mechanical properties, their low density and their high aspect ratio [101] and due to their modifiable surfaces [13]. In work by Guo *et al.* [94] on the formation of a composite consisting of CNT-poly acrylic acid fibers, it is shown that a combination of these two materials resulted in a composite material with enhanced mechanical strength and electrical conductivity in comparison to the individual materials. Another example of these improvements can be seen in work by Wang *et al.* [95] in which a CNT-Nylon composite displays enhanced electrical and mechanical properties.

CNTs are frequently used in the formation of CNT-metal nanoparticle composites in which their function is often to provide high surface area conducting platforms for metal nanoparticle growth and to aid in nanoparticle stabilisation [100]. An example of this can be seen in work by Wang *et al.* [102], in which CNTs were used as a PtNP support for proton exchange fuel cell membranes. They proposed that the surface areas of the PtNPs could be further increased with the use of the CNT supports and that this may be a way to reduce the cost of the fuel cell. Other examples of CNTs being used as nanoparticle supports can be seen in work involving CuNP-CNT [42, 96], PdNP-CNT [81, 99] and PtNP-CNT composites [100], all for the use in electrochemical sensing films for glucose. Other metal nanoparticle composites showing enhanced electrochemical properties include AuNP-CNT [103-107], AuNP-graphene [97, 98] and AuNP modified conducting polymers [108, 109]. Many electrochemical sensors utilising AuNPs/CNT composites have been reported, including various biomedical-type sensors for DNA [110], hydrogen peroxide [111] , glucose [76, 112], for the neurotransmitters cortisol [104], androsterone [104] and dopamine [105] and the neurotransmitter precursor L-DOPA [113]. Environmental sensors using these composites include those for the quantification of toxic metal ions and inorganic and organic pollutants in water including nitrites [106] thiocyanate [107] arsenic [114] mercury [115], nitrobenzene [75] and organophosphates [116].

1.3.3 Synthesis of Gold Nanoparticle-Carbon Nanotube Composites

Various synthetic procedures exist for the production of AuNP/CNT composites, which can be multi-stepped and commonly involve the functionalisation of the CNTs with thiol groups. These surface modifications usually employ the initial

carboxylation of the CNTs using strong acids, followed by an activation of these functionalities with either thionyl chloride [28, 50, 117] or a carbodiimide [118, 119], to form acyl chlorides and carbodiimide esters on the CNT surfaces, respectively. These activations allow the formation of an amide linkage with an amine-thiol [28, 50, 117-119] containing compound to produce the functionalised CNTs that are useful for the self-assembly of pre-prepared AuNPs or their direct reduction onto the CNT surfaces. Although these procedures can provide composites with exceptional AuNP surface coverage, their preparations are often multi-stepped and more simplistic approaches can be explored. Other procedures for the formation of AuNP/CNT composites include those using adsorption of pre-made AuNPs on CNTs during ultrasonication [120], the electrodeposition of AuNPs onto CNT films [106, 107, 116], the one step-synthetic reduction onto CNTs using a reducing agent [87, 103] and even through direct casting of AuNPs onto CNT films [121].

1.4 Electrochemical Glucose Sensors

1.4.1 What is Glucose?

Glucose is a six-carbon sugar, known as a hexose and is also an aldehyde. It is the most abundant monosaccharide in the body and it is used as an energy source during cell respiration [122]. Physiologically it is present at concentrations ranging from 4 – 8 mM [123] in the blood, although these levels vary throughout the day [124]. The structure of an open chain glucose molecule is shown in Figure 1.3.

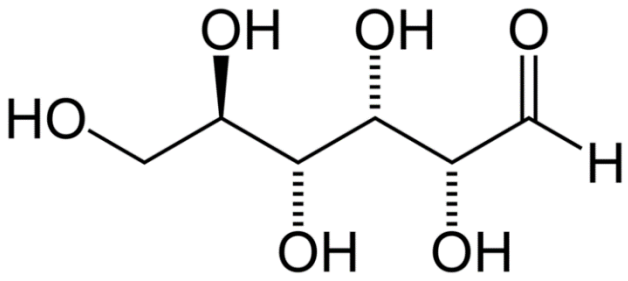

Figure 1.3: Open chain structure of glucose.

1.4.2 Mutarotation of Glucose

Many saccharides including pentoses and hexoses are present as a mixture of open chain and two diastereomeric cyclic structures each exhibiting an additional chiral carbon centre [125]. Diastereomers are produced due to hemiacetal or hemiketal formation and are referred to as anomers. These cyclic forms are more stable than the open chain form and when in solution, the isomers interconvert rapidly until an equilibrium is reached [125]. This interconversion is called mutarotation and in the case of glucose, results in 64% of the β anomer, β-D-glucopyranose and 34% of the α anomer, α-D-glucopyranose, with only trace amounts of the open chain aldehyde form remaining at 0.003% [125-127]. In the β anomer the OH group of the anomeric carbon is positioned in the equatorial position thus making this anomer most thermodynamically stable and abundant [125]. When dissolved in solution, glucose must be left for a period of time to allow its diastereomers to reach equilibrium [126]. In a study by Perles and Volpe [128], it was found that equilibrium between the anomers was reached after 3 to 4 h at room temperature. They made this conclusion through measuring the rotation of the glucose species using a polarimeter. An example of glucose mutarotation in neutral solution can be seen in Scheme 1.2, taken from Silva *et al.* [127].

The enzyme glucose oxidase (GOx) used in commercial glucose sensors is specific for the β form of glucose and as such mutarotation must be given time to take place [129]. For non-enzymatic glucose sensing, the process of mutarotation may also be important. Work by Largeaud *et al.* [130], involving glucose detection at Pt, found that the α form of glucose exhibited poor reactivity at Pt and that the β form was the most reactive. This poor reactivity of the α form may be attributed to the equatorial geometric orientation of the hydrogen atom of the anomeric carbon [130].

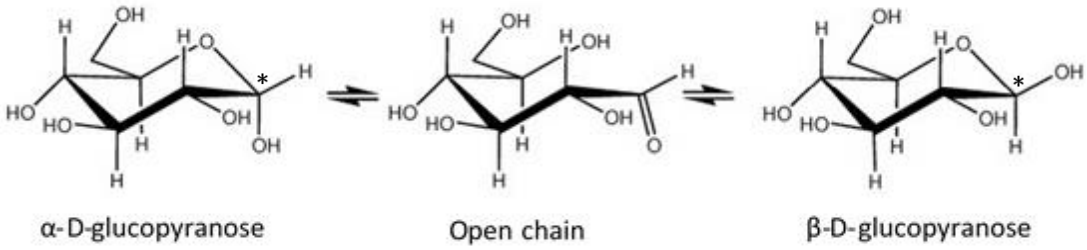

* Position of anomeric carbon atom.

Scheme 1.2: Mutarotation of glucose [127].

1.4.3 Why do we need Glucose Sensors?

Detection of glucose is of utmost importance in society with the present and ever increasing diabetes epidemic. Recent figures put the worldwide diabetes prevalence at an astronomical 6.4% of the world's adult population. This is predicted to increase to 7.7% by 2030 [131]. In Ireland alone there are believed to be 250,000 individuals afflicted with the condition with another 100,000 existing but undiagnosed and possibly a further 100,000 having pre-diabetes [132]. If not diagnosed, managed and treated, diabetes can carry many complications including high blood pressure, heart disease, stroke, kidney disease, blindness, amputation and other serious issues [133].

Other than the possible health complications carried with diabetes, major financial expenditure is associated with it. According to the CODEIRE study, in Ireland alone it is calculated that diabetes costs the Irish health service almost €600 million per annum. This is roughly 6.4% of the total health budget and this figure will rise as diabetes prevalence increases [134]. In the United States, this cost is much higher at $245 billion for both direct and indirect-related expenses [133].

1.4.4 What are Electrochemical Glucose Sensors?

Due to the prevalence of diabetes worldwide, rapid, selective and reliable methods for the determination of blood glucose levels are essential for diabetes testing, management and treatment. As such, over recent years much research and development has been focused on the production of electrochemical glucose sensors. It is estimated that 85% of the biosensor market is composed of glucose sensors, with

the majority of them utilising the enzyme GOx for the detection and quantification of glucose [135]. A conventional glucose monitor consists of a test strip which is inserted to the glucose meter. These tests strips are electrochemically based and typically consist of working, counter and reference electrodes. It is on this test strip that the glucose sensing takes place [136]. An example of a commercialised glucose monitor by Abbott, which uses disposable test strips, is shown in Figure 1.4 [136].

Figure 1.4: Blood glucose monitor by Abbott [136].

1.4.5 Enzymatic and Non-Enzymatic Sensors

The first enzymatic glucose biosensors were developed in 1962 by Clark and Lyons [137], which indirectly quantified glucose concentrations through the measurement of background oxygen consumed during the oxidation of glucose by GOx. This was quantified by measuring the decrease in the currents obtained from the dissolved background oxygen. Although, the varying concentrations of background oxygen caused problems in this sensing system and as such it was developed further by Updike and Hicks to account for these variations [138]. In their work they used two working electrodes with one covered with GOx to correct for the background oxygen variations. Using this method, the differential currents between the working electrodes were measured. The first amperometric enzyme glucose sensor was developed in 1973 by Guilbault and Lubrano [139] which consisted of GOx immobilized

to an electrode surface using cellophane. This sensor showed accuracy, precision, and stability.

GOx is commonly used in enzymatic glucose sensors. This enzyme contains a large redox active region called the flavin adenine dinucleotied (FAD) centre. It is this centre that enables GOx to detect glucose [126]. Upon interaction with glucose, glucose becomes oxidised to gluconolactone and the FAD region becomes reduced to $FADH_2$, as shown in Equation 1.1 [126]. At this point the FAD centre must be regenerated through oxidation to allow glucose sensing to continue. This can be done using naturally present oxygen in the blood, by reacting with a mediator, or through direct oxidation at the electrode [126]. As such, enzymatic sensors can be grouped into three different generations, first, second and third generations, depending on this FAD regeneration mechanism [126].

$$GOx(FAD) + glucose \rightarrow GOx(FADH_2) + glucolactone \qquad 1.1$$

First generation sensors depend on the presence of oxygen to regenerate the FAD centre and to act as an electron mediator between GOx and the electrode surface. Hydrogen peroxide is produced in this reaction, which is subsequently oxidised at the electrode surface and correlates to the quantity of glucose present. This is described by Equation 1.2 [126].

$$GOx(FADH_2) + O_2 \rightarrow GOx(FAD) + H_2O_2 \qquad 1.2$$

The first generation glucose electrodes suffer from two major issues; the reliance of abundant oxygen in the blood being analysed, which can vary considerably, and the possible interference from various redox species [126, 140]. The potentials used to oxidised hydrogen peroxide are sufficient to oxidise various other species, interferants, found in blood [140]. Shown in Scheme 1.3 is a schematic representation of glucose detection at a first generation glucose sensor containing GOx, taken from Park *et al.* [140].

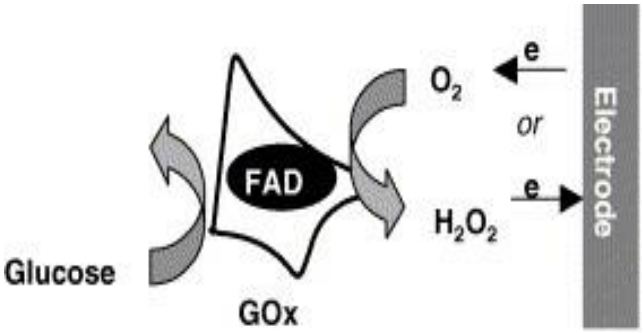

Scheme 1.3: Schematic of a first generation glucose sensor [140].

Due to the issue of oxygen dependence seen in first generation glucose sensors, synthetic redox active mediators can be used for electron transfer and enzyme regeneration [127, 141]. These mediators may include transition metal complexes, including ferrocene and its derivatives, ferricyanide and guinones [141]. An example of the reaction involved between these redox mediators and the reduced FAD domain is shown in Equation 1.3 [141].

$$GOx(FADH_2) + M(ox) \rightarrow GOx(FAD) + M(red) + 2H^+ \qquad 1.3$$

The use of these complexes is suitable as they effectively diffuse to and from the enzyme and electrode surface, they possess lower redox potentials which reduce the possibility of oxidising other interferants present, have high stability and a low toxicity [127]. Although mobility in the electrochemical system is important, it can also be a drawback as problems with leaching into the surrounding solution may occur [141]. Another possible issue in these systems is that the presence of oxygen in the blood sample may also compete with the synthetic redox mediator and contribute to the amount of H_2O_2 produced, thus affecting the sensors accuracy [127]. Also, these mediators may react with certain interferants present in the blood, although they are still less susceptible to interference, in comparison to first generation sensors, due to lower working potentials [141], [127]. Shown in Scheme 1.4 is a schematic representation of glucose detection at a second generation glucose sensor containing GOx, taken from Park *et al.* [140].

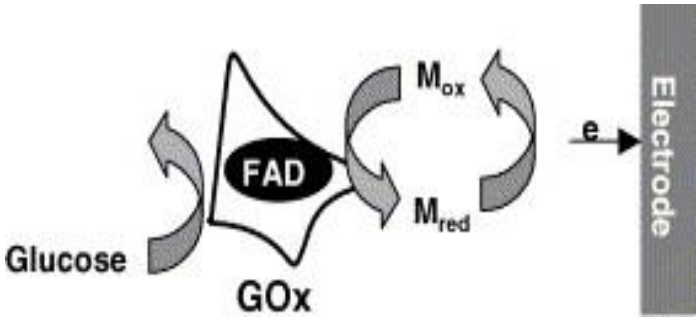

Scheme 1.4: Schematic of a second generation glucose sensor [140].

To overcome the oxygen dependency issues of first generation glucose sensors and the mediator-related issues of the second generation sensors, third generation sensors were developed. These sensors are based on the direct electron transfer between the enzyme and the electrode surface thereby bypassing the need for synthetic mediators or oxygen [140]. An example of a third generation glucose sensors can be seen in work by Zayats *et al.* [142] in which a multi-step process involving the direct electrical contacting of GOx to the electrode surface is reported. The formation of this sensor is multi-stepped, initially involving the self-assembly of pyrroloquinoline quinone (PQQ) electron relay monolayers on the electrode surface, followed by the attachment of a FAD domain and the coupling of this FAD domain with apo-GOx to form the completed GOx enzyme. Apo-GOx is a form of GOx without the redox active FAD domain. This results in an aligned, electrically contacted electrode with exceptional electron-transfer similar to the rates observed between the enzyme with its natural mediator, oxygen. Shown in Scheme 1.5 is a schematic representation of glucose detection at a third generation glucose sensor containing GOx, taken from Zayats *et al* [142].

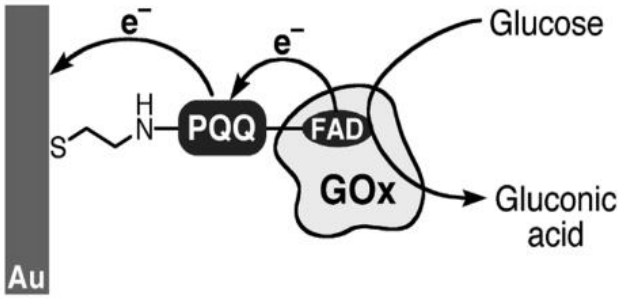

Scheme 1.5: Schematic of a third generation glucose sensor [142].

Although the first, second and third generation enzymatic glucoses sensors provide good selectivity towards glucose, they are still affected by mediator-related issues, oxygen dependency and last but not least, enzyme degradation [140]. Enzymes used such as GOx and glucose dehydrogenase (GDH) exhibit degradation with pH, temperature and humidity changes [140, 143]. These issues may result in inaccurate glucose sensing [140]. One way to possibly resolve these problems and that may provide more accurate glucose detection is to develop enzyme-less sensors, known as non-enzymatic glucose sensors. This is an approach to glucose detection that is gaining much attention as eliminating the use of the enzymes could offer a more stable and accurate glucose detection and also simplicity in sensor design [140, 144]. Rather than facilitating the needs of a delicate and relatively difficult enzyme, non-enzymatic sensors aspire to directly oxidise glucose in the sample [126]. An example of a non-enzymatic glucose sensor comprising Au can be seen in recent work by Prehn *et al.* [135]. In this work it was suggested that the mechanism for the electrocatalytic oxidation of glucose at Au is a multistep process. The most important step involves the chemisorption of OH anions onto the Au surface, forming $AuOH_{ads}$ and it is believed that this adsorbed layer gives Au its catalytic activity towards glucose. The use of Au and other non-enzymatic materials is discussed in further detail in the following sections, Sections 1.4.2.1 – 1.4.2.3. Shown in Scheme 1.6 is a schematic representation of glucose detection at a fourth generation non-enzymatic glucose sensor consisting of Au, taken from Prehn *et al* [135].

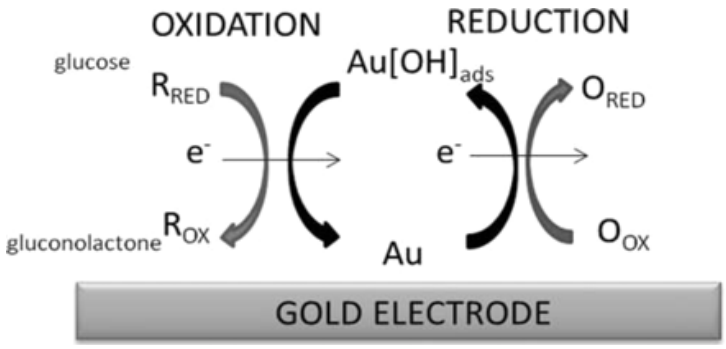

Scheme 1.6: Schematic of a fourth generation glucose sensor [135].

1.4.6 Materials used in Non-Enzymatic Glucose Sensors

1.4.6.1 Metals, Bi-Metallics and Alloys

Enzymatic glucose sensors involving GOx show high sensitivity and selectivity, although as mentioned some disadvantages may exist, including complicated multi-step development procedures, mediator-related issues and thermal and chemical instability [145]. As such much interest over recent years has been paid to the development of non-enzymatic glucose sensors [144]. It has been shown in various works that some noble metals, including Au [77, 135, 146-148] and Pt [149, 150] are useful in these non-enzymatic sensors along with alloys including PtAu [151], PdAu [152], PdCu [153] and various other Au bi-metallics involving Cu, Ag, Ru, Pt, Pd and Cd [154]. Furthermore, many metal oxides, such as CuO [155-158], NiO [145, 159], NiOPt [160] and NiO/TiO_2 [161] have been used for the detection of glucose non-enzymatically.

1.4.6.2 Gold Metal and Detection of Glucose

Au is a frequently used material in non-enzymatic glucose sensing [77, 135, 146-148] and it yields good electroactivity towards the oxidation of glucose, even though it does not possess strong chemisorbing ability due to its filled d orbitals [126]. It even shows better electroactivity in comparison to Pt metal which has also been greatly researched as a non-enzymatic glucose sensing material [126] and it also provides more negative potentials of oxidation in comparison to other substrates [148]. At Au, it has been reported that glucose may be oxidised directly to gluconate, or to gluconolactone

which then can be oxidised to gluconate [146]. Although Au is commonly used in non-enzymatic glucose sensing, the mechanisms of glucose detection are not known exactly and various mechanisms have been suggested, which draw inspiration from detection at Pt metal [162]. One such method has been outlined in work by Zhu *et al.* [76] in which the non-enzymatic detection of glucose was undertaken at an AuNP-CNT-ionic liquid composite film. In this work, a multi-step glucose oxidation process was apparent and various oxidation peaks in the forward and reverse scans were observed for glucose. No reduction peaks for glucose occurred. Zhu *et al.* [76] assigned the oxidation peaks as to an initial oxidation peak, observed in the forward scan, resulting from the electrosorption of glucose at the C1 anomeric carbon onto the Au surface to form an adsorbed intermediate and the subsequent release of the C1 hydrogen atom. These intermediates accumulate on the Au surface and glucose oxidation is inhibited, although as the potential is further scanned in the positive direction, this promotes the formation of OH radicals on the Au surface, forming $Au(OH)_{ads}$, which is believed to be highly catalytically active towards glucose [76, 146, 163, 164]. Zhu *et al.* [76] then suggested that these $(OH)_{ads}$ species may oxidise the adsorbed intermediates thereby yielding fresh Au surfaces for the further oxidation of glucose. This yields the second peak in the forward scan. As more positive potentials are reached, glucose oxidation ceases due to the buildup on Au oxides, which may result in a third peak in the forward scan. Although, during the reverse scan, these oxides are reduced and a fresh Au surface is again exposed. This fresh Au surface results in another glucose oxidation peak, in the reverse scan. Overall in their work, three oxidation peaks occurred in relation to glucose and this detection was carried out at a high pH in NaOH solution. As mentioned, basic media provides more favourable conditions for glucose oxidation possibly due to the increased amounts of $Au(OH)_{ads}$ formed at high pH [76] and it may also increase the % of the β anomer, which may be more sensitive to oxidation [130]. Although much reported work involving non-enzymatic glucose detection at Au and other materials usually conduct glucose detection in alkaline conditions at pHs close to 12 [76, 77, 155, 156, 159, 165, 166], the work discussed in this thesis was successful in detecting glucose at neutral pH in PBS solution.

1.4.6.3 Metal-Carbon Nanotube Composite Materials

As discussed previously, in Sections 1.3.5 and 1.3.8, metal nanoparticles and CNTs show interesting properties individually, although their combination to form composite materials produces a material with characteristics that differ from the comprising materials and are possibly superior [93]. CNTs are frequently used in composite materials due to the varied qualities they can provide including improved strength and electrical conductivity, improved mechanical properties, their low density and high aspect ratio [101] and also due to their modifiable surfaces [13]. The immobilisation of AuNPs onto CNTs to form composite materials with enhanced electrochemical properties has been well reported [73, 74, 106, 167]. In electrochemical systems for non-enzymatic glucose sensing, CNTs are primarily used as high surface area conducting substrates that provide ideal platforms for the localisation of metal nanoparticles and to promote their maximum exposure [76, 126].

Various metal nanoparticle-CNT composites have been reported for use as non-enzymatic glucose sensors. These include Au-CNT composites [76, 165, 168], bi-metallic AuCu-CNT composites [169], PtRu-CNT and PtSn-CNT [170] composites, CuO-CNT [96], Pd-CNT [81, 99] and Pt-CNT [171] composites. Conducing polymer and graphene composites include, Au-polyaniline [109, 172] and Cu-polyaniline composites [173], Au-graphene [91], PtAu-graphene [90], PtNi-graphene [174], Ni-graphene [166] and Ni-chitosan-graphene composites [175].

Overall, Au was chosen as the ideal metal in the form of AuNPs for the non-enzymatic detection of glucose in this thesis work along with its incorporation with multiwalled CNTs to optimise their surface areas. Au is capable of directly oxidising glucose at neutral pH, unlike certain metals including Cu and Ni, which typically work for this purpose at alkaline pH [96, 166, 176]. Pt was neither employed, due to its lesser electroactivity in comparison to Au [126].

1.4.6.4 Nafion®

Interference from negatively charged chemical interferants, including ascorbic acid and uric acid, can be a problem during electrochemical detections [126, 140]. To eliminate interference from these species, the sensors can be coated with Nafion® membranes [126, 172, 177, 178]. Nafion® is a sulfonated Teflon based polymer which carries immobile negative charges. These negative charges arise from the sulfonic groups present in the Nafion® pores. It is these groups that give it its anion-rejection properties, although it is still permeable to cationic and neutrally charged species [179]. Displayed in Figure 1.5 is the chemical structure of Nafion® [180].

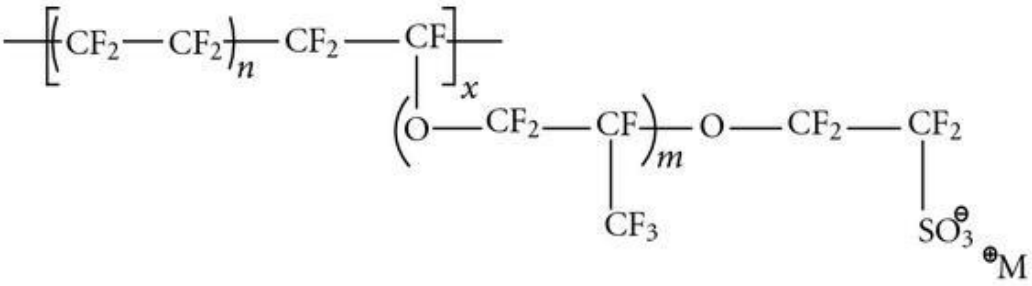

Figure 1.5: Chemical structure of Nafion® [180].

1.5 References

1. A. Moisala, Q. Li, I. A. Kinloch and A. H. Windle, *Composites Science and Technology*, 2006, **66**, 1285-1288.
2. J. Hone, M. C. Llaguno, N. M. Nemes, A. T. Johnson, J. E. Fischer, D. A. Walters, M. J. Casavant, J. Schmidt and R. E. Smalley, *Applied Physics Letters*, 2000, **77**, 666-668.
3. M.-F. Yu, O. Lourie, M. J. Dyer, K. Moloni, T. F. Kelly and R. S. Ruoff, *Science*, 2000, **287**, 637-640.
4. Q. Yuan, L. Li, Q. Li and F. Ding, *The Journal of Physical Chemistry C*, 2013, **117**, 5470-5474.
5. P. R. Bandaru, *Journal of Nanoscience and Nanotechnology*, 2007, **7**, 1239- 1267.
6. A. Oberlin, M. Endo and T. Koyama, *Journal of Crystal Growth*, 1976, **32**, 335-349.
7. S. Iijima, *Nature*, 1991, **354**, 56-58.
8. X. Wang, Q. Li, J. Xie, Z. Jin, J. Wang, Y. Li, K. Jiang and S. Fan, *Nano Letters*, 2009, **9**, 3137-3141.
9. M. Zhang and J. Li, *Materials Today*, 2009, **12**, 12-18.
10. A. Barreiro, C. Kramberger, M. H. Rümmeli, A. Grüneis, D. Grimm, S. Hampel, T. Gemming, B. Büchner, A. Bachtold and T. Pichler, *Carbon*, 2007, **45**, 55-61.
11. D. K. Singh, P. K. Iyer and P. K. Giri, *Diamond and Related Materials*, 2010, **19**, 1281-1288.
12. V. Choudhary and A. Gupta, *Polymer/Carbon Nanotube Nanocomposites, Carbon Nanotubes - Polymer Nanocomposites*, InTech, 2011.
13. M. Vikas, *Carbon Nanotubes Surface Modifications: An Overview, in Surface Modification of Nanotube Fillers*, Wiley-VCH Verlag GmbH & Co. KGaA, Weinheim, Germany, 2011.
14. S. M. Khantimerov, E. F. Kukovitsky, N. A. Sainov and N. M. Suleimanov, *International Journal of Chemical Engineering*, 2013, 4, 157098.
15. R. Zhang, Q. Wen, W. Qian, D. S. Su, Q. Zhang and F. Wei, *Advanced Materials*, 2011, **23**, 3387–3391.
16. C. B. Jacobs, M. J. Peairs and B. J. Venton, *Analytica Chimica Acta*, 2010, **662**, 105-127.
17. M. Steiner, M. Engel, Y.-M. Lin, Y. Wu, K. Jenkins, D. B. Farmer, J. J. Humes, N. L. Yoder, J.-W. T. Seo, A. A. Green, M. C. Hersam, R. Krupke and P. Avouris, *Applied Physics Letters*, 2012, **101**, 053123.
18. V. Sgobba and D. M. Guldi, *Chemical Society Reviews*, 2009, **38**, 165-184.
19. S. Gupta, K. Dharamvir and V. K. Jindal, *Physical Review B*, 2005, **72**, 165428.
20. Z. B. He, J. L. Maurice, C. S. Lee, C. S. Cojocaru and D. Pribat, *Arabian Journal for Science and Engineering*, 2010, **35**, 19.

21. Y. Ando and X. Zhao, *New Diamond and Frontier Carbon Technology*, 2006, **16**, 123-137.
22. M. Kumar and Y. Ando, *Journal of Nanoscience and Nanotechnology*, 2010, **10**, 3739–3758.
23. J. H. Hafner, M. J. Bronikowski, B. R. Azamian, P. Nikolaev, A. G. Rinzler, D. T. Colbert, K. A. Smith and R. E. Smalley, *Chemical Physics Letters*, 1998, **296**, 195-202.
24. A. Szabó, C. Perri, A. Csató, G. Giordano, D. Vuono and J. B. Nagy, *Materials*, 2010, **3**, 3092-3140.
25. O. Salata, *Journal of Nanobiotechnology*, 2004, **2**, 3.
26. J. Zhou, J. Ralston, R. Sedev and D. A. Beattie, *Journal of Colloid and Interface Science*, 2009, **331**, 251-262.
27. F. Xu, L. Zhao, F. Zhao, L. Deng, L. Hu and B. Zeng, *International Journal of Electrochemical Science*, 2014, **9**, 2832-2847.
28. A. Velamakanni, C. W. Magnuson, K. J. Ganesh, Y. Zhu, J. An, P. J. Ferreira and R. S. Ruoff, *ACS Nano*, 2010, **4**, 540-546.
29. Z. Wang, C. Xu, G. Gao and X. Li, *RSC Advances*, 2014, **4**, 13644-13651.
30. M.-C. Daniel and D. Astruc, *Chemical Reviews*, 2003, **104**, 293-346.
31. W. Shen, X. Zhang, Q. Huang, Q. Xu and W. Song, *Nanoscale*, 2014, **6**, 1622- 1628.
32. A. H. Alshehri, M. Jakubowska, A. Młożniak, M. Horaczek, D. Rudka, C. Free and J. D. Carey, *ACS Applied Materials & Interfaces*, 2012, **4**, 7007-7010.
33. D. A. Giljohann, D. S. Seferos, W. L. Daniel, M. D. Massich, P. C. Patel and C. A. Mirkin, *Angewandte Chemie International Edition*, 2010, **49**, 3280-3294.
34. B. Sharma, D. D. Purkayastha, S. Hazra, L. Gogoi, C. R. Bhattacharjee, N. N. Ghosh and J. Rout, *Materials Letters*, 2014, **116**, 94-97.
35. A. I. Lopez-Lorente, B. M. Simonet, M. Valcarcel and B. Mizaikoff, *Analytica Chimica Acta*, 2013, **788**, 122-128.
36. S. Lou, J.-y. Ye, K.-q. Li and A. Wu, *Analyst*, 2012, **137**, 1174-1181.
37. G. Wei, H. Zhou, Z. Liu, Y. Song, L. Wang, L. Sun and Z. Li, *The Journal of Physical Chemistry B*, 2005, **109**, 8738-8743.
38. S. P. Chandran, M. Chaudhary, R. Pasricha, A. Ahmad and M. Sastry, *Biotechnology Progress*, 2006, **22**, 577-583.
39. S. K. Sardana, V. S. N. Chava, E. Thouti, N. Chander, S. Kumar, S. R. Reddy and V. K. Komarala, *Applied Physics Letters*, 2014, **104**, 073903.
40. L.-C. Jiang and W.-D. Zhang, *Biosensors and Bioelectronics*, 2010, **25**, 1402- 1407.
41. S. A. Kumar, H.-W. Cheng, S.-M. Chen and S.-F. Wang, *Materials Science and Engineering: C*, 2010, **30**, 86-91.
42. L.-M. Lu, X.-B. Zhang, G.-L. Shen and R.-Q. Yu, *Analytica Chimica Acta*, 2012, **715**, 99-104.
43. S. Mubeen, T. Zhang, B. Yoo, M. A. Deshusses and N. V. Myung, *The Journal of Physical Chemistry C*, 2007, **111**, 6321-6327.

44. R. K. Petla, S. Vivekanandhan, M. Misra, A. K. Mohanty and N. Satyanarayana, *Journal of Biomaterials and Nanobiotechnology*, 2012, **3**, 14- 19.
45. A. K. Gupta and M. Gupta, *Biomaterials*, 2005, **26**, 3995-4021.
46. M. Mahmoudi, S. Sant, B. Wang, S. Laurent and T. Sen, *Advanced Drug Delivery Reviews*, 2011, **63**, 24-46.
47. N. Lee and T. Hyeon, *Chemical Society Reviews*, 2012, **41**, 2575-2589.
48. B. Nikoobakht and M. A. El-Sayed, *Chemistry of Materials*, 2003, **15**, 1957- 1962.
49. X. Yu, M. Li, M. Xie, L. Chen, Y. Li and Q. Wang, *Nano Research*, 2010, **3**, 51-60.
50. A. M. Showkat, K.-P. Lee, A. I. Gopalan, S.-H. Choi and Y. C. Nho, *Diamond and Related Materials*, 2007, **16**, 1688-1692.
51. W. Lu, S. R. Arumugam, D. Senapati, A. K. Singh, T. Arbneshi, S. A. Khan, H. Yu and P. C. Ray, *ACS Nano*, 2010, **4**, 1739-1749.
52. J. Zeng, Q. Zhang, J. Chen and Y. Xia, *Nano Letters*, 2009, **10**, 30-35.
53. X. Li, H. Xu, Z.-S. Chen and G. Chen, *Journal of Nanomaterials*, 2011, **2011**, 16.
54. J. A. C. Schwarz, Cristian I. Putyera, Karol, *Dekker Encyclopedia of Nanoscience and Nanotechnology, Volume 3*, CRC Press, 2004.
55. J. Zhang, J. Liu, Q. Peng, X. Wang and Y. Li, *Chemistry of Materials*, 2006, **18**, 867-871.
56. A. Kolmakov, D. O. Klenov, Y. Lilach, S. Stemmer and M. Moskovits, *Nano Letters*, 2005, **5**, 667-673.
57. C. Wang, L. Yin, L. Zhang, D. Xiang and R. Gao, *Sensors*, 2010, **10**, 2088- 2106.
58. B. Chertok, B. A. Moffat, A. E. David, F. Yu, C. Bergemann, B. D. Ross and V. C. Yang, *Biomaterials*, 2008, **29**, 487-496.
59. Q. Quan, J. Xie, H. Gao, M. Yang, F. Zhang, G. Liu, X. Lin, A. Wang, H. S. Eden, S. Lee, G. Zhang and X. Chen, *Molecular Pharmaceutics*, 2011, **8**, 1669-1676.
60. M. Vijayakumar, K. Priya, F. T. Nancy, A. Noorlidah and A. B. A. Ahmed, *Industrial Crops and Products*, 2013, **41**, 235-240.
61. M. A. Dar, A. Ingle and M. Rai, *Nanomedicine: Nanotechnology, Biology and Medicine*, 2013, **9**, 105-110.
62. S. Prabhu and E. Poulose, *International Nano Letters*, 2012, **2**, 1-10.
63. H. Lara, E. Garza-Trevino, L. Ixtepan-Turrent and D. Singh, *Journal of Nanobiotechnology*, 2011, **9**, 30.
64. P. Jain, X. Huang, I. El-Sayed and M. El-Sayed, *Plasmonics*, 2007, **2**, 107- 118.
65. M. B. Cortie and A. M. McDonagh, *Chemical Reviews*, 2011, **111**, 3713-3735.
66. D. D. S. Fung, L. Qiao, W. C. H. Choy, C. Wang, W. E. I. Sha, F. Xie and S. He, *Journal of Materials Chemistry*, 2011, **21**, 16349-16356.

67. A. Maringa, E. Antunes and T. Nyokong, *Electrochimica Acta*, 2014, **121**, 93- 101.
68. W. Jin, G. Wu and A. Chen, *Analyst*, 2014, **139**, 235-241.
69. D. Liu, W. Chen, J. Wei, X. Li, Z. Wang and X. Jiang, *Analytical Chemistry*, 2012, **84**, 4185-4191.
70. S. Boca, D. Rugina, A. Pintea, L. Barbu-Tudoran and S. Astilean, *Nanotechnology*, 2011, **22**, 055702.
71. F. Xia, X. Zuo, R. Yang, Y. Xiao, D. Kang, A. Vallée-Bélisle, X. Gong, J. D. Yuen, B. B. Y. Hsu, A. J. Heeger and K. W. Plaxco, *Proceedings of the National Academy of Sciences*, 2010, **107**, 10837-10841.
72. L. Zhao, Y. Jin, Z. Yan, Y. Liu and H. Zhu, *Analytica Chimica Acta*, 2012, **731**, 75-81.
73. N. Alexeyeva, T. Laaksonen, K. Kontturi, F. Mirkhalaf, D. J. Schiffrin and K. Tammeveski, *Electrochemistry Communications*, 2006, **8**, 1475-1480.
74. N. Alexeyeva and K. Tammeveski, *Analytica Chimica Acta*, 2008, **618**, 140- 146.
75. C. Liu, H. Cao, Y. Li and Y. Zhang, *Journal of New Materials for Electrochemical Systems*, 2006, **9**, 139-144.
76. H. Zhu, X. Lu, M. Li, Y. Shao and Z. Zhu, *Talanta*, 2009, **79**, 1446-1453.
77. G. Chang, H. Shu, K. Ji, M. Oyama, X. Liu and Y. He, *Applied Surfice Science*, 2014, **288**, 524-529.
78. A. Kumar, H. Ma, X. Zhang, K. Huang, S. Jin, J. Liu, T. Wei, W. Cao, G. Zou and X.-J. Liang, *Biomaterials*, 2012, **33**, 1180-1189.
79. Y. Song, G. Liu, J. Wang, X. Dong and W. Yu, *Physical Chemistry Chemical Physics*, 2014, **16**, 15139-15145.
80. J. Lan, W. Xu, Q. Wan, X. Zhang, J. Lin, J. Chen and J. Chen, *Analytica Chimica Acta*, 2014, **825**, 63-68.
81. X.-M. Chen, Z.-J. Lin, D.-J. Chen, T.-T. Jia, Z.-M. Cai, X.-R. Wang, X. Chen, G.-N. Chen and M. Oyama, *Biosensors and Bioelectronics*, 2010, **25**, 1803- 1808.
82. J. Turkevich, P. C. Stevenson and J. Hillier, *Discussions of the Faraday Society*, 1951, **11**, 55-75.
83. G. Frens, *Nature Physical Science*, 1973, **241**, 20-22.
84. D. Ghosh and N. Chattopadhyay, *Optics and Photonics Journal*, 2013, **3**, 28878.
85. S. Kumar, J. Aaron and K. Sokolov, *Nature Protocols*, 2008, **3**, 314-320.
86. B. Kumar, K. Smita, L. Cumbal, A. Debut and R. N. Pathak, *Bioinorganic Chemistry and Applications*, 2014, **2014**, 8.
87. R. Zhang, M. Hummelgård and H. Olin, *Materials Science and Engineering: B*, 2009, **158**, 48-52.
88. E. Spain, T. E. Keyes and R. J. Forster, *Biosensors and Bioelectronics*, 2013, **41**, 65-70.
89. J.-J. Lv, S.-S. Li, A.-J. Wang, L.-P. Mei, J.-R. Chen and J.-J. Feng, *Electrochimica Acta*, 2014, **136**, 521-528.

90. J. Leng, W.-M. Wang, L.-M. Lu, L. Bai and X.-L. Qiu, *Nanoscale Research Letters*, 2014, **9**, 99.
91. C. Du, Z. Yao, Y. Chen, H. Bai and L. Li, *RSC Advances*, 2014, **4**, 9133-9138.
92. X. Chen, H. Pan, H. Liu and M. Du, *Electrochimica Acta*, 2010, **56**, 636-643.
93. S. D. Sharma, *International Journal of Mechanical Engineering and Robotics Research*, 2014, **3**, 129-133.
94. W. Guo, C. Liu, X. Sun, Z. Yang, H. G. Kia and H. Peng, *Journal of Materials Chemistry*, 2012, **22**, 903-908.
95. X. Wang, P. D. Bradford, W. Liu, H. Zhao, Y. Inoue, J.-P. Maria, Q. Li, F.-G. Yuan and Y. Zhu, *Composites Science and Technology*, 2011, **71**, 1677-1683.
96. Z. Asadbeigi, A. Khodadadi, M. Vesali-Naseh, *IMCS 2012 – The 14th International Meeting on Chemical Sensors*, 2012, 866-868.
97. L. Ruiyi, X. Qianfang, L. Zaijun, S. Xiulan and L. Junkang, *Biosensors and Bioelectronics*, 2013, **44**, 235-240.
98. N. Jia, B. Huang, L. Chen, L. Tan and S. Yao, *Sensors and Actuators B: Chemical*, 2014, **195**, 165-170.
99. L. Meng, J. Jin, G. Yang, T. Lu, H. Zhang and C. Cai, *Analytical Chemistry*, 2009, **81**, 7271-7280.
100. L.-H. Li and W.-D. Zhang, *Microchimica Acta*, 2008, **163**, 305-311.
101. Z. Spitalsky, D. Tasis, K. Papagelis and C. Galiotis, *Progress in Polymer Science*, 2010, **35**, 357-401.
102. C. Wang, M. Waje, X. Wang, J. M. Tang, R. C. Haddon and Yan, *Nano Letters*, 2003, **4**, 345-348.
103. D. Du, M. Wang, J. Cai, Y. Qin and A. Zhang, *Sensors and Actuators B: Chemical*, 2010, **143**, 524-529.
104. M. Moreno-Guzmán, L. Agüí, A. González-Cortés, P. Yáñez-Sedeño and J. M. Pingarrón, *Journal of Solid State Electrochemistry*, 2013, **17**, 1591-1599.
105. S. Yang, Y. Yin, G. Li, R. Yang, J. Li and L. Qu, *Sensors and Actuators B: Chemical*, 2013, **178**, 217–221.
106. A. Afkhami, F. Soltani-Felehgari, T. Madrakian and H. Ghaedi, *Biosensors and Bioelectronics*, 2014, **51**, 379–385.
107. A. Afkhami, F. Soltani-Felehgari and T. Madrakian, *Sensors and Actuators B: Chemical*, 2014, **196**, 467–474.
108. N. F. Atta, A. Galal and E. H. El-Ads, *International Journal of Electrochemcial Science*, 2014, **9**, 2113 - 2131.
109. V. Mazeiko, A. Kausaite-Minkstimiene, A. Ramanaviciene, Z. Balevicius and A. Ramanavicius, *Sensors and Actuators B: Chemical*, 2013, **189**, 187-193.
110. L. Li, S. Wang, T. Yang, S. Huang and J. Wang, *Biosensors and Bioelectronics*, 2012, **33**, 279-283.
111. J. Narang, N. Chauhan and C. S. Pundir, *Analyst*, 2011, **136**, 4460-4466.
112. Y.-G. Zhou, S. Yang, Q.-Y. Qian and X.-H. Xia, *Electrochemistry Communications*, 2009, **11**, 216-219.
113. G.-Z. Hu, L. Chen, Y. Guo, X.-L. Wang and S.-J. Shao, *Electrochimica Acta*, 2010, **55**, 4711-4716.

114. L. Xiao, G. G. Wildgoose and R. G. Compton, *Analytica Chimica Acta*, 2008, **620**, 44-49.
115. H. Xu, L. Zeng, S. Xing, G. Shi, Y. Xian and L. Jin, *Electrochemistry Communications*, 2008, **10**, 1839-1843.
116. D. Du, W. Chen, W. Zhang, D. Liu, H. Li and Y. Lin, *Biosensors and Bioelectronics*, 2010, **25**, 1370-1375.
117. X. Feng, J. Hu, X. Chen, J. Xie and Y. Liu, *Journal of Physics D: Applied Physics*, 2009, **42**, 042001.
118. S. Park, H. R. Kim, J. Kim, C. Jung, C. K. Rhee, K. Kwon and Y. Kim, *Carbon*, 2011, **49**, 487-494.
119. D. H. Marsh, G. A. Rance, R. J. Whitby, F. Giustiniano and A. N. Khlobystov, *Journal of Materials Chemistry*, 2008, **18**, 2249-2256.
120. G. A. Rance and A. N. Khlobystov, *Dalton Transactions*, 2014, **43**, 7400-7406.
121. B. Wu, Z. Ou, X. Ju and S. Hou, *Journal of Nanomaterials*, 2011, **2011**, 6.
122. E. Solomon, C. Martin, D. Martin and L. Berg, *Biology*, Cengage Learning, 2014.
123. S. Vashist, *Diagnostics*, 2013, **3**, 385-412.
124. C. Wang, L. Lv, Y. Yang, D. Chen, G. Liu, L. Chen, Y. Song, L. He, X. Li, H. Tian, W. Jia and X. Ran, *Clinical Endocrinology*, 2012, **76**, 810-815.
125. C. Wolf, *Dynamic Stereochemistry of Chiral Compounds: Principles and Applications*, Royal Society of Chemistry, 2008.
126. K. E. Toghill and a. R. G. Compton, *International Journal of Electrochemical Science*, 2010, **5**, 1246-1301
127. A. M. Silva, E. C. da Silva and C. O. da Silva, *Carbohydrate Research*, 2006, **341**, 1029-1040.
128. C. E. Perles and P. L. O. Volpe, *Journal of Chemical Education*, 2008, **85**, 686-688.
129. S. B. Bankar, M. V. Bule, R. S. Singhal and L. Ananthanarayan, *Biotechnology Advances*, 2009, **27**, 489-501.
130. F. Largeaud, K. B. Kokoh, B. Beden and C. Lamy, *Journal of Electroanalytical Chemistry*, 1995, **397**, 261-269.
131. J. E. Shaw, R. A. Sicree and P. Z. Zimmet, *Diabetes Research and Clinical Practice*, 2010, **87**, 4-14.
132. K. P. Balanda, A. Jordon and E. McArdle, *Making Diabetes count A systemic approach to estimating population prevalence on the island of Ireland in 2005*, 2006.
133. C. f. D. C. a. Prevention, *National Diabetes Statistics Report: Estimates of Diabetes and Its Burden in the United States, 2014*, 2014.
134. J. J. Nolan, T. J. O'Halloran D Fau - McKenna, R. McKenna Tj Fau - Firth, S. Firth R Fau - Redmond and S. Redmond, *Irish Medical Journal*, 2006, **99**, 307- 310.
135. R. Prehn, M. Cortina-Puig and F. X. Muñoz, *Journal of The Electrochemical Society*, 2012, **159**, F134-F139.

136. S. L. Schwartz, R. M. Bernstein, E. Taylor, J. Ward, S. Alva and R. Ng, *Evaluation of the FreeStyle® Lite Blood Glucose Monitoring System* 2007.
137. L. C. Clark and C. Lyons, *Annals of the New York Academy of Sciences*, 1962, **102**, 29-45.
138. S. J. Updike and G. P. Hicks, *Nature*, 1967, **214**, 986-988.
139. G. G. Guilbault and G. J. Lubrano, *Analytica Chimica Acta*, 1973, **64**, 439- 455.
140. S. Park, H. Boo and T. D. Chung, *Analytica Chimica Acta*, 2006, **556**, 46-57.
141. A. Chaubey and B. D. Malhotra, *Biosensors and Bioelectronics*, 2002, **17**, 441- 456.
142. M. Zayats, E. Katz and I. Willner, *Journal of the American Chemical Society*, 2002, **124**, 2120-2121.
143. D.-M. Kim, M.-y. Kim, S. S. Reddy, J. Cho, C.-h. Cho, S. Jung and Y.-B. Shim, *Analytical Chemistry*, 2013, **85**, 11643-11649.
144. A. Sun, J. Zheng and Q. Sheng, *Electrochimica Acta*, 2012, **65**, 64-69.
145. S. Liu, B. Yu and T. Zhang, *Electrochimica Acta*, 2013, **102**, 104-107.
146. M. Pasta, F. La Mantia and Y. Cui, *Electrochimica Acta*, 2010, **55**, 5561-5568.
147. Y. Li, Y.-Y. Song, C. Yang and X.-H. Xia, *Electrochemistry Communications*, 2007, **9**, 981-988.
148. M. Tominaga, M. Nagashima, K. Nishiyama and I. Taniguchi, *Electrochemistry Communications*, 2007, **9**, 1892-1898.
149. S. H. Kim, J. B. Choi, Q. N. Nguyen, J. M. Lee, S. Park, T. D. Chung and J. Y. Byun, *Physical Chemistry Chemical Physics*, 2013, **15**, 5782-5787.
150. J. Segyeong, P. Sejin, D. Taek, Chung and C. Hee, Kim, *ANALYTICAL SCIENCES*, 2007, **23**, 227-281.
151. H. Qiu and X. Huang, *J. Electroanal. Chem.*, 2010, **643**, 39-45.
152. N. Tavakkoli and S. Nasrollahi, *Australian Journal of Chemistry*, 2013, **66**, 1097-1104.
153. W. Wang, Z. Li, W. Zheng, J. Yang, H. Zhang and C. Wang, *Electrochemistry Communications*, 2009, **11**, 1811-1814.
154. S. B. Aoun, Z. Dursun, T. Koga, G. S. Bang, T. Sotomura and I. Taniguchi, *Journal of Electroanalytical Chemistry*, 2004, **567**, 175-183.
155. B. Qi, H. Yang, K. Zhao, M. M. Bah, X. Bo and L. Guo, *Journal of Electroanalytical Chemistry*, 2013, **700**, 24-29.
156. Z. Ibupoto, K. Khun, V. Beni, X. Liu and M. Willander, *Sensors*, 2013, **13**, 7926-7938.
157. Z. Zhuang, X. Su, H. Yuan, Q. Sun, D. Xiao and M. M. F. Choi, *Analyst*, 2008, **133**, 126-132.
158. L. D. Burke, G. M. Bruton and J. A. Collins, *Electrochimica Acta*, 1998, **44**, 1467-1479.
159. C. Guo, Y. Wang, Y. Zhao and C. Xu, *Analytical Methods*, 2013, **5**, 1644- 1647.
160. Y. Ding, Y. Liu, L. Zhang, Y. Wang, M. Bellagamba, J. Parisi, C. M. Li and Y. Lei, *Electrochimica Acta*, 2011, **58**, 209-214.

161. Z.-D. Gao, Y. Han, Y. Wang, J. Xu and Y.-Y. Song, *Scientific Reports*, 2013, **3**.
162. Y. B. Vassilyev, O. A. Khazova and N. N. Nikolaeva, *Journal of Electroanalytical Chemistry and Interfacial Electrochemistry*, 1985, **196**, 127- 144.
163. F. Matsumoto, M. Harada, N. Koura and S. Uesugi, *Electrochemistry Communications*, 2003, **5**, 42-46.
164. I. G. Casella, M. R. Guascito and M. G. Sannazzaro, *Journal of Electroanalytical Chemistry*, 1999, **462**, 202-210.
165. A. F.-j. Jou, N.-H. Tai and J.-a. A. Ho, *Electroanalysis*, 2014, **26**, 1816-1823.
166. Y. Zhang, X. Xiao, Y. Sun, Y. Shi, H. Dai, P. Ni, J. Hu, Z. Li, Y. Song and L. Wang, *Electroanalysis*, 2013, **25**, 959-966.
167. X. Hou, L. Wang, X. Wang and Z. Li, *Diamond and Related Materials*, 2011, **20**, 1329-1332.
168. M. Gougis, A. Tabet-Aoul, D. Ma and M. Mohamedi, *Sensors and Actuators B: Chemical*, 2014, **193**, 363-369.
169. D. Liu, Q. Luo and F. Zhou, *Synthetic Metals*, 2010, **160**, 1745-1748.
170. S.-Y. Kwon, H.-D. Kwen and S.-H. Choi, *Journal of Sensors*, 2012, **2012**, 8.
171. D. Rathod, C. Dickinson, D. Egan and E. Dempsey, *Sensors and Actuators B: Chemical*, 2010, **143**, 547-554.
172. C. Liao, M. Zhang, L. Niu, Z. Zheng and F. Yan, *J. Mater. Chem. B*, 2013, **1**, 3820-3829.
173. S. T. Farrell and C. B. Breslin, *Electrochimica Acta*, 2004, **49**, 4497-4503.
174. H. Gao, F. Xiao, C. B. Ching and H. Duan, *ACS Applied Materials & Interfaces*, 2011, **3**, 3049-3057.
175. J. Yang, J.-H. Yu, J. Rudi Strickler, W.-J. Chang and S. Gunasekaran, *Biosensors and Bioelectronics*, 2013, **47**, 530-538.
176. X. Kang, Z. Mai, X. Zou, P. Cai and J. Mo, *Analytical Biochemistry*, 2007, **363**, 143-150.
177. M. Vidotti, L. H. Dall'Antonia, E. P. Cintra and S. I. Córdoba de Torresi, *Electrochimica Acta*, 2004, **49**, 3665-3670.
178. H. Dai, X. Wu, H. Xu, M. Wei, Y. Wang and G. Chen, *Electrochemistry Communications*, 2009, **11**, 1599-1602.
179. J. Janata, *Principles of Chemical Sensors*, Springer, 2010.
180. V. Romero, M. V. Martínez de Yuso, A. Arango, E. Rodríguez-Castellón and J. Benavente, *International Journal of Electrochemistry*, 2012, **2012**, 9.

Chapter 2

Experimental

2.1 Introduction

The main focus of this research was related to the synthesis and characterisation of composite materials for applications in the non-enzymatic detection of glucose in a phosphate buffer solution (PBS) at physiological pH of 7.4. Composites containing pristine multiwalled carbon nanotube (MWCNTs) and functionalised multiwalled carbon nanotubes (fMWCNTs) with gold (AuNPs) and palladium nanoparticles (PdNPs) were produced using various synthetic and electrochemical methods and were used to form the glucose sensing films on both glassy carbon (GC) electrodes and screen printed electrode (SPEs). Nafion® was used to aid in selectivity in the presence of chemical interferants. All details relating to the synthesis, application and characterisation of the composite materials are discussed in the following sections along with a description and background of each experimental technique used.

2.2 Experimental Procedures

2.2.1 Chemicals and Materials

The chemicals used throughout this study were purchased primarily from Sigma-Aldrich. Millipore water was used in all aqueous solutions. The working counter and reference electrodes were produced by CH instruments and were purchased from IJ Cambria Scientific Ltd. The screen printed electrodes were produced by DropSens and purchased through Metrohm. Displayed in Table 2.1 is a list of chemicals and materials used throughout this research project and the suppliers. For clarity the chemicals and materials are divided into sections depending on their use.

Table 2.1: List of chemicals and materials used in this study.

Chemicals and Materials	Supplier
Buffers and Electrolytes	
Sodium phosphate dibasic hexahydrate (98-102%)	Sigma-Aldrich
Sodium phosphate monobasic monohydrate (98-102%)	Sigma-Aldrich
Sodium chloride (>98%)	Sigma-Aldrich
Sodium hydroxide (98%)	Sigma-Aldrich
Sulfuric Acid (98%)	Merck
Composite Syntheses	
MWCNTs (>99%)	Sigma-Aldrich
Gold(III) chloride trihydrate (≥99.9%)	Sigma-Aldrich
Palladium(II) sulfate (98%)	Sigma-Aldrich
Sodium borohydride (≥98%)	Sigma-Aldrich
Trisodium citrate dihydrate (99%)	Sigma-Aldrich
Sodium dodecyl sulfate (98%)	Sigma-Aldrich
Nafion® 117 solution ~5%	Sigma-Aldrich
Nitric Acid (69%)	Sigma-Aldrich
Glucose Detection and Interference Studies	
α-D-(+)-glucose (ACS)	Sigma-Aldrich
L-(+)-ascorbic acid (>99%)	Sigma-Aldrich
Uric Acid (≥99%)	Sigma-Aldrich
D-(-)-fructose (>99%)	Sigma-Aldrich
D-(+)-galactose (≥99%)	Sigma-Aldrich
Acetaminophen (≥99.9%)	Sigma-Aldrich
Bovine Serum Albumin Powder (≥96%)	Sigma-Aldrich
Characterisation Work	
Hydrochloric Acid (37%)	Merck
Gold standard for AAS. 1 mg/ml Au in 10-20% HCl	Acros Organics
Potassium Ferrocyanide trihydrate (≥98.5%)	Sigma-Aldrich
Potassium Bromide FT-IR grade (≥99%)	Sigma-Aldrich
Whatman 0.45 µm Nylon membrane	Sigma-Aldrich
Acrodisc® 13 mm Syringe Filters with 0.45 µm GHP Membrane	Pall Life Sciences
Holey carbon on 300 mesh copper grids	Agar Scientific
Electrodes	
CHI Gold, Copper and Glassy Carbon working electrodes (99.99%) (d = 3 mm)	IJ Cambria
Platinum wire (99.95%)	Fisher Scientific
Saturated Calomel Reference	Thermo Scientific
Dropsens SPEs (DRP-150 and DRP-110OMC)	Metrohm
Alluminium Chloride (≥99%)	Sigma-Aldrich
Iron(III) chloride hexahydrate (≥98%)	Sigma-Aldrich
10" MicroCloth® PSA	Buehler

2.2.2 Phosphate Buffers

Phosphate buffer solutions (PBS) with and without saline (NaCl) were used. Both buffer solutions were produced using a 0.07:0.03 molar ratio of Na_2HPO_4:NaH_2PO_4 salts to produce a 0.10 M PBS solution just below pH 7.4. NaCl of 0.10 M was added to this buffer to produce the phosphate buffer saline buffer. The pH was adjusted to pH 7.4 using a NaOH solution.

2.2.3 Electrochemical Setup

Cyclic voltammetry (CV), potentiostatic experiments and constant potential amperometry (CPA), were performed using a conventional three electrode cell consisting of a glassy carbon (GC) working electrode (d = 3 mm), a high surface area platinum (Pt) counter electrode and a saturated calomel (SCE) reference electrode. The GC working electrodes were modified with the composite materials. These experiments were also performed using composite modified screen printed electrodes (SPEs), which consisted of a printed carbon working electrode (d = 4 mm), silver/silver chloride (Ag/AgCl) reference electrode and a platinum counter electrode. These three electrode systems were immersed into glass cells in which the electrolytes and analytes were added. Shown in Figure 2.1 (a) is a typical three electrode setup within a glass cell, taken from Wei *et al.* [1] and Figure 2.1 (b) displays an example of DropSens screen printed electrode also containing the three components [2]. It should be noted that the SPEs originally contained an Ag referenced electrode, although this was converted to an Ag/AgCl electrode for stability through chloridation using Fe(III) chloride as reported by Polk *et al.* [3]. A high concentration of Fe(III) chloride, made in deionised water, was cast onto the Ag reference electrode until a dark purple-grey colour was reached. The salt was then washed off using deionised water.

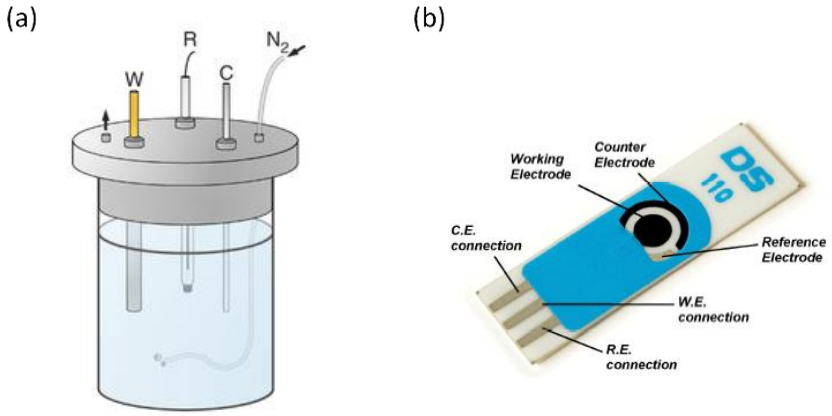

Figure 2.1: Representation of **(a)** a three electrode cell, consisting of a working (W), counter (C) and reference (R) electrode [1], and **(b)** a screen printed electrode also consisting of a working (W), counter (C) and reference (R) electrode [2].

2.2.4 Instrumentation and Software

Electrochemical experiments for potentiometry and CV were performed on a Solartron SI 1287 potentiostat. The Solartron Potentiostat used Scribner Associates Corrware® for Windows Version 2.1 and the resulting data in all cases were analysed using Scribner Associates CorrView® version 3.0. Electrochemical impedance spectroscopy (EIS) was also undertaken on this potentiostat although it was coupled with a frequency response analyser model SI 1250. Scribner Associates ZPlot® version 2.1 was used for this work and ZView® 2.1 was used for data analysis. CPA experiments were performed on a CH Instruments CHI 760C potentiostat using CHI 760C software and CPA data was also analysed using this same software. Plotting and analysis of experimental data was carried out using Microsoft Excel 2010. All other experimental instruments and the models used are listed in Table 2.2.

Table 2.2: Experimental instruments and models used in this study.

Instrument	Model
Potentiostat	Solartron SI 1287 and CH Instruments CHI 760C
UV-Vis Spectrophotometer	Varian Cary 50 UV-Vis
pH Meter	Jenway 370 Enterprise
Sonicator	Branson 1510
Electronic Balance	Sartorius Models TE 2145
Conductivity Meter	Jenway 4510
Hotplate and Stirrer	Stuart CC162
Gold Sputter Coater	Emitech K550x / Agar Scientific
SEM	Hitachi S-3200-N
EDX	Oxford Instrument INCAx-act
TEM	FEI Titan
XRD	PANalytical X'Pert PRO MPD
FT-IR	Perkin Elmer 2000 FT-IR
FAAS	Perkin Elmer Precisely AAnalyst
Raman	LabRAM high resolution
EIS	Solartron SI 1287 coupled with Solartron SI 1255B Frequency Response Analyser

2.2.5 Synthesis of MWCNT-Au_{nano} and fMWCNT-Au_{nano} Composites

2.2.5.1 Functionalisation of Multiwalled Carbon Nanotubes

Prior to the acid reflux, pristine MWCNTs (>99%) were de-aggregated in 69% HNO_3 (5 mg/ml) for 30 min using ultrasonication. This dispersion was then refluxed at 120 ^{o}C for periods of 18, 24 and 48 h. This was undertaken in an oil bath which was heated using a temperature controlled Stuart CC162 hotplate and stirrer. The resulting acid functionalised MWCNTs, named fMWCNTs, were extracted from the acid and purified using centrifugation with repeated cycles of dilution with Millipore water, until the pH was approximately neutral. These fMWCNTs were then isolated on a 0.45 µm Whatman® membrane and again washed with water. This sample was then dried under an infrared lamp and stored in a desiccator.

Studies by Wang *et al.*[4] show that refluxing MWCNTs in concentrated HNO_3 for more than 9 h, produces mainly carboxylic functionalities, although some phenol and lactone functionalities also exist. It has also been shown in work by Saleh [5], that refluxing at 120 ^{o}C in concentrated HNO_3 provides optimum acidic group coverage.

2.2.5.2 Synthesis of pristine, 18 h, 24 h and 48 h fMWCNT-Au_{nano} using Sodium Borohydride

To produce the pristine MWCNT-Au_{nano} composite using the $NaBH_4$ synthesis, the MWCNTs were firstly dispersed into a 1.0% SDS solution (20 ml) at a concentration of 0.5 mg/ml, using ultrasonication to yield a homogeneous and stable dispersion. To this solution under magnetic stirring, a volume of a 1.0% w/v gold(III) chloride trihydrate (≥99.9%) ($HAuCl_4.3H_2O$) solution (600 µl) and 0.75% w/v sodium borohydride (≥98%) ($NaBH_4$) solution (600 µl), were added successively. After 5 min, the resulting composite was then isolated on a 0.45 µm pore size Whatman® membrane and purified using copious amounts of Millipore water. The obtained material named pristine MWCNT-Au_{nano}($NaBH_4$) was fully dried using an infrared lamp and stored in a desiccator.

To produce the 18, 24 and 48 h fMWCNT-Au_{nano} composites using the $NaBH_4$ synthesis, the synthetic procedure discussed above was followed, although the fMWCNTs refluxed for 18, 24 and 48 h were substituted in place of the pristine MWCNTs. The same isolation, purification and drying procedures were used. These composites were named 18 h fMWCNT-Au_{nano}($NaBH_4$), 24 h fMWCNT-Au_{nano}($NaBH_4$) and 48 h fMWCNT-Au_{nano}($NaBH_4$).

2.2.5.3 Synthesis of fMWCNT-Au_{nano} using Trisodium Citrate

The fMWCNT-Au_{nano} composite produced using the trisodium citrate synthesis was quite different to that for the $NaBH_4$ synthesis mentioned previously. Also, only the 24 h fMWCNTs were used.

In the synthesis, the 24 h fMWCNTs (25 mg) were firstly dispersed into a 1.0% $HAuCl_4$ solution (7.88 ml) for a period of 15 min using ultrasonication. This initial

process was undertaken as studies by Zhang and Wang [6] using a similar pre-mixing step show that this could induce the adsorption of $HAuCl_4$ molecules on the nanotubes, thereby stimulating the growth of AuNPs on the CNTs surfaces once trisodium citrate is added. After this pre-mixing step, the mixture was diluted to 100 ml in 1.0% SDS, forming a 0.25 mg/ml dispersion, and this mixture was dispersed for 15 min using ultrasonication. This solution was then transferred into a three-necked round bottom flask and heated to 100 ^{o}C, under magnetic stirring, in a temperature controlled oil bath. A hot solution of 1.0% trisodium citrate (20 ml) was added quickly through the septum and when the temperature again reached 100 ^{o}C, the reaction was left to reflux for 5 min. The resulting composite was then isolated on a 0.45 µm pore size Whatman® membrane and purified using copious amounts of Millipore water. The filtrate presented a wine red colour. The material, named fMWCNT-Au_{nano}(TriSodCit), was fully dried using an infrared lamp and stored in a desiccator.

2.2.6 Formation of MWCNT-Au_{nano} and fMWCNT-Au_{nano} Films on Electrodes

Prior to casting onto the electrode surfaces, the composites were dispersed in 1.0% SDS solutions by use of ultrasonication for 15 min. These casting dispersions were initially produced at a concentration of 2 mg/ml for the pristine MWCNT-Au_{nano}($NaBH_4$) composite and for the 18 h, 24 h and 48 h fMWCNT-Au_{nano}($NaBH_4$) composites, although this was increased to 4 mg/ml for the 24 h fMWCNT-Au_{nano}($NaBH_4$) composite. The fMWCNT-Au_{nano}(TriSodCit) composite, which used the 24 h fMWCNTs, was dispersed in 1.0% SDS at a concentration of 4 mg/ml. In all work, the dispersion concentrations and the casting volumes used to form the modified electrodes are mentioned.

2.2.6.1 Glassy Carbon Electrodes

In all cases, a volume of 5 µl of the 2 mg/ml and 4 mg/ml dispersions was cast onto the GC electrode (d = 3 mm) and this was left to dry fully under an infrared lamp.

2.2.6.2 Carbon Screen Printed Electrodes

Two types of screen printed electrodes (SPEs) were used, the DRP150 SPE consisting of a flat carbon working electrode and the DRP-110OMC SPE consisting of an ordered macroporous carbon working electrode. Only the 4 mg/ml dispersion of the 24 h fMWCNT-Au_{nano}($NaBH_4$) composite was used to modify these electrodes. Due to the larger working electrodes present on these SPEs, a volume of 10 µl of the 4 mg/ml dispersion was cast onto the working electrodes. This was left to dry fully under an infrared lamp.

2.2.6.3 Electrochemical Pre-treatments

All composite modified GC electrodes and SPEs were initially subjected to an electrochemical pre-treatment in 0.3 M NaOH to remove the adsorbed SDS in the composite films. In all work involving the modified GC electrodes, this was carried out using CV by cycling the potential between -0.40 V to 0.60 V vs. SCE at 100 mV s^{-1} for 50 cycles. In work involving the modified SPEs, again 50 cycles were used, although the potential range was adapted to -0.53 V to 0.47 V vs. Ag/AgCl at 100 mV s^{-1}.

After this NaOH step, the modified electrodes were cycled in a 0.10 M PBS solution (pH 7.4) until a steady state current response was achieved. In work involving the modified GC electrodes, this was carried out using CV by cycling the potential between -0.40 V to 0.60 V vs. SCE at 100 mV s^{-1} for approximately 15 cycles. When using the SPEs, this window was altered to -0.65 V to 0.35 V vs. Ag/AgCl at 100 mV s^{-1}, again for approximately 15 cycles.

Electrochemical pre-treatments in H_2SO_4 were carried out as a cleaning step [7]. These pre-treatments were not used in initial studies, but were eventually employed as standard cleaning steps. Cycling in 0.5 M H_2SO_4 was initially employed, although further studies used 1.0 M H_2SO_4. The electrodes were cycled in this acid until a stable background response was achieved. An electrochemical window of between 0.00 V to 1.40 V vs. SCE at 100 mV s^{-1} for 11 cycles was used for cleaning of the modified GC electrodes. This was altered to -0.20 V to 1.20 V vs. Ag/AgCl at 100 mV s^{-1} for

11 cycles for the modified SPEs. After this step, the cycling in PBS was used to obtain a stable background response. The composite films using the 1.0 M H_2SO_4 pre-treatment are often referred to as 'optimsed' films.

2.2.6.4 Coating with Nafion®

All Nafion® coatings were produced using drop cast methods. Prior to casting, the Nafion® 117 solution was diluted by 50% in ethanol absolute. This produced a solution that was easier to cast over the composite films and that was sufficient to reduce chemical interference. Nafion® was only cast onto the films once the relevant electrochemical pre-treatments were carried out. A 5 µl volume was used to cast over the modified GC electrodes and this was sufficient to cover both the working electrode and the surrounding insulating layer, as determined visually. A smaller volume of 3 µl was used to coat the carbon working electrodes of the SPEs. This volume did not cover the surrounding counter and reference electrodes. Once coated, the Nafion® was left to dry at room temperature and the electrodes were then cycled in 0.1 M PBS (pH 7.4) using the relevant potential windows discussed in Section 2.2.6.3. This was carried out for approximately 50 cycles or until stable background currents were obtained.

2.2.7 Synthesis of fMWCNT-Au_{nano}/Pd_{nano} Composite Films

The fMWCNT-Au_{nano}/Pd_{nano} composite was synthesised using a different methodology, as outlined previously for the fMWCNT-Au_{nano} composites. It was produced by electrodepositing palladium (Pd) directly onto the surface of pre-existing fMWCNT-Au_{nano} composite modified GC electrodes and SPEs. These pre-existing fMWCNT-Au_{nano} films were produced on GC electrodes and the SPEs using the 4 mg/ml 24 h fMWCNT-Au_{nano}($NaBH_4$) composite dispersions in SDS, as discussed in Sections 2.2.6.1 and 2.2.6.2, respectively. Prior to Pd electrodeposition, the standard 0.3 M NaOH pre-treatment and the 1.0 M H_2SO_4 pre-treatments, as outlined in Section 2.2.6.3, were used to optimise the films.

Pd electrodeposition on modified GC films was accomplished by applying a potential of 0.45 V vs. SCE for various times of 60, 120, 180 and 240 s in an 2.5 mM $PdSO_4$

solution made in a 0.5 M H_2SO_4. For deposition on composite modified SPEs, the potential was altered to -0.10 V vs. Ag/AgCl. These resulting films, called fMWCNT-Au_{nano}/Pd_{nano}, were then cycled in 0.1 M PBS (pH 7.4), as discussed in Section 2.2.6.3, for stabilisation of the background currents.

2.2.8 Electrodetection of Glucose

2.2.8.1 Cyclic Voltammetry

Prior to glucose detection, all films were subjected to cycling in 0.1 M PBS (pH 7.4). In the systems using the fMWCNT-Au_{nano} and fMWCNT-Au_{nano}/Pd_{nano} composite modified GC electrodes, an electrochemical window of -0.40 V to 0.60 V vs. SCE at 100 mV s^{-1} was used and films were cycled until stable background responses were obtained. This window was altered to -0.65 V to 0.35 V vs. Ag/AgCl at 100 mV s^{-1}, for the modified SPE electrodes. These modified films were then placed into 0.1 M PBS (pH 7.4) solutions containing glucose and the same electrochemical windows and scan rates were used for the detection of glucose.

2.2.8.2 Constant Potential Amperometry

CPA was only conducted using the optimised fMWCNT-Au_{nano} composite modified GC and SPE (DRP-150) electrodes and the optimsied fMWCNT-Au_{nano}/Pd_{nano} modified SPE (DPR-150) electrode with Pd deposition for 240 s.

Glucose detection was carried out at 0.30 V vs. SCE at the fMWCNT-Au_{nano} composite modified GC electrodes and at -0.05 V vs. Ag/AgCl at the fMWCNT-Au_{nano} composite modified SPE electrodes. Detection using CPA was undertaken at -0.45 V and at -0.05 V vs. Ag/AgCl at the fMWCNT-Au_{nano}/Pd_{nano} composite modified SPE electrodes. In all of these experiments, aliquots of glucose were injected from a stock glucose solution into the electrochemical cell and the solutions were stirred under magnetic stirring to ensure homogeneity. These solutions were left to settle before further amperometric measurements were taken. All details of the aliquot volumes, stock solutions used and the final concentrations of glucose in the cell post-injection are displayed in Tables 2.3 and 2.4, for the GC and SPE systems, respectively.

Table 2.3: Glucose stock solution concentration and volumes of the stock used during CPA analysis. This table is employed when using modified GC electrode systems.

Stock / mM	Aliquot / ml	Aliquot / µl	Total Aliquot / ml	Cell Vol. / ml	Cell Conc. / mM
50	0.0	0	0.00	25.00	0.00
50	0.1	50	0.05	25.05	0.10
50	0.1	50	0.10	25.10	0.20
50	0.2	150	0.25	25.25	0.50
50	0.3	250	0.50	25.50	0.98
50	0.5	500	1.00	26.00	1.92
50	0.5	500	1.50	26.50	2.83
50	0.5	500	2.00	27.00	3.70
50	0.5	500	2.50	27.50	4.55
50	0.5	500	3.00	28.00	5.36
50	1.0	1000	4.00	29.00	6.90
50	1.0	1000	5.00	30.00	8.33
50	1.0	1000	6.00	31.00	9.68
50	1.0	1000	7.00	32.00	10.94
50	1.5	1500	8.50	33.50	12.69
50	1.5	1500	10.00	35.00	14.29
50	1.5	1500	11.50	36.50	15.75

Table 2.4: Glucose stock solution concentration and volumes of the stock used during CPA analysis. This table is employed when using modified SPE systems.

Stock / mM	Aliquot / ml	Aliquot / µl	Total Aliquot / ml	Cell Vol. / ml	Cell Conc. / mM
50	0.00	0	0.00	10.00	0.00
50	0.05	50	0.05	10.05	0.25
50	0.05	50	0.10	10.10	0.50
50	0.15	150	0.25	10.25	1.22
50	0.25	250	0.50	10.50	2.38
50	0.50	500	1.00	11.00	4.55
50	0.50	500	1.50	11.50	6.52
50	0.75	750	2.25	12.25	9.18
50	1.00	1000	3.25	13.25	12.26
50	1.50	1500	4.75	14.75	16.10
50	1.50	1500	6.25	16.25	19.23

2.2.9 Interference Studies

Interference studies were carried out using the optimised 24 h fMWCNT-$Au_{nano}(NaBH_4)$ composite modified SPE (DRP-150) electrodes and the optimsied fMWCNT-Au_{nano}/Pd_{nano} modified SPE (DRP-150) electrode with Pd deposition for 240 s. The interferants studied were ascorbic acid, uric acid, galactose, fructose, acetaminophen, bovine serum albums and chloride.

2.2.9.1 Cyclic Voltammetry

The current responses for all of the interferants were monitored initially using CV. A potential window of -0.65 V to 0.35 V vs. Ag/AgCl at 100 mV s^{-1}, was used to monitor any redox processes or chemical poisoning occurring at the composite modified SPEs in the presence of these interferants. Prior to analysis, these films were cycled in 0.1 M PBS (pH 7.4) using the same potential window as that used to obtain stable background responses.

2.2.9.2 Constant Potential Amperometry

The effect of glucose detection in the presence of interferants at the composite modified SPEs was conducted using CPA, along with the oxidation of these interferants in the absence of glucose.

As in Section 2.2.8.2, CPA was undertaken at -0.05 V vs. Ag/AgCl at the 24 h fMWCNT-$Au_{nano}(NaBH_4)$ modified SPEs but at -0.45 V vs. Ag/AgCl at the fMWCNT-Au_{nano}/Pd_{nano} modified SPEs. The potential of -0.45 V vs. Ag/AgCl was used to possibly reduce interference from commonly occurring interferants in the blood which oxidise at more positive potentials [8, 9]. Although this may appear to be a strong reduction potential, there should be no oxidised interferant species in the solution to be reduced. Aliquots of glucose were added into the electrochemical cell initially to observe the current responses and this was followed by aliquots of the interferants from stock solutions. Further injections of glucose were carried out post-interferant to observe any effects on the glucose current responses. All details related to the volumes of aliquots added to the cell, stock solutions and cell concentrations are

displayed in Tables 2.5 – 2.9. The oxidation of these interferants in the absence of glucose was undertaken at the same potentials, aliquot details shown in Table 2.10.

Table 2.5: Stock glucose and ascorbic acid solution concentrations and volumes of the stocks used during CPA analysis. Cell initially contained 10 ml of 0.1 M PBS (pH 7.4).

Stock / mM	Aliquot / ml	Aliquot / µl	Total Aliquot / ml	Cell Vol. / ml	Cell Conc. / mM
Glucose					**Glucose**
200	0	0.0	0.000	10.00	0.00
200	0.204	204.0	0.204	10.20	4.00
Ascorbic Acid					**Ascorbic Acid**
50	0.0205	20.5	0.021	10.22	0.10
50	0.0825	82.5	0.103	10.31	0.50
Glucose					**Glucose**
200	0.2255	225.5	0.430	10.74	8.00
200	0.2285	228.5	0.658	10.97	12.00

Table 2.6: Stock glucose and uric acid solution concentrations and volumes of the stocks used during CPA analysis. Cell initially contained 10 ml of 0.1 M PBS (pH 7.4).

Stock / mM	Aliquot / ml	Aliquot / µl	Total Aliquot / ml	Cell Vol. / ml	Cell Conc. / mM
Glucose					**Glucose**
200	0	0.0	0.000	10.00	0.00
200	0.204	204.0	0.204	10.20	4.00
Uric Acid					**Uric Acid**
10	0.395	395.0	0.395	10.60	0.37
10	0.088	88.0	0.483	10.69	0.45
Glucose					**Glucose**
200	0.2415	241.5	0.446	11.13	8.00
200	0.2365	236.5	0.682	11.37	12.00

Table 2.7: Stock glucose and fructose solution concentrations and volumes of the stocks used during CPA analysis. Cell initially contained 10 ml of 0.1 M PBS (pH 7.4).

Stock / mM	Aliquot / ml	Aliquot / µl	Total Aliquot / ml	Cell Vol. / ml	Cell Conc. / mM
Glucose					**Glucose**
200	0.0000	0.0	0.000	10.00	0.0
200	0.2040	204.0	0.204	10.20	4.0
Fructose					**Fructose**
6	0.0108	10.8	0.011	10.21	0.0063
9	0.0205	20.5	0.031	10.24	0.0277
100	0.2600	260.0	0.291	10.50	2.78
Glucose					**Glucose**
200	0.2335	233.5	0.438	10.93	8.0
200	0.2325	232.5	0.670	11.17	12.0

Table 2.8: Stock glucose and galactose solution concentrations and volumes of the stocks used during CPA analysis. Cell initially contained 10 ml of 0.1 M PBS (pH 7.4).

Stock / mM	Aliquot / ml	Aliquot / µl	Total Aliquot / ml	Cell Vol. / ml	Cell Conc. / mM
Glucose					**Glucose**
200	0.0000	0.0	0.000	10.00	0.00
200	0.2040	204.0	0.204	10.20	4.00
Galactose					**Galactose**
100	0.0252	25.2	0.025	10.23	0.25
100	0.0315	31.5	0.057	10.26	0.55
100	0.0460	46.0	0.103	10.31	1.00
Glucose					**Glucose**
200	0.2255	225.5	0.430	10.74	8.00
200	0.2285	228.5	0.658	10.96	12.00

Table 2.9: Stock glucose and acetaminophen solution concentrations and volumes of the stocks used during CPA analysis. Cell initially contained 10 ml of 0.1 M PBS (pH 7.4).

Stock / mM	Aliquot / ml	Aliquot / µl	Total Aliquot / ml	Cell Vol. / ml	Cell Conc. / mM
Glucose					**Glucose**
200	0.0000	0.0	0.000	10.00	0.00
200	0.2040	204.0	0.204	10.20	4.00
Acetaminophen					**Acetaminophen**
200	0.0680	68.0	0.068	10.27	1.32
200	0.2810	281.0	0.349	10.55	6.61
Glucose					**Glucose**
200	0.2355	235.5	0.440	10.99	8.00
200	0.2340	234.0	0.674	11.23	12.00

Table 2.10: Interferant stock solution concentrations and volumes of each stock used during CPA analysis. This analysis was carried out in the absence of glucose. Cell initially contained 10 ml of 0.1 M PBS (pH 7.4).

Interferant	Stock / mM	Aliquot / ml	Aliquot / µl	Total Aliquot / ml	Cell Vol. / ml	Cell Conc. / mM
Fructose	100	0.0028	2.8	0.0028	10.003	0.0277
Galactose	100	0.0555	55.5	0.0555	10.056	0.55
Ascorbic Acid	50	0.0200	20.0	0.0200	10.020	0.10
Uric Acid	10	0.4750	475.0	0.4750	10.475	0.45
Acetaminophen	20	0.0670	67.0	0.0670	10.067	0.13

2.2.10 Reusability and Shelf-Life Studies

As in the interference studies discussed previously, Section 2.2.9, reusability and shelf-life studies were carried out using the optimised 24 h fMWCNT-$Au_{nano}(NaBH_4)$ composite modified SPE (DRP-150) electrodes and the optimsied fMWCNT-Au_{nano}/Pd_{nano} modified SPE (DRP-150) that used Pd deposition for 240 s. Only CPA was used for the glucose measurements.

2.2.10.1 Sensor Reusability

CPA was undertaken at -0.05 V vs. Ag/AgCl at the 24 h fMWCNT-$Au_{nano}(NaBH_4)$ modified SPEs and at -0.45 V vs. Ag/AgCl at the fMWCNT-Au_{nano}/Pd_{nano} modified

SPEs. An aliquot of glucose was injected to the electrochemical cell from a stock solution under magnetic stirring to yield a concentration of 10.0 mM glucose. Once the cell had settled, the current responses for 10.0 mM glucose were measured. This was conducted 12 times for each sensor and between sensing, the films were cycled in a 0.1 M PBS (pH 7.4) solution, as in Section 2.2.6.3, as to remove any adsorbed glucose from the surfaces.

2.2.10.2 Sensor Shelf-Life and Storage

Shelf-life and storage studies were carried out using the same principles as outlined previously in Section 2.2.10.1. Although, instead of successive glucose testing conducted immediately, the sensors were tested for glucose after being left for certain periods of time, ranging from days to weeks. Between testing, the sensors were stored in either 0.1 M PBS (pH 7.4) or in air and this was carried out to identify the ideal storage conditions.

2.2.11 Scan Rate Analysis

Scan rate analyses were undertaken using CV by measuring the redox current responses of 0.1 mM ferrocyanide, made in 0.1 M KCl, upon varying the scan rates. A potential window of -0.30 V to 0.60 V vs. SCE was used for analyses at the fMWCNT-Au_{nano} modified GC electrodes and SPEs and this same window was used for analyses at the fMWCNT-Au_{nano}/Pd_{nano} modified GC electrode and SPEs (DRP-150). Scan rates of 10, 25, 50, 75, 100, 125, 150, 175 and 200 mV s^{-1} were applied. Prior to and between analyses the films were cycled in 0.1 M KCl to regenerate fresh surfaces and to obtain current background responses in the absence of ferrocyanide for subtraction purposes. These experiments were also conducted on a bare GC electrode (d = 3 mm) for comparison.

The scan rate studies were undertaken in the hopes of applying the Randles-Sevcik equation, Equation 2.1, for estimation of total electroactive surface areas [10, 11] of the composite films and also to measure the redox peak separations (ΔE) of ferrocyanide as a function of scan rate. ΔE was calculated using Equation 2.2 and it is often used to represent the speed of electron transfer at a surface [12, 13].

$$ip = 2.68 \times 10^5 n^{\frac{3}{2}} A D^{\frac{1}{2}} C v^{\frac{1}{2}} \quad 2.1$$

$$\Delta E = Ea - Ec = \frac{59\ \text{mV}}{n} \quad 2.2$$

2.2.12 Gold Surface Area Analysis

Gold electroactive surface areas of the pristine MWCNT-$Au_{nano}(NaBH_4)$, the various fMWCNT-$Au_{nano}(NaBH_4)$ and the fMWCNT-Au_{nano}(TriSodCit) modified electrodes were calculated by cycling the prepared films in 0.5 M H_2SO_4 and by comparing the charge under the Au oxide reduction peak observed in the reverse scan with this charge obtained for an Au electrode of a known surface area [14]. This reduction peak appears at 0.90 V vs. SCE [15]. This analysis was undertaken for the composite modified GC electrodes and SPEs and in each case the films were cycled in H_2SO_4 for 11 cycles. A potential window of 0.00 V to 1.40 V vs. SCE at 100 mV s^{-1} was used for analysis of the modified GC electrodes and of the Au electrodes. A window of -0.20 V to 1.20 V vs. Ag/AgCl at 100 mV s^{-1} was used for analysis of the modified SPEs (DRP-150).

2.2.13 Electrochemical Impedance Spectroscopy of Composite Films

Electrochemical impedance spectroscopy (EIS) was only conducted at the composite modified GC electrodes due to possible instabilities of the modified SPEs over the frequency ranges analysed. EIS was used to determine capacitance and resistance values obtained at the 24 h fMWCNT-$Au_{nano}(NaBH_4)$, the 24 h fMWCNT-Au_{nano}(TriSodCit) and fMWCNT-Au_{nano}/Pd_{nano} composite modified GC electrodes, with and without the H_2SO_4 pre-treatments. Measurements were also taken at unmodified GC electrode (d = 3 mm) and a GC electrode modified with 24 h fMWCNTs for comparison. It is well known that capacitance and resistance is associated with surface areas [16], and as such EIS may provide information related to the film surface areas.

EIS measurements were taken over the wide frequency range of 0.003 Hz to 60,000 Hz and at potentials of -0.10 V, 0.20 V and 0.50 V vs. SCE using a perturbation of 5.0 mV. The composite films were prepared and then polarised at the required potential for a period of 30 min. This period was sufficient to achieve steady-state conditions. EIS was carried out using Scribner Associates ZPlot® version 2.1 and ZView® 2.1 was used for data analysis.

2.3 Experimental Techniques

2.3.1 Electrochemistry

2.3.1.1 Cyclic Voltammetry

Cyclic voltammetry (CV) experiments were carried out on a Solartron SI 1287 potentiostat, for the detection of glucose and interferants, for the electrochemical pre-treatment of composite films and during scan rate analyses of the composite films. CV is a commonly used electrochemical technique in which the potential applied to the electrochemical system is cycled between two specific values in a forward and reverse direction and this results in a voltammogram. The cycling of the potentials are carried out linearly and are controlled at a specific rate, the scan rate. Scan rates used are typically below 1000 mV s^{-1}. As the system is scanned over the applied potential range, the changes in the current responses are measured and these currents can represent either a faradaic process, i.e., the oxidation and/or reduction of a species present, or a non-faradaic process, i.e., capacitance. An oxidation reaction will result in a corresponding positive increase in the current and a reduction reaction will result in an increase in the negative direction. During CV, the working electrode can behave as both an electrochemical oxidant and a reductant, depending on the potentials applied during the cycling. Typically, as the potential is cycled from a more negative potential towards a more positive potential, the working electrode will stimulate the oxidation of a chemical species at its surface and when the scan is reversed back to the more negative potential, the working electrode may facilitate the reduction of a chemical species [17]. A typical faradaic CV, showing both the oxidation and reduction of a chemical species is displayed in Figure 2.2 [18].

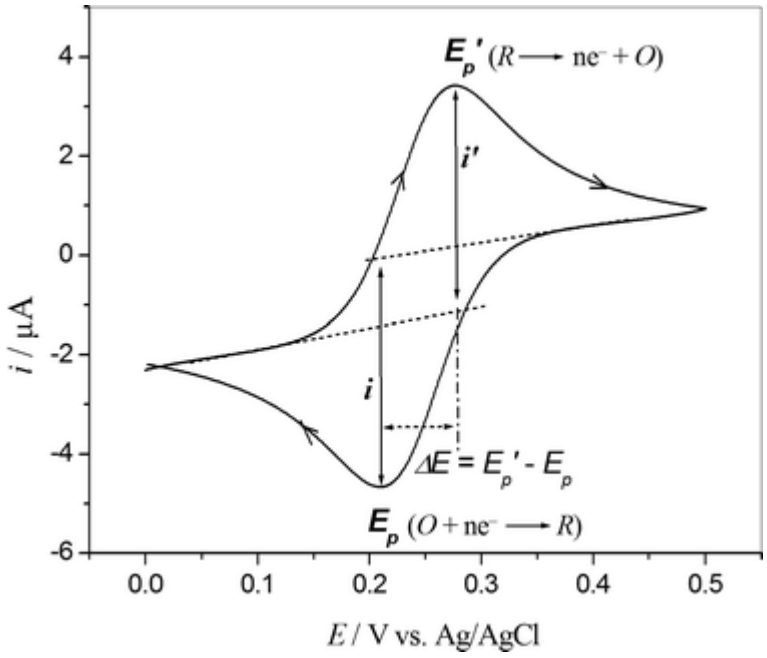

Figure 2.2: Cyclic voltammogram showing a Faradaic process [18].

Faradaic processes may not always be apparent during CV and more capacitive characteristics may result. Capacitance is defined as the ability of a material to store charge [19]. Capacitive currents are obtained when using high surface area conducting materials due to the increased adsorption of ions at the electrode-electrolyte interface, which increases the effects of the electric double layer. The capacitance resulting from this layer is called the double layer capacitance [20]. Using CV, the substantial background responses resulting from capacitive non-faradaic processes can make it difficult to visualise faradaic processes [21]. A typical CV where the capacitance is high is displayed in Figure 2.3 [22].

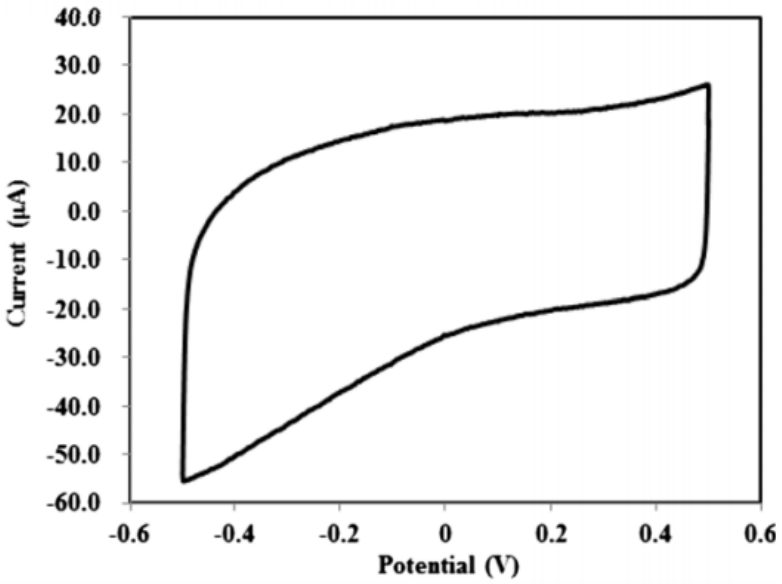

Figure 2.3: Cyclic voltammogram showing a non-faradaic, capacitive, process [22].

2.3.1.2 Potentiostatic Techniques

Potentiometry was carried out on a Solartron SI 1287 potentiostat and amperometric measurements were performed using a CH Instruments CHI 760C potentiostat. Potentiostatic techniques were used for the deposition of Pd metal on the composite films and also for the detection of glucose and interferants. The potentiostatic mode used for the deposition of Pd metal involved a constant potential for a set period of time. The other potentiostatic mode used for the detection of glucose is called constant potential amperometry or CPA. CPA involves applying a constant potential to an electrochemical system that is sufficient to oxidise or reduce the analyte under investigation. The flow of current related to the oxidation or reduction of the species is monitored and displayed as a function of time [23], as displayed in Figure 2.4.

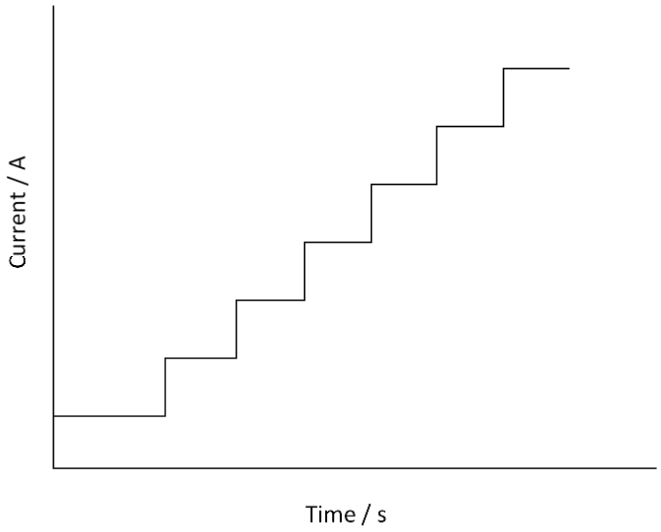

Figure 2.4: Representation of a typical current-time plot obtained during constant potential amperometry upon the addition of successive aliquots of analyte.

2.3.2 Physical Characterisation Techniques

2.3.2.1 Scanning Electron Microscopy

Scanning electron microscopy (SEM) was used in this work for imaging of the bulk fMWCNT-Au_{nano} composites produced using the $NaBH_4$ and trisodium citrate syntheses and for morphological analysis of their composite modified films. SEM was carried out using a Hitachi S-3200-N SEM. This instrument also had an Oxford Instrument INCAx-act EDX system.

SEM is a technique that allows for morphological analyses of materials on a nanometer (nm) to millimeter (mm) scale [24]. The fundamental principle of an electron microscope relies on the interaction between high-energy electrons and the material being analysed [25, 26]. The electrons are fired from an electron gun, which is a cathode, and accelerated through the voltage difference between the cathode and an anode and down the optic column, through an aperture, and towards the sample. This acceleration depends on the voltage applied, the accelerating voltage (keV), and can range from 0.1 keV to 50 keV. The aperture is an opening at the order of milliradians and its diameter can be increased or decreased for lower or higher resolution work,

respectively. Samples are analysed at a set working distance, with longer working distances allowing the investigation of larger areas [25]. The production of an image during SEM, depends on the signals produced upon the interaction with the electron beam and the sample. These interactions are separated into two categories, elastic and inelastic interactions. Elastic interactions are caused by the deflection of the incident electron beam by electrons of similar energy within the nucleus or in the outer energy levels of the specimen being analysed. This type of interaction results in loss in energy and direction change of the scattered electrons. When these electrons are scattered by an angle over 90^0, these are known as backscattered electrons and are the most useful for producing an image. Inelastic interactions occur between the incident electron beam and the atoms in the sample and this results in the excitation of the sample. This excitation produces secondary electrons which are also involved in producing the image [26]. Shown in Figure 2.5 is an example of the interactions taking place at a materials surface during SEM [27].

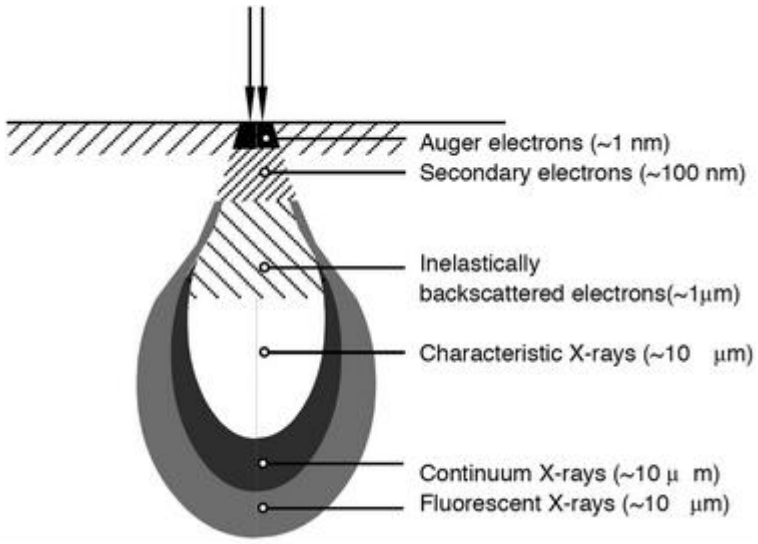

Figure 2.5: Interaction mechanisms of electrons with a solid showing a pear shaped volume of interaction [27].

2.3.2.2 Transmission Electron Microscopy

Transmission electron microscopy (TEM) was used in this work for analysis of the fMWCNT-Au_{nano} composites produced using the $NaBH_4$ and trisodium citrate syntheses. It enabled the visualisation of the fMWCNTs and the AuNPs formed on

their surfaces and was also used to obtain some crystallographic information. TEM work was carried at the CRANN institute at Trinity College Dublin using a FEI Titan TEM with EDX capabilities. Samples were prepared on Holey carbon films with 300 mesh copper grids from a drop cast dispersion made in ethanol absolute.

TEM is an imaging technique that is used for visualisation of nanometer sized materials and details down to the atomic level can be obtained [28]. It relies on many of the same principles as SEM, although it has the advantage of improved magnification and resolution. A TEM generally consists of the following sections, listed from top to bottom, the electron gun, the illumination stage, the objective lens, the magnification and projection system, the detector, photographic camera and a charge-coupled device camera [29]. In a conventional TEM setup, the specimen being analysed is irradiated with a uniform electron beam. Typically the accelerating voltage applied can be between 100 – 3000 keV, depending on the type of system and its resolution [30]. An electron gun emits the electron beam which passes through a multi-stage lens system to allow the variation of the aperture. When passed though the sample the beam is imaged by another set of lenses onto a fluorescent screen and to a computer monitor [30].

As mentioned, TEM can provide information down to the atomic level. During high resolution TEM (HRTEM) mode, under high magnifications, lattice fringes of crystalline materials can be visualised, which are representations of inter-atomic spacings between atoms. The distance of these spacings, known as the d-spacing, can indicate the crystallographic planes of the material [31]. TEM can also yield crystallographic information when operating in diffraction mode with the use of the selected area electron diffraction (SAED) patterns obtained. Using these patterns, the various lattice planes of the crystalline material can be determined, which is complementary to the d-spacing data obtained from lattice fringes measured suing HRTEM mode [32].

2.3.2.3 Energy Dispersive X-Ray Analysis

Energy Dispersive X-Ray Analysis (EDX) was used during both SEM and TEM measurements. It was primarily used for qualitative elemental analysis of the fMWCNT-Au_{nano} and fMWCNT-Au_{nano}/Pd_{nano} composites. During SEM, it was also

used for quantitative elemental analysis, although these values were taken only as estimates.

EDX is a technique commonly used in conjunction with SEMs and TEMs. It allows the detection of elements in a material that have an atomic number higher than Li. EDX relies on X-Ray fluorescence, which is where X-Rays are emitted from a material upon bombardment by high energy radiation in the form of electrons, X-Rays, neutrons, gamma rays and ions. The X-Rays emitted are characteristic of the composing elements and the elements can be identified. These X-Rays are detected by an X-Ray detector, which converts them into an electrical signal proportional to the X-Ray energy. The resulting graph of counts versus keV displays the relative intensity of the peaks which can be related to the atomic concentrations present [33].

2.3.2.4 Atomic Absorption Spectroscopy

Atomic Absorption Spectroscopy (AAS) was used for quantitative analysis of the bulk fMWCNT-Au_{nano} composites produced using the $NaBH_4$ and trisodium citrate syntheses. AAS was carried out using a Perkin Elmer Precisely AAnalyst system. Au standard solutions were prepared using commercial stock solutions.

AAS is a spectroscopic technique which allows for the quantitative analysis of trace metals in solutions. It often functions in conjunction with a flame atomiser, which typically uses an air-acetylene mix. Using AAS coupled with a flame atomiser (FAAS), the number of atoms per cubic centimeter in the flame, i.e., the absorbance, can be calculated which is proportional to the analyte concentration and can related to the Beer-Lambert Law. Atomic absorption corresponds to the atomic transitions from the ground state to an excited state and the function of the flame atomizer is to produce atoms in the ground state. With the use of an air-acetylene mixture, temperatures of 2500 K can be reached [34]. Spectral lamps are used as sources of radiation, in which the hollow-cathode lamp is most commonly used. These lamps emit radiation which is then reduced in intensity upon absorption by the atomic species present. The type of cathode lamp is specific to the elements being analysed. A cathode lamp is constructed using the metal of the element being detected [35].

To carry out AAS, the Au had to be extracted from the composite materials to form $AuCl_4^-$. This was done using a highly corrosive *aqua regia* digestion, similar to that outlined in work by Sheng and Etsell [36]. *Aqua regia* is a mixture of three parts concentrated hydrochloric acid to one part concentrated nitric acid. The composites were added to a volume of freshly prepared *aqua regia* in a beaker (1 mg/ml). This mixture was boiled over a hot plate while being stirred magnetically, as to dissolve the Au from the fMWCNTs. This reaction resulted in gas evolution as outlined in Equations 2.3 – 2.5 [36]. When the solution was almost evaporated, a small quantity of 0.1 M HCl was added and the mixture was agitated to ensure homogeneity. When cooled, the solution was passed through Acrodisc® 13 mm syringe filters to remove the fMWCNTs. This yielded a yellow solution of $AuCl_4^-$ and this solution was diluted appropriately in 0.1 M HCl and analysed using AAS.

$$2HNO_3 + 6HCl \rightarrow 2NO + 4H_2O + 3Cl_2 \qquad 2.3$$

$$2Au + 9HCl + 3HNO_3 \rightarrow 2AuCl_3 + 3NOCl + 6H_2O \qquad 2.4$$

$$3HCl + HNO_3 \rightarrow Cl_2 + NOCl + 2H_2O \qquad 2.5$$

2.3.2.5 X-Ray Diffraction

X-Ray Diffraction (XRD) was used in this work for crystallographic analyses of the composite materials and for estimation of AuNP size. XRD was carried out by Dr. Wynette Redington, at the Materials and Surface Science Institute in The University of Limerick using a PANalytical X'Pert PRO MPD system.

XRD is based on the diffraction effects that are observed when electromagnetic radiation interacts with certain atomic planes of a crystalline material and the scattering of this incident radiation occurs. The incident waves must have wavelengths similar to the spacings between the atoms of the material. There are three types of scattering processes that occur upon X-Ray interaction with the sample. One of these processes involves the liberation of electrons from atomic ground states, a process

known as photoionisation. This process involves the transferal of energy and momentum from the incident beam to the excited electron and this is classified as an inelastic scattering process. Another inelastic process occurs, Compton scattering, whereby energy is transferred to an electron, although this electron is not liberated from the atom. The other type of scattering, Thomson scattering, is an elastic scattering whereby the incident X-Rays are scattered by electrons. This type of scattering is used to obtain the crystallographic information on the material. The wavelength of the incident rays is conserved during this elastic process, although it is not for the inelastic scattering processes [37].

When the incident rays reach the sample, or phase, they scatter from the top and bottom planes, separated by interatomic spacing d, between the rows of atoms. This diffraction occurs at an angle θ, which is called the Bragg's angle and this can be used to identify the crystalline planes present in the sample [38]. A representation of Bragg's diffraction is shown in Figure 2.6, taken from Zhou *et al*. [38].

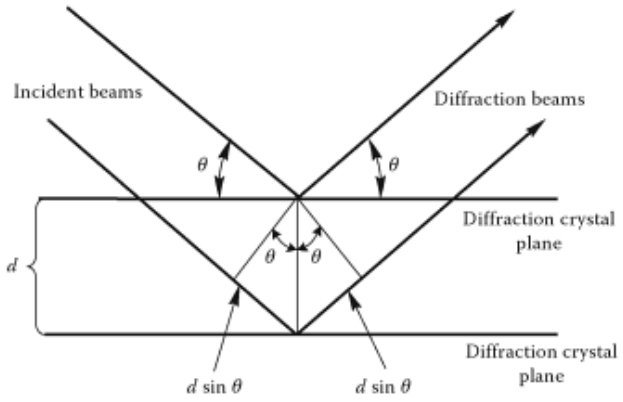

Figure 2.6: Representation of Bragg's diffraction [38].

2.3.2.6 Ultraviolet-Visible Spectroscopy

Ultraviolet-Visible (UV-Vis) spectroscopy was used in this study for investigation of the physical properties of the AuNPs and the composite materials produced. UV-Vis was carried out using a Varian Cary 50 spectrophotometer. All composites were dispersed in 1.0% SDS for UV-Vis analysis, with 1.0% SDS was used as a reference.

UV-Vis spectroscopy is a very useful analytical technique. It provides quantitative and qualitative information on substances that can interact with electromagnetic radiation in the UV-Vis spectrum, which covers wavelengths, ʎ, from 200 – 800 nm. During UV-Vis spectroscopy, either a set wavelength can be applied, at which the species absorbs or a wavelength range can be used. The wavelength at which a species can absorb depends on the electronic transitions possible for that species. Transitions occur during UV-Vis, whereby electrons are excited from the lower energy ground state into higher energy orbitals. This happens upon absorption of energy. Shown in Figure 2.7 is an illustration of the energy levels in a molecule and the three types of absorption, taken from Zhang *et al.* [39].

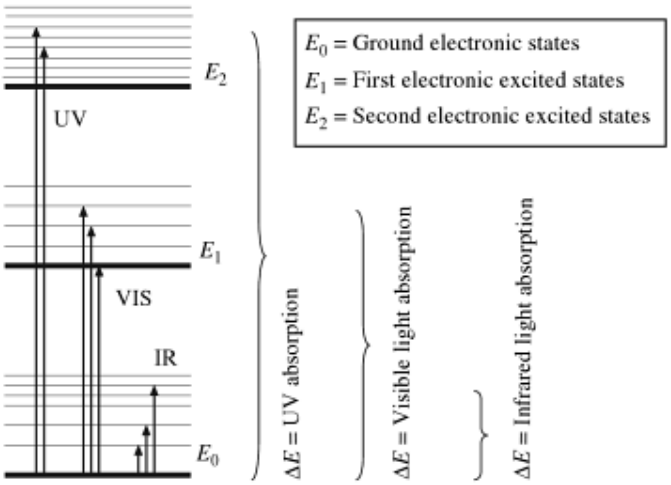

Figure 2.7: Energy levels in a molecule and three types of absorption, UV, visible and infrared [39].

2.3.2.7 Raman Spectroscopy

Raman Spectroscopy was used for qualitative and quantitative analyses of the composite materials. Information related to CNT structural detects can be obtained and surface enhanced Raman scattering (SERS) effects can be observed due to the presence of AuNPs [40]. Raman spectroscopy was undertaken at the FOCUS institute at Dublin Institute of Technology using a LabRAM high resolution Raman spectrometer operating at 660 nm. All samples were prepared in KBr discs for Raman analysis.

In Raman spectroscopy, a laser beam of a particular wavelength in the UV-Vis region is used to irradiate a sample and the incident light is scattered. This scattered light can be of two types, Rayleigh scattering and Raman scattering. Rayleigh scattering is an elastic scattering, whereby the excited molecule returns back to its ground state and emits the same frequency of light as the excitation source. This elastic scattering is useless for characterisation purposes and is filtered out. Raman scattering is an inelastic scattering process, in which the energy emitted is not conserved as it is not of the same frequency of the excitation source. This occurs due to interactions between the incident light and the vibrational energy levels of the molecules in the sample. This type of interaction leads to two possible outcomes; the emitted photon has a lower energy compared to the absorbed photon, which gives Stokes scattering, or the emitted photon may be of a higher energy than the absorbed photon, to give anti-Stokes scattering. Plotting the intensity of this scattered light as a function of the frequency difference, Raman Shift, results in a Raman spectrum [41]. In Figure 2.8 a representation of the energy transfers during Rayleigh scattering, Stokes and anti-Stokes Raman scattering is shown. This is taken from work by Amer [42].

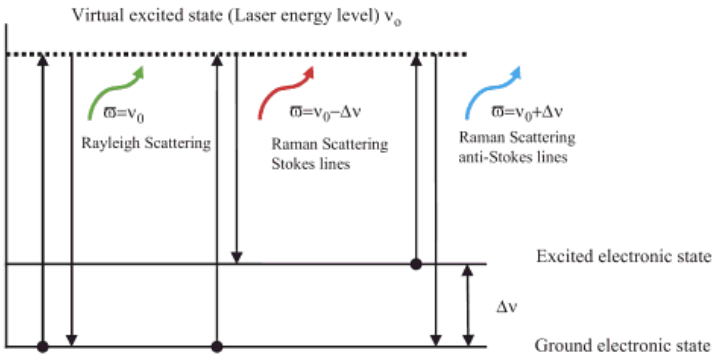

Figure 2.8: Representation of energy transfers during Rayleigh scattering, Stokes and anti-Stokes Raman scattering [42].

During Raman analysis of a sample containing AuNPs, the phenomenon known as surface enhanced Raman scattering (SERS) can occur. This occurs due to the enhancement of the Raman scattering of materials due to the surface plasmon resonance of the AuNPs. When MWCNTs are in contact with AuNPs, the Raman scattering of the MWCNTs is enhanced due to the interaction of the incident laser

beam with the plasmonic AuNPs. Shown in Figure 2.9 is a schematic of the SERS mechanism due to the presence of AuNPs on the surface of MWCNTs. This is taken from work by Sharma *et al.* [40].

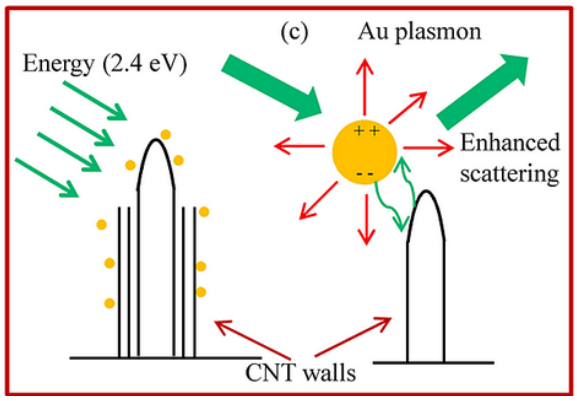

Figure 2.9: Schematic showing the SERS mechanism due to the presence of AuNPs on the surface of MWCNTs [40].

2.3.2.8 Fourier Transform Infrared Spectroscopy

Fourier Transform Infrared spectroscopy (FT-IR) was used for identification of characteristic bands of the fMWCNTs resulting from the acid reflux. FT-IR was carried out using a Perkin Elmer 2000 FT-IR spectrometer. All samples were prepared in KBr discs for FT-IR analysis.

FT-IR is a technique which can provide both qualitative and quantitative information of a sample. It is based on the vibrations within molecular bonds when they are subjected to infrared radiation. These bonds are identified by the frequency at which they absorb, which is associated with their structure. FT-IRs may operate in the near-infrared (14,000 – 4000 cm^{-1}), mid-infrared (4,000 – 400 cm^{-1}) and far-infrared (400 – 4 cm^{-1}) regions of the electromagnetic spectrum. Spectra can be plotted as absorbance versus wavenumber or percentage transmittance versus wavenumber. For quantitative analysis the absorbance plots can be used and the transmittance plot can be used for qualitative analysis [43]. For a molecule to be IR active it must have a dipole moment and a change must occur in this upon vibration. Functional groups have characteristic vibrational modes. The frequency of vibration is governed by Hooke's

law and this law predicts that the frequency of the vibration is related to the mass of the atoms in the bond and the bond strength [44].

2.3.2.9 Potentiometric Titrations

Potentiometric titrations were used to determine the acidic group composition of both the 24 h fMWCNTs and the pristine MWCNTs. This was carried out using a Jenway 370 Enterprise pH meter. A potentiometric titration is a type of titration in which the reaction between an acid and a base is monitored by measuring the pH upon addition of the titrant. The pH is measured throughout and a plot of pH as a function of the titrant added (ml) is constructed. Upon neutralisation, regions of sudden pH change occur and these regions are known as equivalence points (EPs). At the EP in the titration, the concentration of acid equals that of the base, i.e. neutralisation has occurred [45].

An acid-base titration, similar to that employed by Wang *et al.* [4] was used for the quantification of surface acidic groups. In a typical set up, the fMWCNTs (5 mg) were dispersed in a standardised 0.01 M NaOH solution (5 ml) in 0.1 M NaCl, with the aid of a short sonication, and left to stir for 14 h under N_2 bubbling to displace adsorbed CO_2 from the fMWCNTs [46]. The reaction mixture was then filtered through 0.45 µm pore size Acrodisc® 13 mm syringe filters to remove the CNTs and this remaining NaOH solution was titrated with standardised 0.01 M HCl in 0.1M NaCl. For comparison, this titration was repeated with pristine MWCNTs. The difference of the initial-to-final concentration of the NaOH solution was used to determine the total acidic group concentrations on the CNTs, which reportedly largely exist as carboxylic groups according to sources [4, 46].

2.4 References

1. W. Ma, Y.-L. Ying, L.-X. Qin, Z. Gu, H. Zhou, D.-W. Li, T. C. Sutherland, H.-Y. Chen and Y.-T. Long, *Nature Protocols*, 2013, **8**, 439-450.
2. DropSens, Screen-printed electrodes, http://www.dropsens.com/en/screen_printed_electrodes_pag.html.
3. B. J. Polk, A. Stelzenmuller, G. Mijares, W. MacCrehan and M. Gaitan, *Sensors and Actuators B: Chemical*, 2006, **114**, 239-247.
4. Z. Wang, M. D. Shirley, S. T. Meikle, R. L. D. Whitby and S. V. Mikhalovsky, *Carbon*, 2009, **47**, 73-79.
5. T. A. Saleh, *Applied Surface Science*, 2011, **257**, 7746-7751.
6. R. Zhang and X. Wang, *Chemistry of Materials*, 2007, **19**, 976-978.
7. L. M. Fischer, M. Tenje, A. R. Heiskanen, N. Masuda, J. Castillo, A. Bentien, J. Emneus, M. H. Jakobsen and A. Boisen, *Microelectronic Engineering*, 2009, **86**, 1282-1285.
8. J. Leng, W.-M. Wang, L.-M. Lu, L. Bai and X.-L. Qiu, *Nanoscale Research Letters*, 2014, **9**, 99.
9. H. Gao, F. Xiao, C. B. Ching and H. Duan, *ACS Applied Materials & Interfaces*, 2011, **3**, 3049-3057.
10. F. G. Thomas and G. Henze, *Introduction to Voltammetric Analysis: Theory and Practice*, CSIRO Publishing 2001.
11. I. Svancara, K. Kalcher, A. Walcarius and K. Vytras, *Electroanalysis with Carbon Paste Electrodes*, CRC Press, 2012.
12. S. A. Wring and J. P. Hart, *Analyst (London)*, 1992, **117**, 1215-1229.
13. A. J. Bard and L. R. Faulkner, *Electrochemical Methods: Fundamentals and Applications*, John Wiley & Sons, New York, 2001.
14. X. Xiao, H. Li, M. e. Wang, K. Zhang and P. Si, *Analyst*, 2013, **139**, 488-494.
15. Y.-G. Guo, H.-M. Zhang, J.-S. Hu, L.-J. Wan and C.-L. Bai, *Thin Solid Films*, 2005, **484**, 341-345.
16. M. Taketani and M. Baudry, *Advances in Network Electrophysiology: Using Multi-Electrode Arrays*, Springer, 2006.
17. J. Zhang, *PEM Fuel Cell Electrocatalysts and Catalyst Layers: Fundamentals and Applications*, Springer Science & Business Media, 2008.
18. F. Zhao, R. C. T. Slade and J. R. Varcoe, *Chemical Society Reviews*, 2009, **38**, 1926-1939.
19. D. Ross and D. Lowe, *Electronics All-in-One For Dummies*, John Wiley & Sons, Chichester West, Sussex, 2013.
20. P. Simon and Y. Gogotsi, *Nature Materials*, 2008, **7**, 845-854.
21. X. Feng, J. Hu, X. Chen, J. Xie and Y. Liu, *Journal of Physics D: Applied Physics*, 2009, **42**, 042001.
22. H. Xu, Y. Wang, Z. Luo and Y. Pan, *Measurement Science and Technology*, 2013, **24**, 125105.
23. J. M. Irudayaraj, *Biomedical Nanosensors*, CRC Press, 2012.

24. D. Landolt, *Corrosion and Surface Chemistry of Metals*, EFPL Press, 2007.
25. L. Reimer, *Scanning Electron Microscopy: Physics of Image Formation and Microanalysis*, Springer, 1998.
26. W. Zhou and Z. L. Wang, *Scanning Microscopy for Nanotechnology: Techniques and Applications*, Springer, 2007.
27. M. P. Dewar, MSc, University of Alberta, 2013.
28. D. J. Smith, *Materials Today*, 2008, **11**, 30-38.
29. M. De Graef, *Introduction to Conventional Transmission Electron Microscopy*, Cambridge University Press, 2003.
30. L. Reimer and H. Kohl, *Transmission Electron Microscopy: Physics of Image Formation*, Springer, 2008.
31. D. B. Williams and C. B. Carter, *Transmission Electron Microscopy: A Textbook for Materials Science*, Springer, 2009.
32. B. Bhushan, *Springer Handbook of Nanotechnology*, Springer, 2007.
33. P. H. Holloway, P. N. Vaidyanathan, C. R. Brundle and C. A. Evans, *Characterization of Metals and Alloys*, Momentum Press, 2009.
34. L. Ebdon and E. H. Evans, *An Introduction to Analytical Atomic Spectrometry*, John Wiley & Sons, Chichester, West Sussex, 1998.
35. J. A. Van Loon, *Analytical Atomic Absorption Spectroscopy: Selected Methods*, Elsevier Science, 2012.
36. P. P. Sheng and T. H. Etsell, *Waste Management & Research*, 2007, **25**, 380- 383.
37. M. Birkholz, *Thin Film Analysis by X-Ray Scattering*, Wiley-VCH Verlag GmbH & Co. KGaA, Weinheim, Germany 2006.
38. Y. Zhou, L. Yang and Y. Huang, *Micro- and Macromechanical Properties of Materials*, CRC Press, 2013.
39. C. Zhang, *Fundamentals of Environmental Sampling and Analysis*, John Wiley & Sons, New Jersey, 2007.
40. H. Sharma, D. C. Agarwal, A. K. Shukla, D. K. Avasthi and V. D. Vankar, *Journal of Raman Spectroscopy*, 2013, **44**, 12-20.
41. H. Tschesche, *Methods in Protein Biochemistry*, Walter de Gruyter, 2011.
42. M. S. Amer, *Raman Spectroscopy, Fullerenes and Nanotechnology*, Royal Society of Chemistry, 2010.
43. B. C. Smith, *Fundamentals of Fourier Transform Infrared Spectroscopy, Second Edition*, CRC Press, 2011.
44. R. J. Anderson, *Organic Spectroscopic Analysis*, Royal Society of Chemistry, 2004.
45. S. S. Nielsen, *Food Analysis*, Springer, 2010.
46. A. B. González-Guerrero, E. Mendoza, E. Pellicer, F. Alsina, C. Fernández-Sánchez and L. M. Lechuga, *Chemical Physics Letters*, 2008, **462**, 256-259.

Chapter 3

Gold Nanoparticle-Multiwalled Carbon Nanotube Composite Films for Non-Enzymatic Glucose Sensing

3.1 Introduction

In this chapter results are presented and discussed for the detection of glucose at various modified and non-modified electrodes. Initially glucose oxidation was investigated at bare gold (Au), copper (Cu) and glassy carbon (GC) electrodes in NaOH and in a neutral solution of PBS to investigate the effects of pH. Carbon nanotube-gold nanoparticle composites were then synthesised and were used to modify GC electrodes for glucose detection in PBS of pH 7.4. These composite nanomaterials combined both pristine (MWCNTs) and various acid functionalised multiwalled carbon nanotubes (fMWCNTs) with gold nanoparticles (AuNPs). They were produced synthetically through the direct reduction of AuNPs onto the surface of the carbon nanotubes using two reducing agents, sodium borohydride ($NaBH_4$) and trisodium citrate (TriSodCit). Various electrochemical pre-treatments, including NaOH and H_2SO_4 treatments, were utilised to optimise the sensitivity of the sensors. A permselective Nafion® membrane was also used to reduce the interference from interferants. These interference studies are discussed in Chapter 5. Having optimised the system using the modified GC electrodes, the electrochemical system was then miniaturised using screen-printed electrodes (SPEs). In the latter sections of this chapter, in depth characterisation studies are presented to identify the various physical and electrochemical properties of these composites and the resulting composite films.

3.2 Results and Discussion

3.2.1 Detection of Glucose in Alkaline Media at Bare Electrodes

The detection of glucose at gold (Au), copper (Cu) and glassy carbon (GC) electrodes was initially investigated in alkaline solutions of 0.10 M NaOH (pH 12.5). As discussed previously, in Chapter 1, Section 1.4.6.2, alkaline media are commonly used for the electrodetection of glucose. Studies show that alkaline conditions have a positive effect on glucose oxidation, possibly due to the promotion of surface formed $Au(OH)_{ads}$, which is involved in glucose detection [1, 2]. Cyclic voltammograms (CVs) of 10.0 mM glucose oxidation in NaOH at a bare Au electrode (d = 3 mm) are shown in Figure 3.1; coloured both red and green for 1st and 20th cycle, respectively. It can be seen during the initial cycle that no glucose oxidation is apparent in the forward scan until higher potentials are reached, above 0.20 V vs. SCE, but a large and broad oxidation peak is visible in the reverse scan beginning at 0.15 V vs. SCE. With successive cycling, further glucose oxidation is catalysed which can be seen in the 20th cycle. Larger oxidation peaks only begin in the forward scan after the first cycle, possibly due to an increased amount of adsorbed glucose molecules on the Au surface and the accumulation of surface formed $Au(OH)_{ads}$, which reportedly have catalytic properties towards the oxidation of glucose and its intermediates[3-6]. Three major peaks are evident in the voltammograms, two in the forward scan at 0.20 V and 0.40 V and in the reverse scan at 0.50 V vs. SCE. Smaller shoulder peaks at around -0.10 V vs. SCE in the forward scan and at 0.00 V in the reverse scan can also be seen. It is clear that there are many electrochemical processes occurring which may involve both the oxidation of glucose and its intermediates [6]. In NaOH alone, different redox processes are visible with Au electrodes as seen in the blue voltammogram in Figure 3.1. A small Au oxidation peak is seen at approximately -0.10 V and at 0.35 V vs. SCE in the forward scan and in the reverse scan the corresponding Au reduction peaks are seen at 0.00 V and -0.25 V vs. SCE. The oxidation peaks arising from glucose, seen in the red and green traces, seem to coincide with these Au redox transitions in NaOH. Similar results can be seen in work by Pasta *et al.* in which glucose detection was investigated at Au electrodes at alkaline pH [7].

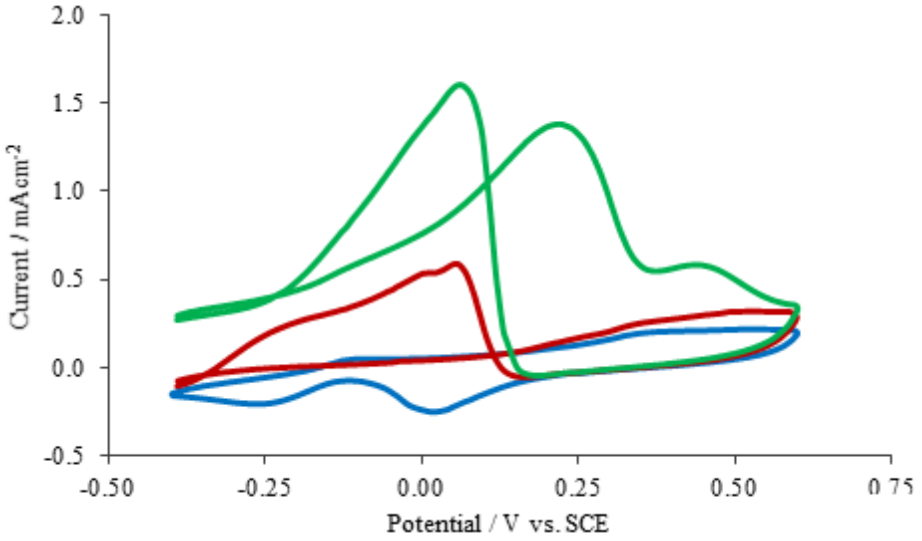

Figure 3.1: Cyclic voltammograms recorded at 100 mV s^{-1} of a bare Au electrode (d = 3 mm) in a — 0.10 M NaOH solution (pH 12.5) and a 0.10 M NaOH solution containing 10.0 mM glucose, — 20th cycle and — the 1st cycle.

The oxidation of glucose at a Cu electrode (d = 3 mm) is shown in Figure 3.2. Again the CVs recorded in NaOH, in the presence and absence of glucose are compared. It is clear that the oxidation of glucose is prominent at more positive potentials at which the onset of higher Cu oxides begins [8]. As with Au, Cu also exhibits surface redox transitions in alkaline solutions. However these typical redox couples are not clearly visible in the resulting voltammogram. In general, two successive anodic peaks occur in the forward scan corresponding to the Cu^0/Cu^{1+} and Cu^{1+}/Cu^{2+} transitions, with the corresponding reduction peaks occurring during the reserve scan. As higher potentials are reached, Cu^{2+}/Cu^{3+} transitions occur which correspond to a significant increase in the glucose oxidation response [8]. It has been suggested that the Cu^{3+} species may act as electron transfer mediators during glucose oxidation [9]. The oxidation of glucose did increase significantly as higher potentials were reached, possibly due to the formation of these higher Cu^{3+} species, as seen in Figure 3.2.

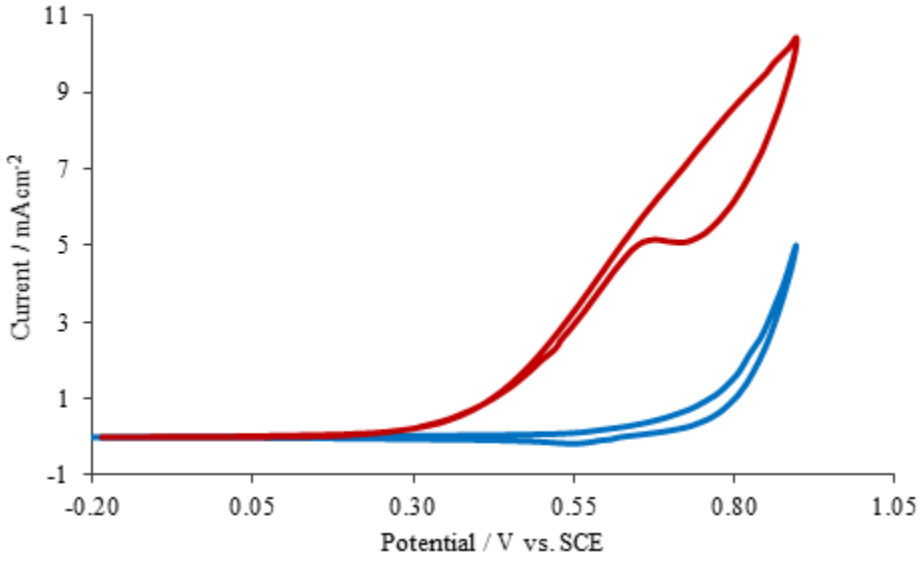

Figure 3.2: Cyclic voltammograms recorded at 100 mV s^{-1} of a bare Cu electrode (d = 3 mm) in a — 0.10 M NaOH solution (pH 12.5) and a — 0.10 M NaOH solution containing 10.0 mM glucose.

The detection of glucose in alkaline media using a GC electrode (d = 3 mm) proved to be ineffective in this study. Typical voltammograms are shown in Figure 3.3. The data recorded are identical in the presence and absence of glucose and no glucose detection is evident regardless of the cycle number. Although the detection of glucose does not occur in this case, work by Ye *et al.*[10] shows that glucose oxidation is possible at GC in NaOH, although much higher concentrations of glucose are used, 30 mM. Also, the current responses for glucose did not appear to be measurable from the resulting CVs. Ye *et al.*[10] achieved glucose detection using a high surface area well-aligned MWCNT modified GC electrode, but again detection of glucose was only observed at high glucose concentrations, 30 mM, and only in alkaline conditions.

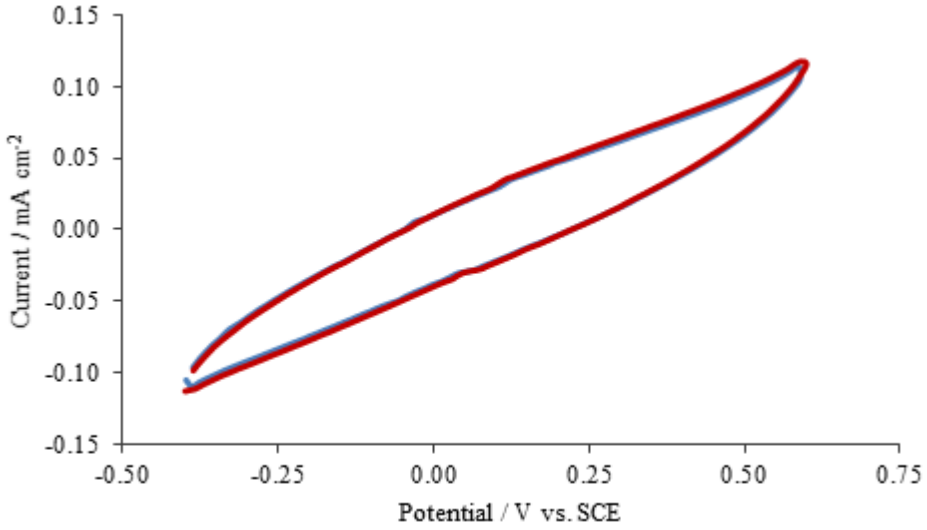

Figure 3.3: Cyclic voltammograms recorded at 100 mV s^{-1} of a bare GC electrode (d = 3 mm) in a — 0.10 M NaOH solution (pH 12.5) and a — 0.10 M NaOH solution containing 10.0 mM glucose.

3.2.2 Detection of Glucose in Neutral Media at Bare Electrodes

The oxidation of glucose was also studied at Au, Cu and GC electrodes (d = 3 mm) at a neutral pH (pH 7.4) using a 0.10 M phosphate buffer (PBS) solution. The voltammograms were recorded using CV at 100 mVs^{-1} with a potential window from -0.40 V to 0.60 V vs. SCE. Typical voltammograms recorded at bare Au are shown in Figure 3.4. The redox activity of Au can be seen in the forward and reverse cycles, between the potentials of 0.00 V and 0.25 V vs. SCE but there is no evidence of glucose oxidation. Even though studies have shown that glucose detection is possible at Au at this pH [4, 6], there is no evidence to support the oxidation of glucose at the bare Au electrode in Figure 3.4. This may be due to the small surface area and lack of surface bound OH_{ads} formed at pH 7.4 [6]. It is also clear from Figure 3.5, that no glucose oxidation is evident at Cu in PBS. High oxidation state Cu oxides are essential for glucose detection and these oxides may not be present or formed in sufficient amounts at this pH. The use of Cu as a sensing material ceases in PBS and as such is not used further in this work.

As can be seen in Figure 3.6, no glucose oxidation occurs at a bare GC electrode of a diameter of 3 mm in PBS of pH 7.4. The GC electrodes do not seem to show any electrochemistry in either NaOH or PBS solutions and therefore are not assumed to contribute to the sensing capabilities of the composite modified film, discussed in the following sections. As was mentioned previously, Ye *et al.*[10] did report the detection of glucose at GC electrodes, but only at high concentrations, 30 mM, and in alkaline solutions.

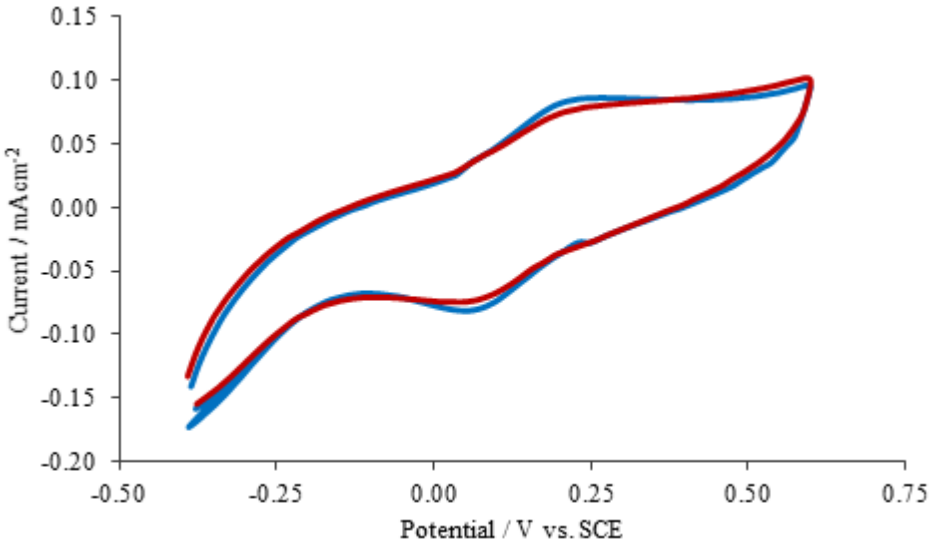

Figure 3.4: Cyclic voltammograms recorded at 100 mV s^{-1} of a bare Au electrode (d = 3 mm) in a — 0.10 M PBS (pH 7.4) solution and a — 0.10 M PBS solution containing 10.0 mM glucose.

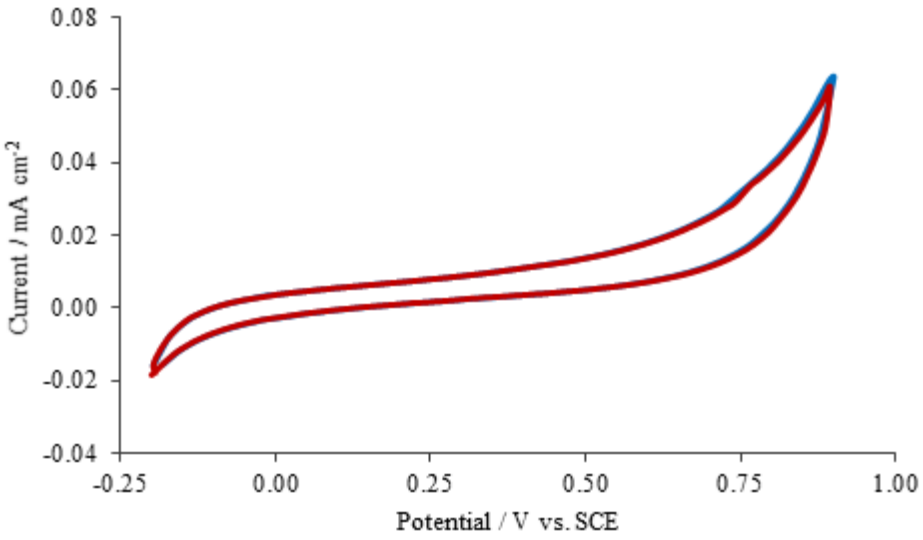

Figure 3.5: Cyclic voltammograms recorded at 100 mV s^{-1} of a bare Cu electrode (d = 3 mm) in a — 0.10 M PBS solution (pH 7.4) and a — 0.10 M PBS solution containing 10.0 mM glucose.

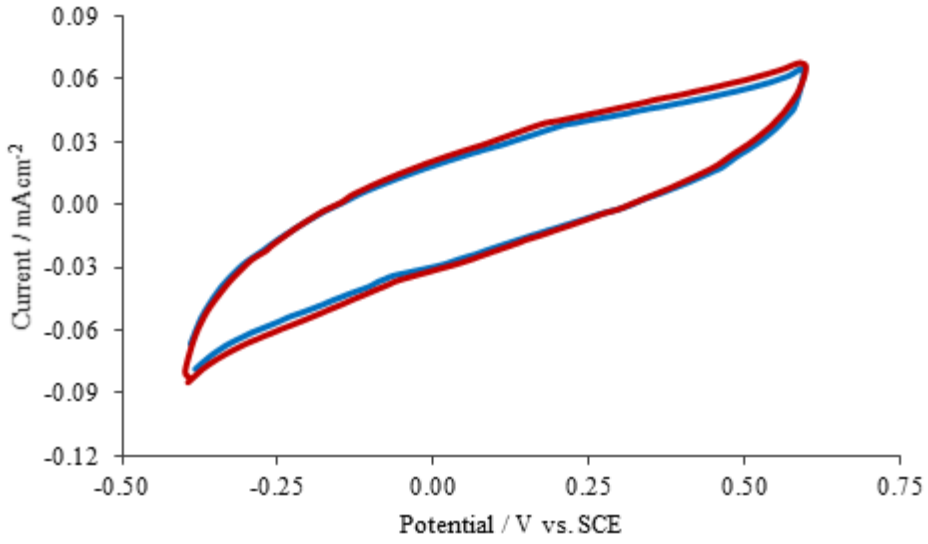

Figure 3.6: Cyclic voltammograms recorded at 100 mV s^{-1} of a bare GC electrode (d = 3 mm) in a — 0.10 M PBS solution (pH 7.4) and a — 0.10 M PBS solution containing 10.0 mM glucose.

3.2.3 Detection of Glucose at MWCNT-$Au_{nano}(NaBH_4)$ and fMWCNT-$Au_{nano}(NaBH_4)$ Composite Films

3.2.3.1 Pristine MWCNT-$Au_{nano}(NaBH_4)$

To Note: *The name of the reducing agent used is included in the composite names for clarity in this chapter as two different reducing agents were used. Similar composites produced using trisodium citrate (TriSodCit) are discussed in Section 3.2.7.*

The formation of AuNPs on pristine MWCNTs was possible using the method discussed in Chapter 2, Section 2.2.5.2. Briefly, pristine MWCNTs were firstly dispersed in a 1.0% sodium dodecyl sulfate (SDS) solution using ultrasonication and to this suspension a 1.0% gold(111) chloride ($HAuCl_4$) solution and a 0.75% $NaBH_4$ solution were added. The reaction was left to stir for 5 min and was then filtered and washed on 0.45 µm pore-sized Whatman® membrane paper. The resulting composite, named MWCNT-$Au_{nano}(NaBH_4)$, was then re-dispersed in a 1.0% SDS solution at a concentration of 2.0 mg/ml to enable casting onto the GC electrodes (d = 3 mm). A volume of 5.0 µl of this dispersion was cast onto GC electrodes to produce the composite films. Finally, an electrochemical pre-treatment was completed before glucose analysis by cycling the modified electrodes in a 0.30 M NaOH solution. This promoted the detection of glucose and it was assumed that this step was important for removing adsorbed SDS from the films. Indeed using UV-Vis spectroscopy an absorbance band assigned to SDS was observed upon cycling in the NaOH solution. The band increased in intensity with cycle number and cycling was continued until the intensity of the absorbance band remained constant. This cycling was carried out as standard for all composite films. The GC electrode is chosen as a substrate as there is no evidence for the oxidation of glucose at this electrode, as shown previously in Figures 3.3 and 3.6, respectively, in Sections 3.2.1 and 3.2.2. The fMWCNT-Au_{nano} composite films were fabricated using a similar method.

The CVs recorded in 0.10 M PBS with concentrations of glucose ranging from 1 to 10.0 mM, are shown in Figure 3.7. This concentration range was chosen during this study and in further studies as it encompasses the physiological levels of glucose in the blood which typically ranges from 4 – 8 mM [11]. It is evident from these

voltammograms that an oxidation peak for glucose occurs at the MWCNT-$Au_{nano}(NaBH_4)$ composite film at approximately 0.25 V vs. SCE in both the forward and reverse scans, however the currents are low. The size of these currents may be related to the levels of Au in the films. Indeed, using energy dispersive X-Ray analysis (EDX) and atomic absorption (AA) analysis, the Au loading in the samples was quantified at only 1.61% wt. and 1.00% wt. of the bulk sample, respectively, data shown in Sections 3.2.9.3 and 3.2.9.6. This lack of Au in the sample could be a result of the limited solubility of the pristine MWCNTs in the SDS solution during AuNP reduction. Several studies also show that AuNPs tend to deposit around the areas of defects on carbon nanotubes, which occur during acid functionalisation[12, 13]. As the pristine MWCNTs were not functionalised these defects may not be present in sufficient concentrations to facilitate the deposition of the AuNPs.

The corresponding calibration curve for the detection of glucose in PBS solution at the NaOH pre-treated MWCNT-$Au_{nano}(NaBH_4)$ composite film is shown in Figure 3.8. This calibration curve was produced using the average peak current response recorded at 0.25 V vs. SCE during the reverse scan, corresponding to the oxidation of glucose. Serial dilutions were employed to give the glucose concentrations between 1.0 and 10.0 mM. Although the R^2 value of 0.9917 indicates a linear calibration curve, the error bars are quite large especially at the higher glucose concentrations. This trend with the error bars is due to the variation in the current responses obtained during each individual experiment, as shown in Figure 3.8 (b). All further work uses the average current values to produce the calibration curves.

In an attempt to increase the oxidation responses for glucose in the PBS solution, new composites using acid functionalised carbon nanotubes (fMWCNTs) were produced. In these syntheses the MWCNTs were refluxed in concentrated HNO_3 for periods of 18 h, 24 h and 48 h and were then used to form the composite materials with higher AuNP loadings. The same synthesis conditions were used for each composite and the only difference in each procedure were the fMWCNTs used.

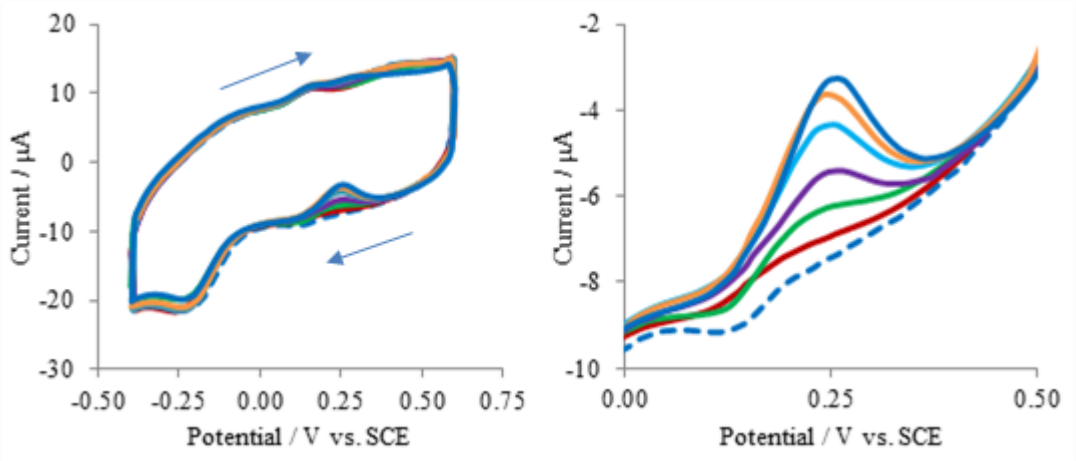

Figure 3.7: Cyclic voltammograms recorded at 100 mV s^{-1} of the MWCNT-Au_{nano}($NaBH_4$) modified GC electrode in a 0.10 M PBS solution (pH 7.4) containing 1.0 – 10.0 mM glucose. Magnified sections showing the oxidation peaks are shown to the right. Arrows indicate the direction of scanning.

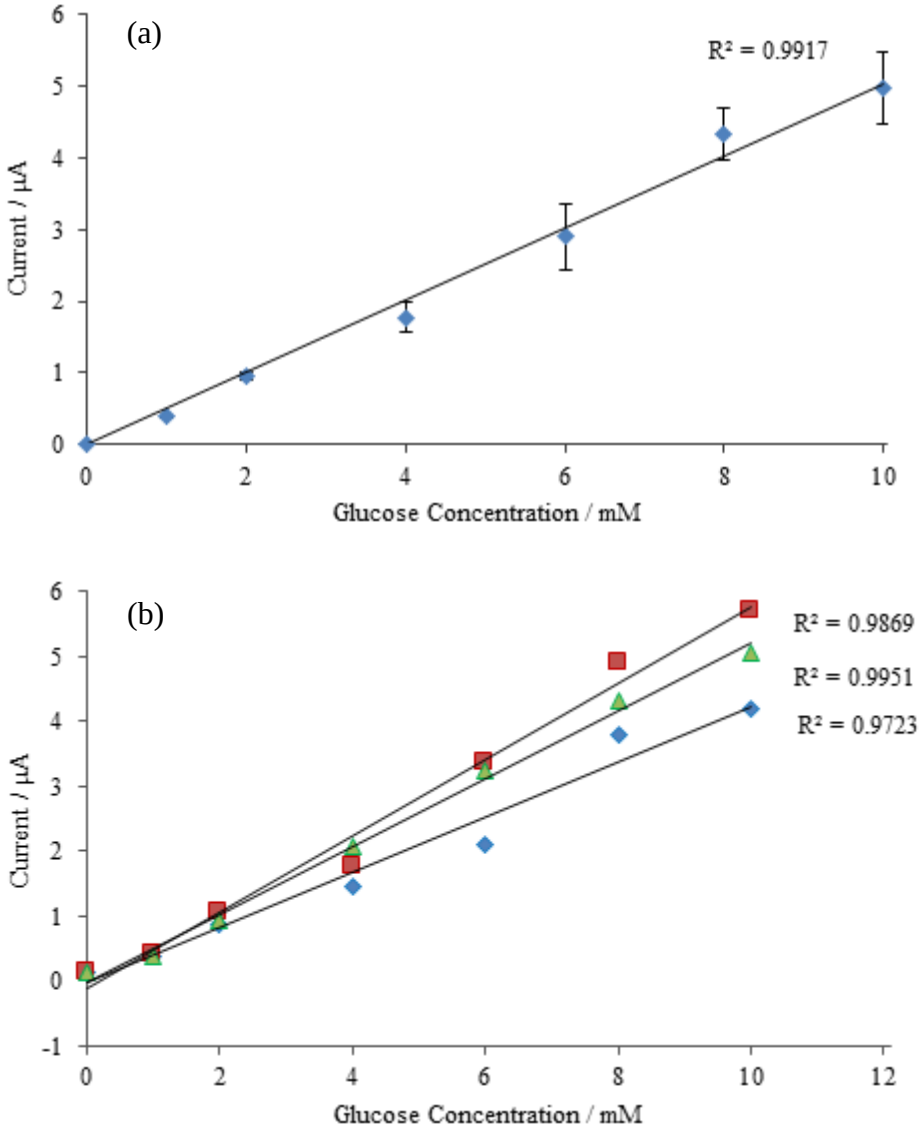

Figure 3.8: (a) Calibration curve for the oxidation of glucose in 0.10 M PBS (pH 7.4) at the pristine MWCNT-$Au_{nano}(NaBH_4)$ modified GC electrode, n = 3. This graph was produced using the mean of the peak currents from three separate experiments. Figure **(b)** displays calibration data for each experiment. Currents measured at 0.25 V vs. SCE.

3.2.3.2 Acid functionalised 18 h fMWCNT-$Au_{nano}(NaBH_4)$

To Note: *The initial prefix representing the reflux time is included in the following sections, Sections 3.2.3.2 – 3.2.3.5, for comparison of the composite materials, although this prefix is removed from Section 3.2.4 onwards for clarity. It should be noted that only the 24 h fMWCNTs were used in further studies.*

In an attempt to increase the AuNP loading into the composite and to increase the solubility of MWCNTs in SDS, the MWCNTs were functionalised in concentrated HNO_3 to introduce polar acid functionalities on their surfaces. This type of acid treatment can be quite destructive to the surface graphene layers and produces acidic defects in the graphitic hexacyclic sp^2 hybridised structures [14]. As mentioned previously, AuNPs tend to deposit at the defect sites of fMWCNTs. The pristine MWCNTs were refluxed in HNO_3 for an 18 h period to produce the 18 h fMWCNTs, as discussed in Chapter 2, Section 2.2.5.1. These fMWCNTs were dispersible in both H_2O and 1.0% SDS, at 2 mg/ml, in contrast to the pristine MWCNTs which were much less dispersible in H_2O. The resulting composite, named 18 h fMWCNT-$Au_{nano}(NaBH_4)$, was then employed as detailed in Section 3.2.3.1 to produce the composite modified GC electrode. Details of this synthesis are discussed in Chapter 2, Section 2.2.5.2.

Typical CVs for the oxidation of glucose at the 18 h fMWCNT-$Au_{nano}(NaBH_4)$ composite films are shown in Figure 3.9. When these voltammograms are compared with the data shown in Figure 3.7, it is clear that the oxidation of glucose is greatly improved as larger current responses are evident in both the reverse and forward scans at around 0.25 V vs. SCE. As in Section 3.2.3.1, the glucose calibration curve, shown in Figure 3.10, was constructed using the current responses for glucose measured in the reverse scans during CV. The sensitivity of this sensor is over 180% higher than that of the previous pristine MWCNT-$Au_{nano}(NaBH_4)$ film, Section 3.2.3.1. The calibration curve generated from these CVs shows good linearity, but large errors are seen, especially at higher glucose concentrations.

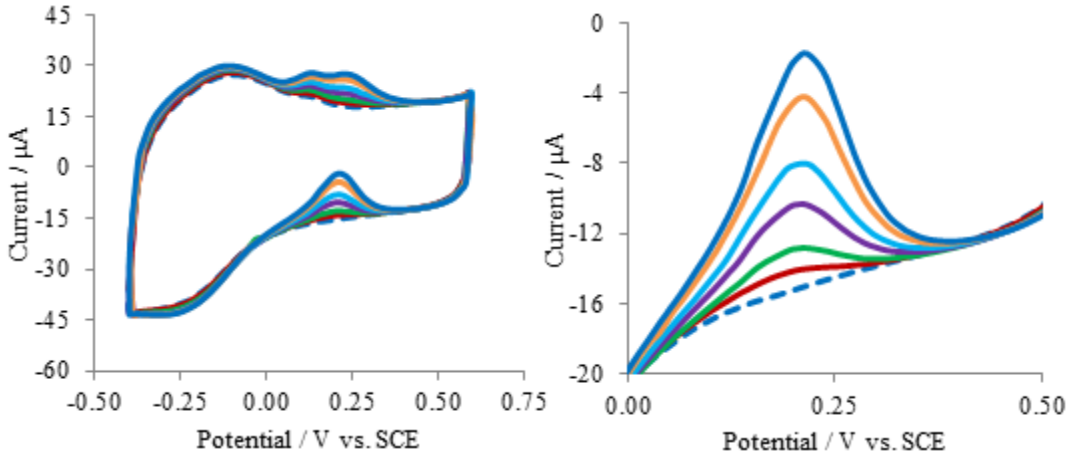

Figure 3.9: Cyclic voltammograms recorded at 100 mV s^{-1} at the 18 h fMWCNT-$Au_{nano}(NaBH_4)$ modified GC electrode in 0.10 M PBS solutions (pH 7.4) containing 1.0 – 10.0 mM glucose. Magnified sections showing the oxidation peaks are shown to the right.

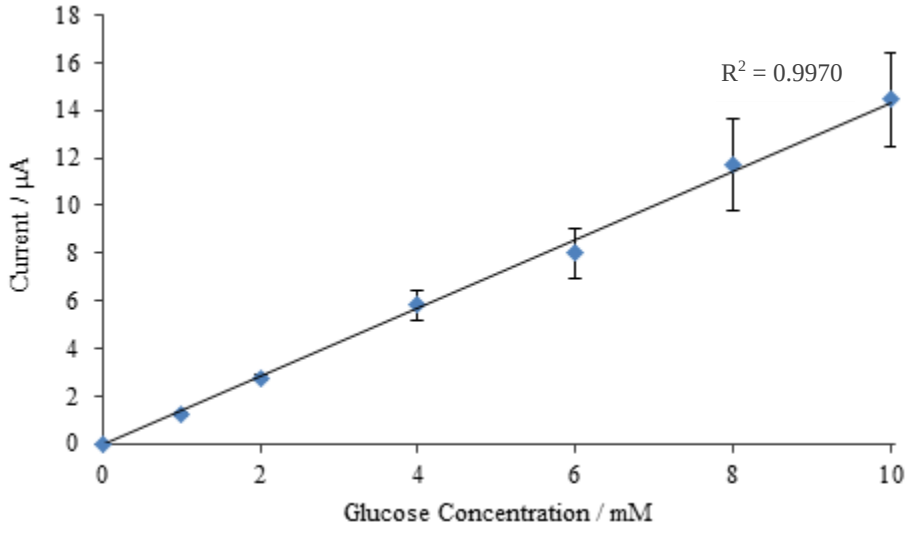

Figure 3.10: Calibration curve for the oxidation of glucose in 0.10 M PBS (pH 7.4) at the 18 h fMWCNT-$Au_{nano}(NaBH_4)$ modified GC electrode, n = 3. Currents measured at approximately 0.25 V vs. SCE.

3.2.3.3 Acid functionalised 24 h fMWCNT-$Au_{nano}(NaBH_4)$

This material, using the MWCNTs refluxed for the longer period of 24 h, resulted in a composite that produced the most sensitive films for glucose. This composite was named 24 h fMWCNT-$Au_{nano}(NaBH_4)$ and details of its synthesis are discussed in Chapter 2, Section 2.2.5.2. The voltammograms recorded, for the detection of glucose using this composite film, are shown in Figure 3.11. The resulting peak currents remain at approximately 0.25 V vs. SCE and are considerably larger in comparison to the data presented in Figure 3.9, for the films produced using the 18 h fMWCNT-$Au_{nano}(NaBH_4)$ composite or in Figure 3.7 for the pristine MWCNTs-$Au_{nano}(NaBH_4)$ composite. This indicates very good detection and the corresponding calibration curve, shown in Figure 3.12, gives very good linearity (R^2 is 0.9927) with smaller errors. To construct these calibrations curves the oxidation responses for glucose in the reverse scan were used. The sensitivity of this sensor is 50% higher than that of the previous 18 h fMWCNT-$Au_{nano}(NaBH_4)$ film, Section 3.2.3.2 and over 300% higher than the pristine MWCNT-$Au_{nano}(NaBH_4)$, Section 3.2.3.1. The films improved sensitivity is most likely due to an increased amount of the AuNPs present in the composite. As mentioned previously, increased AuNP loading may be a result of the larger number of defect sites on the fMWCNTs but may also be due to their improved solubility in SDS during composite synthesis. Analysis of the potentiometric titrations, shown in Section 3.2.9.2, gives the surface coverage of acidic groups of the 24 h fMWCNTs to be at 6.0%, in comparison to a value of 0.0% with the pristine MWCNTs. The Au content is indeed higher in this composite in comparison to the pristine MWCNT-Au_{nano} composite, and is determined to be 2.86% wt. of sample using EDX and 2.0% using AA analysis, shown in Sections 3.2.9.3 and 3.2.9.6, respectively. TEM analysis, presented in Section 3.2.9.4, shows the sizes of the AuNPs formed to be largely under 10.0 nm in diameter with a low size distribution. From comparison of these results, it is clear that the functionalisation of the MWCNTs has a significant role to play in the extent of AuNP loading onto the nanotube surfaces and thus the sensitivity of the composite films towards glucose detection.

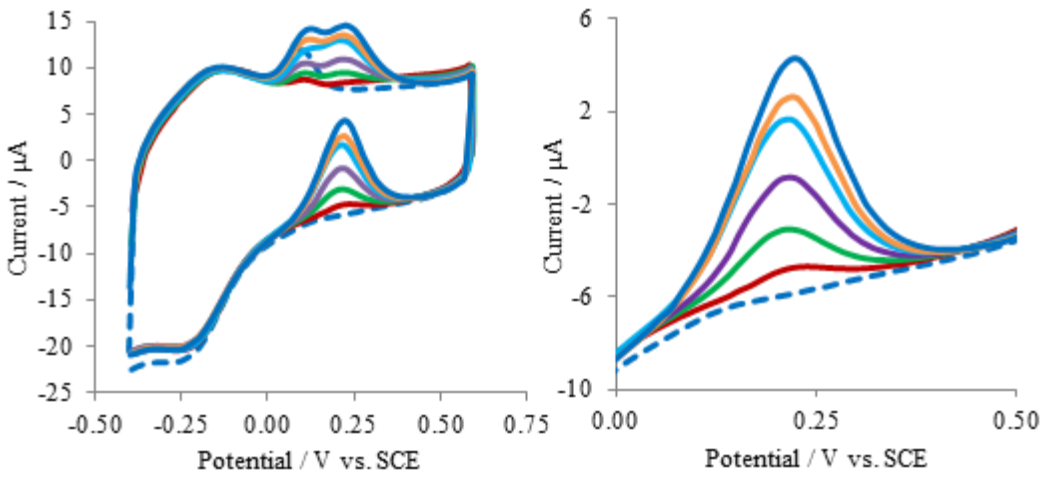

Figure 3.11: Cyclic voltammograms recorded at 100 mV s^{-1} at the 24 h fMWCNT-$Au_{nano}(NaBH_4)$ modified GC electrode in 0.10 M PBS solutions (pH 7.4) containing 1.0 – 10.0 mM glucose. Magnified sections showing the oxidation peaks are shown to the right.

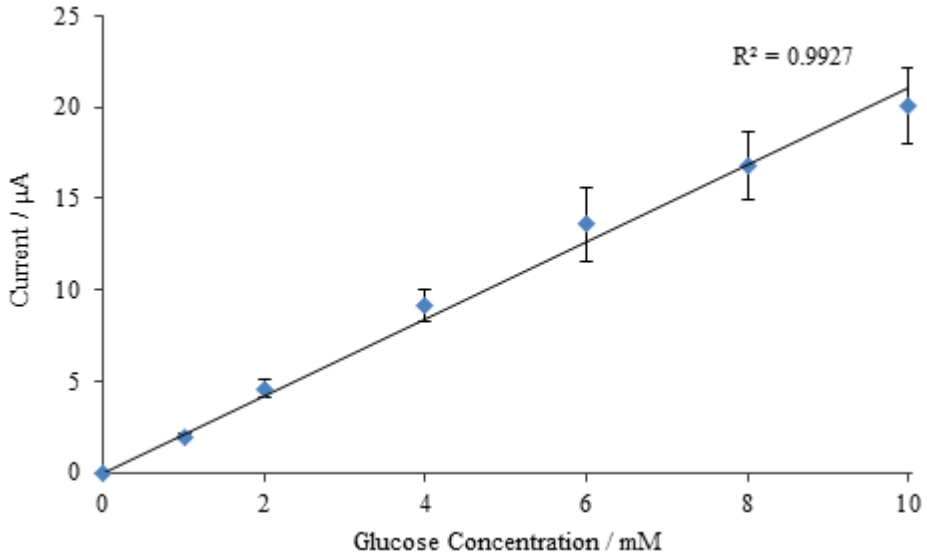

Figure 3.12 Calibration curve for the oxidation of glucose in 0.10 M PBS (pH 7.4) at the 24 h fMWCNT-$Au_{nano}(NaBH_4)$ modified GC electrode, n = 3. Currents measured at approximately 0.25 V vs. SCE.

3.2.3.4 Acid functionalised 48 h fMWCNT-$Au_{nano}(NaBH_4)$

Due to the good sensitivity of the previous composite film for the detection of glucose, Figures 3.11 and 3.12, it was expected that the material produced with 48 h refluxed fMWCNTs may provide even better sensing films. This material was named 48 h fMWCNT-$Au_{nano}(NaBH_4)$ and was produced using the synthesis conditions discussed in Chapter 2, Section 2.2.5.2. Representative CVs recorded in the glucose-containing PBS solutions using the 48 h fMWCNT-$Au_{nano}(NaBH_4)$ modified GC electrode are shown in Figure 3.13, however it is evident that the oxidation currents for glucose are less intense, in comparison to those displayed for the 24 h fMWCNT-$Au_{nano}(NaBH_4)$ film in Section 3.2.3.3. This is also evident in the calibration curve shown in Figure 3.14 which was constructed using the peal currents for glucose in the reverse scans during CV. In comparison to the 24 h fMWCNT-$Au_{nano}(NaBH_4)$ modified GC, Section 3.2.3.3, the sensitivity has decreased by 30% at the 48 h fMWCNT-$Au_{nano}(NaBH_4)$. Although in comparison to the pristine MWCNT-$Au_{nano}(NaBH_4)$ film, the sensitivity has been increased by almost 200%. One possible explanation for the lower currents may be connected to the lengthy acid reflux in HNO_3 which has damaging effects on the MWCNTs. Indeed over 50% of the MWCNT starting material was lost during this 48 h acid reflux.

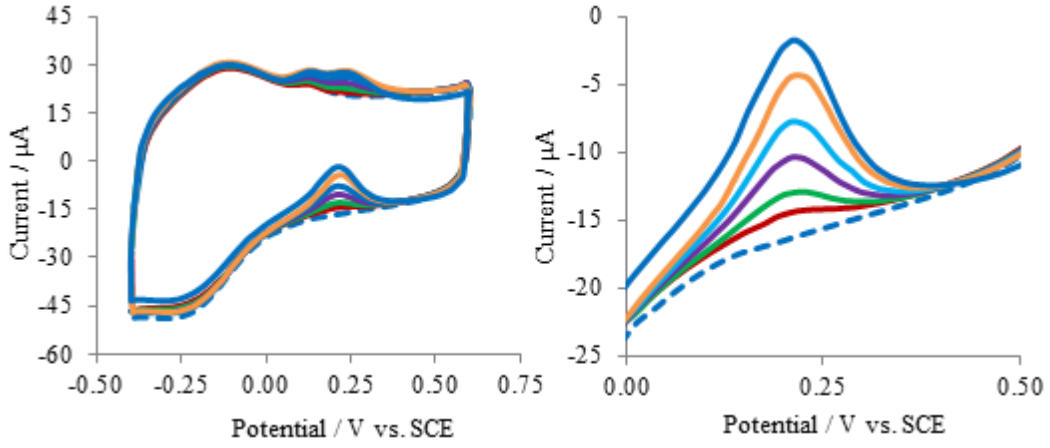

Figure 3.13: Cyclic voltammograms recorded at 100 mV s^{-1} for the 48 h fMWCNT-$Au_{nano}(NaBH_4)$ modified GC electrode in 0.10 M PBS solutions (pH 7.4) containing 1.0 – 10.0 mM glucose. Magnified sections showing the oxidation peaks are shown to the right.

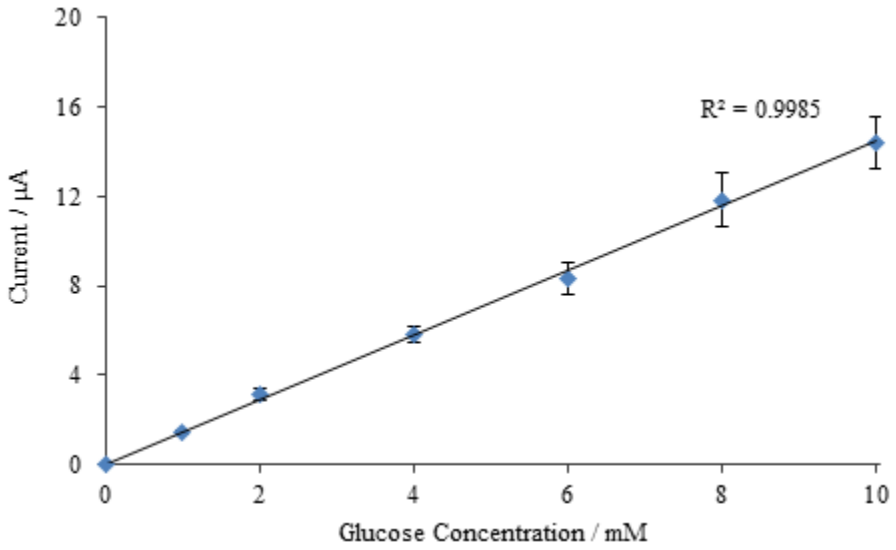

Figure 3.14: Calibration curve for the oxidation of glucose in 0.10 M PBS (pH 7.4) at the 48 h fMWCNT-$Au_{nano}(NaBH_4)$ modified GC electrode, n = 3. Currents measured at approximately 0.25 V vs. SCE.

3.2.3.5 Limits of Detection and Sensitivities at the MWCNT-$Au_{nano}(NaBH_4)$ and fMWCNT-$Au_{nano}(NaBH_4)$ Films

Using the calibration curves presented in Figures 3.8, 3.10, 3.12 and 3.14, the Limits of Detection (LODs) were calculated and compared for the different composite films. These values can be used as an indication of the lowest quantity of an analyte that can be accurately distinguished from background noise [15]. The LODs are calculated using Equation 3.1 where LOD is the concentration, *Sd* is the standard deviation of the blank current response [16]. As LODs are related to the standard deviation of the background response any large fluctuations in this response will have an effect on their values.

$$LOD = 3Sd \qquad 3.1$$

The sensitivities of the films towards the oxidation of glucose have also been calculated from the slope of the linear plot and these data are summarised in Table 3.1. It can be clearly seen that the 24 h fMWCNT-$Au_{nano}(NaBH_4)$ composite exhibits the best detection of glucose with a LOD value of 0.429 µM, in contrast to the LOD value of 1.348 µM for the pristine MWCNT. It is also clearly evident from the data that this

film possessed the highest sensitivity towards glucose at 2.102 µA/mM. This is most likely due to an increased surface coverage of AuNPs. Indeed this was confirmed using AA analysis, shown in Section 3.2.9.6, in which an Au composition of 2.0% wt. was achieved. The Au composition of the pristine MWCNT-$Au_{nano}(NaBH_4)$ material was lower at 1.0% wt. and this is possibly the reason for its lesser sensitivity towards glucose.

Table 3.1: Limits of Detection and film sensitivity values towards the oxidation of glucose at the MWCNT-$Au_{nano}(NaBH_4)$ and fMWCNT-$Au_{nano}(NaBH_4)$ composite films towards glucose oxidation, n = 3.

Composite Film	LOD / µM	Sensitivity / µA/mM	Error / µA/mM
Pristine MWCNT-Au_{nano}	1.348	0.504	± 0.054
18 h fMWCNT-Au_{nano}	2.032	1.431	± 0.227
24 h fMWCNT-Au_{nano}	0.429	2.102	± 0.223
48 h fMWCNT-Au_{nano}	2.474	1.445	± 0.133

3.2.4 Detection of Glucose at fMWCNT-$Au_{nano}(NaBH_4)$/Nafion® Films

Since the 24 h fMWCNT-$Au_{nano}(NaBH_4)$ composite film, discussed in Section 3.2.3.3, provided the most sensitive films with the lowest LOD values, it was chosen as the ideal material for combination with a Nafion® membrane. This membrane was created using 5.0 µl of a 50:50 (vol:vol) Nafion® 117 solution made in ethanol absolute, as discussed in Chapter 2, Section 2.2.6.4. This volume of the Nafion® solution was sufficient to completely cover the composite film and also the surrounding insulating housing. This new film was named fMWCNT-$Au_{nano}(NaBH_4)$/Nafion®. As discussed in Chapter 1, Section 1.4.6.4, Nafion® has anion rejection properties, and it has the potential to reduce interference from anionic species such as ascorbic acid (AA) and uric acid (UA). However, in this work it was also found to reduce the detection of glucose. With the use of Nafion®, the sensitivity of the film produced from 2.0 mg/ml dispersion, Figure 3.15, had decreased by almost 80%, in comparison to the film

without Nafion®, Section 3.2.3.3. In an attempt to enhance the detection of glucose at the Nafion® modified films, a more concentrated dispersion of the fMWCNT-$Au_{nano}(NaBH_4)$, at 4.0 mg/ml was used and compared with the results obtained with a dispersion of 2.0 mg/ml. Again, the composite was re-dispersed in a 1.0% SDS solution and cast onto the GC electrodes.

Results for the detection of glucose at this fMWCNT-$Au_{nano}(NaBH_4)$/Nafion® modified GC electrode are shown in Figure 3.15. In Figure 3.15 (a), results are shown for the detection of glucose at a modified GC electrode containing 5.0 µl of the 2.0 mg/ml fMWCNT-$Au_{nano}(NaBH_4)$ dispersion and data for the higher concentration dispersion of 4.0 mg/ml are presented in Figure 3.15 (b). In both cases, the wave arising from the oxidation of glucose is more clearly shown in a smaller electrochemical window. As seen in Figure 3.15, the detection of glucose is possible with the addition of Nafion®, although the currents recorded at around 0.25 V vs. SCE, for the detection of glucose, appear considerably lower than those obtained at the fMWCNT-$Au_{nano}(NaBH_4)$ modified electrode without Nafion®, Figure 3.11. On comparing the data presented in Figure 3.15 (a) and (b) it is clear that the more concentrated dispersion, 4.0 mg/ml, results in the best detection of glucose in comparison to the 2.0 mg/ml dispersion. Indeed sensitivity has increased by approximately 90%. More concentrated dispersions were used but no further improvements in the detection of glucose were observed.

Calibration curves for the Nafion® encapsulated films, fMWCNT-$Au_{nano}(NaBH_4)$ Nafion®, produced from the 4.0 mg/ml and 2.0 mg/ml dispersions are shown in Figure 3.16. It is clear from these plots that the 4.0 mg/ml dispersion yields the highest sensitivity to glucose with a 90% improvement. However as mentioned the over sensitivity towards glucose has been reduced significantly by 80%. In Table 3.2, the LODs and sensitivities of films towards glucose produced with the 2.0 mg/ml and the higher 4.0 mg/ml dispersions are listed. In an attempt to improve the detection of glucose at these films, the fMWCNT-$Au_{nano}(NaBH_4)$ electrodes were cycled in H_2SO_4, using CV. The cycling of Au materials in H_2SO_4 can be employed in the field of electrochemistry as a general cleaning step [17] and this approach was used with the composite films.

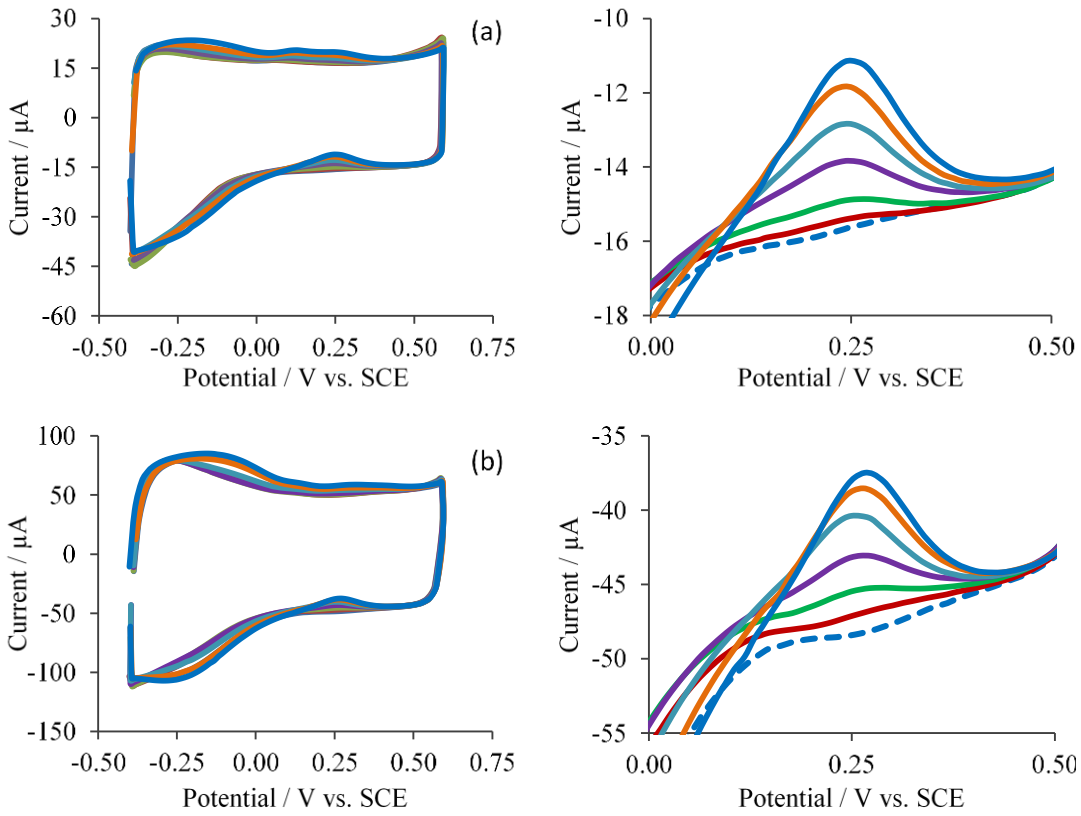

Figure 3.15: Cyclic voltammograms recorded at 100 mV s^{-1} of the fMWCNT-$Au_{nano}(NaBH_4)$/Nafion® modified GC electrodes produced from 5.0 µl of the **(a)** 2.0 mg/ml and **(b)** 4.0 mg/ml dispersions in 0.10 M PBS solutions (pH 7.4) containing 1.0 – 10.0 mM glucose. Magnified sections showing the oxidation peaks are shown to the right.

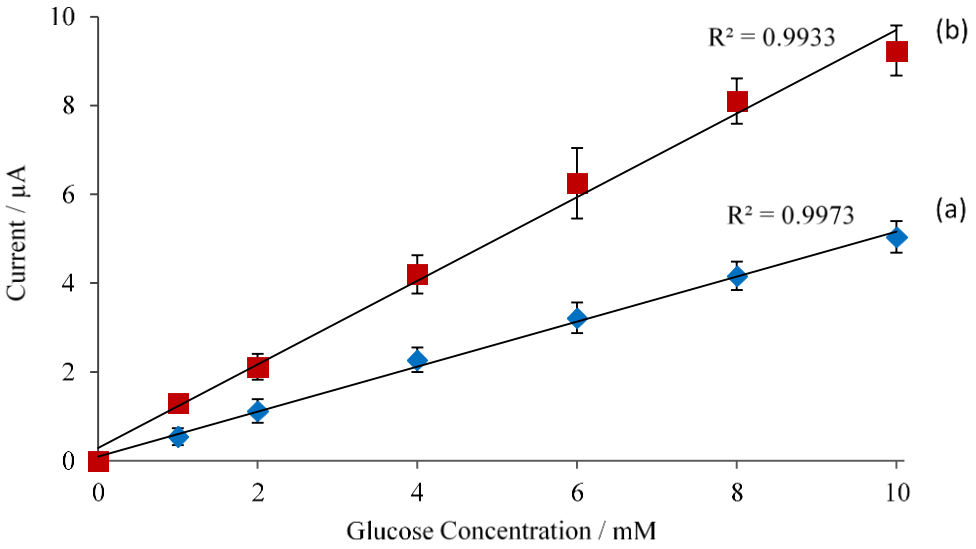

Figure 3.16: Calibration curves for the oxidation of glucose in 0.10 M PBS (pH 7.4) at the fMWCNT-$Au_{nano}(NaBH_4)$/Nafion® modified GC electrodes produced from **(a)** 2.0 mg/ml and **(b)** 4.0 mg/ml dispersions, n = 3. Currents measured at 0.25 V vs. SCE.

Table 3.2: Limits of detection and sensitivities of the films towards the oxidation of glucose at the fMWCNT-$Au_{nano}(NaBH_4)$/Nafion® composite modified GC electrodes produced from the 2.0 mg/ml and 4.0 mg/ml dispersions, n = 3.

Dispersion Concentration / mg/ml	LOD / µM	Sensitivity / µA/mM	Error / µA/mM
2.0	0.632	0.507	± 0.027
4.0	0.894	0.942	± 0.062

3.2.5 Optimisation of Glucose Detection at fMWCNT-$Au_{nano}(NaBH_4)$ Films using Sulfuric Acid Pre-treatments

The fMWCNT-$Au_{nano}(NaBH_4)$ composite films were cycled in 1.0 M and 0.5 M H_2SO_4 using CV and then cycled in PBS with the addition of glucose. It can again be noted that only the 24 h fMWCNT-$Au_{nano}(NaBH_4)$ composites are used in the remaining work. The initial NaOH cycling was also used and this was carried out prior to the pre-treatment in the acid solution. The influence of the H_2SO_4 pre-treatment is shown in Figure 3.17, where voltammograms are presented for the H_2SO_4

pre-treated and untreated films in the PBS background electrolyte with and without 10.0 mM glucose. As observed in the CVs in Figure 3.17, these pre-treatment steps increase the sensitivity of the materials towards glucose detection, of which 1.0 M H_2SO_4 provides optimal results. The 1.0 M H_2SO_4 cycling increased the peak currents measured for glucose in the forward and reverse scans by 70% and 90%, to 4.19 $\times 10^{-5}$A (41.90 µA) and 5.99 $\times 10^{-5}$A (59.93 µA), in comparison to the film without H_2SO_4 pre-treatment, which yields peak currents of 2.46 $\times 10^{-5}$A (24.60 µA) and 3.21$\times 10^{-5}$A (32.10 µA) in the forward and reverse scans, respectively. It is evident that glucose detection occurs over similar potentials in both the reverse and forward scans although with a slight positive shift in the forward scan. Also, it is evident that an increase in the overall capacitance at the composite film occurs, with the most significant increase at potentials lower than 0.10 V vs. SCE. It is clear that the overall capacitance of the films is higher at the 1.0 M H_2SO_4 pre-treated film. To gain further information on the composite films and the effects of the pre-treatment in the H_2SO_4, solutions, electrochemical impedance spectroscopy was conducted. The results of this study are presented and discussed in Section 3.2.9.11. It appears from the data presented in Figure 3.17, that utilisation of the 1.0 M H_2SO_4 pre-treatment gives the best detection of glucose.

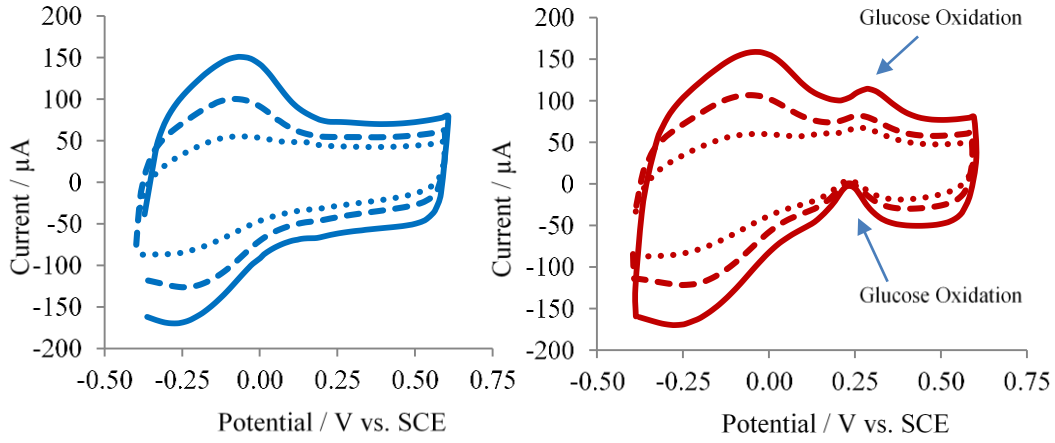

Figure 3.17: Cyclic voltammograms recorded at 100 mV s^{-1} for the H_2SO_4 pre-treated fMWCNT-$Au_{nano}(NaBH_4)$ modified GC electrodes in 0.10 M PBS (pH 7.4) (blue) and in 0.10 M PBS containing 10.0 mM glucose (red) for films pre-treated in ——— 1.0 M H_2SO_4, - - - 0.5 M H_2SO_4 and ····· no pre-treatment in H_2SO_4.

3.2.6 Detection of Glucose using CPA at Pre-treated fMWCNT-$Au_{nano}(NaBH_4)$ and fMWCNT-$Au_{nano}(NaBH_4)$/Nafion® Films

The detection of glucose in 0.10 M PBS was further studied at the H_2SO_4 pre-treated fMWCNT-$Au_{nano}(NaBH_4)$ and fMWCNT-$Au_{nano}(NaBH_4)$/Nafion® composite films using constant potential amperometry (CPA), experimental setups are discussed in Chapter 2, Section 2.2.8.2. CPA is a technique commonly used in electrochemical sensors and involves the application of a constant potential to the sensor and the resulting currents are measured. Various potentials ranging from 0.00 V to 0.50 V vs. SCE were chosen to identify an ideal potential for maximum glucose detection. A potential of 0.30 V vs. SCE, which is located just after the oxidation waves in the forward scans, yielded the best results and was chosen for all CPA experiments. These data were recorded by applying a potential of 0.30 V vs. SCE to the composite films until the current reached a steady state, approximately 1000 s, then aliquots of glucose from a 50 mM stock solution in 0.1 M PBS were added. Details of the volumes of this stock added to the cell and the cell glucose concentrations are listed in Chapter 2, Section 2.2.8.2.

In Figure 3.18, the current-time plots are shown for the oxidation of glucose at 0.30 V vs. SCE for the fMWCNT-$Au_{nano}(NaBH_4)$ modified GC electrodes following no pre-treatment (blue trace), pre-treatment in 0.5 M H_2SO_4 (red trace) and pre-treatment in 1.0 M H_2SO_4 (green trace). It is clear that the acid cycling increases the detection of glucose, with the 1.0 M H_2SO_4 pre-treatment improving the sensitivity by almost 600% using CPA, compared to the untreated composite film. In Figure 3.19, the influence of the Nafion® membrane is shown. These plots were recorded for the fMWCNT-$Au_{nano}(NaBH_4)$ composite with and without the Nafion® membrane following a pre-treatment in 1.0 M H_2SO_4. As discussed in previous sections these membranes were made using 5.0 µl of a 50:50 (vol:vol) solution of Nafion® 117 made in ethanol absolute. The membrane consisted of 5.0 µl of Nafion® 117 cast onto the surface of the fMWCNT-$Au_{nano}(NaBH_4)$ composite. It is clear from these results that the use of Nafion® greatly reduces the detection of glucose and this reduction in sensitivity is calculated to be approximately 80% for the 1.0 M H_2SO_4, 0.5 M H_2SO_4 and non-treated films, data shown in Table 3.3.

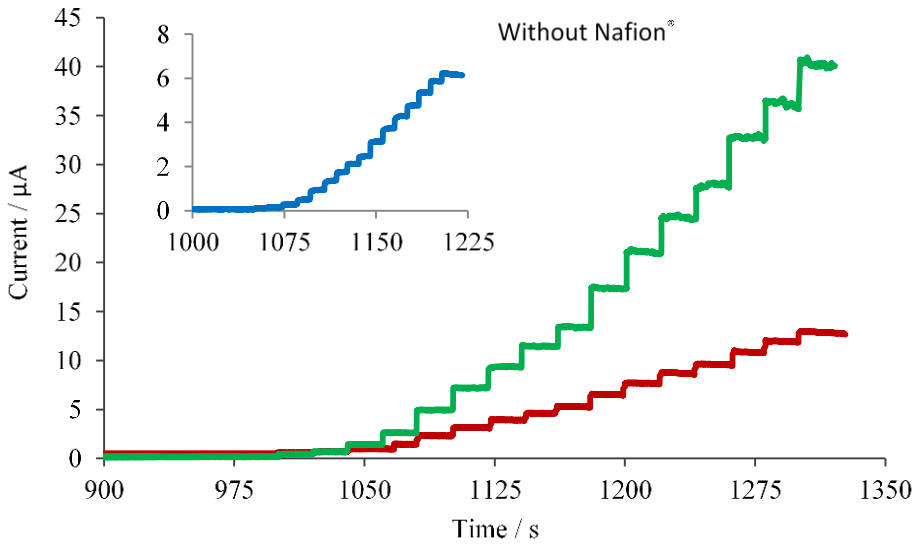

Figure 3.18: Current-time plots for the oxidation of glucose in 0.10 M PBS (pH 7.4) with the successive additions of glucose aliquots from a 50 mM stock solution, made in 0.10 M PBS, recorded at 0.30 V vs. SCE, at the fMWCNT-$Au_{nano}(NaBH_4)$ modified GC electrodes pre-treated in — 0.5 M H_2SO_4, — 1.0 M H_2SO_4 — and no pre-treatment.

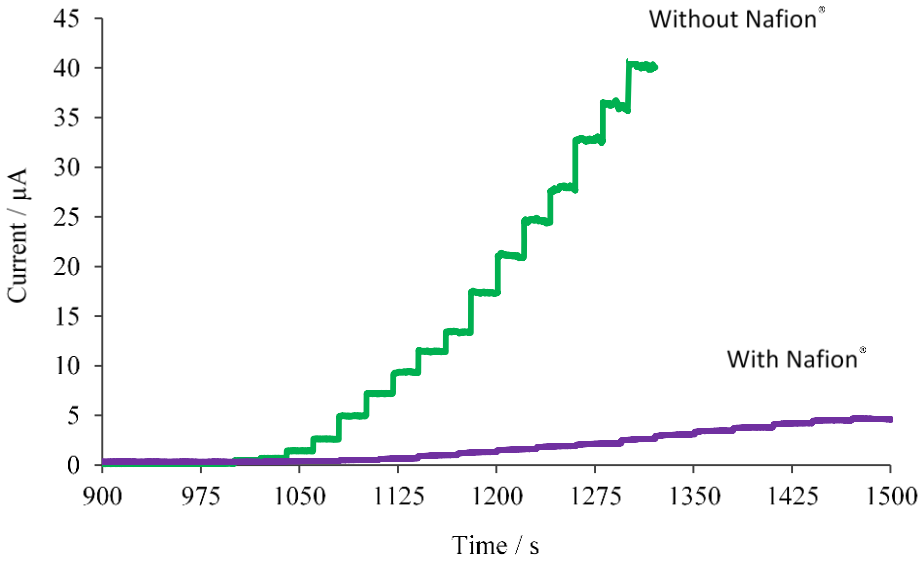

Figure 3.19: Current-time plots for the oxidation of glucose in 0.10 M PBS (pH 7.4) with the successive additions of glucose aliquots from a 50 mM stock solution, made in 0.10 M PBS, recorded at 0.30 V vs. SCE, at the 1.0 M H_2SO_4 pre-treated — fMWCNT-$Au_{nano}(NaBH_4)$ and — fMWCNT-$Au_{nano}(NaBH_4)$/Nafion® modified GC electrodes.

Calibration curves for the detection of glucose using CPA at 0.30 V vs. SCE are shown in Figure 3.20. In Figure 3.20 (a) calibration curves are presented for the fMWCNT-$Au_{nano}(NaBH_4)$ composite following no pre-treatment and pre-treatments in 0.5 M and 1.0 M H_2SO_4, while the corresponding data recorded at the fMWCNT-$Au_{nano}(NaBH_4)$/Nafion® films are presented in Figure 3.20 (b). The calibration curves show good linearity with small errors. In the presence of higher concentrations of glucose, above 12.5 mM, there is some deviation from linearity observed. The errors are small but do increase when the Nafion® membrane is used and when higher concentrations of glucose are present. It is clear from these data that the 1.0 M H_2SO_4 pre-treated fMWCNT-$Au_{nano}(NaBH_4)$ composite, with and without Nafion® gave the best detection of glucose with higher sensitivity. The use of Nafion® reduced the films sensitivity towards glucose and this may be due to an increase in the diffusion barrier and therefore a decreased the rate of glucose diffusion to the electrode surface.

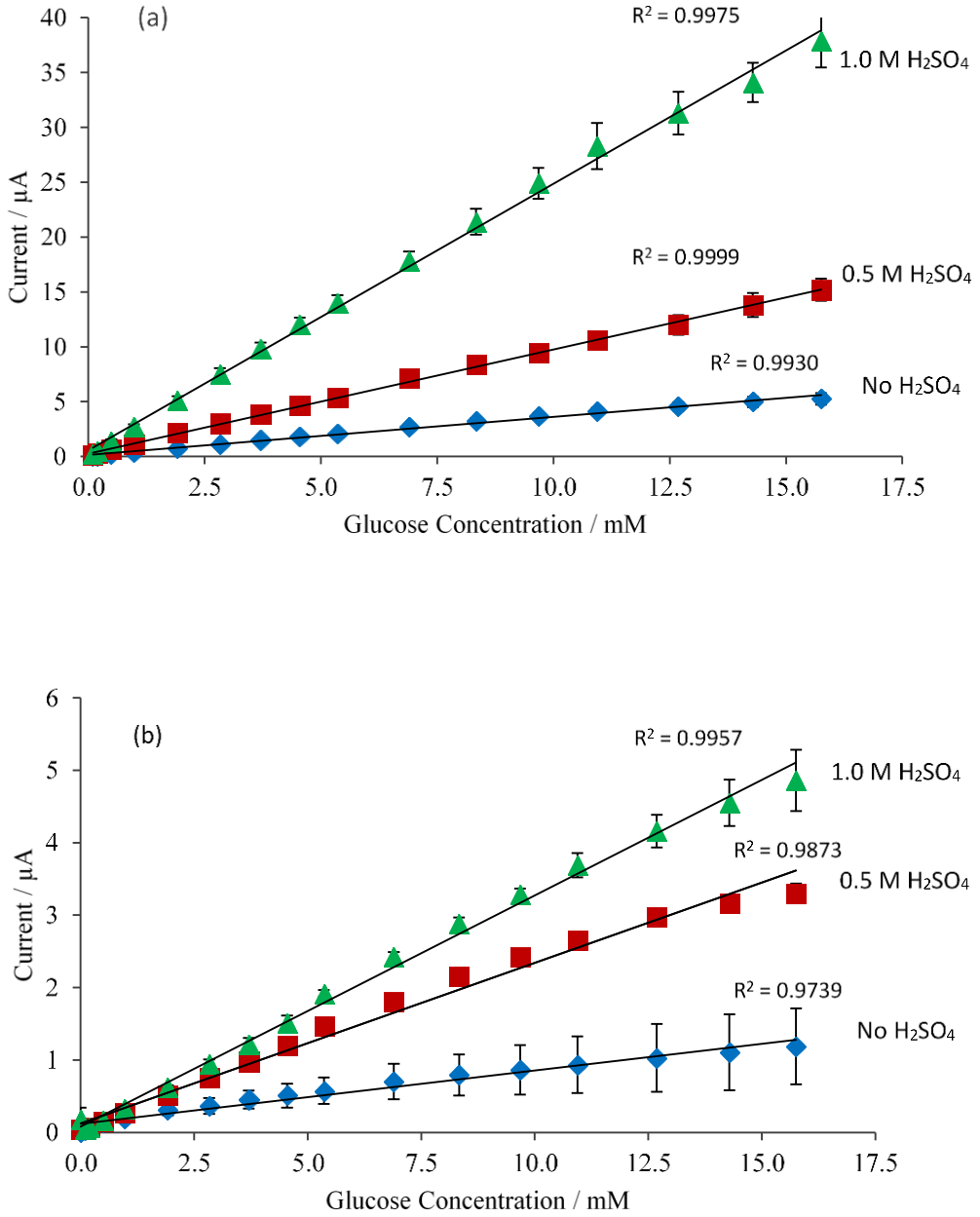

Figure 3.20: Calibration curves for the oxidation of glucose in 0.10 M PBS (pH 7.4) at the H_2SO_4 pre-treated and non-treated **(a)** fMWCNT-$Au_{nano}(NaBH_4)$ and **(b)** fMWCNT-$Au_{nano}(NaBH_4)$/Nafion® modified GC electrodes, n = 3.

The LOD and sensitivity values for the composite films are listed in Table 3.3. Again, it is clear from the sensitivity values at the 1.0 M H_2SO_4 optimised sensors, with or without Nafion® that they result in the highest sensitivities towards glucose. The sensitivity at the 1.0 M H_2SO_4 pre-treated fMWCNT-$Au_{nano}(NaBH_4)$ composite film

is 2.430 µA/mM, compared to a sensitivity of 0.349 µA/mM at the non-treated composite film. This corresponds to almost a 600% increase in sensitivity. The sensitivity of the fMWCNT-Au_{nano}($NaBH_4$)/Nafion® film has been increased by almost 350% with the use of the 1.0 M H_2SO_4 pre-treatment. However its sensitivity is reduced considerably, by 90%, in comparison to the optimised film without Nafion®, fMWCNT-Au_{nano}($NaBH_4$). Since the 1.0 M H_2SO_4 pre-treatment resulted in the most sensitive films towards glucose, this was utilised in all further studies as standard, along with the NaOH pre-treatments. These acid treated sensors may be referred to as 'optimised' sensors in the following sections.

Table 3.3: Limits of detection and sensitivities towards the oxidation of glucose at the fMWCNT-Au_{nano}($NaBH_4$) composite films pre-treated in H_2SO_4 with and without the Nafion® membranes, n = 3.

Without Nafion®				With Nafion®		
Pre-Treatment	**LOD / µM**	**Sensitivity / µA/mM**	**Error / µA/mM**	**LOD / µM**	**Sensitivity / µA/mM**	**Error / µA/mM**
1.0 M H_2SO_4	0.072	2.430	± 0.0351	0.027	0.317	± 0.0025
0.5 M H_2SO_4	0.228	0.954	± 0.0680	0.029	0.222	± 0.0070
No H_2SO_4	0.213	0.349	± 0.1530	0.053	0.073	± 0.0240

3.2.7 Detection of Glucose at fMWCNT-Au_{nano} Films using Trisodium Citrate as a Reducing Agent

Due to the glucose sensing limitations of the fMWCNT-Au_{nano}($NaBH_4$)/Nafion® composites films, new composite films were produced using a new composite material which was produced using a differed reducing agent and synthesis conditions. This was carried out in an attempt to increase the loading of the AuNPs onto the fMWCNTs. Trisodium citrate (TriSodCit) was used as the reducing agent to produce the composite named fMWCNT-Au_{nano}(TriSodCit) and the procedure used is detailed in Chapter 2, Section 2.2.5.3. The 24 h fMWCNTs were again used as they yielded the best results previously. As with the previous composite, a dispersion of 4.0 mg/ml in 1.0% SDS was prepared and a 5.0 µl volume of this was again cast onto the GC

surface. Due to the success of the H_2SO_4 pre-treatments, this was utilised further. The previous composite, produced with the $NaBH_4$, consisted of Au at 2.0% wt., which was determined using AA analysis, Section 3.2.9.6, and the new composite generated using the TriSodCit yielded an increased Au composition of 5.0%. As before, CPA at an applied potential 0.30 V vs. SCE was used for the detection of glucose. The current-time plots recorded for the oxidation of glucose, at 0.30 V vs. SCE, at the 1.0 M H_2SO_4 pre-treated fMWCNT-Au_{nano}(TriSodCit) and fMWCNT-Au_{nano}($NaBH_4$) modified electrodes are shown in Figure 3.21 for comparison. The corresponding calibration curves are shown in Figure 3.22. It is clear from these data that the fMWCNT-Au_{nano}(TriSodCit) composite films provide a larger current response to glucose and as a result give improved glucose detection. This is most likely due to the increased presence of AuNPs on the fMWCNTs. Larger AuNPs, typically around 25 nm in size, were also formed using this new procedure, as shown in the TEM analysis in Section 3.2.9.4. Again the calibration curves show good linearity but with a slight deviation at higher glucose concentrations, Figure 3.22. The errors increase at these higher concentrations. It is clear that the sensitivity of this optimised fMWCNT-Au_{nano}(TriSodCit) film towards glucose oxidation is much improved at 4.070 µA/mM, Table 3.4. This is 70% higher than the sensitivity of 2.430 µA/mM obtained at the previous optimised fMWCNT-Au_{nano}($NaBH_4$) film. The LOD value remains at an acceptable level of 0.304 µM, which compares well with the LOD values of the previous sensor.

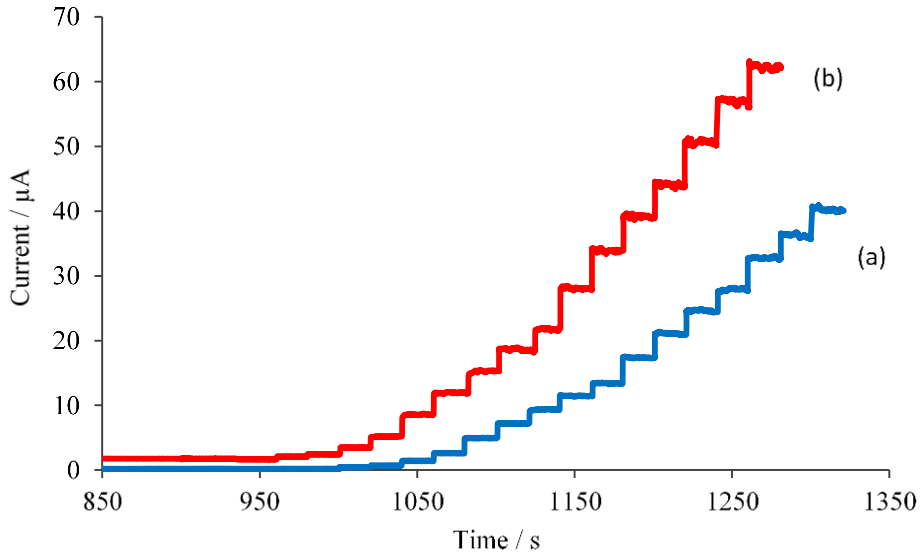

Figure 3.21: Current-time plots for the oxidation of glucose in 0.10 M PBS (pH 7.4) with the successive additions of glucose aliquots from a 50 mM stock solution, made in 0.10 M PBS, recorded at 0.30 V vs. SCE, at the 1.0 M H_2SO_4 pre-treated **(a)** fMWCNT-Au_{nano}($NaBH_4$) and **(b)** fMWCNT-Au_{nano}(TriSodCit) modified GC electrodes.

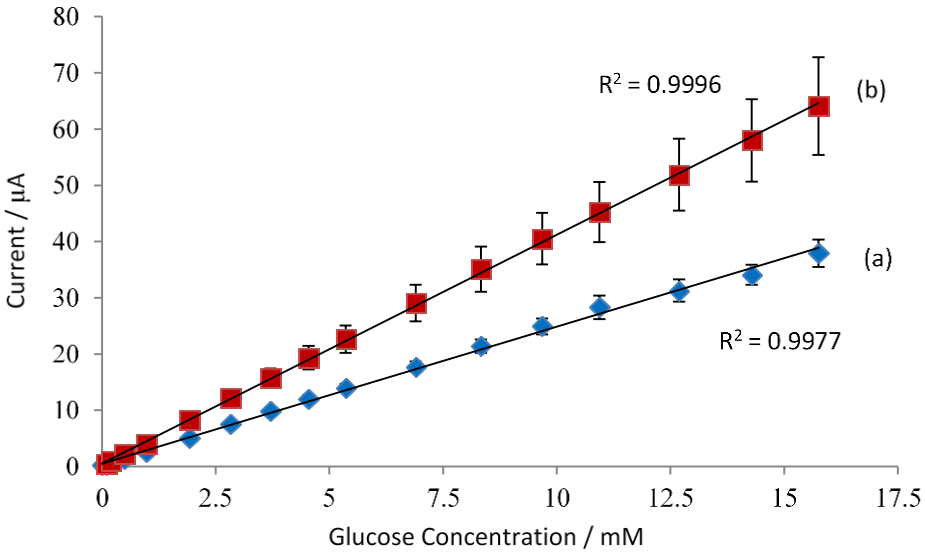

Figure 3.22: Calibration curves for the oxidation of glucose in 0.10 M PBS (pH 7.4), recorded at 0.30 V vs. SCE, at the 1.0 M H_2SO_4 pre-treated **(a)** fMWCNT-Au_{nano}($NaBH_4$) and **(b)** fMWCNT-Au_{nano}(TriSodCit) modified GC electrodes, n = 3.

Naturally the next step would have been to investigate glucose detection in the presence of a Nafion® membrane. However the use of this fMWCNT-

Au_{nano}(TriSodCit) material for glucose sensing was ceased hereafter due to the instability of the composite material. This conclusion was reached as batches of this material only yielded sensitive films for a period of days and as such it was not an efficient direction to proceed with. It was assumed that AuNP aggregation was occurring both in the drop cast dispersal solutions and in the dry powder, possibly due to the higher AuNP loading and larger size.

Table 3.4: Limits of detection and sensitivities towards the oxidation of glucose at the optimised fMWCNT-Au_{nano}(TriSodCit) composite film, n = 3.

Without Nafion®				With Nafion®		
Pre-Treatment	**LOD / µM**	**Sensitivity / µA/mM**	**Error / µA/mM**	**LOD / mM**	**Sensitivity / µA/mM**	**Error / µA/mM**
1.0 M H_2SO_4	0.304	4.070	± 0.5293	ǂ	ǂ	ǂ

ǂ Experiment was not conducted

3.2.8 Detection of Glucose at fMWCNT-Au_{nano}($NaBH_4$) and fMWCNT-Au_{nano}($NaBH_4$)/Nafion® Modified Screen Printed Electrodes

Two types of screen printed electrodes (SPEs) were used and were both supplied from DropSens. The initial SPE of choice was the DRP-150 SPE which was a regular SPE consisting of a printed planar working electrode made of carbon, a platinum counter electrode and a silver (Ag) reference electrode. The other SPE (DRP-110OMC) consisted of high surface area ordered macroporous carbon working electrode, a carbon counter electrode and an Ag reference electrode. These Ag reference electrodes were converted into silver/silver chloride (Ag/Ag/AgCl) pseudo-reference electrodes using iron(111) chloride, as discussed in Chapter 2, Section 2.2.3. This was conducted as initial experiments found that potential drifts were a problem using the unmodified Ag reference. Upon investigating a series of potentials for CPA analysis, in proximity to the glucose oxidation peaks appearing in the forward and revers scans, a constant potential of -0.05 V vs. Ag/AgCl was applied, which provided the highest current responses for glucose. This potential coincided with the glucose oxidation

peak in the reverse scan of the CVs, a similar observation to the modified GC system using the SCE reference electrode, in which a potential of 0.30 V vs. SCE was used.

As mentioned, the fMWCNT-$Au_{nano}(NaBH_4)$ composite was only used in this work and in further work. Again this composite was dispersed in SDS at a concentration of 4.0 mg/ml for casting onto the electrode, although a larger quantity of 10.0 µl of the 4.0 mg/ml dispersion was found to provide optimum results on the SPEs due to their larger geometric area. Figure 3.23 (a), shows the CVs obtained at the 1.0 M H_2SO_4 pre-treated and untreated films in a PBS solution with and without 10.0 mM glucose. These CVs somewhat resemble those obtained from glucose detection at the modified GC electrodes, although the background currents appear more capacitive and the glucose oxidation peaks cannot be observed clearly. For better visualisation of the glucose oxidation peak at the optimised film in the reverse scan, a current differential plot was constructed by plotting the background-subtracted oxidation wave, shown in Figure 3.23 (b).

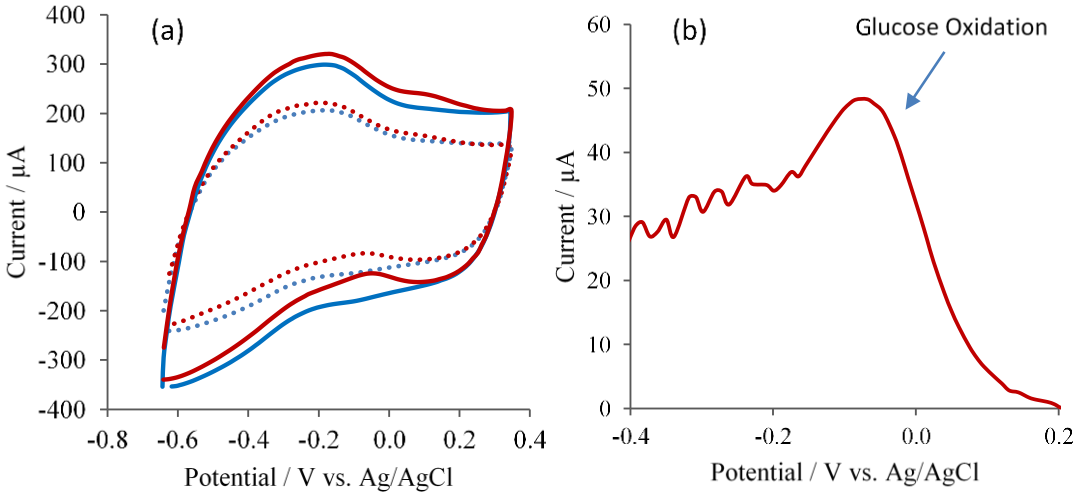

Figure 3.23: (a) Cyclic voltammograms recorded at 100 mV s^{-1} for the fMWCNT-$Au_{nano}(NaBH_4)$ modified SPE electrodes (DRP-150) in 0.10 M PBS (pH 7.4) (blue) and in 0.10 M PBS containing 10.0 mM glucose (red) for films pre-treated in ▬ 1.0 M H_2SO_4 and ▪▪▪▪▪ no pre-treatment in H_2SO_4. Figure **(b)** is a current differential plot displaying the glucose oxidation peak in the reverse scan at the 1.0 M H_2SO_4 pre-treated modified SPE.

CPA studies were then undertaken at these composite films with and without Nafion®. To produce the Nafion® membrane, a volume of 3.0 µl was cast solely onto the composite modified working electrode from a 50:50 (vol:vol) Nafion® 117 solution made in ethanol absolute. This 3.0 µl volume was considered to be equal with the 5 µl used at the previous system using the modified GC electrodes, in which the surface surrounding the working electrode was also encapsulated in Nafion®. Using CPA at a potential of -0.05 V vs. Ag/AgCl, typical current-time plots are obtained for the optimised sensor with and without Nafion®, shown in Figures 3.24 (a) and 3.25 (a). Details of the volumes of the glucose stock solution added to the cell and the cell glucose concentrations are listed in Chapter 2, Section 2.2.8.2. A linear trend in data can be seen in the resulting calibration curves, although the use of Nafion® reduced the sensitivity for glucose by 90%, Figures 3.24 (b) and 3.25 (b). This reduction in sensitivity compares very well with that observed at the fMWCNT-$Au_{nano}(NaBH_4)$/Nafion® modified GC electrodes, Section 3.2.6. Although there has been a reduction in sensitivity, the sensor response stability has improved as the current responses for glucose retain stability over time, as seen in Figure 3.25 (a). It has been reported that the use of membranes in electrochemical sensors helps control the diffusion of species to the electrode surface and that such diffusional barriers also improves a sensors response stability [18]. In contrast, the sensor without the membrane, Figure 3.24 (a), possesses a lower response stability and this may be due to the exhaustion of glucose at the high surface area sensing surface during analysis.

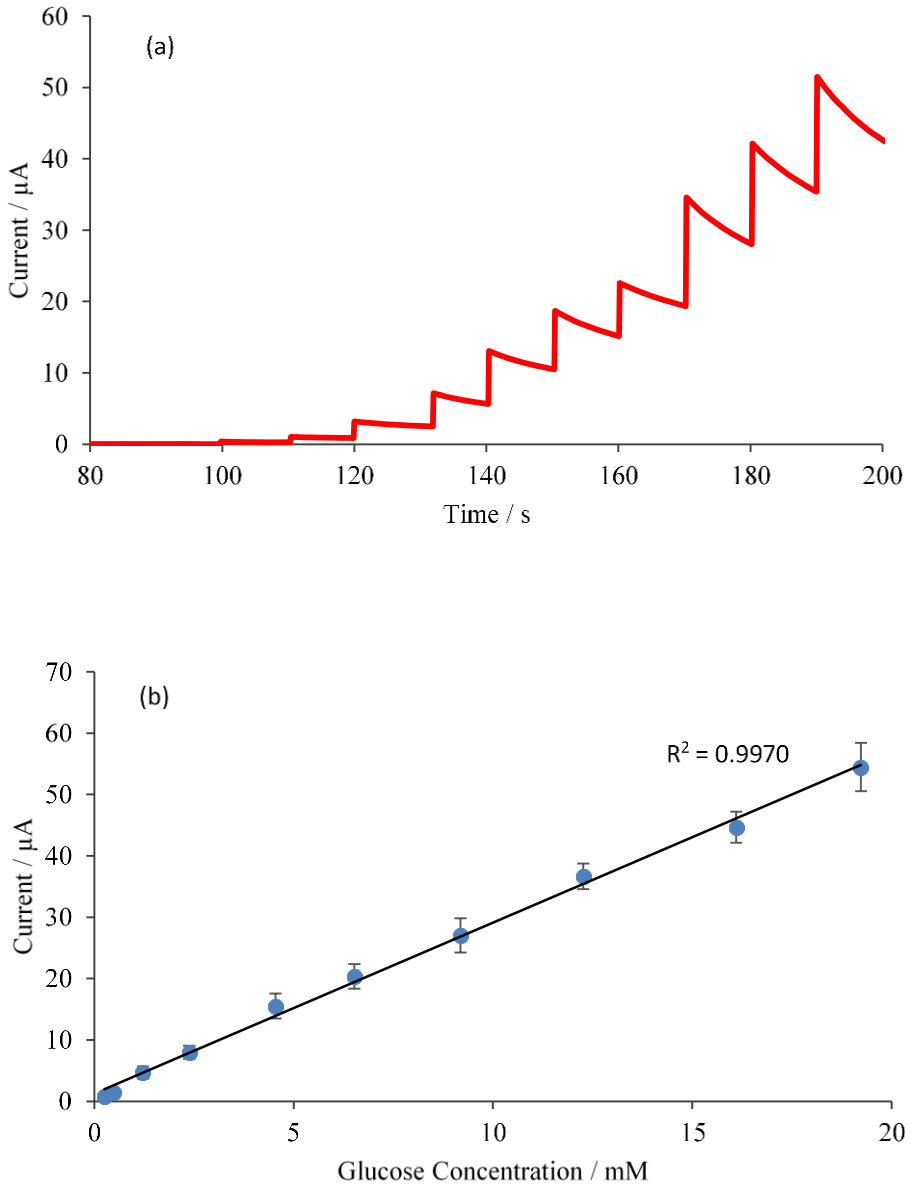

Figure 3.24: (a) Current-time plots for the oxidation of glucose in 0.10 M PBS (pH 7.4) with the successive additions of glucose aliquots from a 50 mM stock solution, made in 0.10 M PBS, recorded at -0.05 V vs. Ag/AgCl, at the 1.0 M H_2SO_4 pre-treated fMWCNT-Au_{nano}($NaBH_4$) modified SPE electrode (DRP-150) and **(b)** the corresponding calibration curve for glucose oxidation.

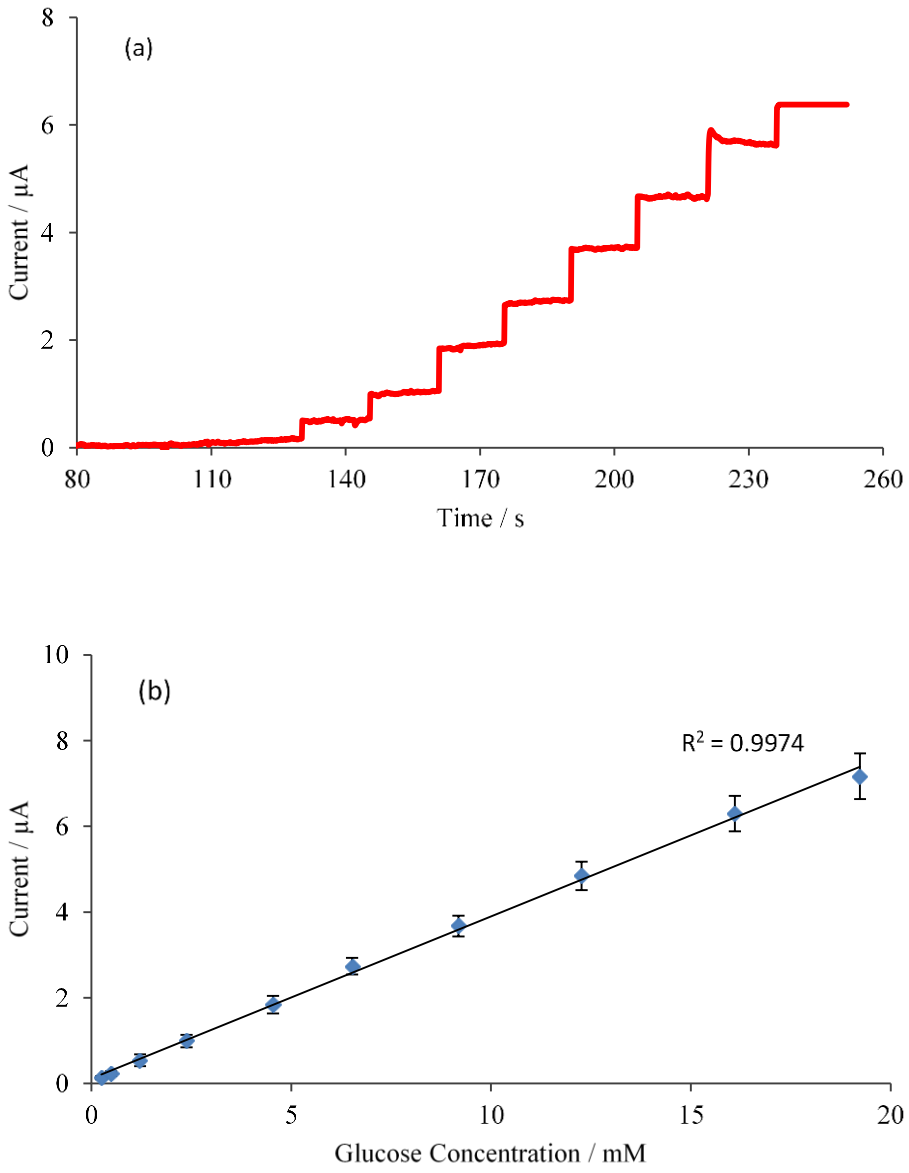

Figure 3.25: (a) Current-time plots for the oxidation of glucose in 0.10 M PBS (pH 7.4) with the successive additions of glucose aliquots from a 50 mM stock solution, made in 0.1 M PBS, recorded at -0.05 V vs. Ag/AgCl, at the 1.0 M H_2SO_4 pre-treated fMWCNT-$Au_{nano}(NaBH_4)$/Nafion® modified SPE electrode (DRP-150) and **(b)** the corresponding calibration curve for glucose oxidation.

The optimised fMWCNT-$Au_{nano}(NaBH_4)$ composite films formed on the SPEs provided similar sensitivities to glucose to those formed on the GC electrodes, although it was hoped that these sensitivities could be increased. In an attempt to increase sensitivity, macroporous SPEs (DRP-110OMC) were used, which according to DropSens have significantly higher surface areas (no surface area values supplied).

These DRP-110OMC SPEs consist of a high surface area working electrode made of ordered macroporous carbon. Results however showed that sensitivities did not improve using these SPEs, as indicated from the CVs in Figure 3.26 (a) and from the current differential plot of the glucose oxidation peak at the optimised film in the reverse scan, Figure 3.26 (b). This may be due to the bulky nature of the composite drop cast dispersions which may have merely formed a layer over the macroporous structures, instead of lining the inside of the pores. Further work was not carried out using these macroporous SPEs.

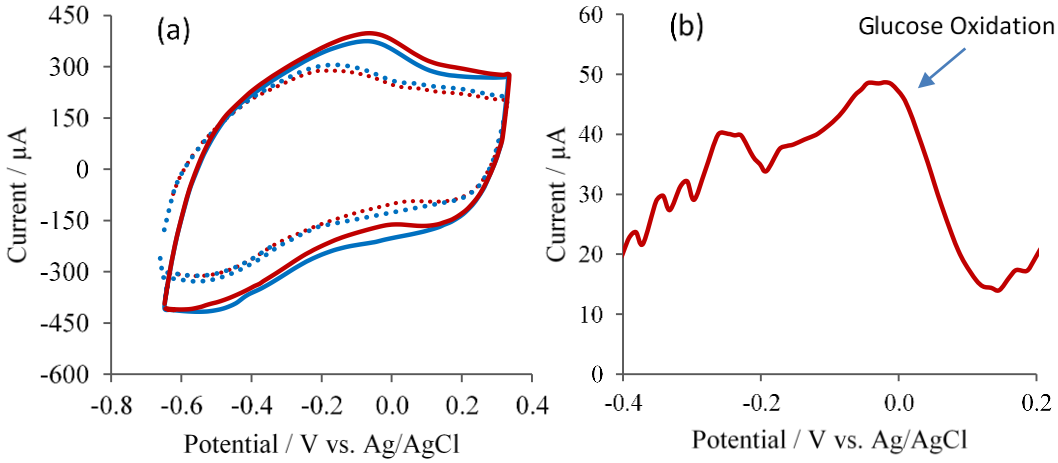

Figure 3.26: (a) Cyclic voltammograms recorded at 100 mV s^{-1} for the fMWCNT-$Au_{nano}(NaBH_4)$ modified macroporous SPE electrodes (DRP-110OMC) in 0.10 M PBS (pH 7.4) (blue) and in 0.10 M PBS containing 10.0 mM glucose (red) for films pre-treated in ▬ 1.0 M H_2SO_4 and ▪▪▪▪▪ no pre-treatment in H_2SO_4. Figure **(b)** is a current differential plot displaying the glucose oxidation peak in the reverse scan at the 1.0 M H_2SO_4 pre-treated modified SPE.

Although the sensitivity towards glucose could not be increased significantly using the SPE electrodes, it was noticed that steady state responses could be obtained much faster, after approximately 60 s, during CPA, which is beneficial for faster glucose analysis, current-time plots shown in Figures 3.24 and 3.25. Using the modified GC electrodes, steady-state responses took approximately 1000 s, as discussed in Section 3.2.6. Sensitivity data and LODs for the modified SPEs are displayed in Table 3.5. It can be seen that the sensitivities for glucose have increased by 20% and 15% using the modified SPEs with and without Nafion®, respectively, in comparison to the modified GC electrodes with and without Nafion®, data displayed in Table 3.3. Also,

the resulting LODs obtained were below relevant physiological concentrations of glucose in the blood, which range from 4 – 8 mM [11].

Table 3.5: Limits of detection and sensitivities towards the oxidation of glucose at the fMWCNT-Au_{nano}($NaBH_4$) composite modified SPE electrode (DRP-150) pre-treated in H_2SO_4 with and without the Nafion® membranes, n = 3.

Without Nafion®			With Nafion®		
LOD / µM	**Sensitivity /A/mM**	**Error / µA/mM**	**LOD / µM**	**Sensitivity / µA/mM**	**Error / µA/mM**
0.049	2.766	± 0.1529	0.193	0.378	± 0.0347

3.2.9 Characterisation of All Composites and Composite Films

3.2.9.1 Dispersion in Water

It is difficult to disperse pristine MWCNTs in water due to their hydrophobic nature combined with Van der Waals interactions and π-π stacking interactions between the carbon nanotubes [19]. However, by functionalising their sidewalls with acidic polar functionalities using concentrated acid, their dispersal in water is improved. Several different acids and acid combinations are used for the functionalisation of MWCNTs, of which HNO_3 and H_2SO_4 are commonly used [20-22].

The photographic images shown in Figure 3.27, compare the dispersion of the 24 h fMWCNTs in deionised H_2O with the pristine MWCNTs at a concentration of 2.0 mg/ml. In both cases the 24 h fMWCNTs and the pristine MWCNTs were ultrasonicated for 15 min. It is clear by eye that the fMWCNTs are considerably more dispersed in H_2O in comparison to the pristine MWCNTs, with only a small proportion appearing aggregated. These small aggregates may be due to the relatively concentrated dispersion used, of 2.0 mg/ml, which may be past the point of dispersibility for these particular fMWCNTs in H_2O.

Although these fMWCNTs are clearly dispersible in H_2O without SDS, SDS is used in the synthetic procedures as it provides improved dispersal of CNTs [23]. The SDS molecule is composed of a hydrophobic hydrocarbon chain and a hydrophilic sulfate

head [23]. The hydrophobic chain interacts with the surface of the hydrophobic carbon nanotubes and the sulfate head associates with the water through ion-dipole interactions. Once a sufficient number of SDS molecules are adsorbed on the surface of the CNTs, the binding energy between the CNTs and adjacent tubes can be overcome which aids in their separation and improves dispersal in solution [23].

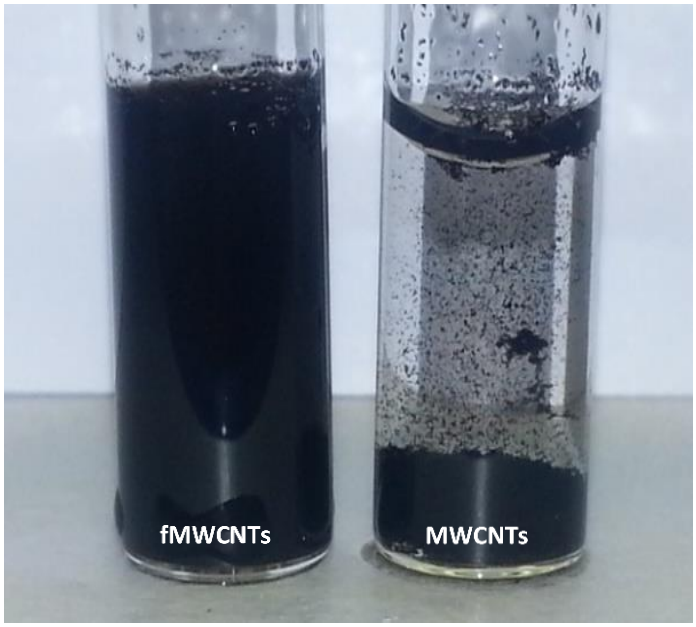

Figure 3.27: Dispersions of the 24 h fMWCNTs and pristine MWCNTs in deionised H_2O at a concentration of 2.0 mg/ml.

3.2.9.2 Potentiometric Acid-Base Titrations

Titrations are commonly used to determine acid and base concentrations in the field of chemistry. The pH approach known as a potentiometric titration, has been frequently used for the determination of surface acidity of carbon nanotubes and can be termed a 'Boehm Titration' [22, 24-27]. In a potentiometric titration, the pH is plotted as a function of the acid (or base) volume added to the titration reaction and regions of sudden pH transitions, known as equivalence points (EPs), are easily observed. Using these titrations it was possible to work out the acidic surface group coverage on the fMWCNTs.

As discussed in Chapter 2, Section 2.3.2.9, the 24 h fMWCNTs were firstly reacted with a standardised volume of 0.01 M NaOH for a period of time under nitrogen. This

solution reacted with the acidic surface groups on the fMWCNTs and on the adsorbed polycyclic carbonaceous fragments (CFs) but an excess of unreacted NaOH remained in solution. Having removed the CNTs by filtration, the remaining solution was titrated with the standardised 0.01 M HCl made in 0.10 M NaCl, thus yielding the excess unreacted concentration of NaOH in solution. Using these data the surface acidic group coverage was calculated.

Typical potentiometric titration curves for 24 h fMWCNTs (red) and the pristine MWCNTs (blue) are shown in Figure 3.28. It is clear that only one equivalent point is present for the pristine MWCNTs and its position indicates that no acidic groups are present. Although it is possible that this method is not sensitive enough to detect such a small difference in the concentration of the NaOH solution. On the other hand, the results for the 24 h fMWCNTs are very different, and two equivalent points are clearly visible. The EP at pH 8.0 results from the protonation of the remaining NaOH by HCl and is related to the total surface acidity of the fMWCNTs including that of the surface adsorbed CFs. The second EP at pH 5.0 is related to the carboxylate salts of the CFs that are desorbed from the surface of the fMWCNTs during the reaction with NaOH [22, 28].

The calculations, discussed below, are consistent with a total coverage of 4.92×10^{-6} moles acidic groups / 1.0 mg fMWCNTs (4.92 μmols), while no acidic groups were detectable with the pristine MWCNTs. The 0.01 M HCl (2.54 ml) was required to yield the first EP. This corresponded to 2.54×10^{-5} moles of HCl, which is equivalent to the moles of NaOH remaining. By subtracting this value from the initial NaOH concentration prior to the reaction with the fMWCNTs, the acidic group concentration was calculated to be 2.46×10^{-5}/5 mg of fMWCNTs or 4.92×10^{-6} moles acidic groups/1.0 mg fMWCNTs. Using this information, the % acidic group coverage of the fMWCNTs could be estimated. Assuming that the molecular weight of carbon is 12 g/mol, and using the calculated acidity and the moles of carbon present in 1.0 mg of MWCNTs, it was calculated that 6.0% of the fMWCNTs were functionalised with acidic groups. This acidity is consistent with the good solubility of the fMWCNTs in the H_2O and improved solubility in the SDS solution.

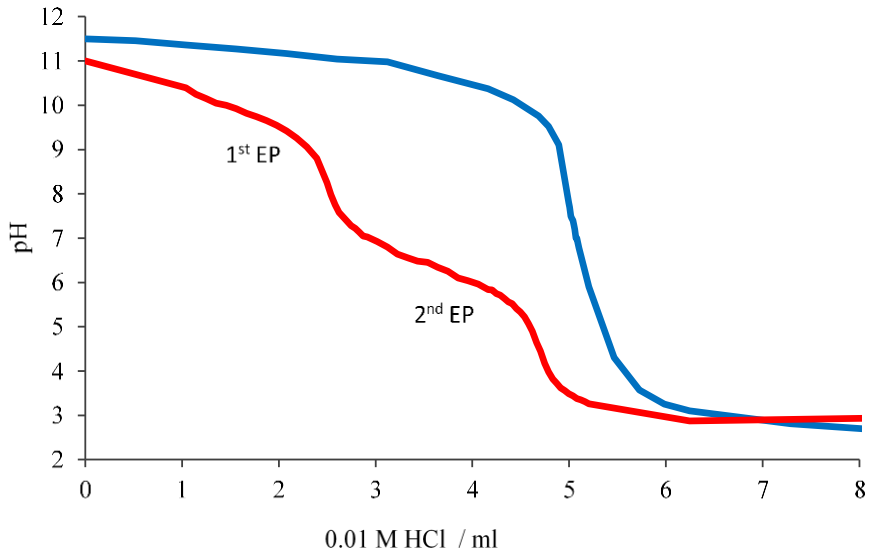

Figure 3.28: Potentiometric titrations of the — pristine MWCNTs and — 24 h fMWCNTs.

3.2.9.3 Scanning Electron Microscopy and Energy Dispersive X-Ray Analysis

Scanning Electron Microscopy (SEM) was employed to obtain information on the bulk composites and the resulting films formed on the GC electrodes. Energy Dispersive X-Ray Analysis (EDX) was used for qualitative analysis and for quantitative elemental estimations. EDX may not be an accurate quantitative technique in this work due to possible interference from the underlying substrate and the need for standards. However, in this study EDX was used to estimate the Au loading, Table 3.6, and these estimates were compared with the data obtained using atomic absorption (AA) analysis, discussed in Section 3.2.9.6.

In Figure 3.29, SEM micrographs and the corresponding EDX spectra of the pristine MWCNTs and the pristine MWCNT-$Au_{nano}(NaBH_4)$ composite are shown. It is evident from the micrographs that no detailed morphological information can be obtained at this magnification, due to the nanometer sized carbon nanotubes and AuNPs and due to the nature of the bulk sample. However, it is evident that no micron-sized Au particles or aggregates are present in the composites. This suggests that the Au particles may be nanoparticulate. From EDX analysis of the pristine MWCNTs, Figure 3.29 (a), it is clear that the material is composed mainly of carbon, estimated at 98.72% wt. and a slight amount of oxygen at 1.28% wt., data shown in Table 3.6. On

the other hand, the EDX analysis of this material with the addition of the Au particles shows peaks for Au, with the most prominent peak at 2.2 keV. The positions of these peaks are consistent with those seen in the literature for metallic Au [29-33]. The Au composition is estimated at 1.61% wt., while the oxygen content is slightly lower at 0.76% wt., shown in Table 3.6.

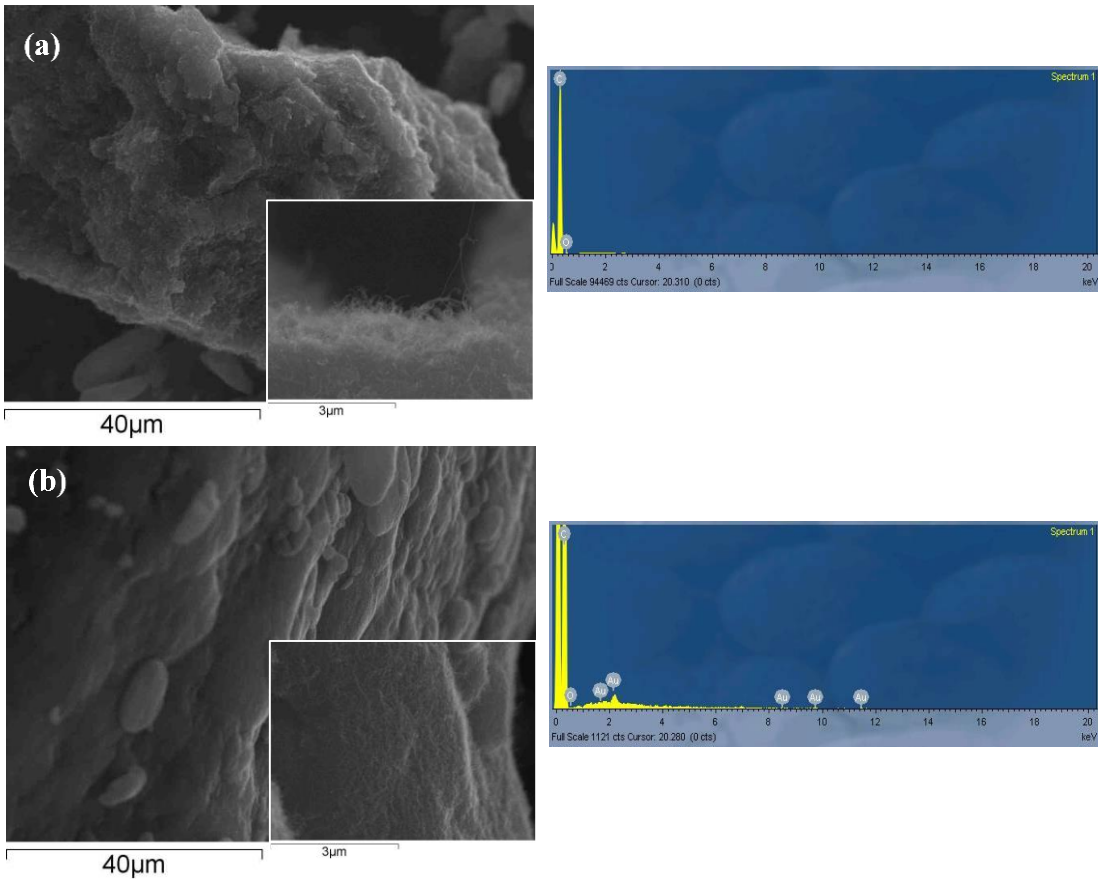

Figure 3.29: SEM micrographs and corresponding EDX spectra of the **(a)** pristine MWCNTs and **(b)** pristine MWCNT-$Au_{nano}(NaBH_4)$ composite.

The SEM micrographs and EDX spectra of the 24 h fMWCNTs and the fMWCNT-$Au_{nano}(NaBH_4)$ and fMWCNT-Au_{nano}(TriSodCit) composites, are shown in Figure 3.30. Quantitative EDX estimations are displayed in Table 3.6. Again, the micrographs do not provide detailed morphological information due to the limitations with magnification and resolution at the bulk sample, although EDX analysis does provide interesting qualitative and quantitative information. It is clear from EDX analysis that the 24 h fMWCNT material is estimated to have a much higher quantity of oxygen, at 8.59% wt., in comparison to 1.28% wt. obtained for the pristine

MWCNTs, Table 3.6. Although these are only estimates, it appears that the reflux stage has introduced oxygen containing functionalities into this material. The Au loading is also estimated at 2.86% wt., for the fMWCNT-Au_{nano}($NaBH_4$) composite, and a higher loading of 6.49% wt. is estimated for the fMWCNT-Au_{nano}(TriSodCit) composite.

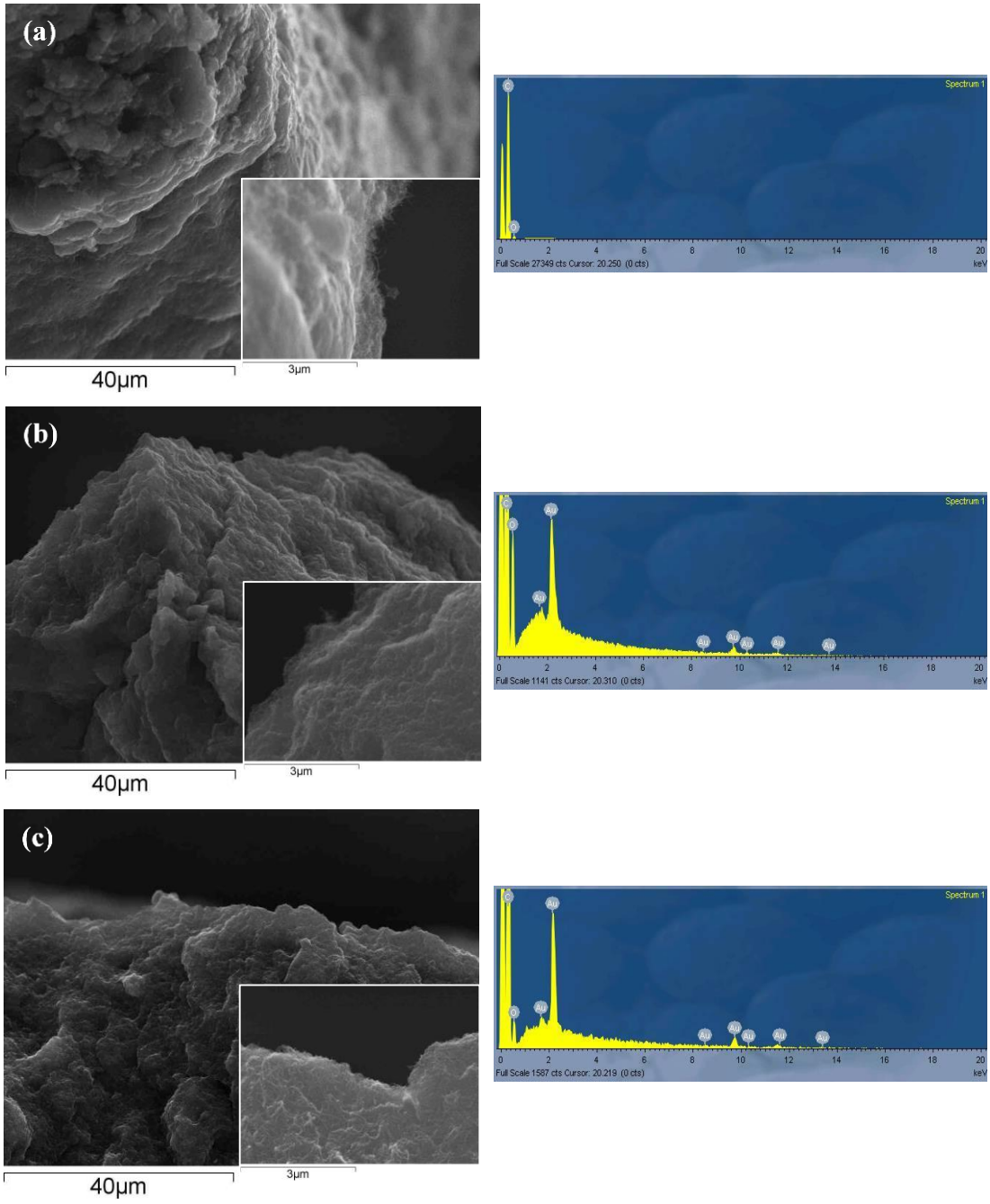

Figure 3.30: SEM micrographs and corresponding EDX spectra of **(a)** the 24 h fMWCNTs, the **(b)** fMWCNT-Au_{nano}($NaBH_4$) and **(c)** fMWCNT-Au_{nano}(TriSodCit) composites.

Table 3.6: Elemental % Weight data obtained from EDX analysis for the pristine MWCNTs, fMWCNTs and the resulting composites.

Materials and Composites	C% wt.		O% wt.		Au% wt.	
Pristine MWCNTs	98.72	± 0.14	1.28	± 0.14	-	-
24 h fMWCNTs	91.41	± 0.37	8.59	± 0.37	-	-
Sodium Borohydride Reducing Agent						
Pristine MWCNT-Au_{nano}	97.62	± 0.71	0.76	± 0.61	1.61	± 0.37
24 h fMWCNT-Au_{nano}	88.08	± 0.39	9.06	± 0.37	2.86	± 0.16
Trisodium Citrate Reducing Agent						
24 h fMWCNT-Au_{nano}	88.20	± 0.64	5.31	± 0.58	6.49	± 0.36

SEM analyses of the resulting composite modified films are shown in Figures 3.31 (a – d). Only films formed on a GC electrode are studied. It can be seen in the lower magnification SEM micrographs, Figures 3.31 (a) and (c), of the fMWCNT-Au_{nano}($NaBH_4$) and fMWCNT-Au_{nano}(TriSodCit) films that both show relatively good surface homogeneity. This implies that even surfaces are created upon film formation and this homogeneity may have reduced errors during electrochemical analyses. Higher magnification micrographs of these films are shown in Figure 3.31 (b) and (d). At this magnification, bundles of the carbon nanotubes can be seen although there is no clear evidence of AuNPs on their surfaces. This was due to the limitations in the resolution and magnification of the SEM used. Further analysis using TEM was undertaken.

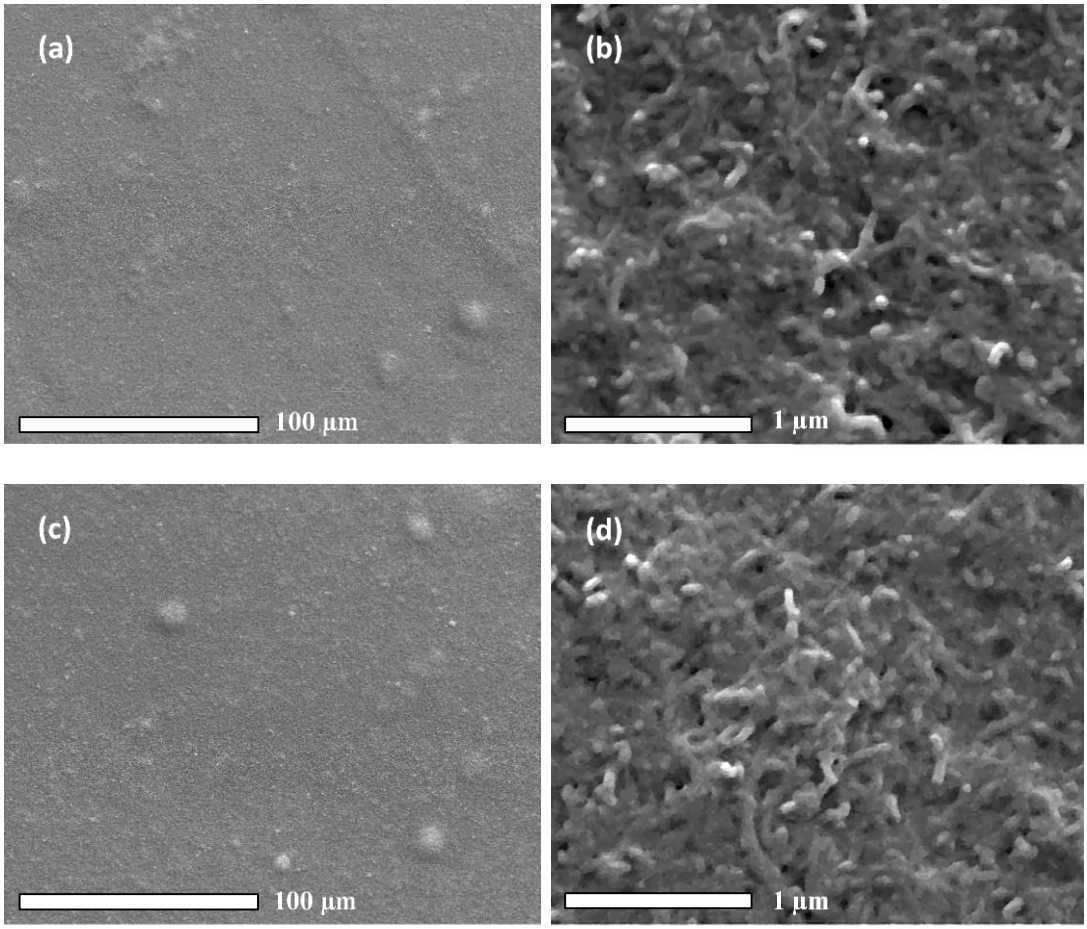

Figure 3.31: Low and high magnification SEM micrographs of the optimised **(a)** and **(b)** fMWCNT-Au_{nano}($NaBH_4$) and **(c)** and **(d)** fMWCNT-Au_{nano}(TriSodCit) composite films formed on a GC electrode (d =3 mm).

3.2.9.4 Transmission Electron Microscopy

As SEM analysis could not yield information on AuNP size and distribution, Transmission Electron Microscopy (TEM) was employed. All samples were loaded onto 400 mesh Cu grids, with a holey carbon backing, from dispersions in ethanol. TEM micrographs are shown in Figures 3.32, (a – c) for the fMWCNT-Au_{nano}($NaBH_4$) composite, while the diameter size distribution of the AuNPs is shown in Figure 3.32 (d). As seen in the high-resolution TEM (HRTEM) micrograph in Figure 3.32 (a), some material aggregation occurred upon sample loading onto the TEM grids which is expected during solvent evaporation and due to the solubility issues of the material in ethanol. It is evident from these data that the AuNPs do not appear to be evenly dispersed along the entirety of the CNTs, but nonetheless they all appear to

exist in the nanoscale region with the majority being below 10 nm in diameter. Also, the individual graphene layers of the carbon nanotubes can be visualized, as seen in the HRTEM shown in Figure 3.32 (c). This mode is ideal for atomic-scale imaging and visualisation of lattice fringes, which are representations of interatomic spacings. These can be used to provide useful crystallographic information when the distances between the fringes are measured [34, 35].

The size distribution histogram, presented in Figure 3.32 (d), shows the size distribution of the AuNPs on the surface of the fMWCNTs. The AuNPs range in diameter from 5.5 to 12.5 nm, with a mode diameter of 7.5 nm. This statistical analysis was conducted on 100 random AuNPs using IMAGE J software. The fMWCNTs themselves ranged from 15 to 20 nm in diameter and contained a degree of surface roughness which may represent the defect sites produced during the harsh functionalisation process [36, 37]. The caption for the following micrographs is displayed on page 111.

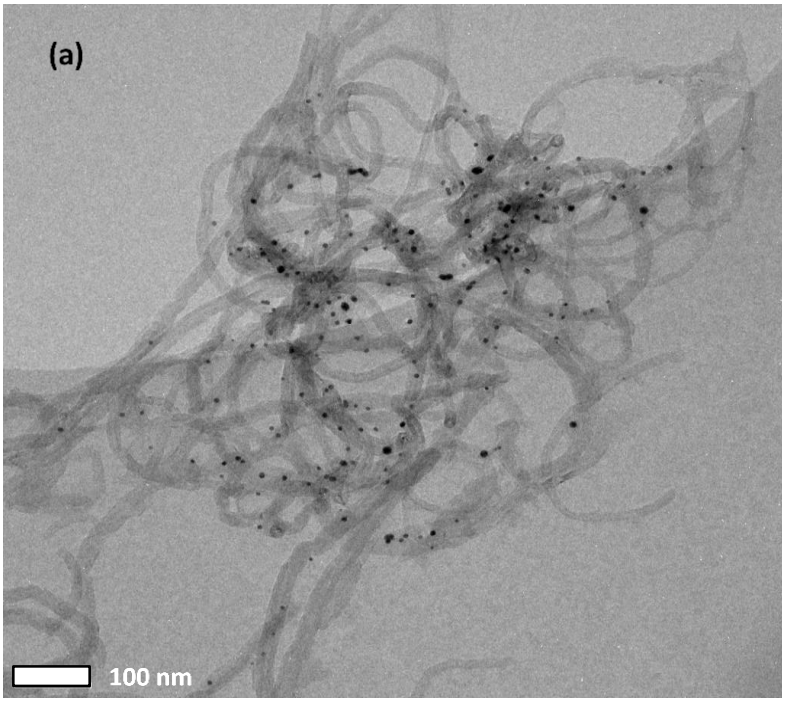

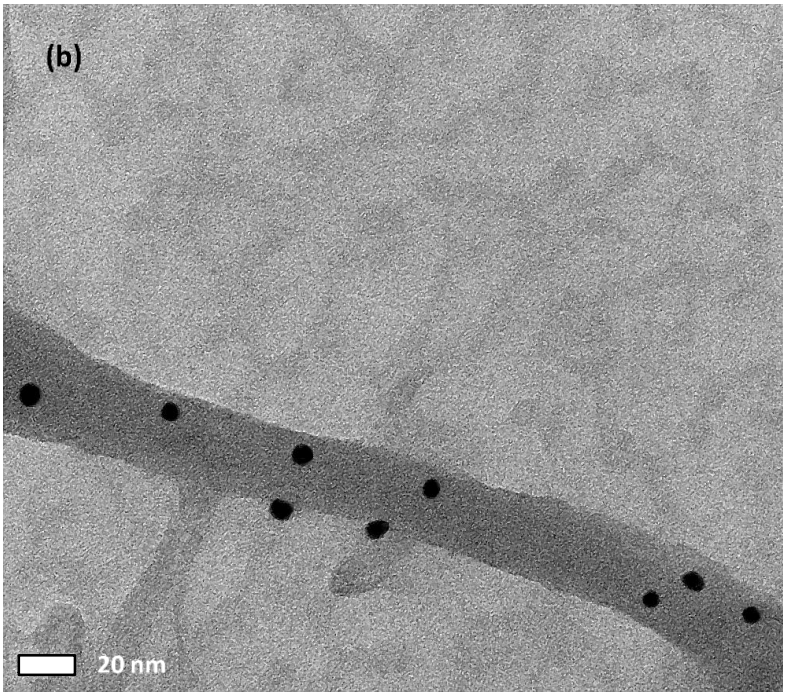
(b)
20 nm

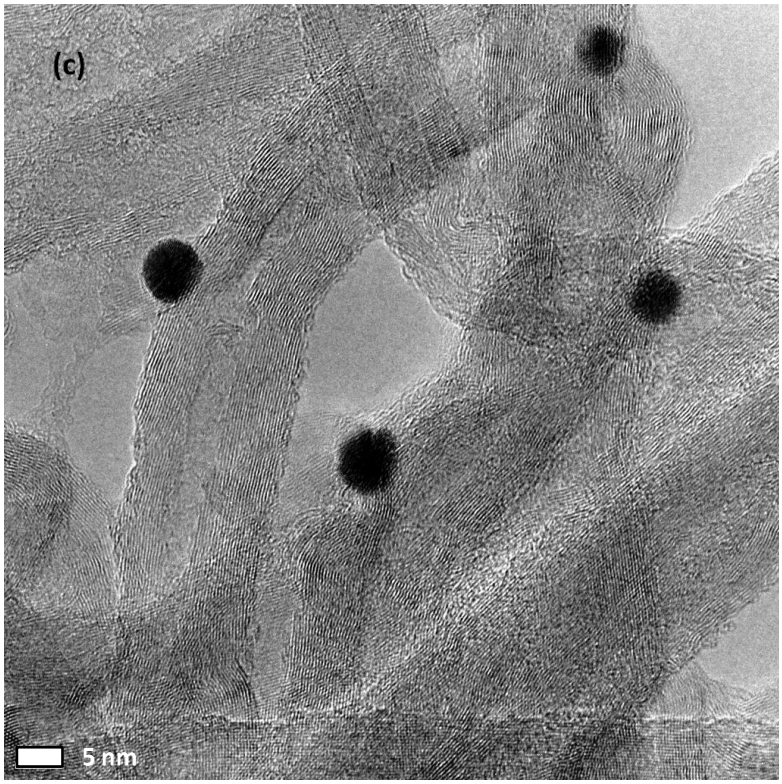
(c)
5 nm

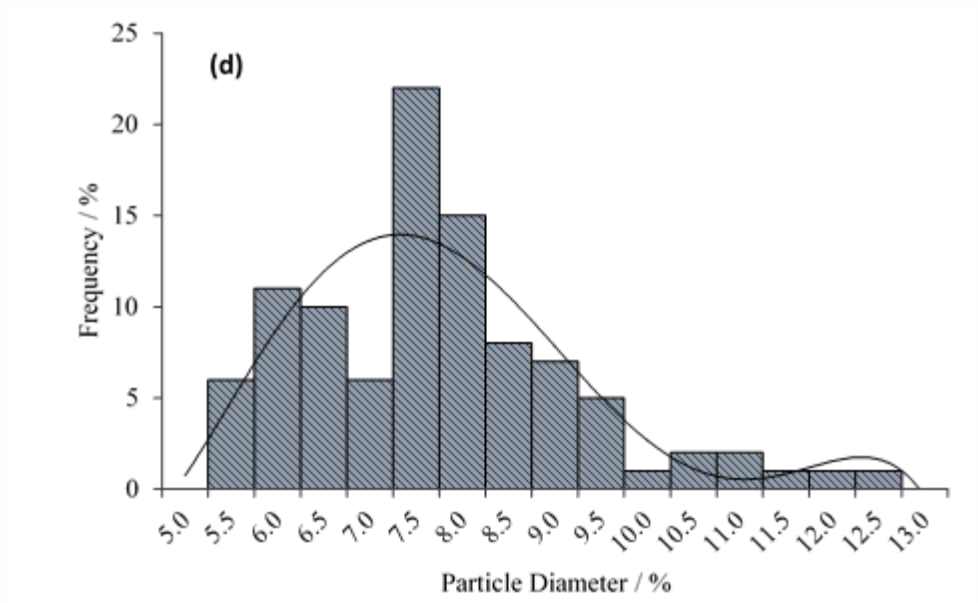

Figure 3.32: (a), (b) and **(c)** TEM micrographs of the fMWCNT-$Au_{nano}(NaBH_4)$ composite with **(d)** the corresponding AuNP size distribution histogram where 100 surface AuNPs were analysed.

To undertake EDX analysis of this material, scanning transmission electron microscopy (STEM) mode was used as it is ideal for the focusing of higher electron beam currents on very narrow spots and as such is useful for EDX of nanomaterials [38]. In the STEM micrograph, Figure 3.33, small red boxes labeled 1 and 2 are shown, which correspond to the areas selected for EDX analysis of a randomly selected AuNP and a fMWCNT, respectively. The resulting EDX spectra (1) and (2) are shown in Figure 3.33. The spectrum corresponding to the AuNP shows that Au is indeed present and that of the fMWCNT has a large carbon signal. Copper and silicon are also evident during analysis but these can be explained by the presence of the copper TEM grid and other internal interferences.

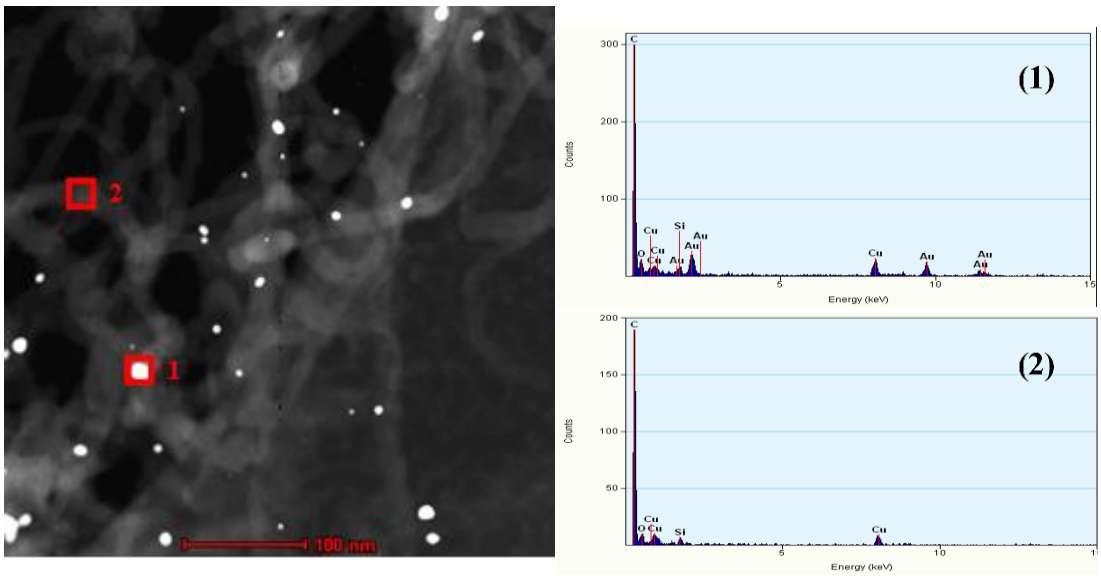

Figure 3.33: STEM micrograph of the fMWCNT-Au_{nano}($NaBH_4$) composite and the corresponding EDX spectra of a surface attached AuNP **(1)** and a fMWCNT **(2)**, both randomly selected.

TEM micrographs of the fMWCNT-Au_{nano}(TriSodCit) composite are shown in Figure 3.34 (a), (b) and (c) and the corresponding histogram of the AuNP size distribution is shown in Figure 3.34 (d). Again, these data are obtained using a statistical analysis on 100 random AuNPs using IMAGE J software. As with the previous composite, it seems as if some sample aggregation occurs during the preparation of the TEM sample grid and this is prominent with the AuNPs. The AuNPs appear much larger than those produced using $NaBH_4$, with a mode diameter of 23 and 24 nm, as seen in Figure 3.34 (d).

The micrograph presented in Figure 3.34 (c), is a high magnification micrograph of a large AuNP taken in HRTEM mode which shows good resolution of the lattice fringes. By measuring the distance between these fringes, the inter-atomic spacing between the parallel lines of Au atoms is determined as 2.35 Å, which corresponds to the (111) plane of crystalline Au [39-44]. The caption for the following micrographs is shown on page 114.

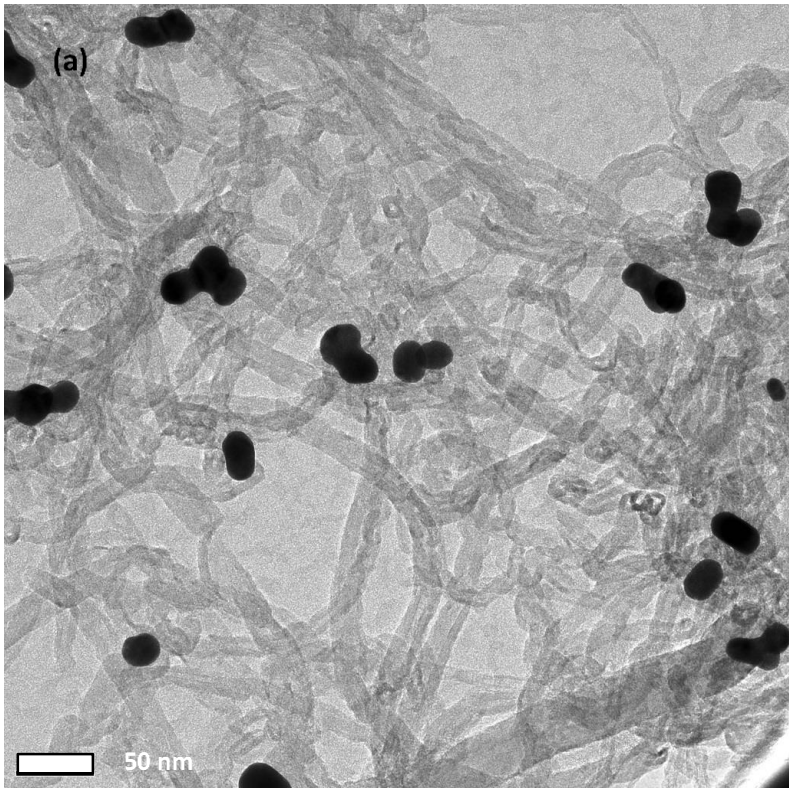
(a)
50 nm

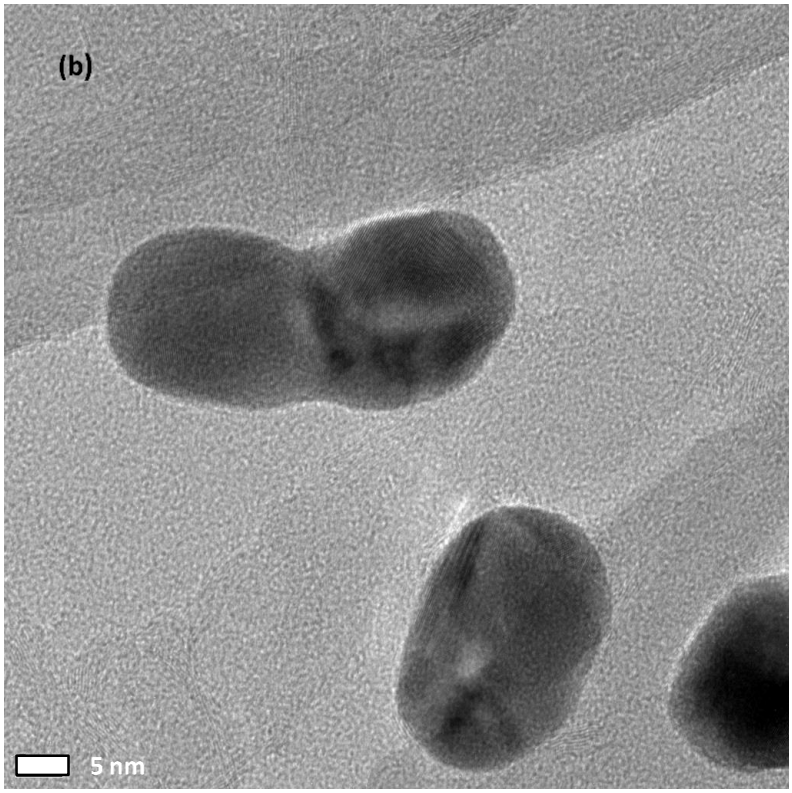
(b)
5 nm

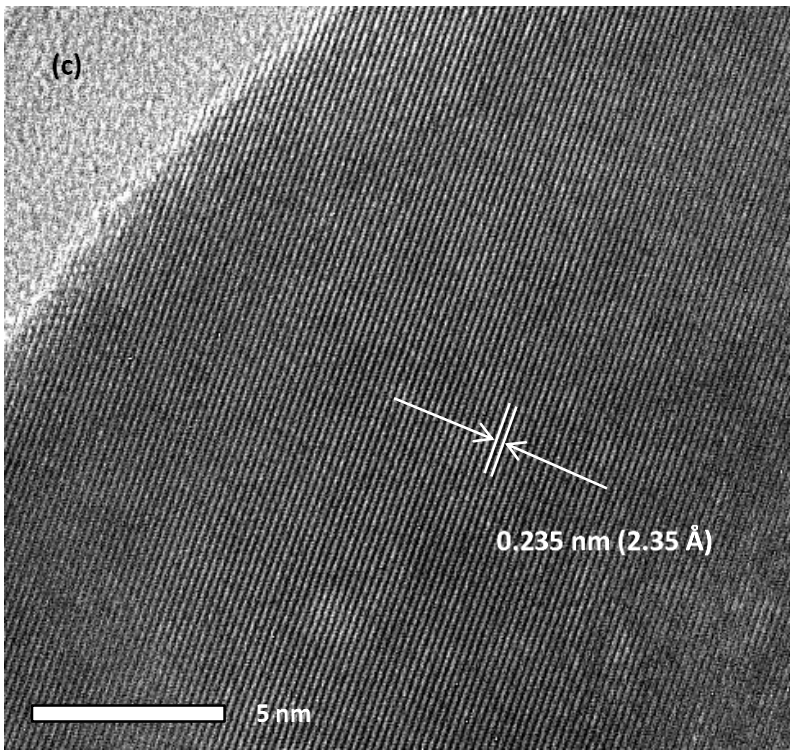

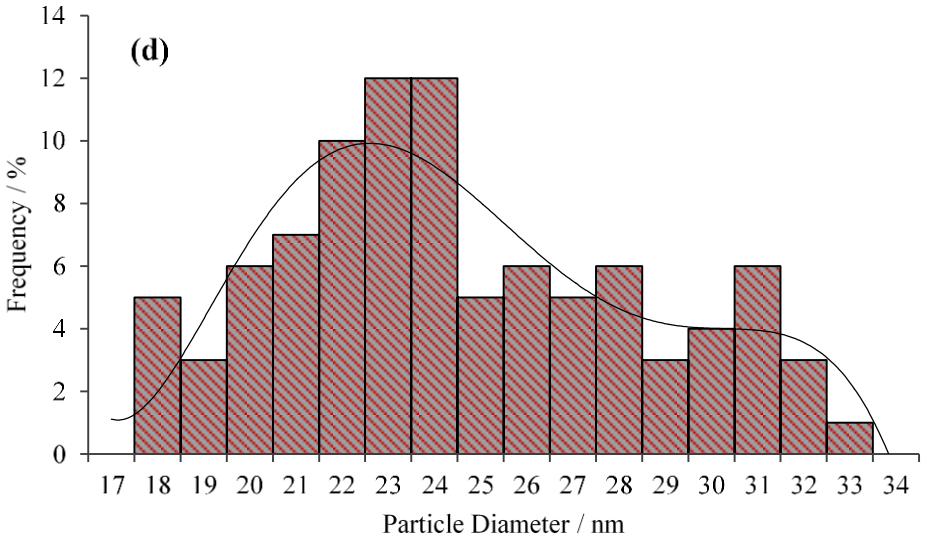

Figure 3.34: (a), (b) and **(c)** TEM micrographs of the fMWCNT-Au_{nano}(TriSodCit) composite with **(d)** the corresponding AuNP size distribution histogram where 100 surface AuNPs were analysed. Figure **(c)** shows the inter-atomic spacings of the AuNPs.

3.2.9.5 X-Ray Diffraction Spectroscopy

X-Ray Diffraction Spectroscopy (XRD) is a non-destructive technique which is useful for determining crystallographic information of a material, including its various crystal planes, inter-atomic spacings and crystal structure [45]. With this technique, an incident X-Ray beam is focussed on the material in question and the angles of diffraction, 2θ, from the angles of incidence are measured. These angles of diffraction are related to the various crystal faces within the sample and are plotted on the x-axis of the X-Ray spectra with intensity plotted on the y-axis [45].

In Figure 3.35, the XRD spectrum of the fMWCNT-Au_{nano}($NaBH_4$) composite is shown. The characteristic crystalline planes of Au present in the AuNPs are evident, along with planes corresponding to the fMWCNTs. The XRD spectrum displays (002), (101) and (004) planes corresponding to the carbon nanotubes and the (111), (200), (220), (311) and (222) planes corresponding to the AuNPs[39, 46-48]. It is clear that the peak corresponding to the (111) plane of Au, at $2\theta = 38.23°$, is the most abundant orientation of Au in these AuNPs. This peak is associated with an interatomic d-spacing of 2.353 Å. In Figure, 3.36, the XRD spectrum of the fMWCNT-Au_{nano}(TriSodCit) composite is shown. This spectrum appears very similar to that shown in Figure 3.35, with the (111) plane of Au again being the most prominent. This (111) plane occurs at $2\theta = 38.21°$ with an interatomic d-spacing of 2.35 Å. These data correspond very well to the d-spacing of 2.35 Å measured using HRTEM, Section 3.34, Figure 3.34 (d).

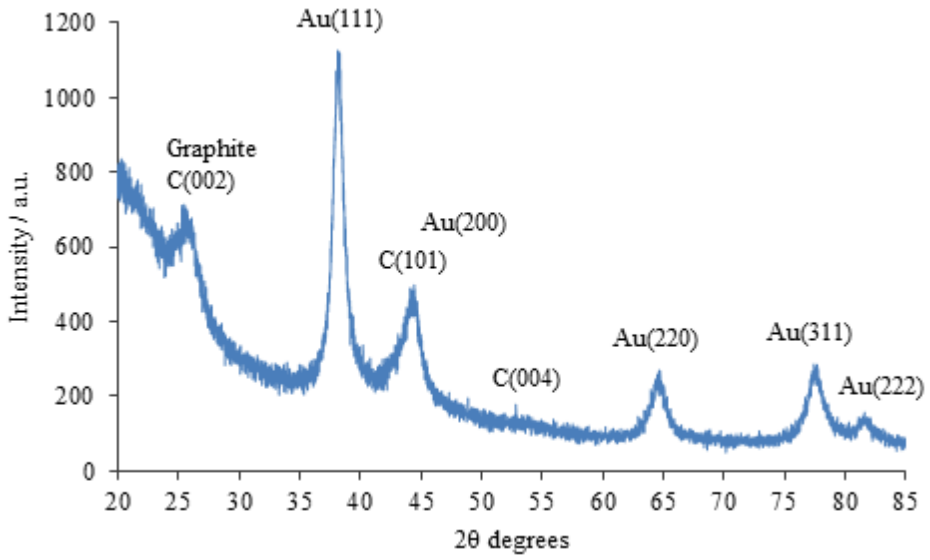

Figure 3.35: XRD spectrum of the fMWCNT-Au_{nano}($NaBH_4$) composite.

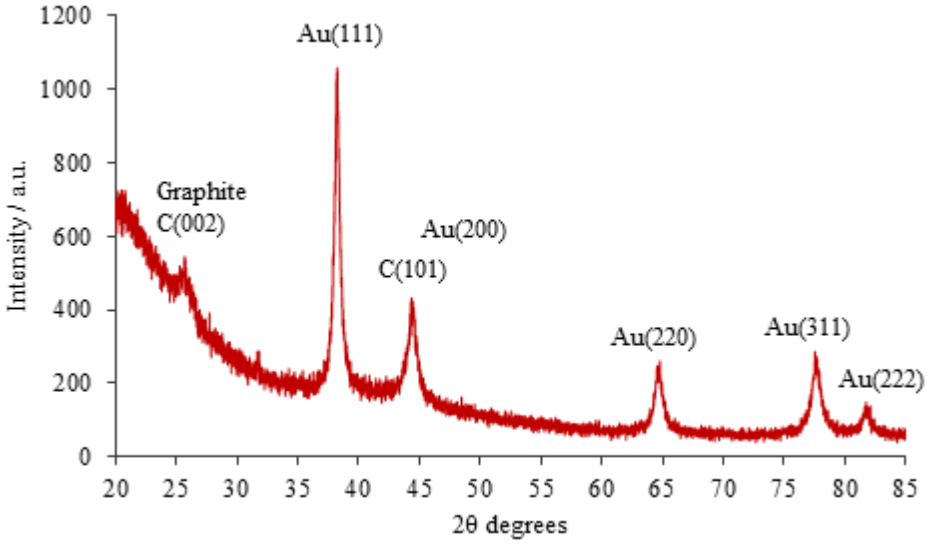

Figure 3.36: XRD spectrum of the fMWCNT-Au_{nano}(TriSodCit) composite.

The sizes of the AuNPs in both composites were estimated by using the Scherrer equation, Equation 3.2, in which *D* equals the average diameter of a spherical particle, *B* is the full width at half maximum of the most intense reflection - expressed in radians, θ is the position of this peak, λ is the wavelength and 0.89 is a Scherrer constant [49].

$$D = \frac{0.89\lambda}{B\cos\theta} \qquad 3.2$$

For estimation of the AuNP sizes in the fMWCNT-Au_{nano} composites, the following values of 38.23° and 38.21° for 2θ were used for the $NaBH_4$ and TriSodCit-produced composites, respectively. These values correspond to the most intense, (111), reflections of the AuNPs. The values of *B* for both were also calculated using these peaks and the wavelength, λ, used was the K alpha value of 1.5418 Å. It was found that the AuNPs of the fMWCNT-Au_{nano}($NaBH_4$) composite had an average particle size of 7.92 nm, which agrees very well with that of 7.5 nm obtained from TEM, Section 3.2.9.4, and those of the fMWCNT-Au_{nano}(TriSodCit) composite had a larger estimated diameter of 20.29 nm, which also was close to the values of 23 and 24 nm obtained from TEM, Section 3.2.9.4.

3.2.9.6 Atomic Absorption Spectroscopy

In order to quantify the amount of Au present in the material as a percentage of the composite firstly Au was extracted from the surface of the fMWCNTs using a concentrated acid treatment and converted back into the original $HAuCl_4$ salt using an Au extraction method which is discussed in Chapter 2, Section 2.3.2.4. This method utilised *aqua regia* to yield a yellow-coloured $HAuCl_4$ which was then isolated in 0.10 M HCl. Atomic absorption spectroscopy (AAS) equipped with a flame atomiser was used. All standard solutions for the calibration curves were produced from a commercial Au standard stock solution of 1000 ppm, which consisted of 1.0 mg/ml of pure Au in 10.0 to 20.0% HCl. Standard solutions of 2.0, 5.0, 10.0 and 20.0 ppm were prepared in 0.10 M HCl to yield a linear calibration curve with a high correlation coefficient of 0.9944, shown in Figure 3.37. Having produced this calibration curve, its accuracy was checked using the same standard solutions. Once the errors in these test quantifications were negligible, sample analysis was undertaken. The concentration of Au in ppm was determined using this curve and the Au% wt. in the samples was calculated. These data are summarised in the table shown in Figure 3.37 inset. Again it is clear that higher loadings of Au are present in the fMWCNT-

Au_{nano}(TriSodCit) composite. These loadings compare well with the values obtained using EDX analysis.

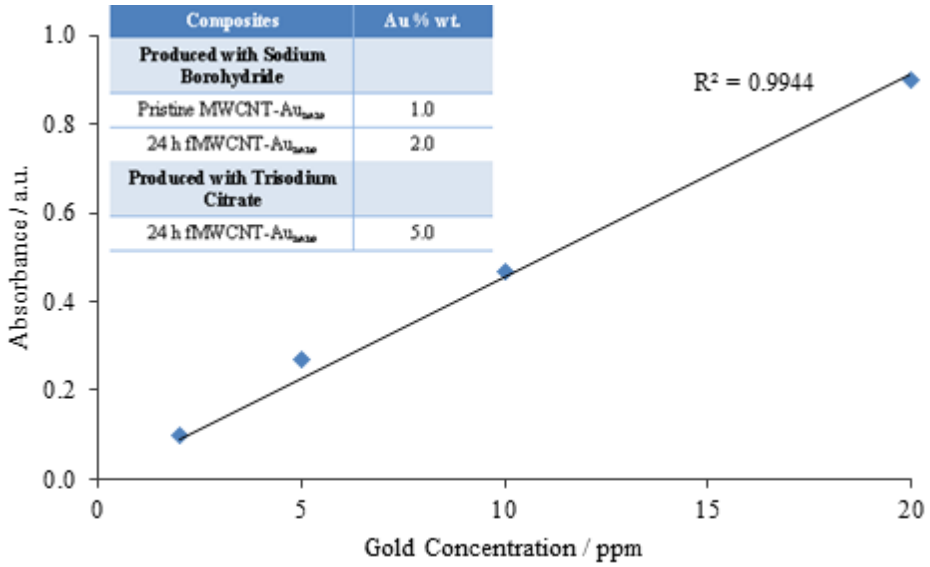

Figure 3.37: Calibration curve of the Au standard solutions with absorbance plotted as a function of the Au concentration in ppm.

3.2.9.7 Ultraviolet-Visible Spectroscopy

The Ultraviolet-Visible (UV-Vis) spectrum of the 24 h fMWCNTs, solubilised in 1.0% SDS, is shown in Figure 3.38. It is clear that only one absorbance band is present at 252 nm, which can be attributed to carbon nanotubes [40, 50]. It would be expected when the AuNPs are introduced onto the fMWCNT surface that a second absorbance band would appear in the 500 nm region, due to surface plasmon resonance of the AuNPs and this wavelength position can be associated with their size [39, 46, 47, 51, 52].

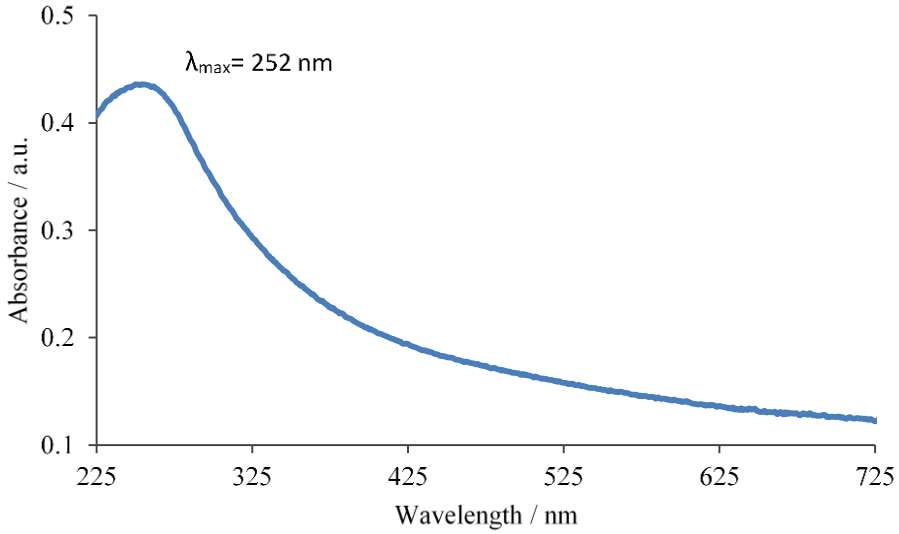

Figure 3.38: UV-Visible spectrum of the 24 h fMWCNTs dispersed in a 1.0% SDS solution.

Figure 3.39, shows the UV-Vis spectrum of the fMWCNT-$Au_{nano}(NaBH_4)$ composite dispersed in SDS. Two bands appear at 263 nm and at 519 nm, which can be assigned to the fMWCNTs and the AuNPs on their surface, respectively. The latter band at 519 nm is very small which may be related to a low concentration of AuNPs or by peak masking by the strong background absorption of the fMWCNTs. It is evident that the π plasmon absorbance band of the fMWCNTs has red-shifted by 11 nm and this may be due to the π-π binding interactions between the AuNPs and the fMWCNTs [53]. For comparison, AuNPs produced by this same procedure were synthesised in the absence of any fMWCNTs. The absorbance spectrum for this is shown in Figure 3.39 inset, and shows a similar band at 525 nm. This may imply that the AuNPs, formed both in the absence and presence of fMWCNTs in this particular synthesis, are a different size.

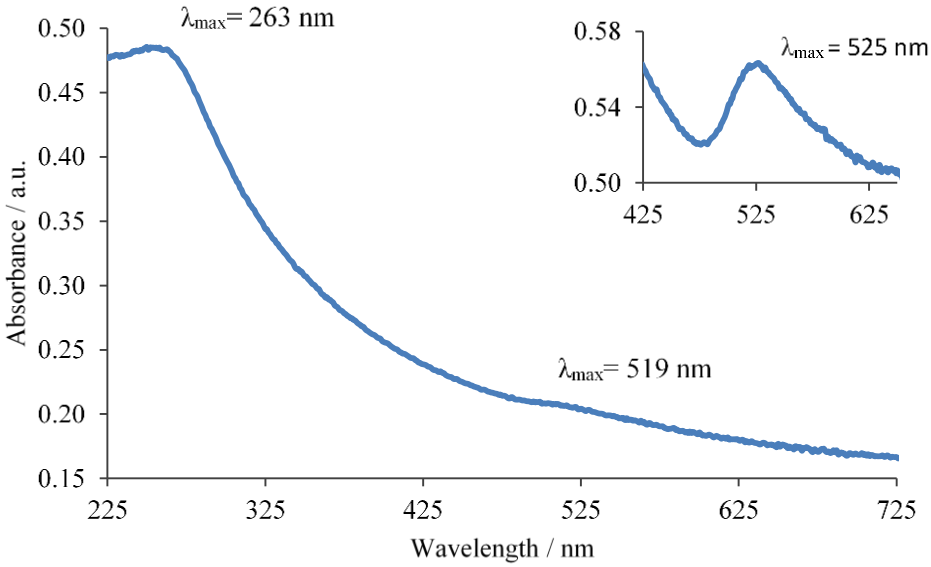

Figure 3.39: UV-Visible spectra of fMWCNT-Au_{nano}($NaBH_4$) composite dispersed in a 1.0% SDS solution and the AuNPs synthesised in the absence of fMWCNTs, inset.

Similar data are shown for the fMWCNT-Au_{nano}(TriSodCit) composite, Figure 3.40. Again two bands appear, but that of the AuNPs occurs at the higher wavelength of 535 nm and is much larger in intensity in comparison to that of the previous material, Figure 3.39. This is possibly due to a higher concentration of AuNPs and a difference in size of the AuNPs. Also, this absorbance band appears relatively broad in comparison to that of the previous material. Absorbance band broadening can indicate a larger size distribution of the AuNPs [54] and this correlates well with the size distribution histogram shown previously in Section 3.2.9.4, Figure 3.34 (c). The UV-Vis spectrum of the AuNPs formed in the absence of fMWCNTs, which is presented in the inset in Figure 3.40, shows a lower absorbance wavelength of 525 nm. Since the wavelength is proportional to the size of the AuNPs, it may be assumed that the AuNPs formed without the fMWCNTs present are of a different size.

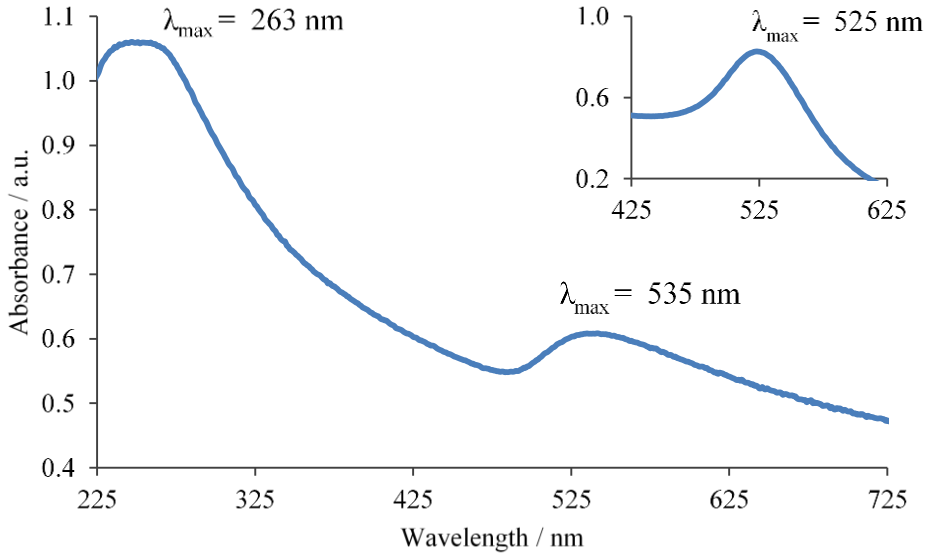

Figure 3.40: UV-Visible spectra of the fMWCNT-Au_{nano}(TriSodCit) dispersed in a 1.0% SDS solution and the AuNPs synthesised in the absence of fMWCNTs, inset.

3.2.9.8 Fourier Transform-Infrared Spectroscopy

Fourier Transform-Infrared spectroscopy (FT-IR) was used to obtain additional qualitative information on the pristine MWCNTs and the 24 h fMWCNTs. The FT-IR, spectra of these are shown in Figure 3.41. A small peak at 1725 cm^{-1} observed only with the fMWCNTs can be attributed to the C=O stretching of the surface covered COOH groups [21, 55-57]. This peak is not present with the pristine MWCNTs. Only a section of the spectra are shown for easier visualisation of the C=O stretching peak. A large peak at around 3400 cm^{-1} was seen in all spectra, attributed to OH stretching [21, 55-57], although this has been ascribed mainly to the presence of water in the samples and is not shown in the spectra displayed.

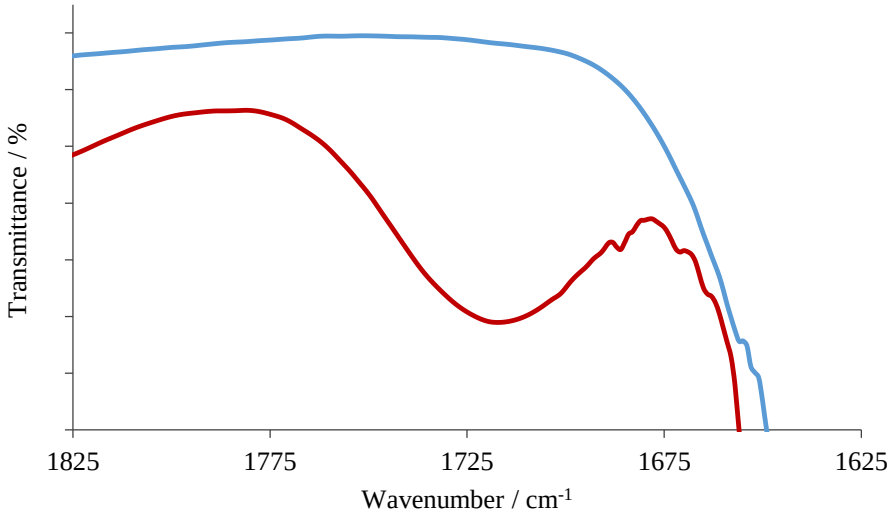

Figure 3.41: FT-IR spectra of the pristine MWCNTs and 24 h fMWCNTs in KBr.

3.2.9.9 Raman Spectroscopy

Raman spectroscopy is a very useful tool for the characterisation of carbon nanotubes. Typically two main bands appear and these are named the disorder band (D band) and the graphitic band (G band). The G band is a C-C stretching vibration within the hexagonal sp^2 hybridised graphitic rings and the D band is a C-C breathing vibration of these graphitic rings in the presence of symmetry containing defects. An increase in the D band relative to the G band can represent structural damage induced to the surface of the nanotube which may occur upon acid reflux due to the introduction of carbonyl containing functional groups [12, 51, 56-59]. This damage can also result in the presence of another disorder induced band, named D', which appears at a higher frequency and on the side of the G band and is proportional to the acid reflux time [58].

The Raman spectra of the pristine MWCNTs and the 24 h fMWCNTs are shown and compared in Figure 3.42. The D band appears at 1316 cm^{-1}, the G band at 1574 cm^{-1} and D' band at 1602 cm^{-1} for the pristine MWCNTs and at lower values of 1312 cm^{-1}, 1568 cm^{-1} and 1595 cm^{-1} for the 24 h fMWCNTs. In comparison to the pristine MWCNTs, all bands of the fMWCNTs have red-shifted slightly to lower wavenumbers.

It is expected that with the pristine MWCNTs, the G band would be more intense than the D band, but this is not the case. This suggests that the pristine MWCNTs had a degree of surface damage, possibly resulting from the manufacturing process. This damage is only detectable using Raman spectroscopy and not with FT-IR or during the potentiometric titrations. The D:G ratio of the pristine MWCNTs was 1.9:1.0 however this ratio does increase upon acid reflux. Upon reflux for 24 h, the D:G ratio increases to 2.5:1.0, which represents an increase in the D band of 30%. This is consistent with the acidic surface functionalities, introduced during the reflux in HNO_3.

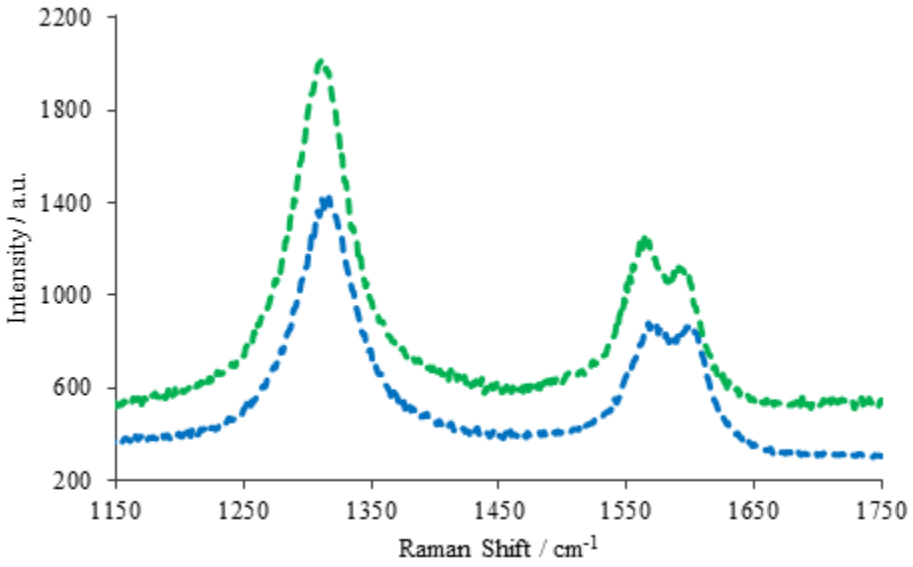

Figure 3.42: Raman spectra of the — pristine MWCNTs and — the 24 h fMWCNTs in KBr.

In Figure 3.43, the Raman spectra for the pristine MWCNTs and the pristine MWCNT-$Au_{nano}(NaBH_4)$ composites are shown. A slight increase in the G and D band intensities is observed with the MWCNT-$Au_{nano}(NaBH_4)$ composite, in comparison to the MWCNT sample containing no AuNPs. This increase in intensity may be due to a surface enhanced Raman scattering effect (SERs), that occurs when AuNPs are present on the nanotubes. With SERs, the Raman scattering intensity is enhanced due to the electric field created at the AuNPs surfaces [12, 60, 61]. Overall there is an increase of around 10% for all bands and this can be attributed to this SERs effect. The Raman spectra of the 24 h fMWCNTs and the fMWCNT-$Au_{nano}(NaBH_4)$

composite are shown in Figure 3.44. Since the fMWCNT-$Au_{nano}(NaBH_4)$ composite contained a higher proportion of Au, at 2.0% wt., it was expected that the SERs effect would be more intense. This is indeed the case, and both bands increase by about 20%, as shown in Figure 3.44. The peaks for the D, G and D' band appear at 1314 cm^{-1}, 1570 cm^{-1} and 1600 cm^{-1}, respectively, which also indicate a slight red-shift in comparison with the pristine MWCNTs.

As sodium dodecyl sulfate (SDS) was present during the syntheses of the composite materials, a Raman spectrum of SDS was recorded and this is shown in Figure 3.45. On comparing this spectrum with the data recorded with the pristine MWCNT-$Au_{nano}(NaBH_4)$ and the fMWCNT-$Au_{nano}(NaBH_4)$ samples, it is clear that there is no evidence of the SDS in the composites and it can be concluded that it is entirely removed during the sample filtration, in good agreement with the EDX results, Section 3.2.9.3.

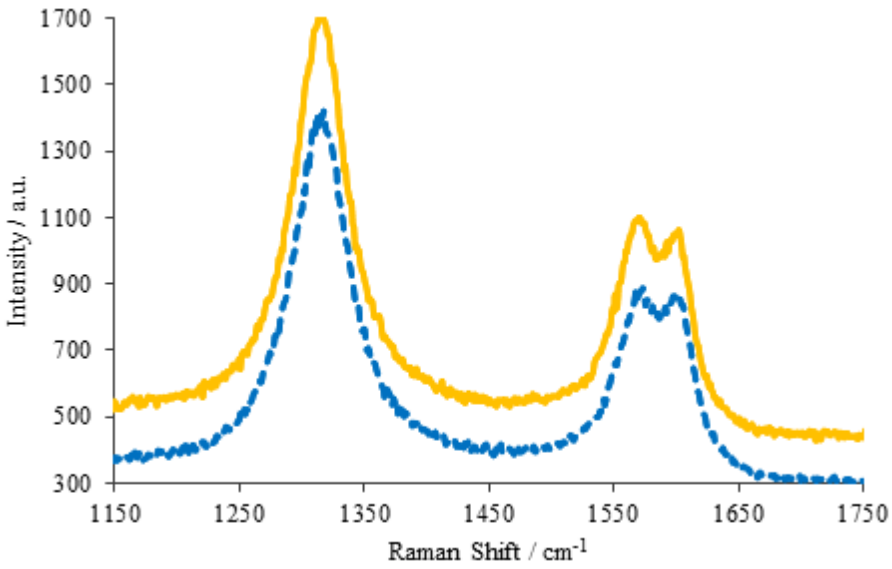

Figure 3.43: Raman spectra of the pristine MWCNTs and the MWCNT-$Au_{nano}(NaBH_4)$ composite in KBr.

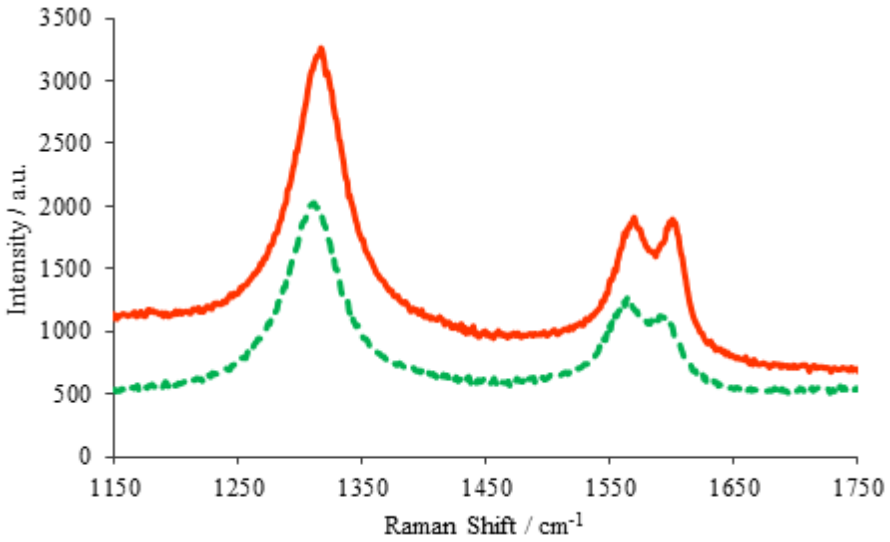

Figure 3.44: Raman spectra of — the 24 h fMWCNTs and — the fMWCNT-$Au_{nano}(NaBH_4)$ composite in KBr.

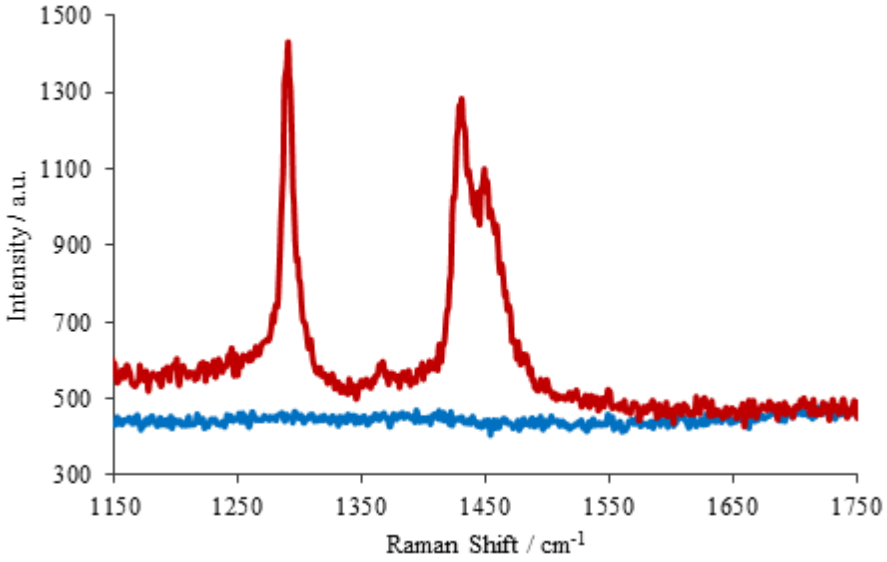

Figure 3.45: Raman spectra of — SDS in KBr and — a blank KBr disk.

3.2.9.10 Scan Rate and Gold Surface Area Analyses

As shown in previous sections, the various fMWCNT-Au_{nano} composite films exhibit different sensitivities towards glucose. It is also evident that sensitivity can be improved with H_2SO_4 cycling. These improvements in glucose sensing may correspond to an increased amount of the exposed Au and an increase in the

electroactive surface areas (ESA) of the films. The ESA represents the area that effectively transfers the charge of the species in solution [62] and these for each film may be estimated from the slope of the Randles-Sevcik relationship described by Equation 3.3. In this equation, *n* is the number of electrons, *v* is the scan rate, *D* is the diffusion coefficient, *A* the area of the electrode and *C* is the concentration [63-65].

$$i_p = 2.68 \times 10^5 n^{\frac{3}{2}} A D^{\frac{1}{2}} C v^{\frac{1}{2}} \qquad 3.3$$

Firstly, the diffusion coefficient of ferrocyanide was calculated at a GC electrode (d = 3 mm) using a 1.0 mM potassium ferrocyanide solution made in a 0.10 M KCl electrolyte. Experimental details and parameters are discussed in Chapter 2, Section 2.2.11. It is observed that the redox peaks increased linearly with the square root of the scan rate, as shown in Figure 3.46 (b), with a correlation coefficient of 0.9985 which signified a semi-infinite diffusion-controlled (SID) kinetic process rather than a surface-controlled, adsorption process [64, 65]. To create this linear plot, the peak currents were measured at each scan rate. Peak currents were measured from a manual background correction extending from the base of the peak to the peak current. Measurements taken from this theoretical line or from a background voltammogram in the 0.10 M KCl electrolyte provided very similar results. The surface area of the 3 mm GC electrode (0.0706 cm^2) was used and the slope of the linear plot, given in Equation 3.4, was used to obtain the diffusion coefficient of ferrocyanide. The diffusion coefficient of ferrocyanide was calculated as 6.10×10^{-6} cm^2 s^{-1} which is close to that of 6.30×10^{-6} cm^2 $s^{-1,}$ measured in KCl, reported by Morrin *et al.*[66].

$$\text{Slope} = 2.68 \times 10^5 n^{\frac{3}{2}} D^{\frac{1}{2}} C A \qquad 3.4$$

Having determined the diffusion coefficient of ferrocyanide, it was hoped that the estimated ESAs of the various materials following their pre-treatments could be calculated. Each material was cycled at various scan rates in 0.10 M KCl containing 1.0 mM potassium ferrocyanide, and the peak currents were plotted as a function of

the square root of the scan rate. The slope values obtained from the best fit plots may then be used with the diffusion coefficient of ferrocyanide to calculate the area A, Equation 3.4. This analysis was conducted for films produced both on a GC electrode and the carbon SPE (DRP-150). For clarity, the CVs and current plots shown correspond to the pristine MWCNT-$Au_{nano}(NaBH_4)$ and fMWCNT-$Au_{nano}(NaBH_4)$ modified GC electrodes and data for the remaining modified GC electrode and SPEs are listed in Tables 3.7 and 3.8, respectively.

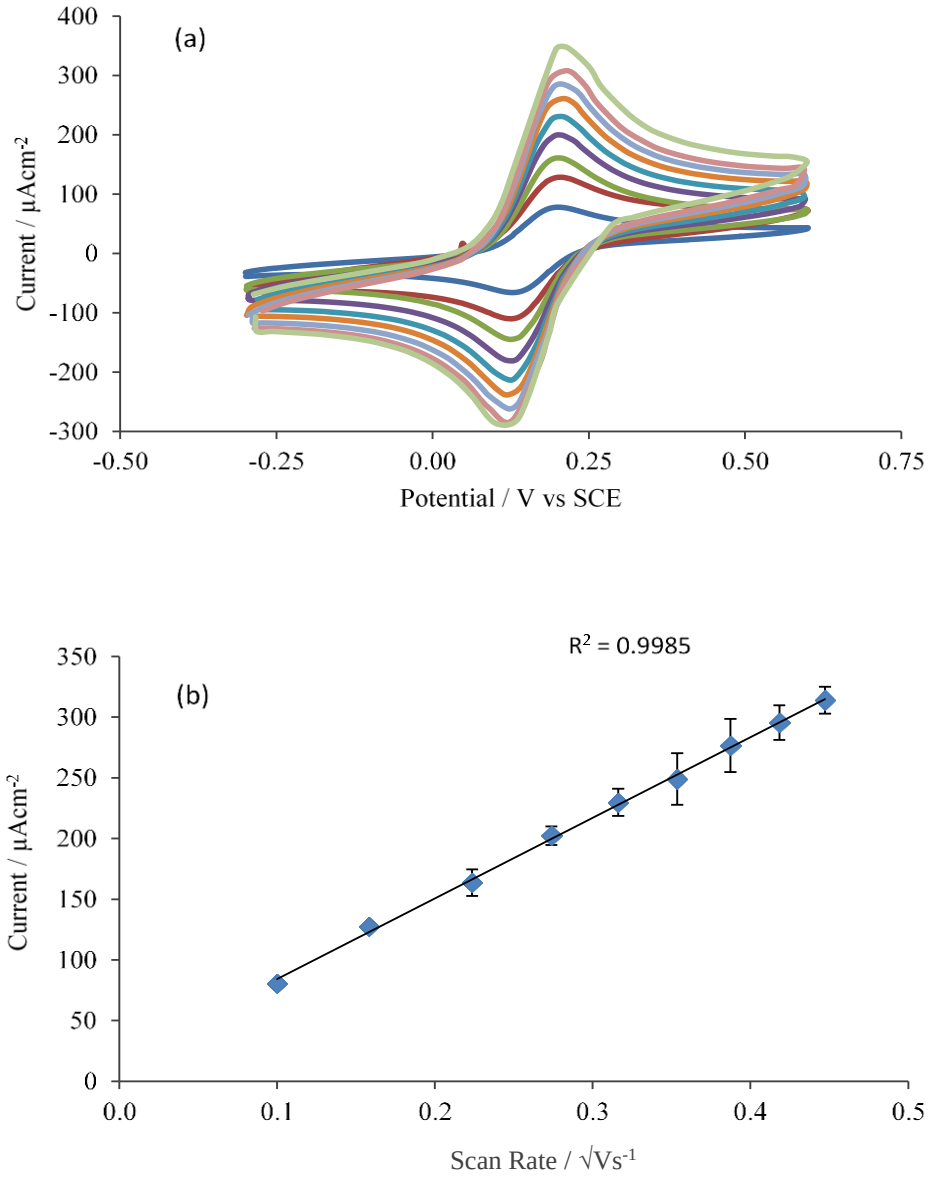

Figure 3.46: (a) Cyclic voltammograms of a polished GC electrode (d =3 mm) cycled in a 1.0 mM ferrocyanide solution made in 0.1 M KCl at scan rates of 10, 25, 50, 75, 100, 125, 150, 175 and 200 mV s^{-1}, and **(b)** corresponding plot of peak current plotted as a function of the square root of the scan rate, n = 3.

The CVs recorded for the pristine MWCNT-$Au_{nano}(NaBH_4)$ and the fMWCNT-$Au_{nano}(NaBH_4)$ composite modified GC electrodes following a pre-treatment in 1.0 M H_2SO_4 are shown in Figure 3.47 (a) and (b). The voltammograms recorded for the pristine MWCNT-$Au_{nano}(NaBH_4)$ composite are similar to that obtained with the GC electrode. In contrast, the voltammograms recorded for the fMWCNT-$Au_{nano}(NaBH_4)$ composite films show relatively high overall capacitance. The corresponding plots, for the peak currents plotted as a function of the square root of scan rate, are shown in Figure 3.47 (c). Again, high correlation values of 0.9962 and 0.9832 for the MWCNT-$Au_{nano}(NaBH_4)$ material and the optimised fMWCNT-$Au_{nano}(NaBH_4)$ film are obtained, respectively. These values both imply a SID electrochemical process, as discussed previously. Although a slight deviation in linearity is observed in the plot of the optimised fMWCNT-$Au_{nano}(NaBH_4)$ composite film.

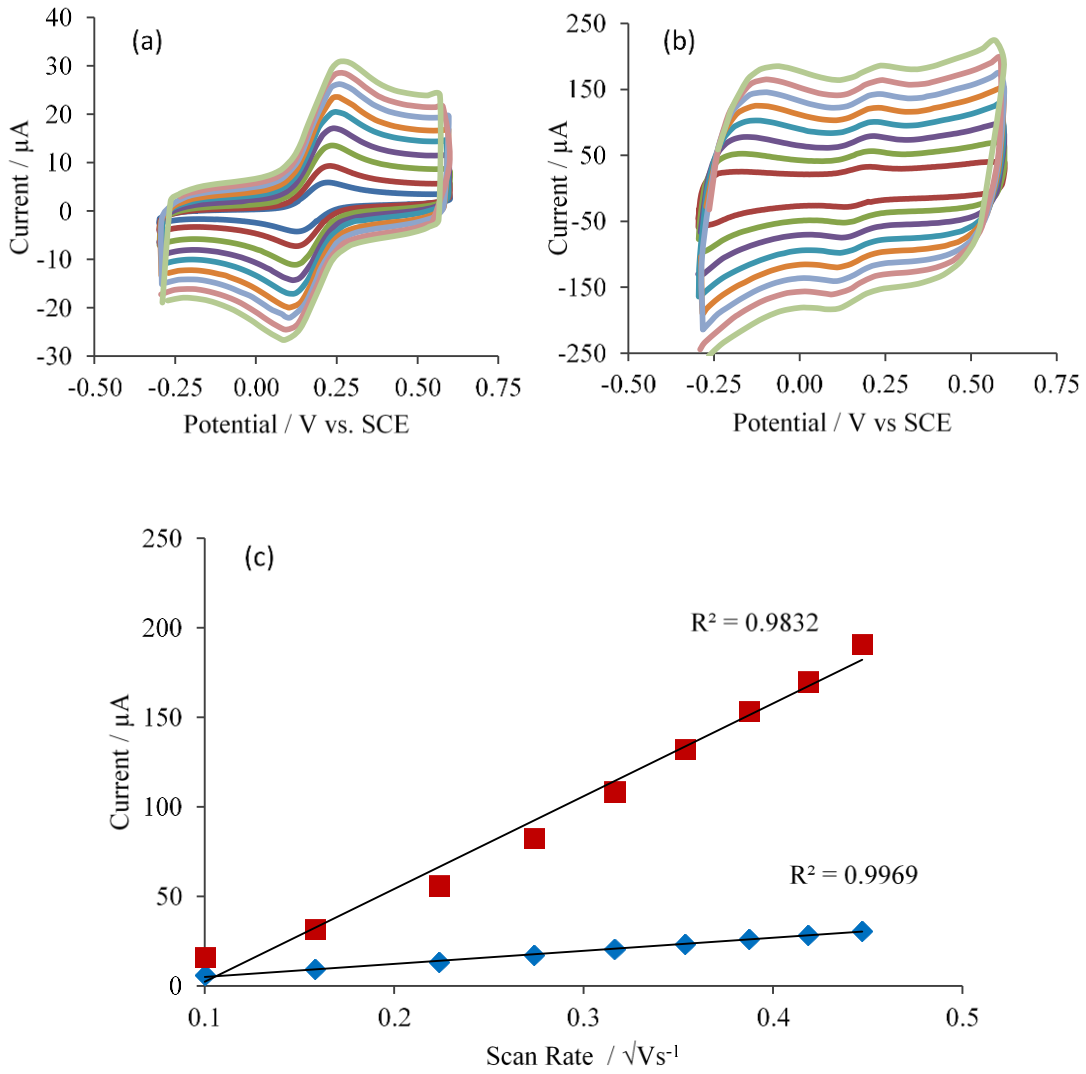

Figure 3.47: Cyclic voltammograms of the **(a)** pristine MWCNT-$Au_{nano}(NaBH_4)$ composite made using 5.0 µl of the 2.0 mg/ml dispersion, the **(b)** optimised fMWCNT-$Au_{nano}(NaBH_4)$ film formed using 5.0 µl of the 4.0 mg/ml dispersion cycled in 1.0 mM ferrocyanide made in 0.1 M KCl at scan rates of 10, 25, 50, 75, 100, 125, 150, 175 and 200 mV s^{-1} and **(c)** plot of the peak currents as a function of the square root of the scan rate, n = 3.

Another way to determine a SID or adsorption controlled process is to plot the logarithm of the peak current as a function of the logarithm of the scan rate. A slope value close to 0.5 represents a SID process and when closer to a value of 1 this represents an adsorption-controlled process [67]. These logarithmic plots and the Randles-Sevcik plots were prepared for each composite film and pre-treatment and these data are summarised in Table 3.7. It is apparent that the redox process of ferrocyanide appears to deviate to higher values than 0.5. Similar results are discussed in work by Lu *et al.* [68], in which larger slopes of around 0.65 are obtained when using a similarly-natured porous carbon electrode. It was concluded that this deviation from the theoretical value of 0.5 is due to the electrode not being of a smooth planar type, although they still accepted that SID was occurring.

Figures 3.48 (a), shows plots obtained for a film produced with the pristine MWCNT-$Au_{nano}(NaBH_4)$ composite and the optimised fMWCNT-$Au_{nano}(NaBH_4)$ modifed GC electrode. The slope value resulting from the pristine MWCNT-$Au_{nano}(NaBH_4)$ composite almost agrees with a SID process and as such may possibly be suitable for ESA estimations, although that of the other film shows a higher value. The optimised fMWCNT-$Au_{nano}(NaBH_4)$ composite yielded a slope of 0.84, which deviates far from the ideal value. To add to this finding, a plot of the current versus the scan rate 'absorption plot' is constructed for the optimised composite film, Figure 3.48 (b). This adsorption plot also yields a linear relationship as with the diffusion plot, both having high correlation values. Similar trends occurred at all other composite films although the fMWCNT-Au_{nano}(TriSodCit) composite films result in slightly lower slope values, shown in Table 3.7.

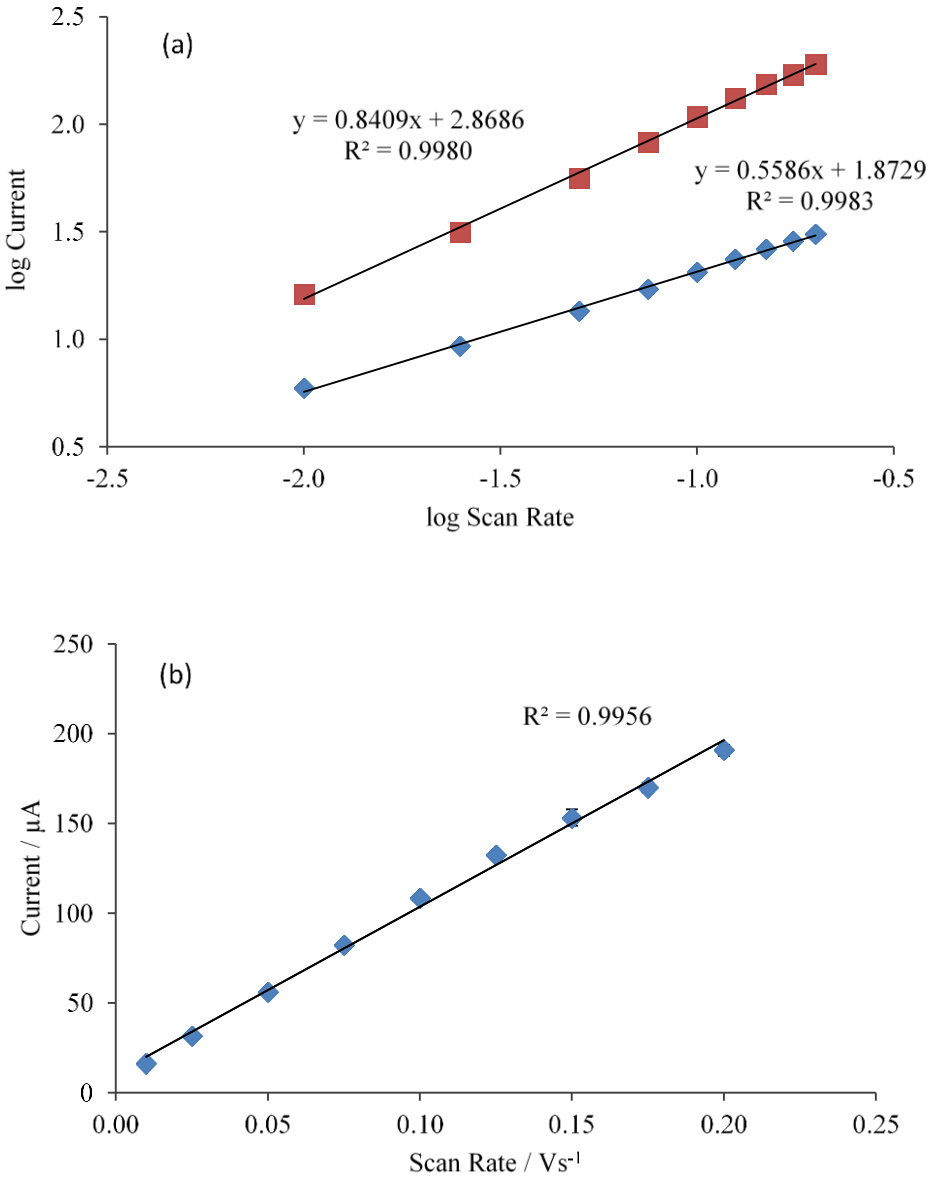

Figure 3.48: Plots of the logarithm of the peak current as a function of the logarithm of the scan rate for the films produced with the **(a)** pristine MWCNT-$Au_{nano}(NaBH_4)$ composite (blue points) and the optimised fMWCNT-$Au_{nano}(NaBH_4)$ composite (red points), n = 3 and **(b)** the plot of the peak currents as a function of the scan rate at the fMWCNT-$Au_{nano}(NaBH_4)$ composite film, n = 3.

Overall it seems as if a process other than SID is contributing to the redox current responses at the composite films. These deviations in slope values suggest that thin layer diffusion (TLD) occurs, which is in keeping with previous studies with carbon nanotubes and other porous systems [69-74]. It is also evident that these deviations are more significant when film thickness is increased using the 4.0 mg/ml dispersions. Indeed, work by Sims *et al.* [70] with MWCNT films shows that the effects of TLD are most prominent when the film thickness is increased.

TLD can occur in carbon nanotube films like those used in this work, due to the porous nature of the casted films. With TLD, pockets of the analyte-containing solution diffuse inside the porous layers of film, thereby contributing to the current responses [70]. Also, the presence of TLD may indicate that the active surface area of the film may not remain constant during scan rate changes [69]. Due to the effects of TLD and the possibility of film surface area changes over scan rates, it was concluded that total ESA measurements were not possible using Randles-Sevcik analysis at the carbon nanotube-containing films.

Below, in Table 3.7, the correlation coefficients (R^2 values) obtained from the diffusion plots are listed for each composite modified GC electrode, as well as the slope values obtained from the log-log adsorption plots. R^2 values close to 1 represent a SID controlled process and slope values close to 0.5, from the log plot, also indicate a SID process.

Table 3.7: Table of the correlation coefficients, R^2 values, obtained from the plots of peak current versus the square root of scan rate and slope values from the log of peak current versus log of scan rate for all composite films.

Composite Film and Pre-treatment	R^2 Values of Diffusion Plots	Slope Values of Log Plots	Diffusion Processes
Sodium Borohydride Reducing Agent			
(2.0 mg/ml)			
0 h MWCNT-Au_{nano}	0.9969	0.5586	SID + TLD
18 h fMWCNT-Au_{nano}	0.9966	0.5670	SID + TLD
24 h fMWCNT-Au_{nano}	0.9914	0.6262	SID + TLD
48 h fMWCNT-Au_{nano}	0.9980	0.5964	SID + TLD
(4.0 mg/ml)			
24 h fMWCNT-Au_{nano}	0.9927	0.6244	SID + TLD
24 h fMWCNT-Au_{nano} + 0.5 M H_2SO_4	0.9841	0.8023	SID + TLD
24 h fMWCNT-Au_{nano} + 1.0 M H_2SO_4	0.9833	0.8408	SID + TLD
Trisodium Citrate Reducing Agent			
(4.0 mg/ml)			
24 h fMWCNT-Au_{nano}	0.9949	0.6864	SID + TLD
24 h fMWCNT-Au_{nano} + 0.5 M H_2SO_4	0.9851	0.6986	SID + TLD
24 h fMWCNT-Au_{nano} + 1.0 M H_2SO_4	0.9686	0.7886	SID + TLD
24 h fMWCNT			
(4.0 mg/ml)			
24h fMWCNT	0.9944	0.6532	SID + TLD

When this experimental analysis was applied to the modified SPE system, a very similar trend was observed. Linearity in the 'diffusion plots' was seen but high gradient values close to 1 were obtained in the 'log-log' plot, data shown in Table 3.8.

Again this implies that another process is occurring at the electrode surface, other than SID and is most probably TLD. The effects of TLD may be slightly more significant at this composite modified SPE as a higher slope of 0.9000 is achieved. This may be a result of the porous nature of the SPE surface along with a possibly thicker composite film formed.

Table 3.8: Table of the correlation coefficients, R^2 values, obtained from the diffusion plots of the peak current versus the square root of scan rate and slope values from the plots of the log of peak current versus log of scan rate for the composite modified SPE (DRP-150).

Composite Film and Pre-treatment	R^2 Values of Diffusion Plots	Slope Values of Log Plots	Diffusion Processes
fMWCNT-Au_{nano}($NaBH_4$) + 1.0 M H_2SO_4	0.9647	0.9000	SID + TLD

Additional kinetic information was extracted from the Randles-Sevcik plots. In this case, the redox peak separations (ΔE) of ferrocyanide as a function of scan rate were measured for the various materials and these are plotted as bar charts in Figures 3.49, 3.50 and 3.51 for the modified GC films and in Figure 3.52 for the modified SPEs (DRP-150). The peak separations were obtained using Equation 3.5, where, *Ea* is the peak potential of the oxidation wave, *Ec* is the peak potential of the reduction peak and *n* is the number of electrons transferred in the redox process[75]. ΔE can provide interesting information on the rate of the electron transfer at electrodes when the system is under SID control, values of 59 mV/*n* signify a reversible redox couple, which is a fast electron transfer process [76]. Values higher than this represent a quasi-reversible process, which is a slower process [67, 75].

$$\Delta E = Ea - Ec = \frac{59\ \text{mV}}{n} \qquad 3.5$$

Since TLD was occurring at the modified films the peak separation information obtained was not related to the SID model, although ΔE can still be calculated at each film. In work by Keeley and Lyons [69] and Streeter *et al.* [74] it is suggested that the SID model may not be used when systems are effected by TLD. Also,

comparisons in ΔE can only be undertaken when the mass transport regime at each of the electrochemical films is the same [74]. Since the effects of TLD varied at each composite film, it was not deemed accurate to compare values of ΔE between the films, unless the effects of TLD were very similar. The slope values obtained from the 'log-log' plots can provide an indication of the level of TLD occurring at each film.

It can be seen in the following data displayed from Figures 3.49 – 3.52, that ΔE varies between each material and treatment. The smallest ΔE values are obtained at the GC electrode, Figure 3.49. These values may be compared with the theoretical value of 59 mV associated with a system under SID control, as previous studies in this section suggested that SID was occurring at GC. The peak separations obtained at the pristine MWCNT-$Au_{nano}(NaBH_4)$ composite film are much larger than those obtained at the GC electrode. The values for ΔE obtained at these films may be compared, as SID is also deemed to be the main process occurring at the MWCNT-$Au_{nano}(NaBH_4)$ film, due to the slope value of 0.5586 obtained from the 'log-log' plot, data shown in Table 3.7. As such, it can be said that slower electron transfer is occurring at the MWCNT-$Au_{nano}(NaBH_4)$ film in comparison to the GC electrode. In work by Beguin and Frackowiak [68], involving the use of porous carbon electrodes, the redox processes were still considered to be under SID control even when slope values, from the 'log-log' plots, deviated as high as 0.65.

Peak separation data obtained at the 18 h fMWCNT-$Au_{nano}(NaBH_4)$ film may also be compared with both the GC and MWCNT-$Au_{nano}(NaBH_4)$ films, as a similar slope of 0.5670, was obtained from the 'log-log' plot, data shown in Table 3.7. The values of ΔE are much smaller for the 18 h fMWCNT-$Au_{nano}(NaBH_4)$ film, in comparison to those obtained at the MWCNT-$Au_{nano}(NaBH_4)$ film and, as such, it may be concluded that faster electron transfer is occurring at the 18 h fMWCNT-$Au_{nano}(NaBH_4)$ film. Studies by Ramesh and Sampath [77] show that the oxygen/carbon ratio of rough graphitic materials is related to the electrochemical kinetics and that materials with a high oxygen/carbon ratio show an increase in these kinetics. Since 18 h fMWCNTs are used to produce the 18 h fMWCNT-$Au_{nano}(NaBH_4)$ composite, their oxygen/carbon ratio is higher than that of the

pristine MWCNTs and this is consistent with the faster kinetics observed at this composite film.

Peak separation values calculated at the various fMWCNT-Au_{nano} composite films, with and without H_2SO_4 pre-treatments, shown in Figures 3.50 – 3.52, are similar and all are increasing with scan rate. Although, as discussed previously, the effects of TLD differed at each of these films and, as such, the results may not be comparable.

Two films that may be compared are the optimised 24 h fMWCNT-Au_{nano}($NaBH_4$) modified GC electrode and SPE. This is due to the slope values obtained from the 'log-log' plots having similar values of 0.8408 and 0.9000 for the modified GC electrode and SPE, respectively, data displayed in Table 3.7. Much slower electron transfer is observed at the modified SPEs and it is possibly these kinetic limitations that may explain the lower-than-expected glucose currents observed at these modified SPEs, data shown in Section 3.2.8.

Overall it is observed that larger peak separations occur at the composite modified electrodes in comparison to the GC electrode. Although these may not be compared, this was not expected due to the effects of TLD at these films which typically results in a decrease in peak separations [69]. In a study by Keeley and Lyons [69], involving the formation CNT films by drop cast methods, it was discussed that some of the solvent used in the drop cast dispersion remained in the CNT sensing film and that this increased the values of ΔE during scan rate studies involving ferrocyanide. Although much of the SDS was removed during NaOH cycling, it may be possible that some SDS was remaining in the sensing films and that this was increasing these peak separations.

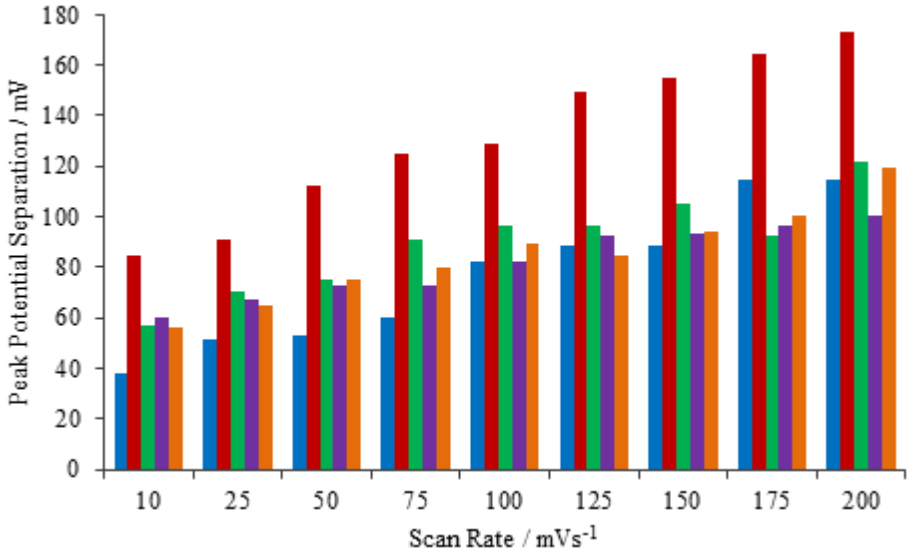

Figure 3.49: Plot of the ferrocyanide redox peak separations, ΔE, as a function of the scan rate for the — polished GC electrode, — pristine MWCNT-$Au_{nano}(NaBH_4)$ composite, — 18 h fMWCNT-$Au_{nano}(NaBH_4)$, — 24 h fMWCNT-$Au_{nano}(NaBH_4)$ and — 48 h fMWCNT-Au_{nano}(NaBH4) composite films, produced on a GC electrode using 5.0 µl of the 2.0 mg/ml dispersions.

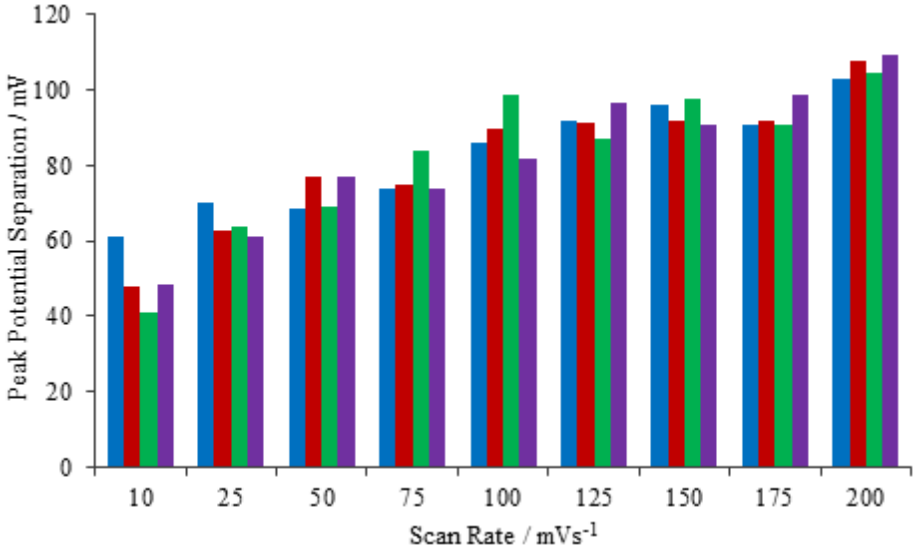

Figure 3.50: Plots of the ferrocyanide redox peak separation, ΔE, as a function of the scan rate for the — 24 h fMWCNT and fMWCNT-$Au_{nano}(NaBH_4)$ films, on a GC electrode using 5.0 µl of the 4.0 mg/ml dispersions with — no H_2SO_4, — the 0.5 M H_2SO_4 and —1.0 M H_2SO_4 pre-treatments.

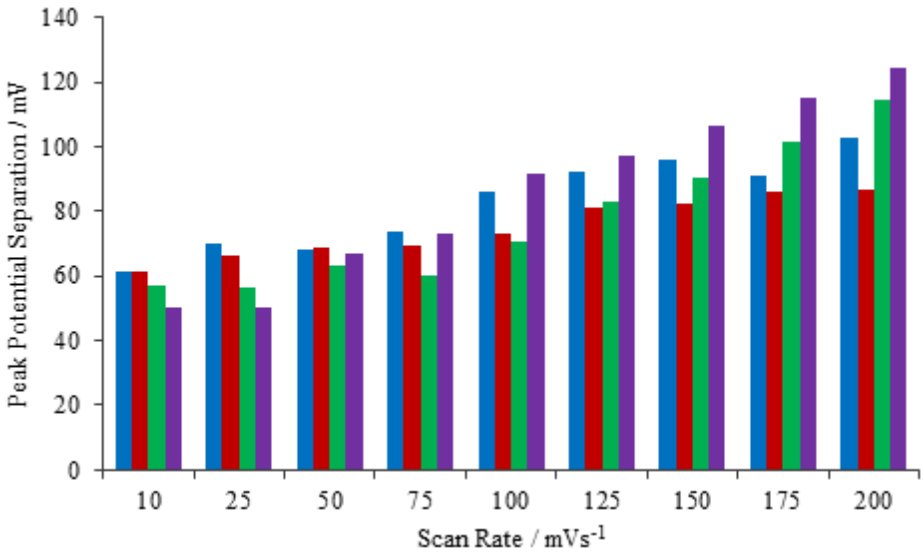

Figure 3.51: Plots of the ferrocyanide redox peak separation, ΔE, as a function of the scan rate for the — 24 h fMWCNT and fMWCNT-Au_{nano}(TriSodCit) films, on a GC electrode using 5.0 µl of the 4.0 mg/ml dispersions with — no H_2SO_4, — the 0.5 M H_2SO_4 and — 1.0 M H_2SO_4 pre-treatments.

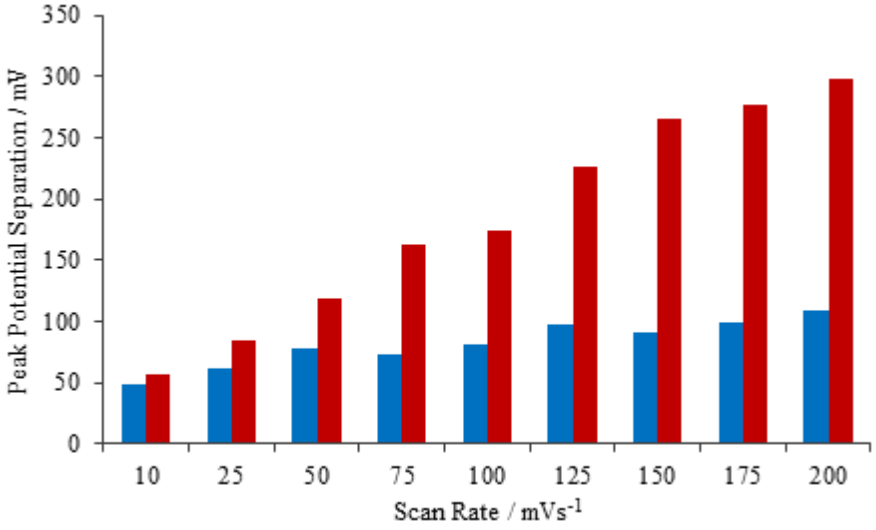

Figure 3.52: Plots of the ferrocyanide redox peak separation, ΔE, as a function of the scan rate for the 1.0 M H_2SO_4 pre-treated fMWCNT-Au_{nano}($NaBH_4$) composite films, on a — GC electrode using 5.0 µl of the 4.0 mg/ml dispersion and on a — SPE using 10.0 µl of the 4.0 mg/ml dispersion.

Due to the effects of TLD it was not deemed accurate to estimate the total ESAs of the composite films using the Randle-Sevcik equation. Although using a different method, it was possible to estimate the collective surface areas of the AuNPs within

the prepared films. This was achieved by cycling the films in a 0.5 M H_2SO_4 solution using CV and by measuring the charge under the characteristic Au oxide reduction peak, which appears at around 0.90 V vs. SCE [78-80]. This peak results from the Au oxide layer formed at more positive potentials in the forward scan. It can be assumed that a value of 450 µC/cm^2 exists for the Au oxide reduction at 0.90 V vs. SCE and as such, data can be used comparatively [78]. The intensity of this peak is proportional to the surface area of Au present and this area can be estimated by comparing the charge under these peaks with those obtained from Au electrodes of known surface areas [80].

In Figure 3.53, a CV of a 3 mm (0.0706 cm^2) Au electrode cycled in 0.5 M H_2SO_4 for 11 cycles is presented. Prior to the experiment, the electrode was polished to a mirror finish with a 0.5 µm aluminium oxide paste and then sonicated in a 50:50 volume absolute ethanol:deionised water mixture for 10 min. A voltammogram recorded of a polished GC electrode of the same surface area which was subjected to the H_2SO_4 cycling is shown in Figure 3.53, inset. It is clear that only an oxide reduction peak is present at around 0.90 V vs. SCE for the Au electrode. The charge under the reduction peak is plotted for the various Au electrodes as a function of their geometrical areas and a linear calibration curve is generated, as shown in Figure 3.54. The composite films were subjected to the same H_2SO_4 cycling and the charges under the Au oxide reduction peaks were compared with this calibration curve.

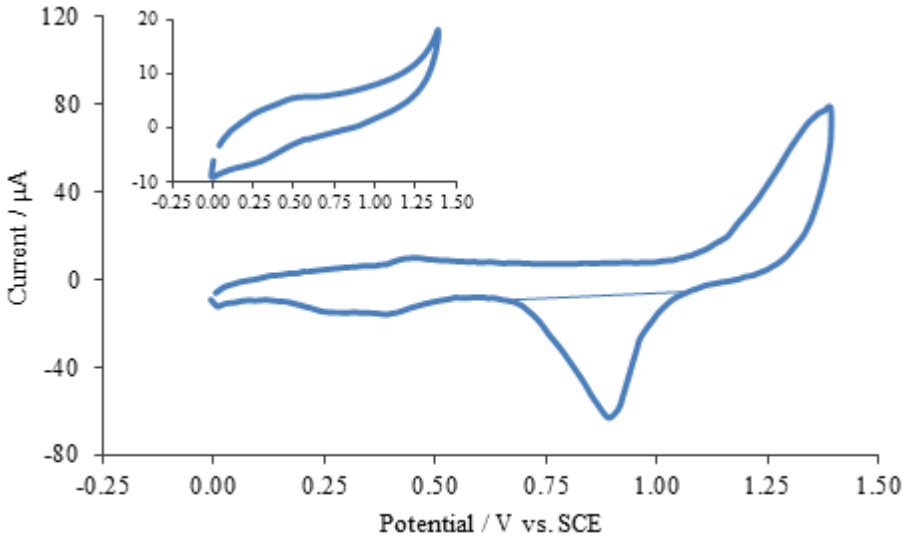

Figure 3.53: Cyclic voltammograms recorded at 100 mV s^{-1} of a polished Au (d = 3 mm) and a GC (d = 3 mm) electrode, inset, in a 0.5 M H_2SO_4 solution.

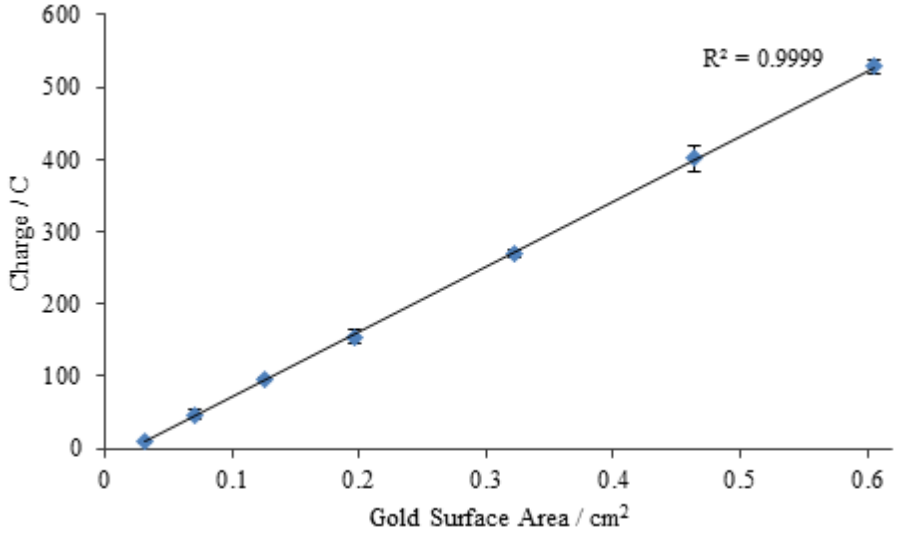

Figure 3.54: Calibration curve of the charge of the Au oxide reduction peak plotted as a function of the corresponding standard geometrical Au electrode surface areas. All electrodes were cycled at 100 mV s^{-1} in a 0.5 M H_2SO_4 solution for 11 cycles, n = 3.

To outline the importance of the NaOH pre-treatment on the films, the collective surface areas of the AuNPs within the composite films were obtained for the fMWCNT-$Au_{nano}(NaBH_4)$ composite film with and without the NaOH pre-treatment. In both cases 5.0 µl of 4.0 mg/ml dispersions were used. As detailed earlier, the composites were cycled in a 0.5 M H_2SO_4 solution and the voltammograms recorded are shown in Figure 3.55. As a control, the 24 h fMWCNT material was used and the voltammogram recorded in 0.5 M H_2SO_4 is included in Figure 3.55. There is no evidence of any reduction peak for the 24 h fMWCNT without the AuNPs. The Au oxide reduction peak is clearly evident at approximately 0.90 V vs. SCE for the 24 h fMWCNT-$Au_{nano}(NaBH_4)$ film pre-treated in NaOH. Furthermore, the peak current is higher than that observed with the polished Au electrode (d = 3 mm). However, when no NaOH pre-treatment is used, the reduction peak is negligible indicating a very low area for Au. This highlights the importance of the pre-treatment in NaOH. Also it can be noticed that the films appear significantly more capacitive when treated in the NaOH solution. The capacitive background currents of the fMWCNT-$Au_{nano}(NaBH_4)$ film and the 24 h fMWCNT film are similar, indicating that the increase in capacitance, following the NaOH pre-treatment is not connected to the presence of the AuNPs.

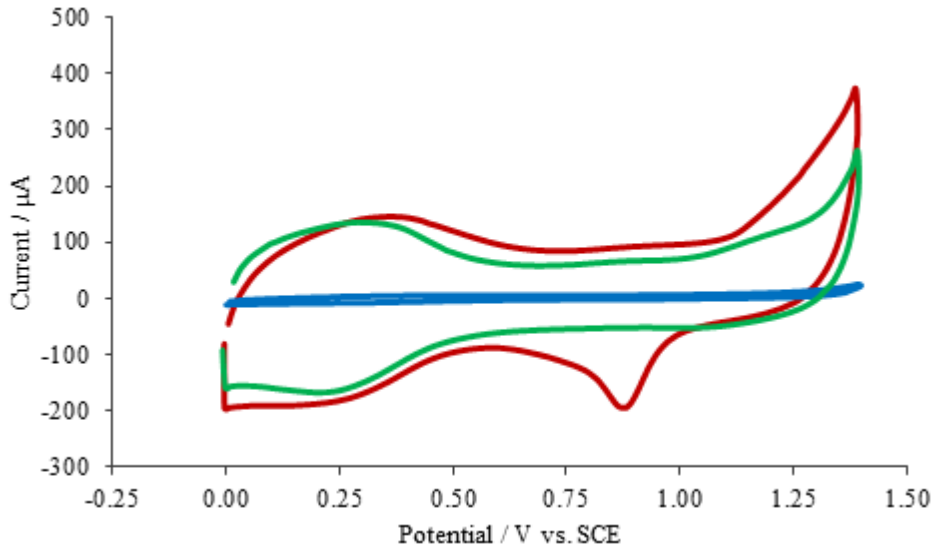

Figure 3.55: Cyclic voltammograms recorded at 100 mV s^{-1} in 0.5 M H_2SO_4 of a fMWCNT-$Au_{nano}(NaBH_4)$ composite — with and — without NaOH pre-treatment and of a — 24 h fMWCNT film with NaOH pre-treatment, where 5.0 µl of 4.0 mg/ml dispersions were used.

Other than the NaOH pre-treatment it was seen that H_2SO_4 cycling further increased the Au oxide reduction peak, at around 0.90 V vs. SCE. This is evident in Figure 3.56 where voltammograms are shown for the fMWCNT-$Au_{nano}(NaBH_4)$ composite film with pre-treatments in 0.5 M and 1.0 M H_2SO_4. It is clear that a larger peak current is obtained when the composite is cycled in 1.0 M H_2SO_4, in comparison to the 0.5 M H_2SO_4. This increase is measured at almost 60% and indicates a significant increase in the Au surface area. Clearly this cycling exposes a higher electroactive area of Au and yields the optimised sensor. The charge computed for the Au reduction peaks and the corresponding calculated surface areas for Au are listed in Table 3.9. No total ESAs of the various films are included, although the slope values of the 'diffusion' plots are shown for comparison. The composite produced with TriSodCit provided films with the highest Au ESAs overall. It was this greater presence of Au which may explain the films higher sensitivity towards glucose.

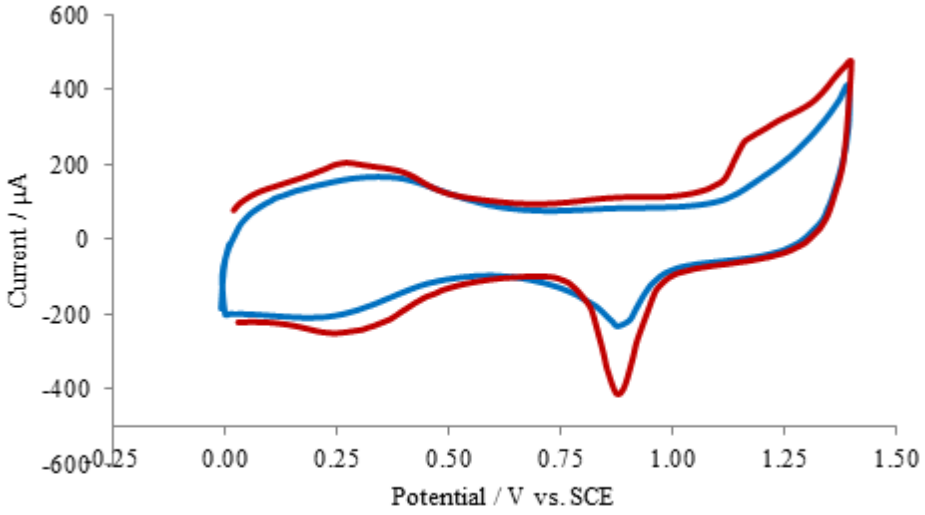

Figure 3.56: Cyclic voltammograms recorded at a 100 mV s^{-1} of a fMWCNT-$Au_{nano}(NaBH_4)$ composite film with — 0.5 M and — 1.0 M H_2SO_4 pre-treatments in a 0.5 M H_2SO_4 solution, where 5.0 µl of a 4.0 mg/ml dispersion was used.

Table 3.9: Estimated collective AuNPs surface areas (Au ESA) of the composite modified GC electrodes using the charge of the Au oxide reduction peak obtained in a 0.5 M H_2SO_4 solution, n = 3. †

Composite Film and Pre-treatment	Slope Values / $A\sqrt{Vs^{-1}}$	Charge Under $Au_{ox.}$ Reduction peak / C	Au ESA / cm^2
Sodium Borohydride Reducing Agent			
(2.0 mg/ml)			
0 h MWCNT-Au_{nano}	7.292×10^{-5}	4.436×10^{-5}	0.0547
18 h fMWCNT-Au_{nano}	7.825×10^{-5}	7.670×10^{-5}	0.0918
24 h fMWCNT-Au_{nano}	9.488×10^{-5}	1.003×10^{-4}	0.1200
48 h fMWCNT-Au_{nano}	7.913×10^{-5}	7.069×10^{-5}	0.0846
(4.0 mg/ml)			
24 h fMWCNT-Au_{nano}	1.687×10^{-4}	1.672×10^{-4}	0.2002
24 h fMWCNT-Au_{nano} + 0.5 M H_2SO_4	3.827×10^{-4}	2.399×10^{-4}	0.2874
24 h fMWCNT-Au_{nano} + 1.0 M H_2SO_4	5.181×10^{-4}	3.810×10^{-4}	0.4562
Trisodium Citrate Reducing Agent			
(4.0 mg/ml)			
24 h fMWCNT-Au_{nano}	2.317×10^{-4}	2.114×10^{-4}	0.2530
24 h fMWCNT-Au_{nano} + 0.5 M H_2SO_4	3.700×10^{-4}	3.112×10^{-4}	0.3736
24 h fMWCNT-Au_{nano} + 1.0 M H_2SO_4	5.674×10^{-4}	4.956×10^{-4}	0.5930
24 h fMWCNT			
(4.0 mg/ml)			
24h fMWCNT	1.744×10^{-4}	0	0

† Films not suitable for total ESA estimations using this technique.

The same scan rate and Au ESA analyses were conducted at the modified SPE electrodes. As mentioned previously, only the fMWCNT-Au_{nano}($NaBH_4$) composite was used to modify the SPEs due to the instability of the fMWCNT-Au_{nano}(TriSodCit). Also, a larger volume of 10.0 µl of this dispersion was cast onto the SPEs due to their increased diameter size of 4 mm. As expected, a larger slope value is obtained from the diffusion plot which may imply a larger ESA, although this value is not used to estimate the ESA due to the effects of TLD, data shown in Table 3.8. The charge under the Au oxide reduction peak is quite significant at this modified SPE and corresponded with larger calculated Au ESA of 1.0819 cm^2, in comparison to that of the modified GC electrode which is calculated to be 0.5930 cm^2. Although there is an apparent increase in this Au area, the films sensitivity towards glucose is not as substantially increased. This might be a result of the lag in kinetics at this modified SPE, as discussed previously.

Table 3.10: Estimated collective AuNP surface areas (Au ESA) of the composite modified SPE (DRP-150) using the charge of the Au oxide reduction peak obtained in a 0.5 M H_2SO_4 solution, n = 3. †

Composite Film and Pre-treatment	Slope Values / $A\sqrt{V}s^{-1}$	Charge Under $Au_{ox.}$ Reduction peak / C	Au ESA / cm^2
24 h fMWCNT-Au_{nano} + 1.0 M H_2SO_4	9.515×10^{-4}	9.042×10^{-4}	1.0819

† Films not suitable for total ESA estimations using this technique.

3.2.9.11 Electrochemical Impedance Spectroscopy

Electrochemical Impedance Spectroscopy (EIS) was carried out to measure and compare the changes in the capacitance and resistance at the composite films before and after the acid pre-treatments. As observed in the CVs shown in Section 3.25, there is a noticeable increase in the systems overall capacitance during the cycling in PBS when H_2SO_4 pre-treatments are used and especially at lower potentials. EIS measurements were taken over the wide frequency range of 0.003 Hz to 60,000 Hz and at potentials of -0.10 V, 0.20 V and 0.50 V vs. SCE using a perturbation of 5.0

mV. The composite films were prepared and then polarised at the required potential for a period of 30 min. This period was sufficient to achieve steady-state conditions.

Impedance data can be presented as Complex plane or Nyquist plots and as Bode plots. The imaginary and real components of the impedance are plotted to give the Complex plane or Nyquist plots, while the Bode plots are generally separated into two plots displaying the magnitude of the impedance and the phase angle as a function of the logarithm of frequency[81]. Using ZView® software, the experimental data were fitted to the equivalent circuit depicted in Figure 3.57 using a non-linear least squares fitting minimisation method. This circuit was used for all the composites while the data recorded for the GC electrode were modelled using a constant phase element, denoted as CPE2, in place of the capacitor, C1. The Rs component represents the solution resistance, R1 represents the charge-transfer resistance and CPE1 and CPE2 are constant phase elements with C1 representing a capacitor. CPEs are frequently used in circuit modelling and are ideal when surface inhomogeneities exist [82]. The Impedance, Z, of a CPE can be defined using Equation 3.6, where Q represents the magnitude of the capacitance, ω is the angular frequency of the alternating potential perturbation, and α represents the exponent [81].

$$Z_{CPE} = \frac{1}{Q(j\omega)^{a}} \qquad 3.6$$

This equation can represent the impedance of a capacitor, Q = C, when α = 1.0. Exponent values of 1.0 correspond to an ideal capacitor and when close to 1.0 it can be regarded as a non-ideal capacitor. When the exponent adopts a value of 0.5 this corresponds to a diffusional process [81]. The carbon nanotube materials used in this study resulted in exponent values close to 1.0 and as such the CPE2 components were replaced with a capacitor, C1. This resulted in better model fitting with lower errors. The two-time constant model shown in Figure 3.57 and the corresponding parameters with low errors is an example of the fitting obtained with the 24 h fMWCNT film.

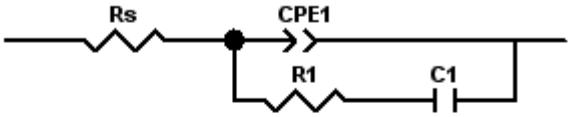

Element	Freedom	Value	Error	Error %
Rs	Free(±)	779	5.9731	0.76677
CPE1-T	Free(±)	8.4133E-05	1.6145E-06	1.919
CPE1-P	Free(±)	0.6692	0.0039846	0.59543
R1	Free(±)	2789	108.29	3.8828
C1	Free(±)	0.00010896	3.0129E-06	2.7651

Figure 3.57: Equivalent circuit used to fit the impedance data and an example of the parameters and errors represent the fitting of the data recorded for the 24 h fMWCNT film.

In Figure 3.58 impedance data are shown for the optimised fMWCNT-$Au_{nano}(NaBH_4)$ composite film and a 1.0 M H_2SO_4 pre-treated 24 h fMWCNT film and a GC electrode. These data are recorded at 0.2 V vs. SCE in a 0.10 M PBS solution at a pH of 7.40. All the measured data are not shown in the plots for clarity. It is clear from these plots that the impedance response of the GC electrode is very different to the fMWCNT-$Au_{nano}(NaBH_4)$ or the fMWCNT films. These impedance data are fit to the equivalent circuit shown in Figure 3.57 and the resistance, R1, values and the values of the constant phase element CPE1 and capacitor C1 are displayed as a function of the applied potential. The capacitance values, obtained from the CPE1 components, are shown in Figure 3.59 for the fMWCNT-$Au_{nano}(NaBH_4)$ composite films with no H_2SO_4, 0.50 M H_2SO_4 and 1.0 M H_2SO_4 pre-treatments and a 1.0 M H_2SO_4 pre-treated 24 h fMWCNT film without AuNPs. It is clear from these data that the capacitance is high at – 0.10 V vs. SCE and this is consistent with the CV data in which the capacitance is observed to increase at lower potentials, Section 3.2.5. Lower capacitance values are obtained at 0.2 and 0.5 V vs. SCE. The capacitance values of the fMWCNT-$Au_{nano}(NaBH_4)$ composite films are similar and do not vary significantly with the pre-treatments in 0.5 M H_2SO_4 and 1.0 M H_2SO_4, but it is clear that the 24 h fMWCNT films give the lowest capacitance. Data obtained from the CPE1 element may not fully reflect the capacitance of the material and may be largely a result of an electrochemical double layer formed at the electrochemical interface [83].

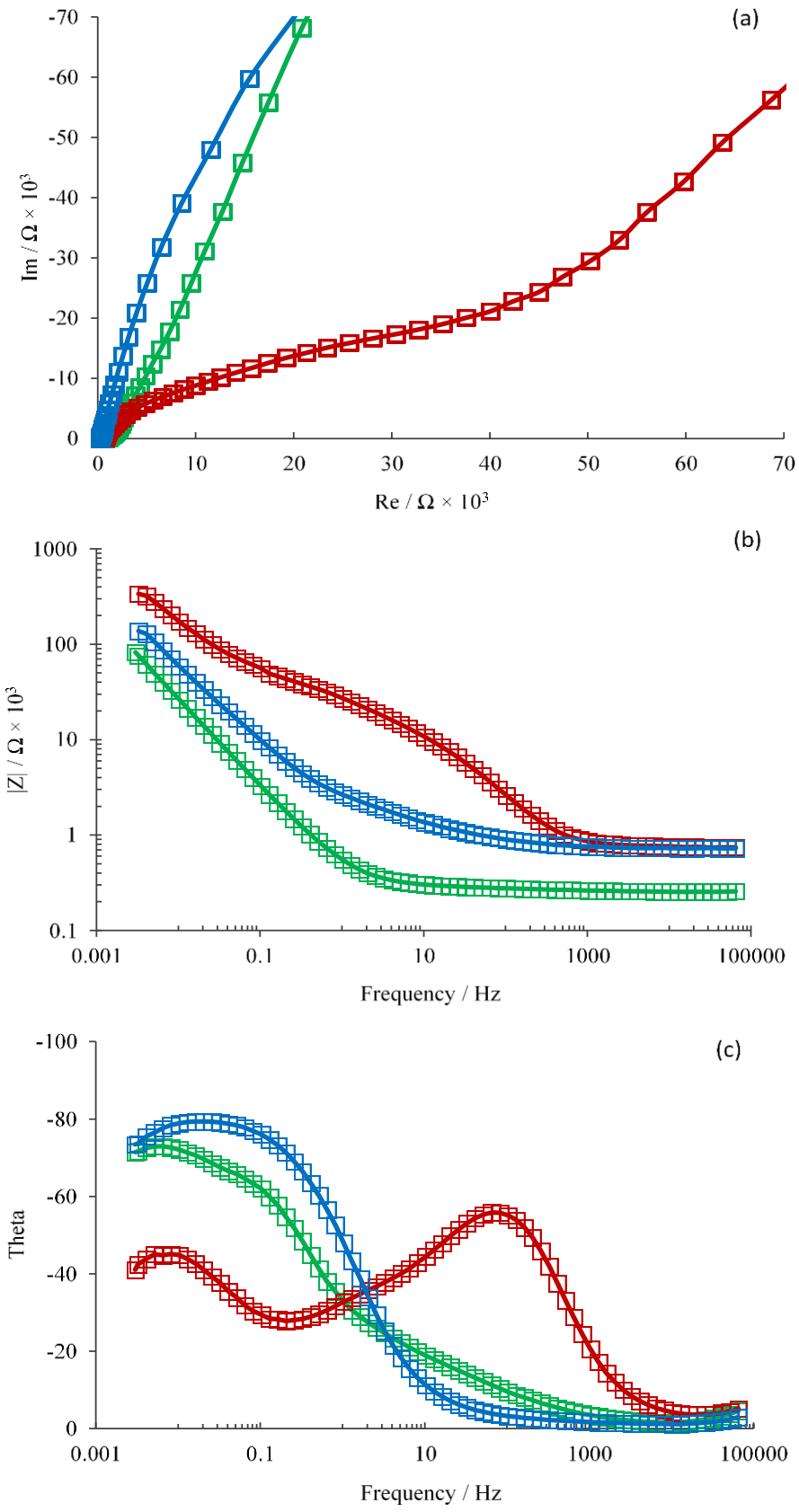

Figure 3.58: (a) Complex Plane (Nyquist) plot, **(b)** and **(c)** Bode plots recorded in 0.10 M PBS solution (pH 7.4) at 0.2 V vs. SCE of the 1.0 M H_2SO_4 pre-treated — fMWCNT-$Au_{nano}(NaBH_4)$ composite film — the 24 h fMWCNT film and — a GC electrode

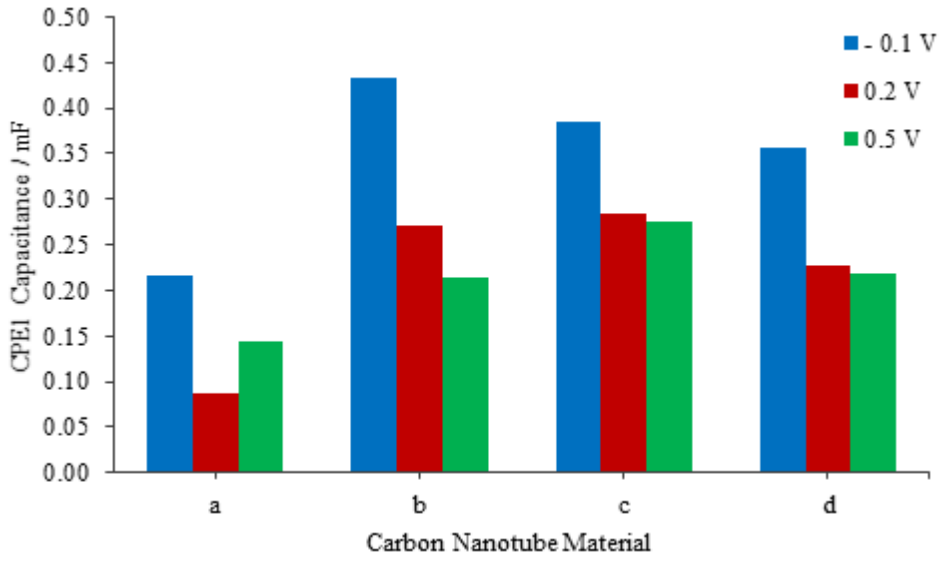

Figure 3.59: Plots of the CPE1 capacitance values obtained at potentials of -0.1 V, 0.2 V and 0.5 V vs. SCE for the composites produced with $NaBH_4$. **(a)** displays the 24 h fMWCNT film with 1.0 M H_2SO_4 pre-treatment and **(b), (c)** and **(d)** display the fMWCNT-$Au_{nano}(NaBH_4)$ composite film with no H_2SO_4 pre-treatment**,** 0.5 M H_2SO_4 pre-treatment and 1.0 M H_2SO_4 pre-treatment, respectively.

Capacitance values were obtained from the C1 components in the circuit and these are displayed in Figure 3.60. As mentioned, these capacitance values may correspond more so to the capacitance of the material and not to the electrochemical double layer at the solution-film interface. From these data, it appears that the capacitance of the composite materials increases when the H_2SO_4 pre-treatments are used. Also, it can be seen that the films containing the AuNPs have a higher capacitance. Furthermore, the capacitance is higher at –0.1 V vs. SCE. This characteristic was also evident in the voltammetry data recorded for these materials, Section 3.25. The corresponding charge-transfer resistance values R1 are displayed in Figure 3.61, and these correspond well with the capacitance values, with a decrease in the resistance when AuNPs are present. Also, it is clear that the H_2SO_4 pre-treatments greatly decrease the resistance values.

As the surface areas of the films change depending on the pre-treatments, discussed in Section 3.2.9.10, these changes in the capacitance and resistance may correspond to the changes in the films surfaces areas. It is well known that the magnitude of the

capacitance and the resistance depends on the materials surface area [84]. Consequently, the EIS results may better correlate with the changes in surface area and not specifically the electronic nature of the films. For an accurate comparison of the EIS data, the total surface area of the materials must be taken into consideration during data analysis but these were not available.

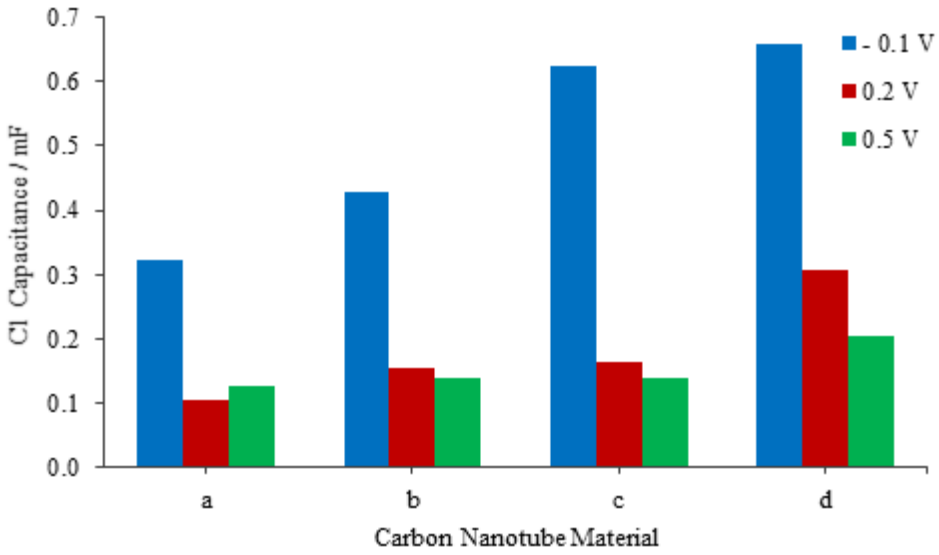

Figure 3.60: Plots of the C1 capacitance values obtained at potentials of -0.1 V, 0.2 V and 0.5 V vs. SCE for the composites produced with $NaBH_4$. **(a)** displays the 24 h fMWCNT film with 1.0 M H_2SO_4 pre-treatment and **(b), (c)** and **(d)** display the fMWCNT-$Au_{nano}(NaBH_4)$ composite film with no H_2SO_4 pre-treatment**,** 0.5 M H_2SO_4 pre-treatment and 1.0 M H_2SO_4 pre-treatment, respectively.

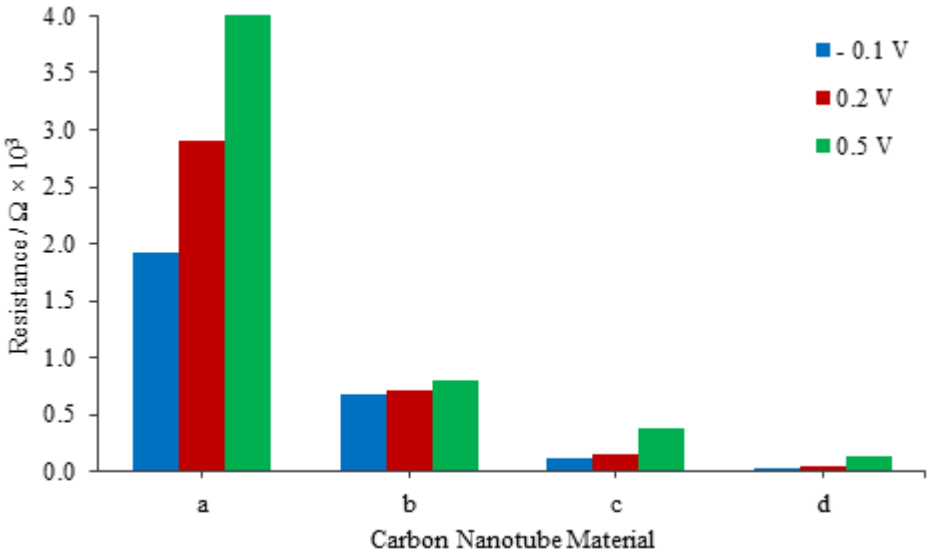

Figure 3.61: Plots of the R1 resistance values obtained at potentials of -0.1 V, 0.2 V and 0.5 V vs. SCE for the composites produced with $NaBH_4$. **(a)** displays the 24 h fMWCNT film with 1.0 M H_2SO_4 pre-treatment and **(b), (c)** and **(d)** display the fMWCNT-$Au_{nano}(NaBH_4)$ composite film with no H_2SO_4 pre-treatment**,** 0.5 M H_2SO_4 pre-treatment and 1.0 M H_2SO_4 pre-treatment, respectively.

The impedance response of the fMWCNT-Au_{nano}(TriSodCit) composite films was also measured using a similar approach. Typical complex-plane impedance plots and Bode plots recorded for the optimised fMWCNT-Au_{nano}(TriSodCit) composite film, the 1.0 M H_2SO_4 pre-treated 24 h fMWCNT film and a GC electrode are shown in Figure 3.62, while the corresponding plots of CPE1, C1 and R1 are presented in Figures 3.63, 3.64, and 3.65. Again, it is clear that the impedance response of the GC electrode is considerably different to the composites, while the impedance of the fMWCNT-Au_{nano}(TriSodCit) composite film and the 24 h fMWCNT film is similar. As shown in Figure 3.63, the CPE1 values are plotted as a function of the applied potential. The capacitance seems to increase slightly with the materials containing the AuNPs. The CPE1 values do not seem to be as dependent on the applied potential for the 24 h fMWCNT-Au_{nano}(TriSodCit) composite films pre-treated in 0.5 and 1.0 M H_2SO_4 and are somewhat higher at -0.1 V vs. SCE for the 24 h fMWCNT film and the fMWCNT-Au_{nano}(TriSodCit) with no acid pre-treatment.

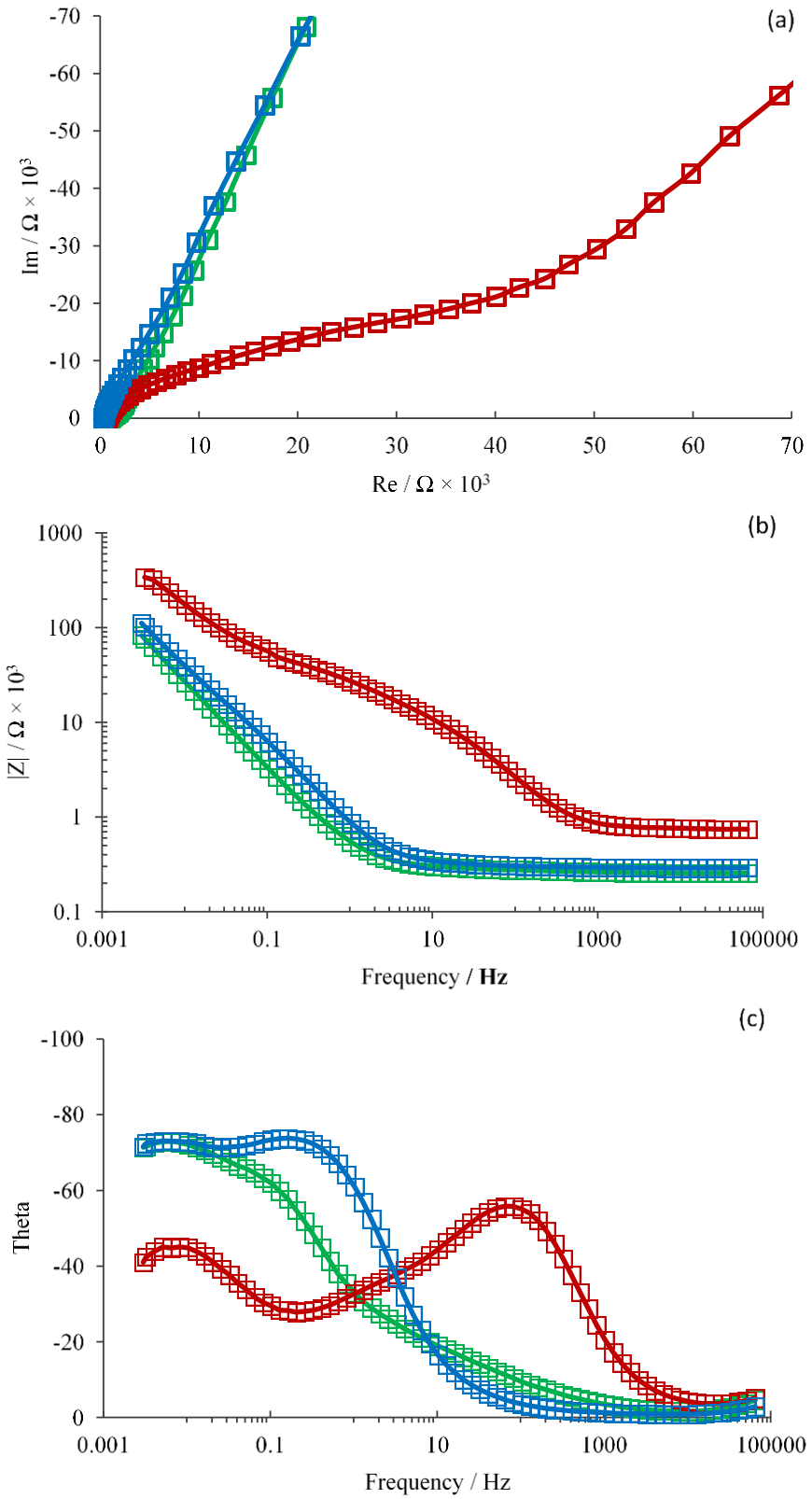

Figure 3.62: (a) Complex Plane (Nyquist) plot, **(b)** and **(c)** Bode plots recorded in 0.10 M PBS solution (pH 7.4) at 0.2 V vs. SCE of the 1.0 M H_2SO_4 pre-treated — fMWCNT-Au_{nano}(TriSodCit) composite film — the 24 h fMWCNT film and — a GC electrode

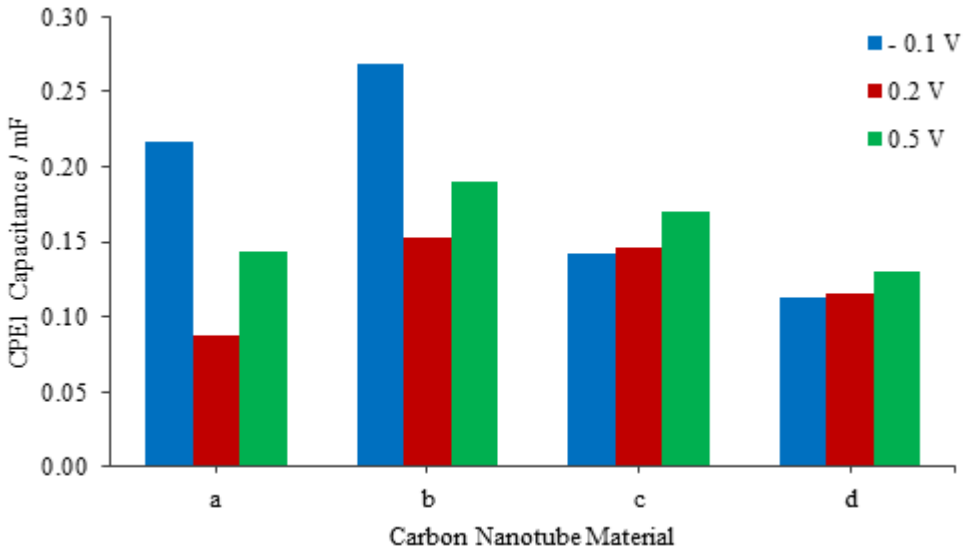

Figure 3.63: Plots of the CPE1 capacitance values obtained at potentials of -0.1 V, 0.2 V and 0.5 V vs. SCE for the composites produced with TriSodCit. **(a)** displays the 24 h fMWCNT film with 1.0 M H_2SO_4 pre-treatment and **(b), (c)** and **(d)** display the fMWCNT-Au_{nano}(TriSodCit) composite film with no H_2SO_4 pre-treatment**,** 0.5 M H_2SO_4 pre-treatment and 1.0 M H_2SO_4 pre-treatment, respectively.

The C1 values are shown in Figure 3.64 plotted as a function of the applied potential. Higher capacitance values are obtained at -0.1 V vs. SCE and the capacitance is higher for the fMWCNT-Au_{nano}(TriSodCit) composite films pre-treated in 0.5 M and 1.0 M H_2SO_4. Again, the 1.0 M H_2SO_4 cycling provides a material with the largest capacitance, which is in good agreement with the results recorded using the fMWCNT-Au_{nano}($NaBH_4$) composite films, Figure 3.60. The resistance values, R1, plotted for the different materials as a function of the applied potential are shown in Figure 3.65. The resistance decreases upon acid cycling. This was also observed with the films produced using the previous composite, shown in Figure 3.61, in which the optimised film resulted in a lower resistance value. However, as the surface area of the films are different this may result in inaccurate comparisons.

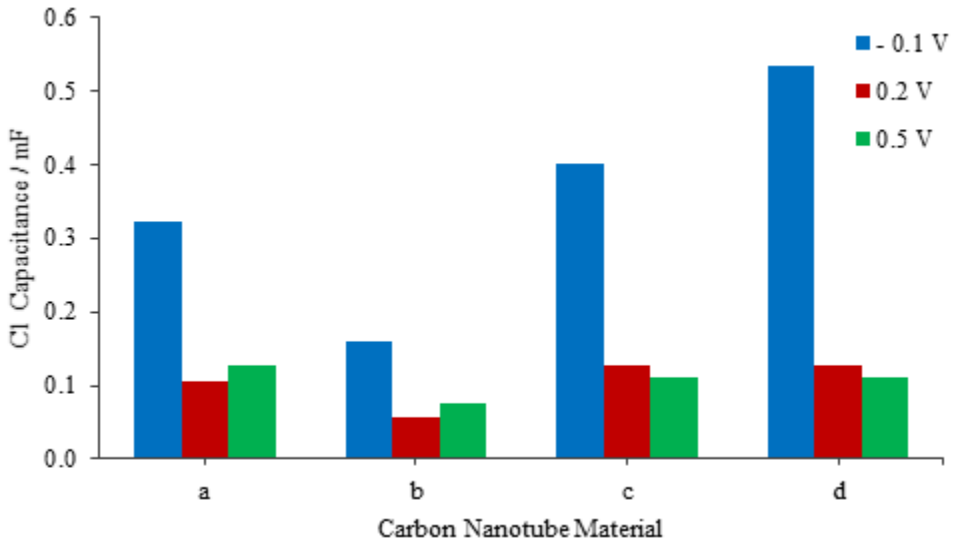

Figure 3.64: Plots of the C1 capacitance values obtained at potentials of -0.1 V, 0.2 V and 0.5 V vs. SCE for the composites produced with TriSodCit. **(a)** displays the 24 h fMWCNT film with 1.0 M H_2SO_4 pre-treatment and **(b), (c)** and **(d)** display the fMWCNT-Au_{nano}(TriSodCit) composite film with no H_2SO_4 pre-treatment**,** 0.5 M H_2SO_4 pre-treatment and 1.0 M H_2SO_4 pre-treatment, respectively.

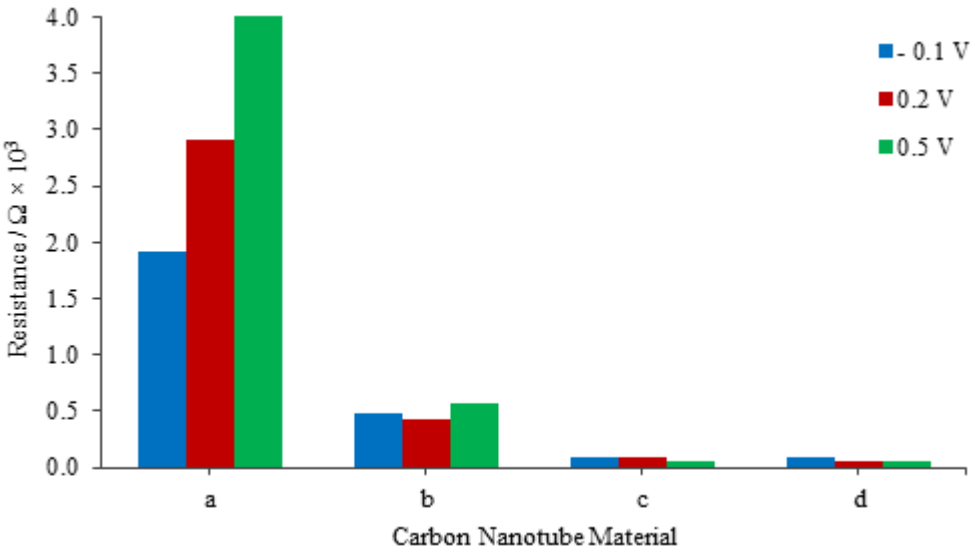

Figure 3.65: Plots of the R1 resistance values obtained at potentials of -0.1 V, 0.2 V and 0.5 V vs. SCE for the composites produced with TriSodCit. **(a)** displays the 24 h fMWCNT film with 1.0 M H_2SO_4 pre-treatment and **(b), (c)** and **(d)** display the fMWCNT-Au_{nano}(TriSodCit) composite film with no H_2SO_4 pre-treatment**,** 0.5 M H_2SO_4 pre-treatment and 1.0 M H_2SO_4 pre-treatment, respectively.

As a control, EIS experiments were carried out on a polished GC electrode (d = 3 mm) as all the composite films used in this study were cast onto the GC electrodes. The impedance data of the GC electrode were modelled using the two-time constant circuit model shown in Figure 3.66 (a), with a CPE component in place of the previously used C1 component, Figure 3.57. The exponent values of the CPE2 were not close to 1.0 and it cannot be considered a capacitor. Plots of CPE1 and CPE2, and the corresponding exponent values obtained for CPE1 and CPE2, are shown in Figure 3.66. The resistance values are presented in Figure 3.67. These results are very different to that observed with the composite materials and it is clear that the acid pre-treatments have no influence on the magnitude of CPE1 or CPE2, or the corresponding exponent values. Again, the resistance remains essentially constant following the acid pre-treatments. It can be concluded that the GC substrate remains stable and inert during the electrochemical processes and the data recorded for the composite materials reflect the properties of the composite films.

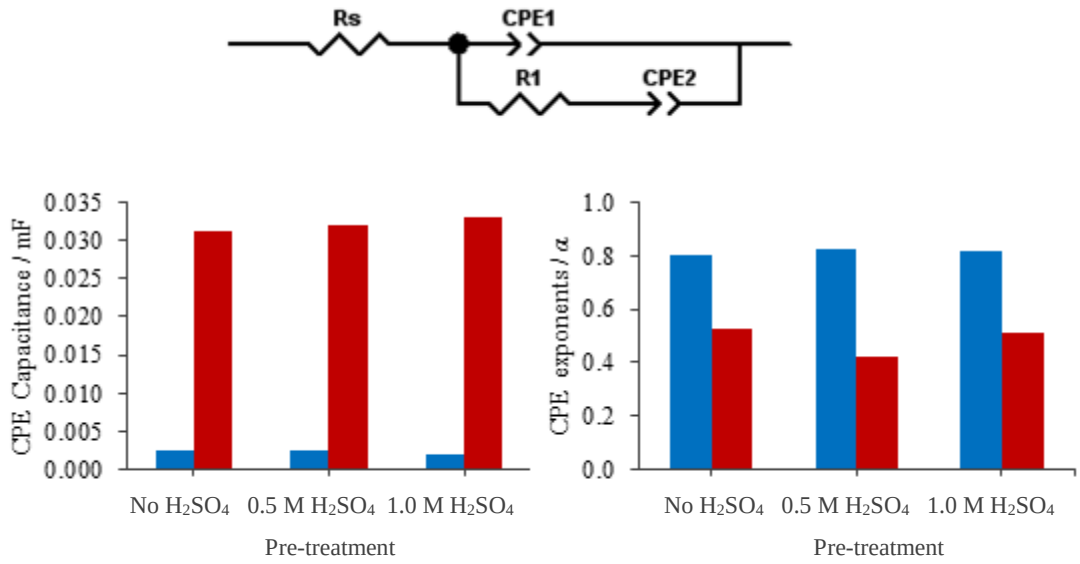

Figure 3.66: (a) Equivalent circuit used to fit the data of the GC electrode (d = 3 mm), **(b)** CPE1 (blue) and CPE2 (red) values of the GC electrodes recorded at 0.2 V vs. SCE in 0.10 M PBS with and without H_2SO_4 pre-treatments and **(c)** exponent values of the CPE1 (blue) and CPE2 (red) elements, for the GC electrode with and without H_2SO_4 pre-treatments.

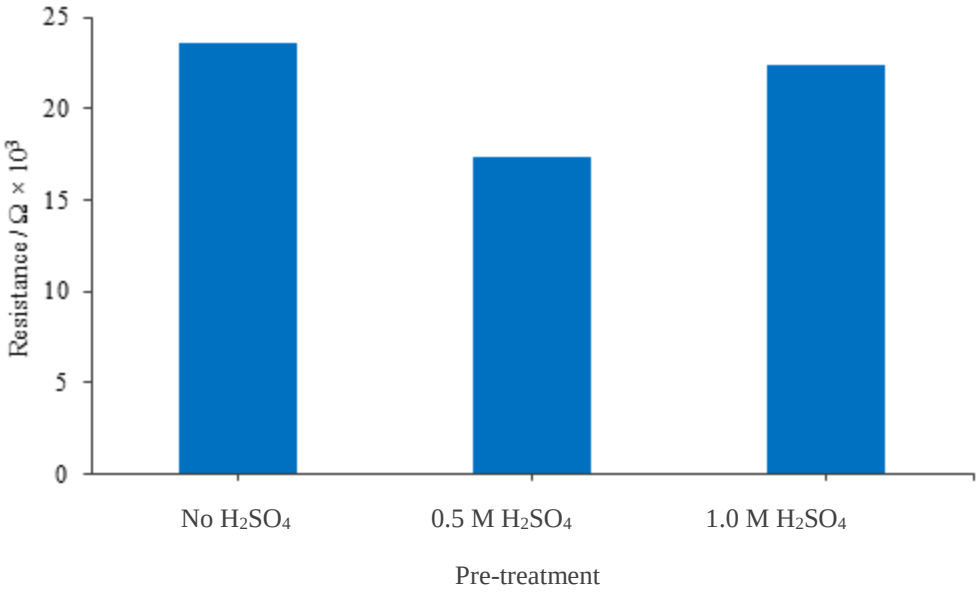

Figure 3.67: Plots of the resistance, R1, obtained at a potential of 0.2 V vs. SCE in a 0.10 M PBS solution (pH 7.4) for a polished GC electrode (d = 3 mm) with and without H_2SO_4 pre-treatments.

3.3 Summary of Results

In this chapter results are presented on the synthesis and characterisation of the pristine MWCNT-$Au_{nano}(NaBH_4)$, fMWCNT-$Au_{nano}(NaBH_4)$ and fMWCNT-Au_{nano} (TriSodCit) composites and their use as sensing films for the non-enzymatic detection of glucose. The AuNPs were synthetically reduced onto the surface of the carbon nanotubes using two different reducing agents, $NaBH_4$ and TriSodCit and through different synthesis conditions. It was found that the composites produced with the 24 h fMWCNTs resulted in more sensitive films towards glucose in comparison to those produced with the pristine MWCNTs. This was explained in terms of the increased solubility and dispersibility of the fMWCNTs in SDS during AuNP formation and also due to the increased loading of AuNPs onto the surface of the fMWCNTs. This enhanced solubility was due to the introduction of acidic surface groups during the HNO_3 acid reflux. Potentiometric titrations determined the acidic group coverage to be 6.0% for the 24 h fMWCNTs and 0.0% for the pristine MWCNTs. Using FT-IR spectroscopy, a C=O stretch was apparent for the fMWCNTs, consistent with the presence of carboxylic groups.

The sensors were produced by casting dispersions made in SDS solution onto GC and screen printed electrodes. It was found that cycling the films in NaOH helped to remove the adsorbed SDS from the films. Nafion® membranes were used to reduce interferences from negatively charged substances, including AA and UA, but it was found that they also reduced the sensitivity of the films towards glucose. Electrochemical pre-treatments using H_2SO_4 were utilised to help counteract this decrease in sensitivity and to optimise the performance of the sensors. These treatments were regarded as cleaning treatments and they greatly increased the sensitivity of the materials for glucose and also increased the surface areas of the films.

The materials were further characterised using microscopy and spectroscopy. SEM was not successful in identifying the presence of AuNPs but Au was detected in the corresponding EDX analysis. In an attempt to observe the AuNPs, TEM was used and their sizes were obtained. For the fMWCNT-$Au_{nano}(NaBH_4)$ composite, the AuNPs were under 10 nm, with a mode diameter of 7.5 nm and with a low size distribution. The fMWCNT-Au_{nano}(TriSodCit) composite contained AuNPs with mode diameters

of 23 and 24 nm and with a larger size distribution. UV-Vis also confirmed the presence of AuNPs with absorption bands in the mid 500 nm range.

Using TEM analysis the lattice fringes, representing interatomic Au spacings, were measured as 2.35 Å which corresponds to the (111) plane of Au. This was confirmed during XRD measurements. The (111) orientation was clearly identified and found to be present at the highest abundance in both composites and the interatomic spacings were measured as 2.35 Å. Using the data, the Scherrer equation was employed to estimate AuNP size. The calculated values were close to those obtained from TEM analyses.

To quantify the Au loading in the composite films, AAS analysis and EDX were used. For the AA analysis, the composites were digested in concentrated acids to remove the AuNPs from the nanotubes and the quantity of Au, in the form of $HAuCl_4$, was determined at 2.0% wt. for the fMWCNT-Au_{nano}($NaBH_4$) composite and at 1.0% wt. for the pristine MWCNT-Au_{nano}($NaBH_4$) composite. The fMWCNT-Au_{nano}(TriSodCit) composite had the highest amount of Au at 5.0% wt. These results compared well with the EDX analysis.

Raman spectroscopy was used to identify the presence of surface defects and surface acidic groups on the nanotubes. The G, D and D' bands were evident, and these correspond to the graphitic rings in the nanotubes and the introduced defects, respectively. It was evident that the D bands increased in intensity relative to the G-band with the 24 h fMWCNTs, in comparison to that of the pristine MWCNTs. This increase was significant at about 30%. With the pristine MWCNTs, a large D-band was still present which indicates a degree of surface defects, however these were not observed in the titration or FT-IR results. A SERs effect was observed with both the MWCNT-Au_{nano}($NaBH_4$) and fMWCNT-Au_{nano}($NaBH_4$) composites due to the presence of the AuNPs.

Since the films produced with these materials were optimised with H_2SO_4 pre-treatments, a scan rate analysis was used with ferrocyanide as an electrochemical probe as to estimate the total ESAs of these films. It was found that TLD was occurring at the films and as such ESAs could not be calculated using this method.

However useful information was obtained by measuring the redox separations of ferrocyanide, ΔE. Estimations of the collective Au ESAs of each film could be calculated by cycling in sulfuric acid. EIS was used to measure the changes in the capacitance and resistance at the films and it was assumed that these changes may be associated with the films surface areas.

Overall, AuNP-carbon nanotube composites were successfully produced using different reducing agents, with crystalline AuNPs of different sizes and in different amounts. These materials proved useful in non-enzymatic sensing films for glucose and have been combined with Nafion® membranes which may provide improved selectivity.

3.4 References

1. H. Zhu, X. Lu, M. Li, Y. Shao and Z. Zhu, *Talanta*, 2009, **79**, 1446-1453.
2. C.-W. Kung, C.-Y. Lin, Y.-H. Lai, R. Vittal and K.-C. Ho, *Biosensors and Bioelectronics*, 2011, **27**, 125-131.
3. G. Chang, H. Shu, K. Ji, M. Oyama, X. Liu and Y. He, *Applied Surfice Science*, 2014, **288**, 524-529.
4. Y. Li, Y.-Y. Song, C. Yang and X.-H. Xia, *Electrochemistry Communications*, 2007, **9**, 981-988.
5. H. Qiu and X. Huang, *Journal of Electroanalytical Chemistry*, 2010, **643**, 39- 45.
6. L. Y. Chen, X. Y. Lang, T. Fujita and M. W. Chen, *Scripta Materialia*, 2011, **65**, 17-20.
7. M. Pasta, F. La Mantia and Y. Cui, *Electrochimica Acta*, 2010, **55**, 5561-5568.
8. L. D. Burke, G. M. Bruton and J. A. Collins, *Electrochimica Acta*, 1998, **44**, 1467-1479.
9. X. Kang, Z. Mai, X. Zou, P. Cai and J. Mo, *Analytical Biochemistry*, 2007, **363**, 143-150.
10. J.-S. Ye, Y. Wen, W. De Zhang, L. Ming Gan, G. Q. Xu and F.-S. Sheu, *Electrochemistry Communications*, 2004, **6**, 66-70.
11. S. Vashist, *Diagnostics*, 2013, **3**, 385-412.
12. H. Sharma, D. C. Agarwal, A. K. Shukla, D. K. Avasthi and V. D. Vankar, *Journal of Raman Spectroscopy*, 2013, **44**, 12-20.
13. C. Muratore, A. N. Reed, J. E. Bultman, S. Ganguli, B. A. Cola and A. A. Voevodin, *Carbon*, 2013, **57**, 274-281.
14. H. Murphy, P. Papakonstantinou and T. I. T. Okpalugo, *Journal of vacuum science & technology. B, Microelectronics and nanometer structures: processing, measurement, and phenomena*, 2006, **24**, 715-720.
15. C. Liao, M. Zhang, L. Niu, Z. Zheng and F. Yan, *Journal of Materials Chemistry B*, 2013, **1**, 3820-3829.
16. F. G. Banica, *Chemical Sensors and Biosensors: Fundamentals and Applications*, John Wiley & Sons, Chichester, West Sussex, 2012.
17. L. M. Fischer, M. Tenje, A. R. Heiskanen, N. Masuda, J. Castillo, A. Bentien, J. Emneus, M. H. Jakobsen and A. Boisen, *Microelectronic Engineering*, 2009, **86**, 1282-1285.
18. D. R. Thevenot, K. Tóth, R. A. Durst and G. S. Wilson, in *Pure and Applied Chemistry*, 1999, vol. 71, pp. 2333 - 2348.
19. O. V. Kharissova, B. I. Kharisov and C. O. E. G. de, *RSC Advances*, 2013, **3**, 24812-24852.
20. V. Datsyuk, M. Kalyva, K. Papagelis, J. Parthenios, D. Tasis, A. Siokou, I. Kallitsis and C. Galiotis, *Carbon*, 2008, **46**, 833-840.

21. N. M. Vesali, A. A. Khodadadi, Y. Mortazavi, S. O. Alizadeh, F. Pourfayaz and S. S. Mosadegh, *International Journal of Chemical and Biological Engineering*, 2009, **2**, 66-68.
22. Z. Wang, M. D. Shirley, S. T. Meikle, R. L. D. Whitby and S. V. Mikhalovsky, *Carbon*, 2009, **47**, 73-79.
23. W. H. Duan, Q. Wang and F. Collins, *Chemical Science*, 2011, **2**, 1407-1413.
24. J. L. Figueiredo, M. F. R. Pereira, M. M. A. Freitas and J. J. M. Órfão, *Carbon*, 1999, **37**, 1379-1389.
25. J. L. Figueiredo and M. F. R. Pereira, *Catalysis Today*, 2010, **150**, 2-7.
26. Y. S. Kim, S. J. Yang, S. W. Kim, H. J. Lim, T. Kim and C. R. Park, presented in part at the 18th International Conference on Composite Materials, 2011.
27. C. Samorì, R. Sainz, C. Ménard-Moyon, F. M. Toma, E. Venturelli, P. Singh, M. Ballestri, M. Prato and A. Bianco, *Carbon*, 2010, **48**, 2447-2454.
28. S. Hanelt, G. Orts-Gil, J. F. Friedrich and A. Meyer-Plath, *Carbon*, 2011, **49**, 2978-2988.
29. A. Chu, J. Cook, R. J. R. Heesom, J. L. Hutchison, M. L. H. Green and J. Sloan, *Chemistry of Materials*, 1996, **8**, 2751-2754.
30. B. Kim and W. M. Sigmund, *Langmuir*, 2004, **20**, 8239-8242.
31. A. E. Shanahan, J. A. Sullivan, M. McNamara and H. J. Byrne, *Xinxing Tan Cailiao*, 2011, **26**, 347-355.
32. S. Lou, J.-y. Ye, K.-q. Li and A. Wu, *Analyst*, 2012, **137**, 1174-1181.
33. J. W. H. De, M. C. Burger, M. A. Verheijen and R. E. Geertsma, *Materials*, 2010, **3**, 4681-4694.
34. D. B. Williams and C. B. Carter, *Transmission Electron Microscopy: A Textbook for Materials Science*, Springer, 2009.
35. R. Divakar and V. S. Raghunathan, *Sadhana*, 2003, **28**, 47-62.
36. A. Amiri, M. Maghrebi, M. Baniadam and S. Zeinali Heris, *Applied Surface Science*, 2011, **257**, 10261-10266.
37. H. Khani and O. Moradi, *Journal Of Nanostructure in Chemistry*, 2013, **3**.
38. W. Vielstich, H. Yokokawa and H. A. Gasteiger, *Handbook of fuel cells: fundamentals technology and applications. Advances in electrocatalysis, materials, diagnostics and durability*, John Wiley & Sons, Chichester, West Sussex, 2009.
39. R. Sreeja, P. M. Aneesh, K. Hasna and M. K. Jayaraj, *Journal of the Electrochemical Society*, 2011, **158**, K187-K191.
40. S. Li, X. Yu, G. Zhang, Y. Ma, J. Yao, B. Keita, N. Louis and H. Zhao, *Journal of Materials Chemistry*, 2011, **21**, 2282-2287.
41. X. Lv and J. Weng, *Scientific Reports*, 2013, **3**, 3285.
42. M. C. Scott, C.-C. Chen, M. Mecklenburg, C. Zhu, R. Xu, P. Ercius, U. Dahmen, B. C. Regan and J. Miao, *Nature (London, U. K.)*, 2012, **483**, 444- 447.
43. Z. Wang, Q. Zhang, D. Kuehner, A. Ivaska and L. Niu, *Green Chemistry*, 2008, **10**, 907-909.

44. H. Kang, Y. Zhu, X. Yang, J. Shen, C. Chen and C. Li, *New Journal of Chemistry*, 2010, **34**, 2166-2175.
45. N. Kasai and M. Kakudo, *X-Ray Diffraction by Macromolecules*, 2005.
46. X. Hou, L. Wang, X. Wang and Z. Li, *Diamond and Related Materials*, 2011, **20**, 1329-1332.
47. Y. Shi, R. Yang and P. K. Yuet, *Carbon*, 2009, **47**, 1146-1151.
48. G.-Z. Hu, L. Chen, Y. Guo, X.-L. Wang and S.-J. Shao, *Electrochimica Acta*, 2010, **55**, 4711-4716.
49. B. D. Cullity, *Elements Of X Ray Diffraction*, Addison-Wesley, 1956.
50. X. Cheng, J. Zhong and J. Meng, *Journal of Nanomaterials*, 2011, **2011**, 406087.
51. R. Zhang and X. Wang, *Chemistry of Materials*, 2007, **19**, 976-978.
52. M. M. Rabbani, C. H. Ko, J.-S. Bae, J. H. Yeum, I. S. Kim and W. Oh, *Colloids and Surfaces A: Physicochemical and Engineering Aspects*, 2009, **336**, 183- 186.
53. G. A. Rance, D. H. Marsh, R. J. Nicholas and A. N. Khlobystov, *Chemical Physics Letters*, 2010, **493**, 19-23.
54. M. Murawska, A. Skrzypczak and M. Kozak, *Acta Physica Polonica A*, 2012, **121**, 888-892.
55. B. P. Vinayan, R. Nagar, V. Raman, N. Rajalakshmi, K. S. Dhathathreyan and S. Ramaprabhu, *Journal of Materials Chemistry*, 2012, **22**, 9949-9956.
56. R. Yudianti, H. Onggo, Sudirman, Y. Saito, T. Iwata and J.-i. Azuma, *The Open Materials Science Journal*, 2011, **5**, 242-247.
57. H.-C. Kuan, C.-C. M. Ma, W.-P. Chang, S.-M. Yuen, H.-H. Wu and T.-M. Lee, *Composites Science and Technology*, 2005, **65**, 1703-1710.
58. I. D. Rosca, F. Watari, M. Uo and T. Akasaka, *Carbon*, 2005, **43**, 3124-3131.
59. J.-M. Yeh, K.-Y. Huang, S.-Y. Lin, Y.-Y. Wu, C.-C. Huang and S.-J. Liou, *Journal of Nanotechnology*, 2009, Article ID 217469.
60. A. I. Lopez-Lorente, B. M. Simonet, M. Valcarcel and B. Mizaikoff, *Analytica Chimica Acta*, 2013, **788**, 122-128.
61. T. Assmus, K. Balasubramanian, M. Burghard, K. Kern, M. Scolari, N. Fu, A. Myalitsin and A. Mews, *Applied Physics Letters*, 2007, **90**, 173109/173101.
62. D. Salinas-Torres, F. Huerta, F. Montilla and E. Morallón, *Electrochimica Acta*, 2011, **56**, 2464-2470.
63. F. G. Thomas and G. Henze, *Introduction to Voltammetric Analysis: Theory and Practice*, CSIRO Publishing 2001.
64. I. Svancara, K. Kalcher, A. Walcarius and K. Vytras, *Electroanalysis with Carbon Paste Electrodes*, CRC Press, 2012.
65. T. Ndlovu, O. A. Arotiba, S. Sampath, R. W. Krause and B. B. Mamba, *International Journal of Electrochemical Science*, 2012, **7**, 9441-9453.
66. A. Morrin, A. J. Killard and M. R. Smyth, *Analytical Letters*, 2003, **36**, 2021- 2039.
67. A. J. Bard and L. R. Faulkner, *Electrochemical Methods: Fundamentals and Applications*, John Wiley & Sons, New York, 2001.

68. M. Lu, F. Beguin and E. Frackowiak, *Supercapacitors: Materials, Systems and Applications*, Wiley-VCH Verlag GmbH & Co. KGaA, Weinheim, Germany, 2013.
69. G. P. Keeley and M. E. G. Lyons, *International Journal of Electrochemical Science*, 2009, **4**, 794 - 809
70. M. J. Sims, N. V. Rees, E. J. F. Dickinson and R. G. Compton, *Sensors and Actuators B: Chemical*, 2010, **144**, 153-158.
71. M. Gara and R. G. Compton, *New Journal of Chemistry*, 2011, **35**, 2647-2652.
72. M. C. Henstridge, E. J. F. Dickinson, M. Aslanoglu, C. Batchelor-McAuley and R. G. Compton, *Sensors and Actuators B: Chemical*, 2010, **145**, 417-427.
73. L. Xiao, G. G. Wildgoose and R. G. Compton, *Sensors and Actuators B: Chemical*, 2009, **138**, 524-531.
74. I. Streeter, G. G. Wildgoose, L. Shao and R. G. Compton, *Sensors and Actuators B: Chemical*, 2008, **133**, 462-466.
75. S. A. Wring and J. P. Hart, *Analyst (London)*, 1992, **117**, 1215-1229.
76. H. S. Nalwa, *Handbook of Surfaces and Interfaces of Materials, Five-Volume Set*, Academic Press, 2001.
77. P. Ramesh and S. Sampath, *Analytical Chemistry*, 2003, **75**, 6949-6957.
78. Y.-G. Guo, H.-M. Zhang, J.-S. Hu, L.-J. Wan and C.-L. Bai, *Thin Solid Films*, 2005, **484**, 341-345.
79. M. M. Collinson, *ISRN Analytical Chemistry*, 2013, 692484, 692421 pp.
80. X. Xiao, H. Li, M. e. Wang, K. Zhang and P. Si, *Analyst*, 2013.
81. V. F. Lvovich, *Impedance Spectroscopy: Applications to Electrochemical and Dielectric Phenomena*, John Wiley & Sons, New Jersey, 2012.
82. E. Barsouko and J. R. Mac Donald, *Impedance Spectroscopy: Theory, Experiment, and Applications*, John Wiley & Sons, New York, 2005.
83. A. Ramanavicius, A. Finkelsteinas, H. Cesiulis and A. Ramanaviciene, *Bioelectrochemistry*, 2010, **79**, 11-16.
84. M. Taketani and M. Baudry, *Advances in Network Electrophysiology: Using Multi-Electrode Arrays*, Springer, 2006.

Chapter 4

Gold Nanoparticle-Multiwalled Carbon Nanotube Composite Films Modified with Palladium Nanoparticles for Non-Enzymatic Glucose Sensing

4.1 Introduction

In this chapter results are presented and discussed for the detection of glucose at palladium (Pd) modified composite films (fMWCNT-Au_{nano}/Pd_{nano}). Films were initially produced glassy carbon (GC) electrodes and were then miniaturised on screen-printed electrodes (SPEs). The Pd nanoparticles (PdNPs) were electrodeposited onto the pre-existing fMWCNT-Au_{nano} films which were produced using the fMWCNT-Au_{nano}($NaBH_4$) composite discussed in Chapter 3. Glucose detection was carried out initially using cyclic voltammetry (CV), followed by constant potential amperometry (CPA) and detection of glucose at more negative potentials was possible, which can be beneficial for selectivity. In the latter sections of this chapter, characterisation studies are presented to identify the various physical and electrochemical properties of these composite films.

The fMWCNT-Au_{nano} films were modified with Pd as this metal and its alloys can facilitate the non-enzymatic detection of glucose. Also, it can be easily electrodeposited and has stability and electrochemistry. The fMWCNT-Au_{nano} films were also modified with other metals, including copper, silver, tin, zinc and iron, although these bimetallic systems did not enable or improve glucose detection. These studies are not included in the following chapter.

4.2 Results and Discussion

4.2.1 Detection of Glucose at fMWCNT-Au_{nano}/Pd_{nano} Composite Films

These fMWCNT-Au_{nano}/Pd_{nano} composite modified GC and SPEs were produced by electrodepositing palladium (Pd) onto the surfaces of pre-existing fMWCNT-Au_{nano} modified GC (d = 3 mm) and SPE electrodes (d = 4 mm). In all cases the fMWCNT-Au_{nano} modified GC electrode and SPEs were produced using the procedures outlined in Chapter 2, Sections 2.2.6.1 and 2.2.6.2, respectively. As mentioned in Chapter 3, only the fMWCNT-Au_{nano}($NaBH_4$) composite, produced using the $NaBH_4$ reducing agent was used in the following work due to stability issues with the other fMWCNT-Au_{nano}(TriSodCit) composite, produced using trisodium citrate. It should be noted that in the following sections, that the abbreviated composite name, fMWCNT-Au_{nano}($NaBH_4$), has been shortened to 'fMWCNT-Au_{nano}' for clarity.

4.2.1.1 Detection of Glucose using CV at GC/fMWCNT-Au_{nano}/Pd_{nano} Composite Films

CV was employed initially to identify a suitable potential for Pd electrodeposition. The optimised fMWCNT-Au_{nano} composite modified GC electrode, formed from a 5.0 µl drop cast of a 4.0 mg/ml dispersion in SDS, was cycled in a solution of 2.5 mM $PdSO_4$ made in a 0.5 M H_2SO_4 electrolyte using CV. A reduction wave for the Pd metal is visible in the resulting CV in the reverse scan from 0.80 V to 0.45 V vs. SCE, shown in Figure 4.1. The standard electrode potential for the reduction of Pd(11), as shown in Equation 4.1, in an aqueous solution is 0.915 V vs. NHE [1]. This can be converted to 0.671 vs. SCE, which is in good agreement with the reduction potential observed.

$$Pd(II)_{(aq)} + 2^{e-} \rightleftharpoons Pd_{(s)} \qquad 4.1$$

From the position of this reduction peak, a suitable potential can be chosen for use in a potentiostatic Pd electrodeposition. It is clear that this peak is a result of the Pd as it does not occur in the CV obtained in 0.5 M H_2SO_4 without Pd salt. A suitable potential

of 0.45 V vs. SCE was then chosen for Pd electrodeposition using potentiometry. This was chosen due to its position just after the reduction wave which may be sufficient to deposit a maximum amount of Pd.

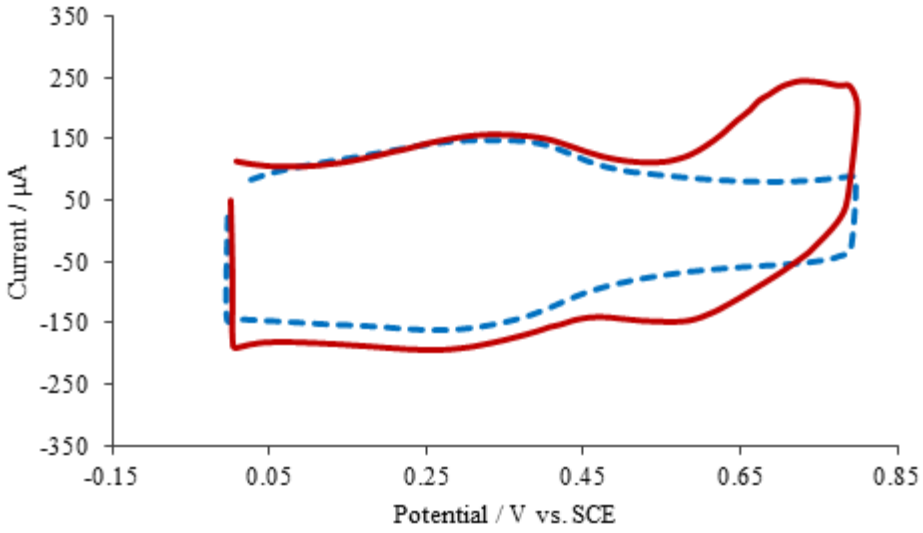

Figure 4.1: Cyclic voltammograms recorded at 100 mV s^{-1} of the fMWCNT-Au_{nano} modified GC electrode in a - - - 0.5 M H_2SO_4 solution and a — 0.5 M H_2SO_4 solution containing 2.5 mM $PdSO_4$.

The next step was to investigate the amount of Pd needed on the composite films for optimal glucose detection. This was accomplished by electrodepositing Pd directly on the prepared fMWCNT-Au_{nano} composite films at 0.45 V for various times of 60, 120, 180 and 240 s and the resulting films were then cycled firstly in a 0.1 M PBS solution and a PBS solution containing 10 mM glucose, as shown in Figures 4.2 (a), (b), (c) and (d). A potential window of -0.40 V to 0.60 V vs SCE was employed at 100 mV s^{-1}. It is evident in the voltammograms that the onset of glucose oxidation begins at a more negative potential at the fMWCNT-Au_{nano}/Pd_{nano} composite films, in comparison to the previous fMWCNT-Au_{nano} composite film produced on GC electrodes, in which oxidation began at around -0.10 V vs. SCE, as shown in Chapter 3, Section 2.5. It is also observed that the sensitivity of the composite film towards glucose is proportional to the amount of Pd present and that the current responses for glucose plateau at a certain loading of Pd. The composite film formed from Pd deposition for a period of 240 s provides the optimum sensitivity, with a peak current

of 7.26 × 10^{-5}A (72.60 µA) observed for 10 mM glucose at -0.25 V vs. SCE, Figure 4.2 (d). The composite film formed from Pd electrodeposition for 60 s yields a peak current of 2.10 × 10^{-5}A (21.07 µA) for glucose at -0.25 V vs. SCE. This corresponds to over a 200% increase in sensitivity.

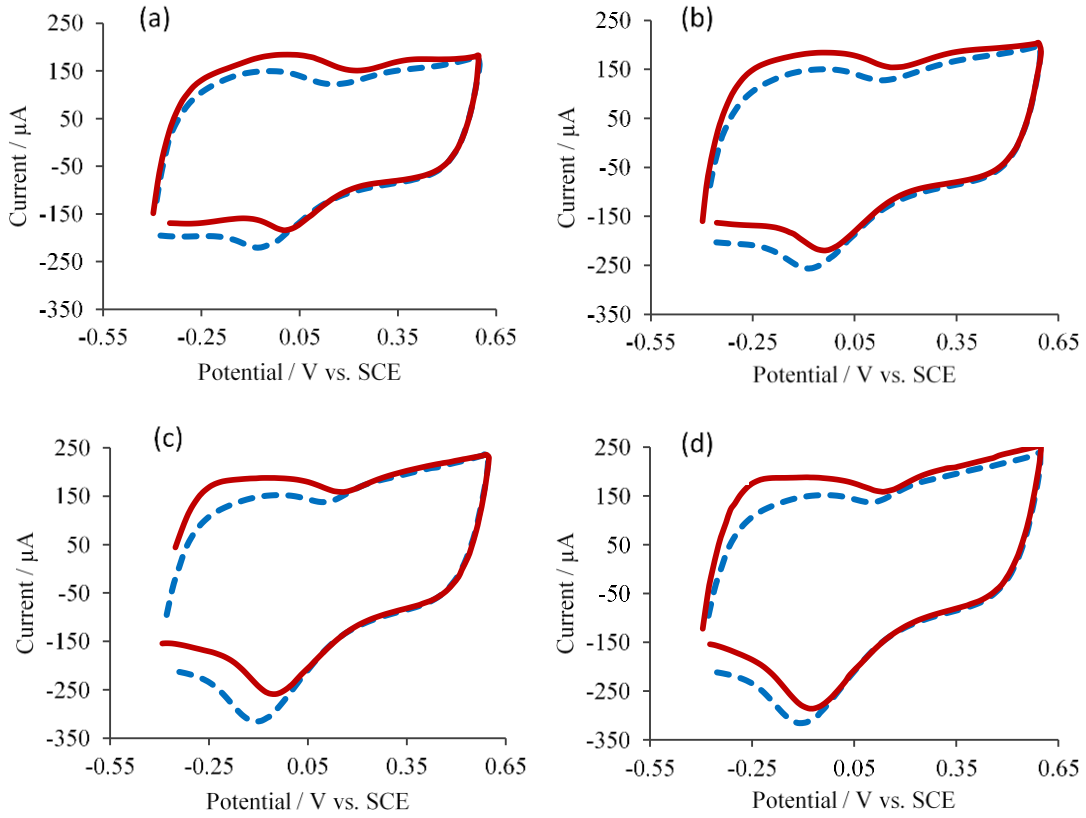

Figure 4.2: Cyclic voltammograms recorded at 100 mV s^{-1} of the fMWCNT-Au_{nano}/Pd_{nano} modified GC electrodes in a - - - 0.1 M PBS solution (pH 7.4) and a — 0.1 M PBS solution containing 10 mM glucose. Figures **(a)**, **(b)**, **(c)** and **(d)** show glucose detection at the fMWCNT-Au_{nano}/Pd_{nano} films formed from Pd electrodeposition at 0.45 V vs. SCE for 60, 120, 180 and 240 s, respectively.

Other than a shift in the glucose oxidation potential at this fMWCNT-Au_{nano}/Pd_{nano} film, relative to the fMWCNT-Au_{nano} films, an increase in sensitivity towards glucose is apparent during the forward scan. For comparison, glucose detection at the optimised fMWCNT-Au_{nano} and fMWCNT-Au_{nano}/Pd_{nano} films are shown in Figure 4.3. Using CV, it appears that the current responses for glucose have increased at the Pd modified composite film and an increase in the overall capacitance is seen, which

is possibly due to an increase in the surface area [2]. As mentioned previously, a peak current of 7.26×10^{-5}A (72.60 µA) is measured for 10 mM glucose at -0.25 V vs. SCE at the fMWCNT-Au_{nano}/Pd_{nano} modified GC electrode. That measured in the forward scan at 0.30 V vs. SCE at the fMWCNT-Au_{nano} modified GC electrode is 4.27×10^{-5}A (42.70 µA). This corresponds to a 70% increase in sensitivity. It was assumed that this shift in the oxidation potential and the improvements in sensitivity were related to the relationship between the AuNPs and PdNPs. Studies suggest that the formation of alloy and bimetallic systems can provide many beneficial properties in electrochemical sensors [3-9]. Previous studies have shown that the formation of Au, alloys and other bi-metallic materials can provide catalytic improvements at non-enzymatic glucose sensors, including increases in sensitivities [4, 6, 7], anti-interfering [4] and anti-poisoning capabilities [5]. It has also been observed that shifts in oxidation potentials can occur due to a change in the work functions of the bi-metallic systems, which occurs when the charge is transferred from one metal to the other in the inter-metallic bond [5, 10]. This change can shift the films potential of zero charge (pzc) towards the negative direction and thus can make the electrode surface more positively charged at more negative potentials [4, 6-8, 10]. This may favour the adsorption of hydrous oxide radicals $Au(OH)_{ads,}$ on the metal surface [6-10]. As discussed in Chapter 1, Section 1.4.6.2, the occurrence of OH_{ads} on Au is beneficial in non-enzymatic glucose sensors [6, 8, 11, 12]. This theory is supported in studies by Chen *et al.* using core shell Au-PdNPs combined with ionic liquids, in which it was determined that more positive films were formed due to differences in the Au and Pd work functions [4]. Work by Stamenkovic *et al.* determined that increased anion adsorption occurred at bi-metallic films composed of Pt and Sn [10]. This was ascribed to the lowering of the work function of the Pt by Sn and a shift in the pzc. Further work by Lomocso and Baranova involving Pt and Pd bi-metallic sensors determined that the use of bi-metallics decreased the onset potentials of analyte oxidation [5].

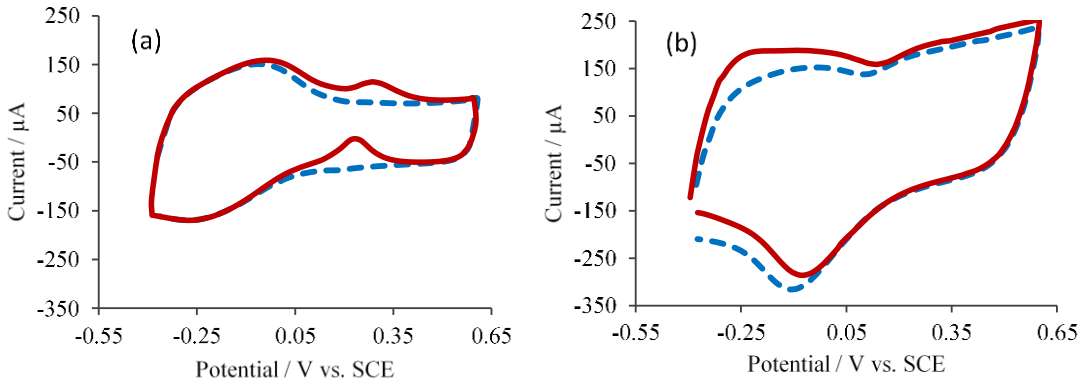

Figure 4.3: Cyclic voltammograms recorded at 100 mV s^{-1} of the **(a)** optimised fMWCNT-Au_{nano} and **(b)** fMWCNT-Au_{nano}/Pd_{nano} modified GC electrodes in a - - - 0.1 M PBS solution (pH 7.4) and a — 0.1 M PBS solution containing10 mM glucose.

4.2.1.2 Detection of Glucose using CV at GC/fMWCNT-Pd_{nano} Composite Films

To determine if the presence of Au was necessary in this new Pd composite, a control experiment was conducted whereby Pd was electrodeposited onto a fMWCNT film containing no Au. This film was produced using the same fMWCNT dispersion concentration, drop cast volume, electrochemical pre-treatments and using the same conditions for Pd electrodeposition. These films were then cycled firstly in PBS and in a PBS solution containing 10 mM glucose. As seen in Figures 4.4 (a), (b), (c) and (d), no measurable glucose responses are apparent at the Pd modified fMWCNT films containing varying amounts of Pd, even with the electrodeposition of Pd for 240 s. This indicates that the presence of Au in the composite was important and that the relationship between the AuNPs and PdNPs may facilitate the oxidation of glucose at the more negative potentials.

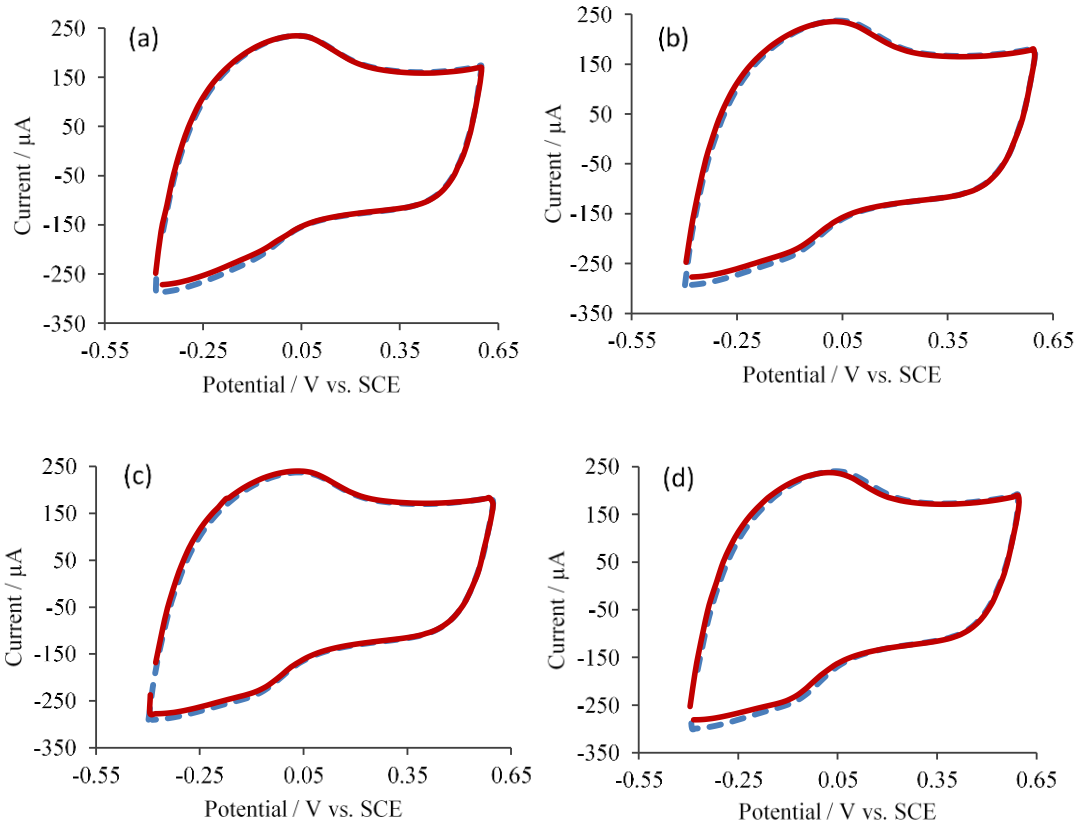

Figure 4.4: Cyclic voltammograms recorded at 100 mV s^{-1} of the fMWCNT-Pd_{nano} modified GC electrodes in a - - - 0.1 M PBS solution (pH 7.4) and a — 0.1 M PBS solution containing 10 mM glucose. Figures **(a)**, **(b)**, **(c)** and **(d)** show glucose detection at the fMWCNT-Pd_{nano} films formed from Pd electrodeposition at 0.45 V vs. SCE for 60, 120, 180 and 240 s, respectively.

Glucose detection using CV was also undertaken at a fMWCNT film for comparison with the optimised fMWCNT-Pd_{nano} film, Figure 4.5. No measurable response is apparent at the Pd modified film and at the fMWCNT film. These results indicate that the dual Au-Pd bimetallic system in the composite provided the enhanced results and as such this fMWCNT-Au_{nano}/Pd_{nano} composite film is utilised further.

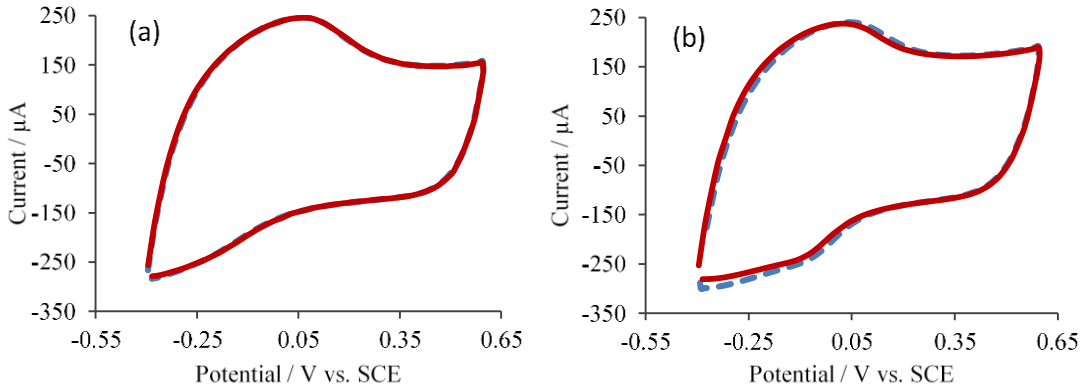

Figure 4.5: Cyclic voltammograms recorded at 100 mV s^{-1} of the **(a)** fMWCNT and **(b)** fMWCNT-Pd_{nano} modified GC electrodes in a - - - 0.1 M PBS solution (pH 7.4) and a — 0.1 M PBS solution containing10 mM glucose.

4.2.1.3 Detection of Glucose using CV at SPE/fMWCNT-Au_{nano}/Pd_{nano} Films

Since this system had now been optimised on the GC substrate, it was miniaturised using SPEs. Only the planar DRP-150 SPEs were used and not the macroporous DRP-110O SPEs as no improvements in sensitivity were seen with these electrodes in previous studies, discussed in Chapter 3, Section 3.2.8. The same Pd deposition process was carried out for the modified SPE electrodes, although the pre-existing fMWCNT-Au_{nano} composite films were formed using 10 µl of the fMWCNT-Au_{nano} composite dispersion in SDS, as discussed in Chapter 2, Section 2.2.6.2. To determine an ideal potential for Pd electrodeposition at this new system, CV experiments were carried out initially in a solution of 2.5 mM $PdSO_4$ made in 0.5 M H_2SO_4. Due to the use of the Ag/AgCl reference electrode, the potential range investigated was adapted to -0.40 to 0.60 V. A current increase in the reverse scan is observed for the reduction of Pd at the composite surface, as can be seen in Figure 4.6. This reduction peak appears quite broad in comparison to that of the reduction of Pd at the modified GC electrode, which may indicate that Pd can be deposited over a wider potential range. Nonetheless a suitable potential of -0.10 V vs. Ag/AgCl can be chosen for Pd electrodeposition and this provides similar results to the potential applied using the previous electrochemical system, Section 4.2.1.1. Also, a more negative potential may deposit more Pd and reduce deposition control.

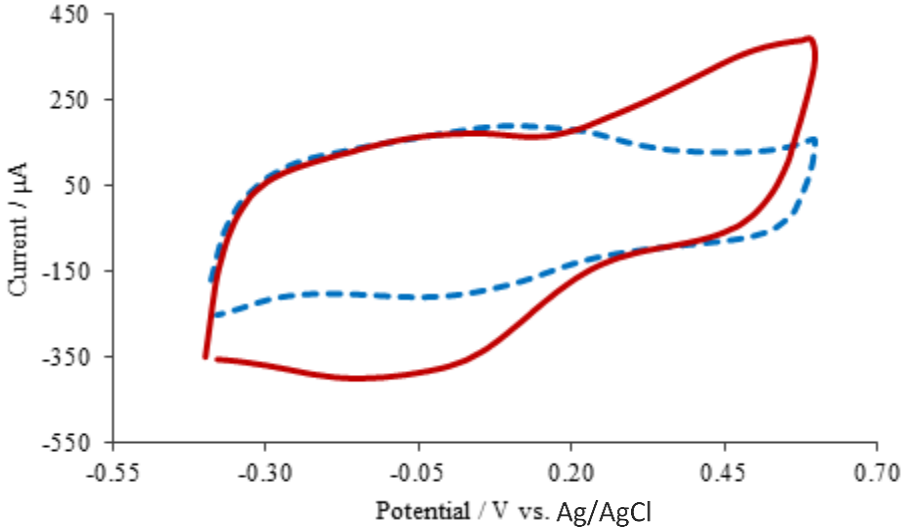

Figure 4.6: Cyclic voltammograms recorded at 100 mV s^{-1} of the fMWCNT-Au_{nano} modified SPE electrode in a - - - 0.5 M H_2SO_4 solution and a — 0.5 M H_2SO_4 containing 2.5 mM $PdSO_4$.

Pd electrodeposition at the fMWCNT-Au_{nano} modified SPE was again carried out for the same times of 60, 120, 180 and 240 s at -0.10 V vs. Ag/AgCl, as used in Section 4.2.1.1. Similar trends between Pd electrodeposition time and glucose detection can be observed at this system. The intensity of the current response for glucose oxidation is proportional to the amount of Pd present in the composite, with electrodeposition for 240 s providing the most sensitive film, as shown in Figure 4.7 (d). The peak current for 10 mM glucose at this optimised film, measured at -0.45 V vs. Ag/AgCl, is 9.58×10^{-5} A (95.85 µA). That measured at the fMWCNT-Au_{nano}/Pd_{nano} film formed from Pd deposition for 60 s results in a peak current of 3.76×10^{-5} A (37.67 µA), CV shown in Figure 4.7 (a). This corresponds to over a 150% increase in sensitivity.

As mentioned in the previous section, Section 4.2.1.1, the peak current for glucose measured at the optimised fMWCNT-Au_{nano}/Pd_{nano} modified GC electrode was 7.26×10^{-5}A (72.60 µA). When compared to that measured at the fMWCNT-Au_{nano}/Pd_{nano} modified SPE electrode at -0.45 V vs. Ag/Ag/AgCl, this corresponds to an increase in sensitivity of over 30%. This signifies that the composite modified SPEs provide better glucose detection than the modified GC electrodes and as such further glucose sensing was carried out at this improved system.

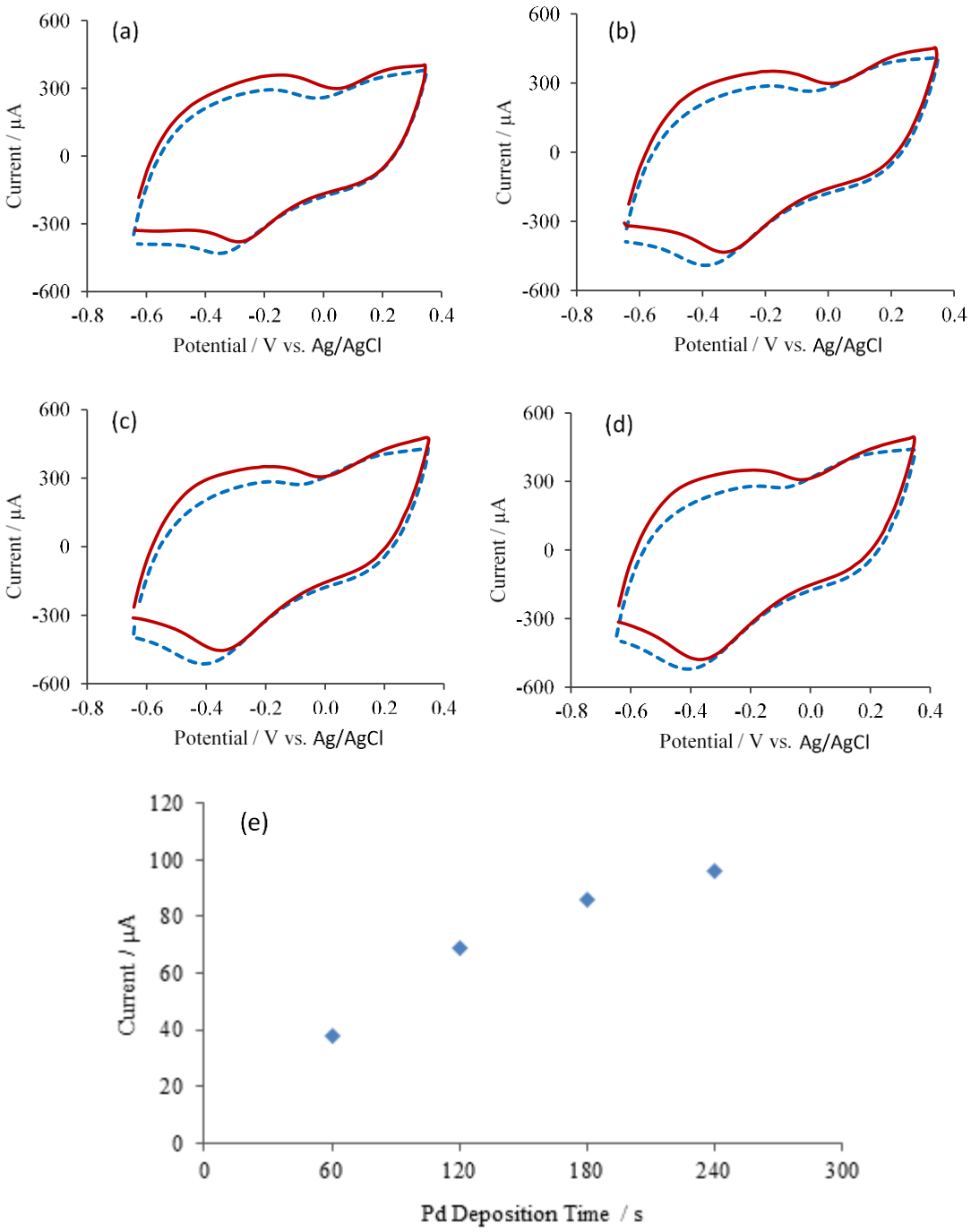

Figure 4.7: Cyclic voltammograms recorded at 100 mV s^{-1} of the fMWCNT-Au_{nano}/Pd_{nano} modified SPE electrodes in a - - - 0.1 M PBS solution (pH 7.4) and a — 0.1 M PBS solution containing 10 mM glucose. Figures **(a)**, **(b)**, **(c)** and **(d)** show glucose detection at the fMWCNT-Au_{nano}/Pd_{nano} films formed from Pd electrodeposition at -0.10 V vs. Ag/AgCl for 60, 120, 180 and 240 s, respectively. Figure **(e)** shows a plot of the glucose current response at -0.45 V vs. Ag/AgCl with different loadings of Pd.

An increase in the peak current for glucose at -0.45 V vs. Ag/Ag/AgCl can also be observed at the optimised fMWCNT-Au_{nano}/Pd_{nano} modified SPE, in comparison to the optimised fMWCNT-Au_{nano} modified SPE, CVs shown in Figure 4.8. A peak current of 2.93×10^{-5} A (29.39 µA) is measured at -0.05 V vs. Ag/Ag/AgCl at the fMWCNT-Au_{nano} modified SPE and that measured at the fMWCNT-Au_{nano}/Pd_{nano} modified SPE is 9.58×10^{-5} A (95.85 µA). This corresponds to over a 200% increase in sensitivity.

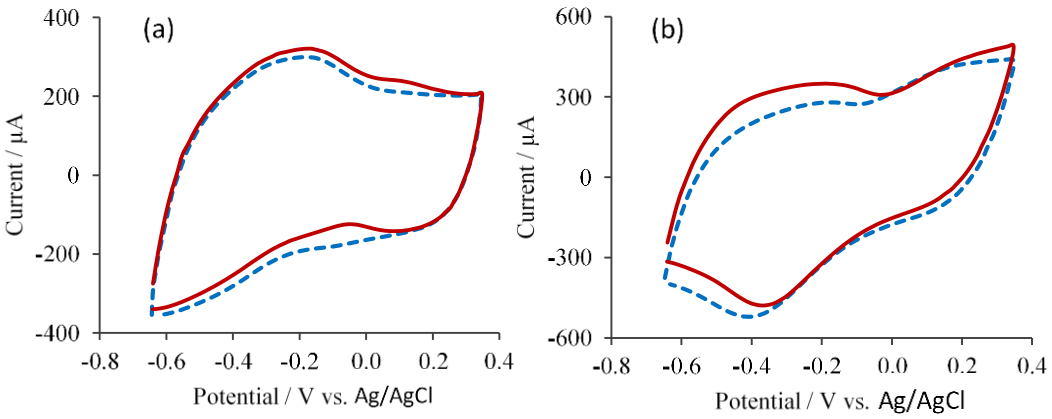

Figure 4.8: Cyclic voltammograms recorded at 100 mV s^{-1} of the **(a)** fMWCNT-Au_{nano} and the **(b)** fMWCNT-Au_{nano}/Pd_{nano} modified SPE in a - - - 0.1 M PBS solution (pH 7.4) and a — 0.1 M PBS solution containing10 mM glucose.

4.2.1.4 Detection of Glucose using CPA at SPE/fMWCNT-Au_{nano}/Pd_{nano} Films

Detection of glucose using CPA was possible at the fMWCNT-Au_{nano}/Pd_{nano} modified SPEs. This was initially investigated at the potential of -0.05 V vs. Ag/AgCl for comparison with the fMWCNT-Au_{nano} modified system, Chapter 3, Section 3.2.8, and due to its position just after the large forward glucose oxidation wave. Detection was also carried out at -0.45 V vs. Ag/AgCl due to the sensitivity at this region, apparent using CV. At this negative potential the oxidation of certain interferants, including ascorbic acid and uric acid, which typically occur at more positive potentials, may be eliminated [13, 14].

CPA conducted at -0.05 V vs. Ag/AgCl yields a typical relationship between glucose concentration and current response as can be seen in Figure 4.9 (a). The resulting

glucose calibration curve, shown in Figure 4.9 (b), shows good linearity (R^2 = 0.9994) with relatively low errors.

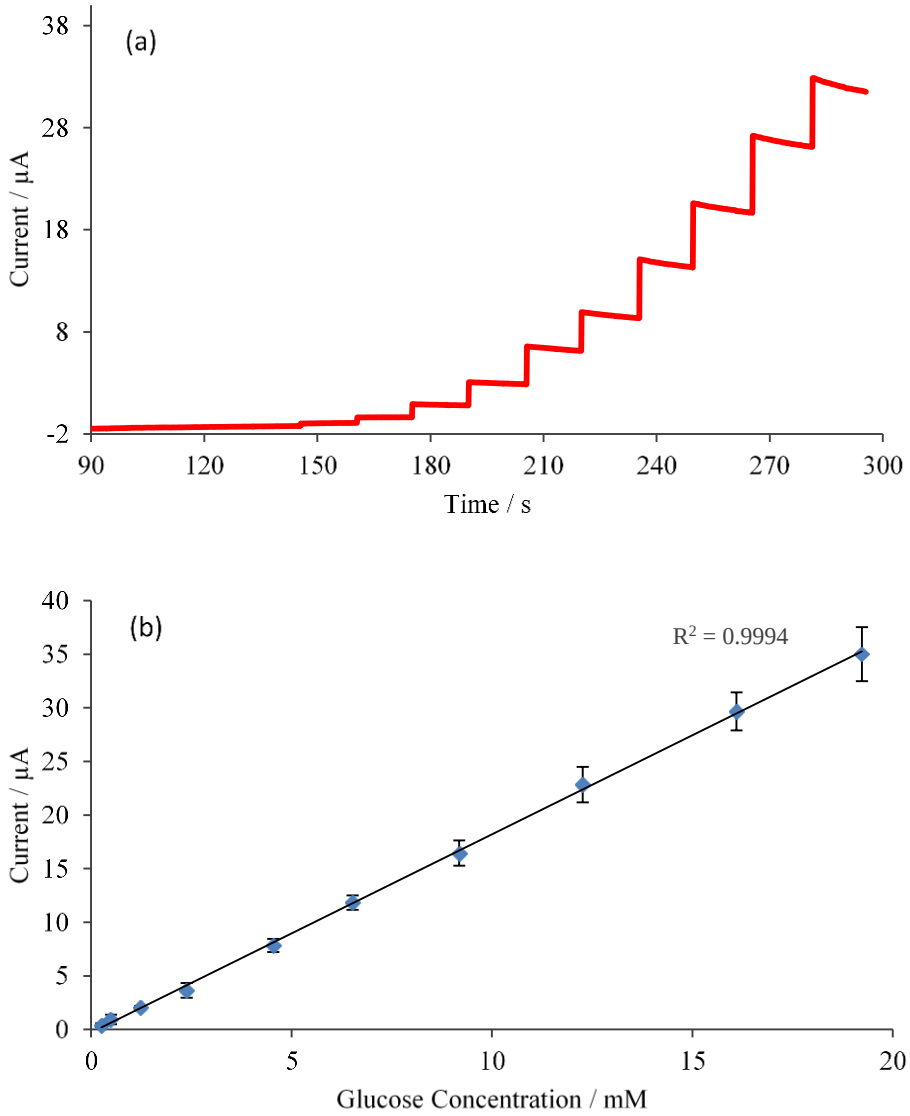

Figure 4.9: (a) Current-time plots for the oxidation of glucose, recorded at -0.05 V vs. Ag/AgCl, at the optimised fMWCNT-Au_{nano}/Pd_{nano} modified SPE electrode (DRP-150) in 0.1 M PBS (pH 7.4) with the successive additions of glucose aliquots from a 50 mM stock solution, made in 0.1 M PBS and **(b)** the corresponding calibration curve for glucose oxidation, n = 3.

When the experiment outlined above is repeated using the more negative potential of -0.45 V vs. Ag/AgCl, slightly different current-time plots are evident with lower than expected current responses occurring as the glucose concentration was increased, Figure 4.10 (a). This relationship is emulated in the corresponding glucose calibration curve in which a non-linear relationship between the data is apparent, Figure 4.10 (b). A polynomial trendline is used and a high correlation coefficient of 0.9976 is obtained. The error bars are small within the relevant physiological range of glucose, 4 – 8 mM [15], although they are large at higher glucose concentrations. These errors mean that accurate glucose detection is not possible at these higher glucose concentrations. This composite shows potentially promising properties at this negative potential as it may be possible to detect glucose selectively in the presence of certain interferants. Ascorbic acid and uric acid are two electroactive interferants that can be oxidised at positive potentials [13, 14] and therefore oxidation of these interferants may be avoidable. At metallic and carbon materials the oxidation of AA can occur around 0.4 V vs. SCE [16] and the oxidation of UA can occur at 0.36 V vs. SCE [17]. It was hoped that this composite film would provide good sensitivity towards glucose at this potential along with selectivity as to eliminate the use of Nafion®. However, as discussed in Chapter 3, Section 3.2.8, the use of a Nafion® membrane reduced sensitivity towards glucose at the fMWCNT-Au_{nano} modified SPE films by almost 90%.

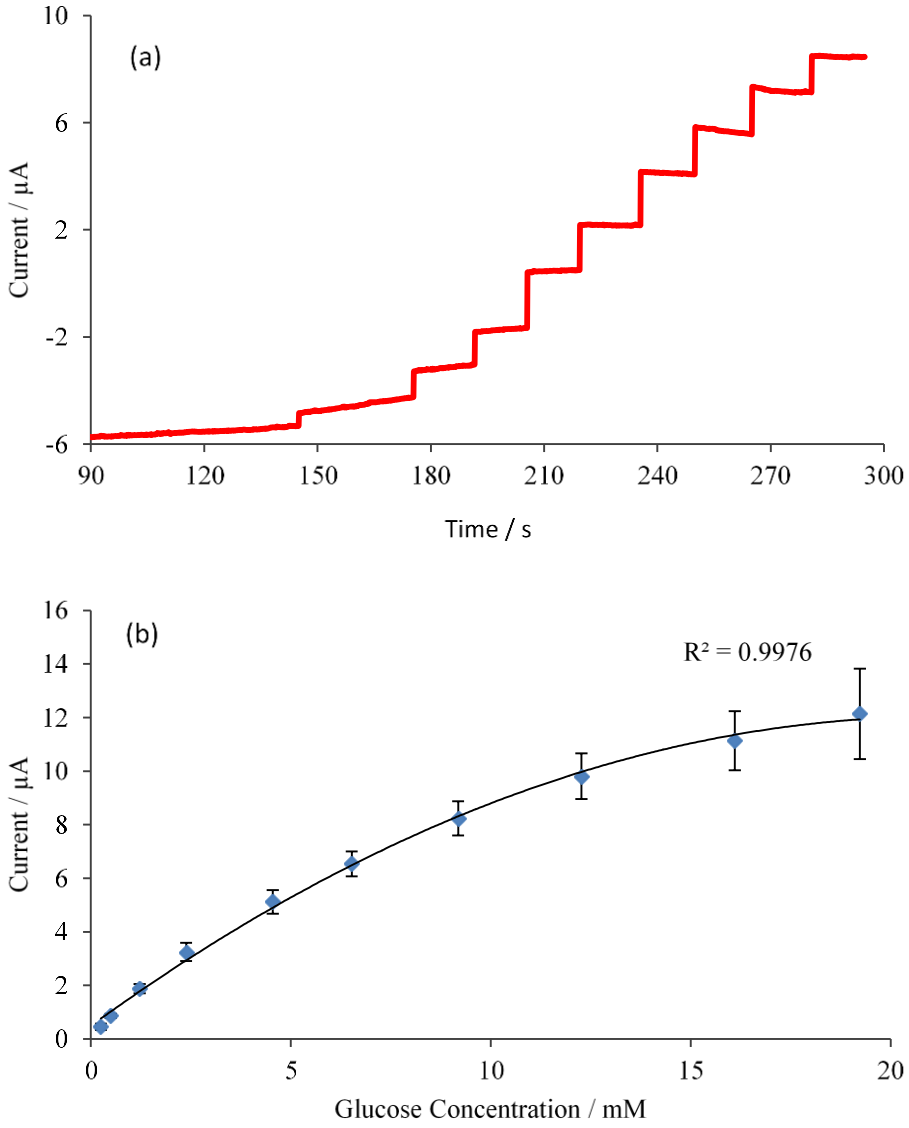

Figure 4.10: (a) Current-time plots for the oxidation of glucose, recorded at -0.45 V vs. Ag/AgCl, at the optimised fMWCNT-Au_{nano}/Pd_{nano} modified SPE electrode (DRP-150) in 0.1 M PBS (pH 7.4) with the successive additions of glucose aliquots from a 50 mM stock solution, made in 0.1 M PBS and **(b)** the corresponding calibration curve for glucose oxidation, n = 3.

4.2.1.5 Limits of Detection and Sensitivity for Glucose at SPE/fMWCNT-Au_{nano}/Pd_{nano} Films

The limit of detection (LOD) is the lowest quantity of an analyte that can be accurately distinguished from background noise [18]. The LODs are calculated using Equation 4.2 where LOD is the concentration, *Sd* is the standard deviation of the blank current

response [19]. Sensitivity values represent the slopes of the linear calibration plots for glucose.

$$LOD = 3Sd \qquad 4.2$$

LOD and sensitivity values for glucose were calculated using this equation when the potentials of -0.05 V vs Ag/AgCl and -0.45 V vs. Ag/Ag/AgCl were used during CPA, data shown in Table 4.1. Using data obtained at -0.05 V, a sensitivity value of 1.846 µA/mM and a LOD of 0.136 µM can be calculated for the fMWCNT-Au_{nano}/Pd_{nano} Film. At -0.45 V vs. SCE, a sensitivity value could not be calculated due to the non-linear trend, although a LOD of 0.350 µM was measured. Both of these LODs are below normal physiological levels of glucose present in the blood. This sensitivity at -0.05 V vs. Ag/AgCl is lower than that obtained at the same potential at the fMWCNT-Au_{nano} modified SPE, shown in Chapter 3, Section 3.2.8, which has a value of 2.766 µA/mM. This corresponds to over a 30% decrease in sensitivity. The fMWCNT-Au_{nano} modified SPE also results in a lower LOD of 0.049 µM. These results indicate that the fMWCNT-Au_{nano} modified SPEs are more suitable than the fMWCNT-Au_{nano}/Pd_{nano} modified SPE for the detection of glucose at -0.05 V vs. Ag/AgCl. As such, further investigations are not undertaken at this potential using the fMWCNT-Au_{nano}/Pd_{nano} modified SPEs.

Table 4.1: LOD and film sensitivity values towards the oxidation of glucose at the optimised fMWCNT-Au_{nano}/Pd_{nano} composite modified SPE electrode (DRP-150), n = 3.

Potential / V vs. SCE	LOD / µM	Sensitivity / µA/mM	Error / A/mM
-0.05	0.136	1.846	± 0.112
-0.45	0.350	†	-

† Sensitivity value not determined.

4.2.2 Characterisation of Composite Films

4.2.2.1 Scanning Electron Microscopy and Energy Dispersive X-Ray Analysis

SEM and EDX analyses were carried out on the fMWCNT-Au_{nano}/Pd_{nano} composite films prepared on both the GC electrodes and the SPEs, for comparison. Analysis was also undertaken for the fMWCNT-Pd_{nano} composite films formed on both the GC electrodes and SPEs to observe any differences in PdNP size or coverage, which could possibly help explain why glucose detection was not significant at these films. SEM micrographs of the fMWCNT-Au_{nano}/Pd_{nano} modified GC film can be seen in Figure 4.11. It is clear that PdNPs are formed and that they are distributed relatively evenly over the surface of the composite film. A large distribution in the particle diameter is evident in the resulting size distribution histogram with a mode diameter of 95 nm. As seen in the SEM micrographs of the fMWCNT-Pd_{nano} modified GC electrode, Figure 4.12, PdNPs are also formed uniformly over the film surface. Again, a large size distribution is seen in particle diameter and slightly larger PdNPs are formed, as can be seen in the size distribution histogram in Figure 4.12. PdNPs existed largely between 80 and 100 nm in diameter. Due to the similarities in particle sizes and coverage of Pd between the fMWCNT-Au_{nano}/Pd_{nano} film and the fMWCNT-Pd_{nano} control film, it is again assumed that the interesting glucose sensing properties at the fMWCNT-Au_{nano}/Pd_{nano} film are a result of the coexistence of both Au_{nano} and Pd_{nano} and not simply due to a difference in PdNP size or coverage.

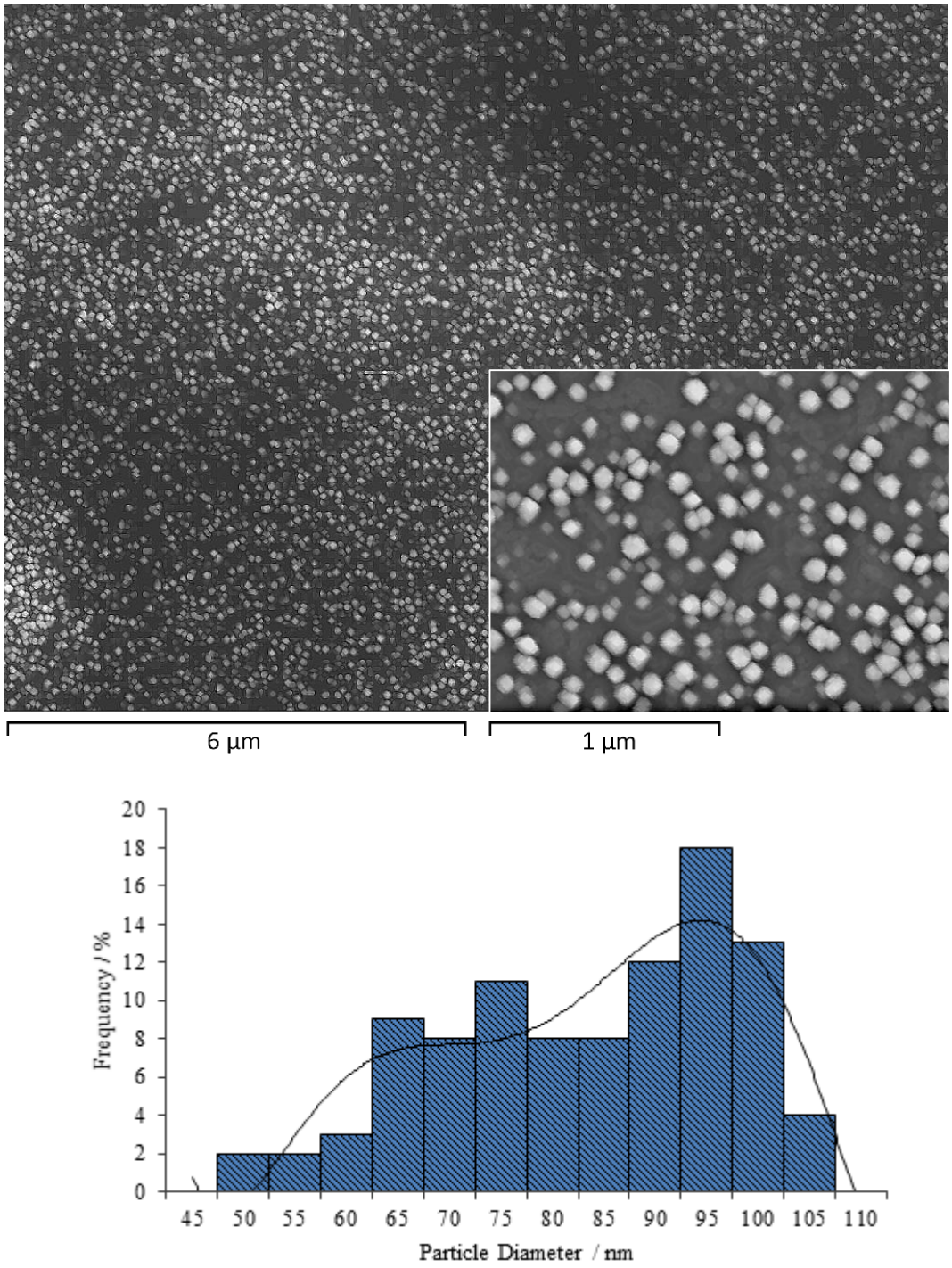

Figure 4.11: SEM micrographs and corresponding size distribution histogram of the fMWCNT-Au_{nano}/Pd_{nano} composite film formed on a GC electrode.

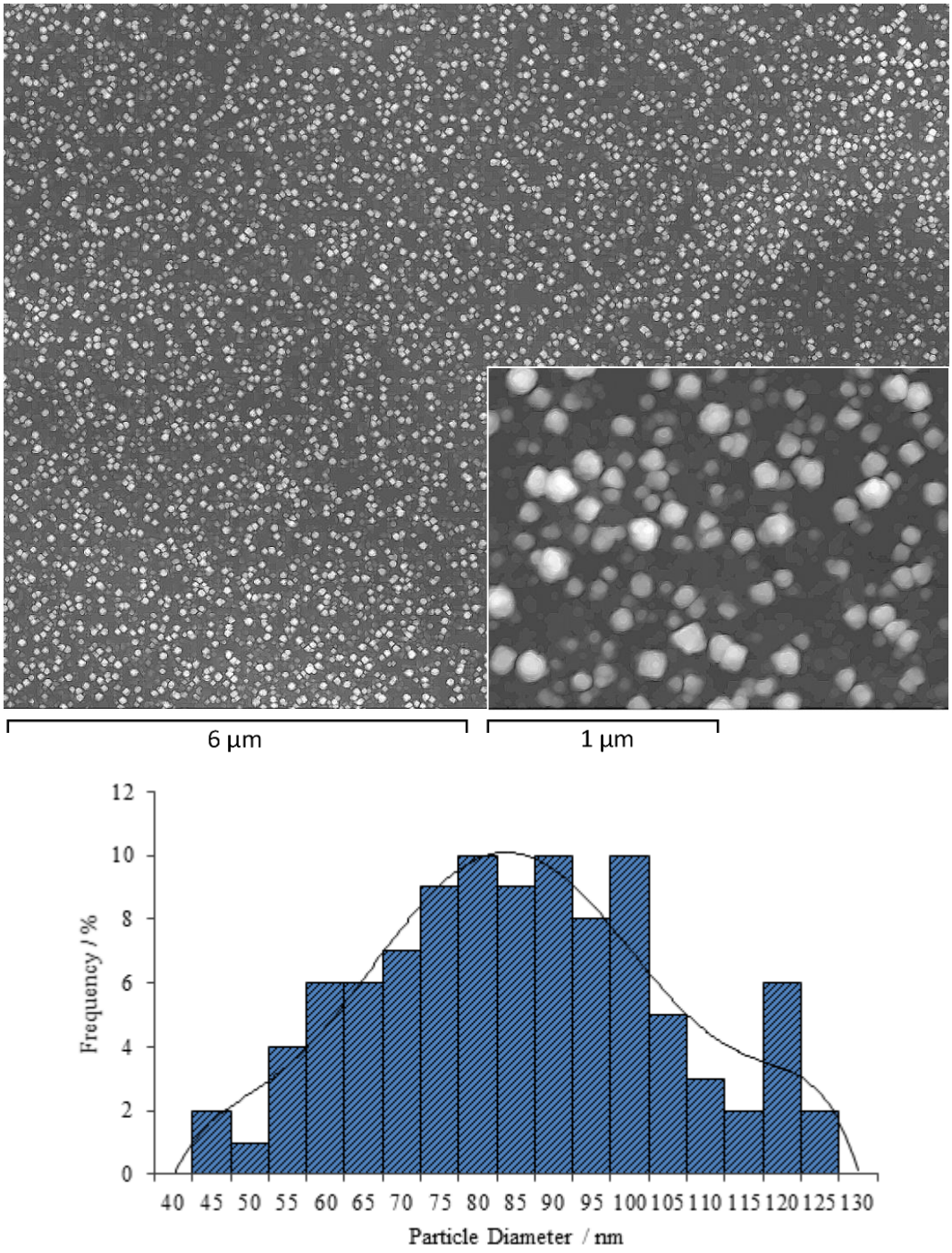

Figure 4.12: SEM micrographs and corresponding size distribution histogram of the fMWCNT-Pd_{nano} composite film formed on a GC electrode.

SEM analysis of the fMWCNT-Au_{nano}/Pd_{nano} modified SPE yields very similar results, as seen in Figure 4.13. A large size distribution is again apparent, with particles having a mode diameter of 95 nm, Figure 4.13. This compares very well will data obtained from the fMWCNT-Au_{nano}/Pd_{nano} modified GC electrode. SEM analysis is also included for the fMWCNT-Pd_{nano} modified SPE, as shown in Figure 4.14. Again a size distribution histogram is constructed and a large size distribution in PdNP diameter is observed, Figure 4.14. Like the fMWCNT-Pd_{nano} modified GC electrode, Figure 4.12, slightly larger particles are formed. Nevertheless, PdNPs exist between 90 and 95 nm in diameter, which compares well with those existing on the fMWCNT-Au_{nano}/Pd_{nano} modified electrode. Since very similar sizes and coverages of Pd are apparent at both composite films, it is again assumed that the interesting glucose sensing properties at the modified SPEs are a result of the formation of the bi-metallic Au_{nano}/Pd_{nano} composite and not due to a difference in particle size or coverage.

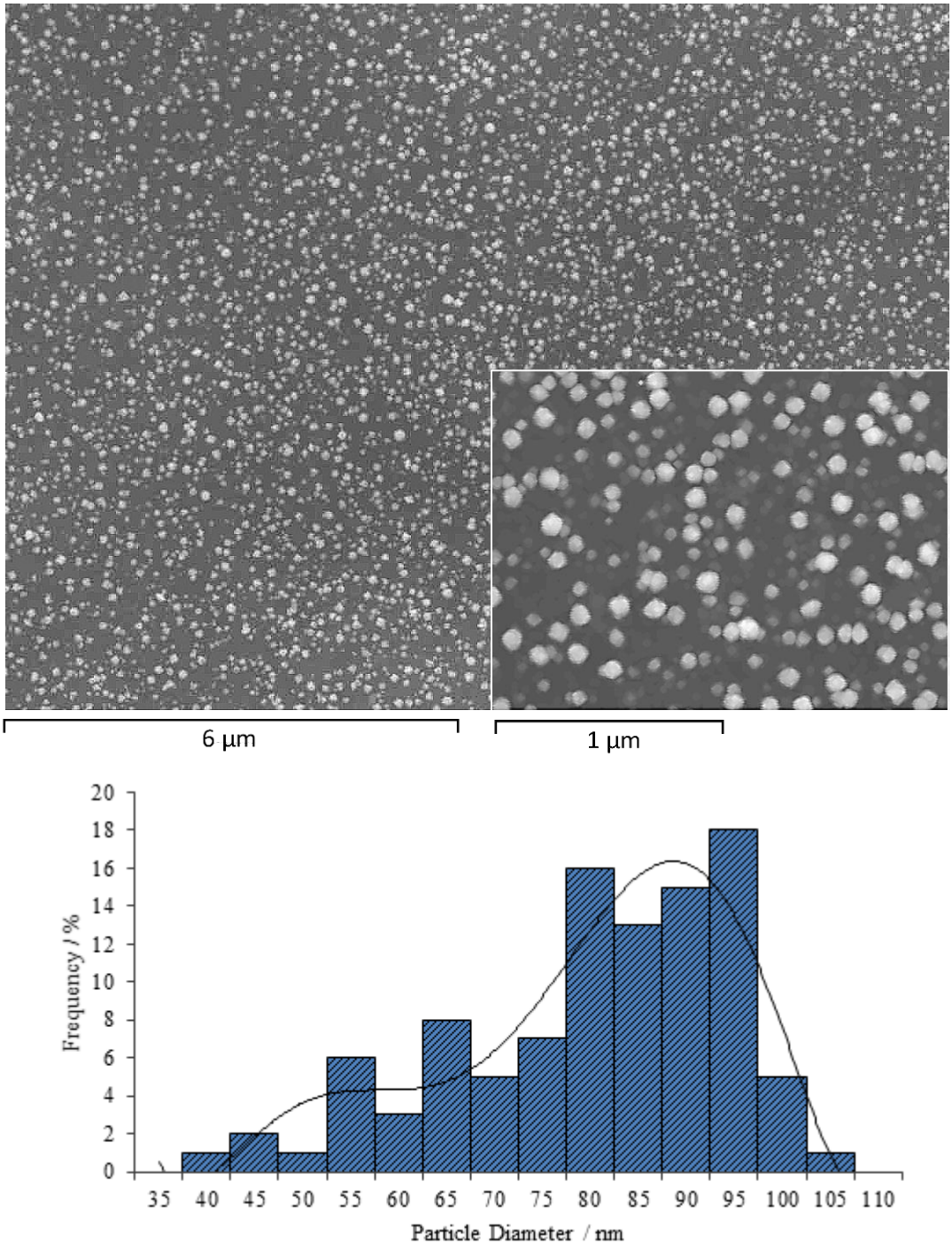

Figure 4.13: SEM micrographs and corresponding size distribution histogram of the fMWCNT-Au_{nano}/Pd_{nano} composite film formed on a SPE.

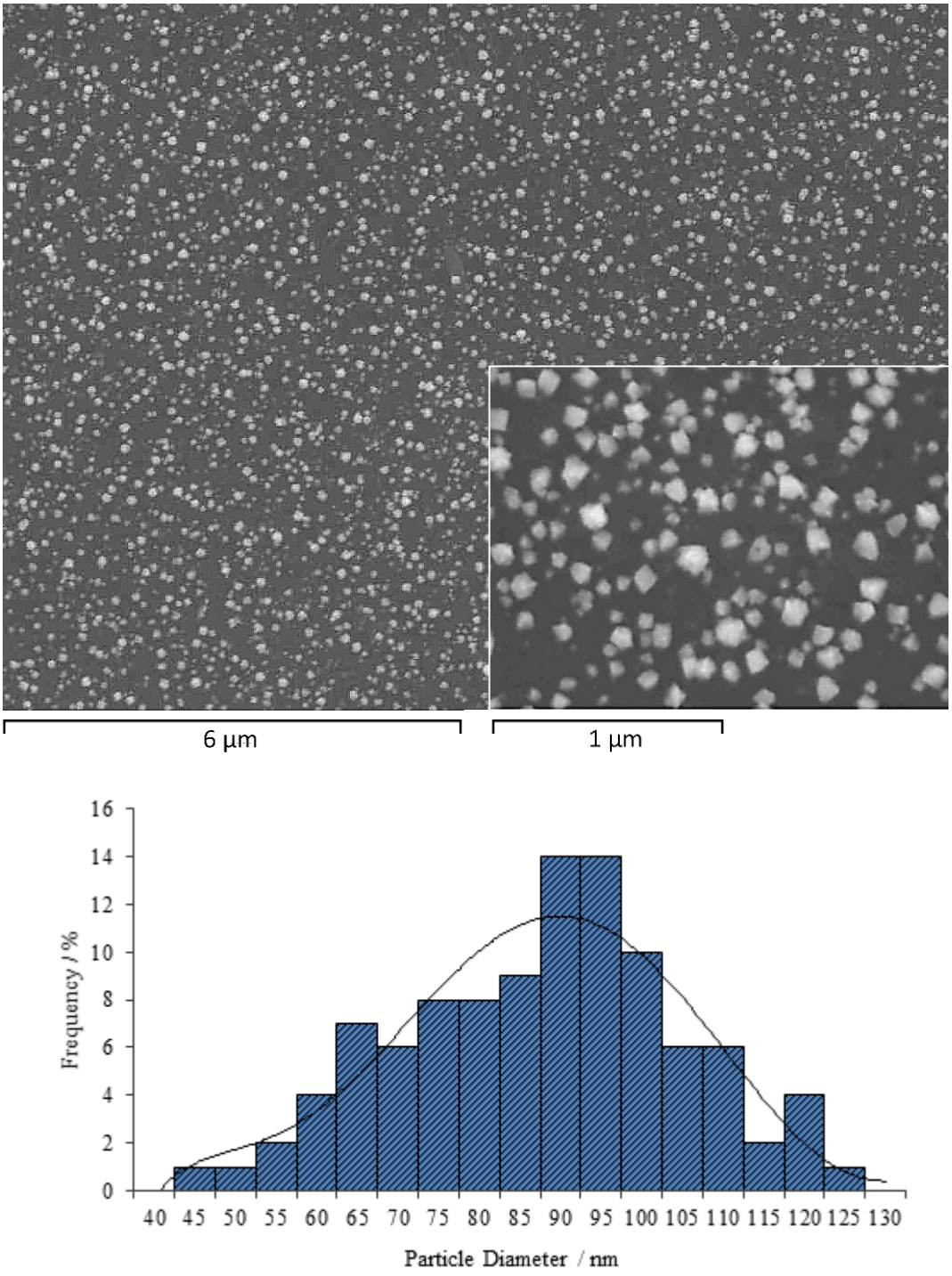

Figure 4.14: SEM micrographs and corresponding size distribution histogram of the fMWCNT-Pd_{nano} composite film formed on a SPE.

EDX analysis was undertaken on both the fMWCNT-Au_{nano}/Pd_{nano} and fMWCNT-Pd_{nano} films formed on both the GC electrodes and SPEs. Spectra are displayed in Figures 4.15 (a) to (d), along with a table of elemental % weights of all films, Table 4.2. As expected, peaks for Au and Pd are both present in the spectra for the fMWCNT-Au_{nano}/Pd_{nano} films. In the film formed on the GC electrode, the Pd composition is estimated at 2.96% wt. and that at the modified SPE is a similar value of 3.05% wt. Au is estimated at 1.69% wt. at the modified GC and at 1.75% wt. at the modified SPE. It is evident from the EDX spectra and resulting data that a significantly larger amount of Pd is present at these composite films in comparison to Au. Very similar Pd concentrations of 3.10 and 3.15% wt. are estimated for the control experiments at the fMWCNT-Pd_{nano} modified GC electrode and SPE. The presence of similar concentrations of Pd in the control composite films, again suggest that the glucose sensing properties of the fMWCNT-Au_{nano}/Pd_{nano} composite film are a result of the bi-metallic Au_{nano} and Pd_{nano} relationship and not due to different concentrations of Pd present. Peaks for C, O, Na, Cl and S occur in the spectra. The C and O signals arise mainly from the fMWCNTs and the Na probably results from the NaOH pre-treatment step. The Cl is only detected in the composite modified SPEs, Figures 4.15 (c) and (d), and is due to the pre-existing presence of Cl in the SPEs. The presence of sulfur is only apparent in the spectrum of the fMWCNT-Pd_{nano} modified SPE, Figure 4.15 (d), and is probably again due to interference from the underling substrate. It may be noticed that the Au% wt. in the composite films is slightly lower than that of 2.86% wt. obtained from EDX analysis of the bulk fMWCNT-Au_{nano} composite, Chapter 3, Section 3.2.9.3. This underestimation may result from interference from the underlying GC electrode and SPE working electrode. Both of these working electrodes are reported to consist of carbon and this may be contributing to the elemental data. Other elemental % weights may also be affected.

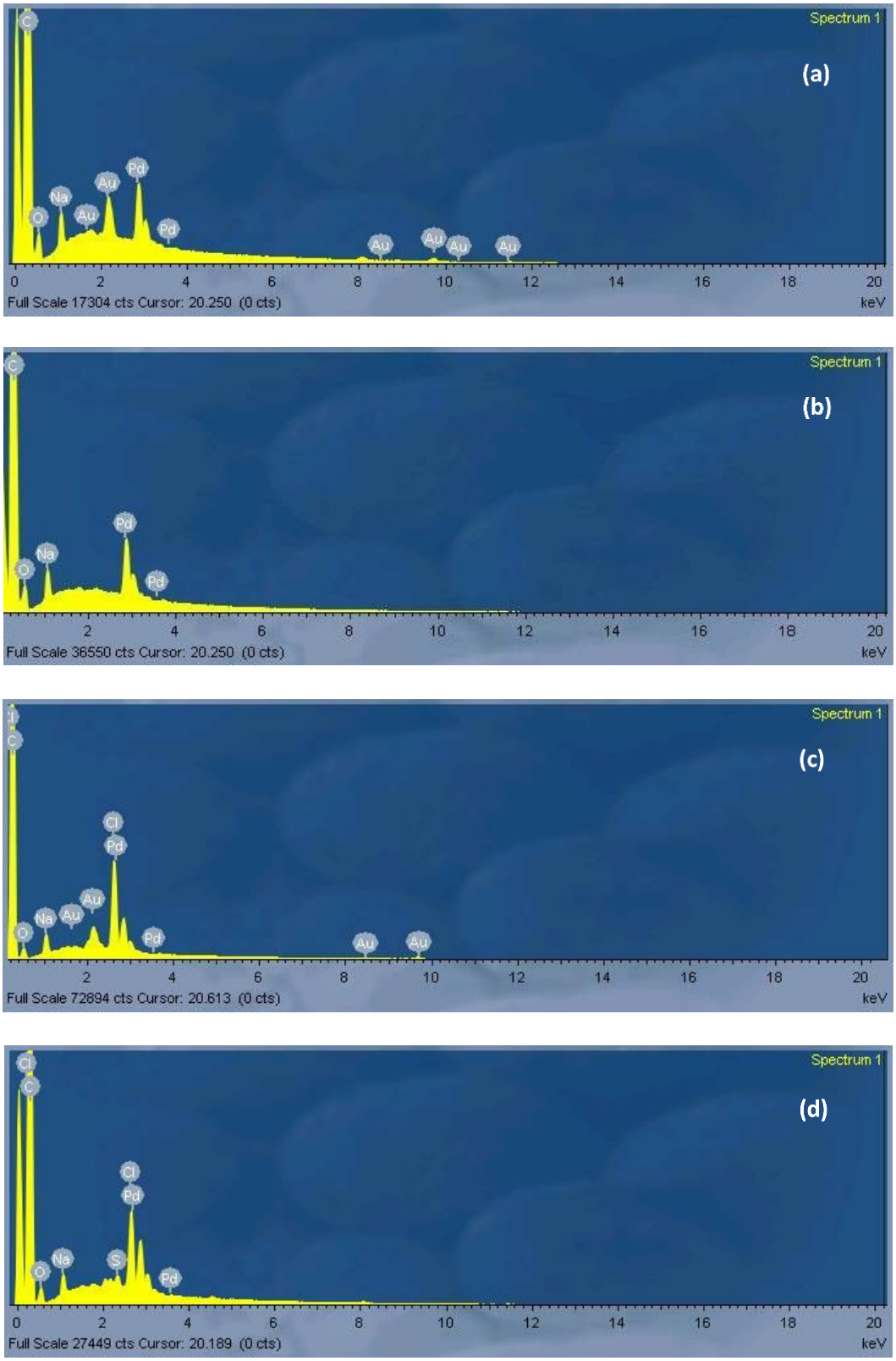

Figure 4.15: EDX spectra of the **(a)** fMWCNT-Au_{nano}/Pd_{nano} and **(b)** fMWCNT-Pd_{nano} composite modified GC and the **(c)** fMWCNT-Au_{nano}/Pd_{nano} and **(d)** fMWCNT-Pd_{nano} composite modified SPE.

Table 4.2: Table of elemental % weights of the **(a)** fMWCNT-Au_{nano}/Pd_{nano} and **(b)** fMWCNT-Pd_{nano} composite modified GC and the **(c)** fMWCNT-Au_{nano}/Pd_{nano} and **(d)** fMWCNT-Pd_{nano} composite modified SPE.

	GC/fMWCNT-Au_{nano}/Pd_{nano}		GC/fMWCNT-Pd_{nano}		SPE/fMWCNT-Au_{nano}/Pd_{nano}		SPE/fMWCNT-Pd_{nano}	
C% wt.	87.02	± 0.13	86.88	± 0.11	85.06	± 0.12	86.27	± 0.14
O% wt.	7.75	± 0.13	9.33	± 0.11	6.30	± 0.10	6.64	± 0.13
Au% wt.	1.69	± 0.04	-	-	1.75	± 0.04	-	-
Pd% wt.	2.96	± 0.03	3.10	± 0.03	3.05	± 0.04	3.15	± 0.04
Na% wt.	0.58	± 0.01	0.69	± 0.01	0.57	± 0.01	0.73	± 0.01
Cl% wt.	-	-	-	-	3.27	± 0.02	3.01	± 0.02
S% wt.	-	-	-	-	-	-	0.20	± 0.01

4.2.2.2 X-Ray Diffraction Spectroscopy

As discussed in Chapter 3, X-Ray Diffraction (XRD) is a non-destructive technique which is useful for determining crystallographic information of a crystalline material, including its various crystal planes, inter-atomic spacings and crystal structure [20]. XRD was carried out on the fMWCNT-Au_{nano}/Pd_{nano} composite which was produced on the SPEs and also on a fMWCNT-Au_{nano} and a fMWCNT-Pd_{nano} modified SPE for comparison.

In Figures 4.16, 4.17 and 4.18, the XRD spectra obtained from the fMWCNT-Au_{nano}/Pd_{nano}, fMWCNT-Au_{nano} and the fMWCNT-Pd_{nano} modified SPE are shown. It is clear from these spectra that no detailed information can be obtained due to the presence of many large overlapping peaks that are not related to the actual composite materials. As such, estimations of nanoparticle sizes cannot be calculated using the Scherrer equation, Equation 4.3 [21]. These overlapping peaks are identified as Al_2O_3 and TiO_2, which are present in the SPEs. For comparison, a XRD spectrum of the SPE substrate is included and results are shown in Figure 4.19. This spectrum shows much similarity to those of the composite films and this indicates that the SPEs are sources of interference during XRD. As such, peaks are not assigned on the actual spectra. Although not much useful information could be obtained from the resulting spectra, qualitative data was obtained and is displayed in Table 4.3. This XRD

analysis was conducted at The Materials and Surface Science Institute, University of Limerick, Ireland, and a the resulting data files are included in the Appendix.

$$D = \frac{0.89\lambda}{B cos\theta} \qquad 4.3$$

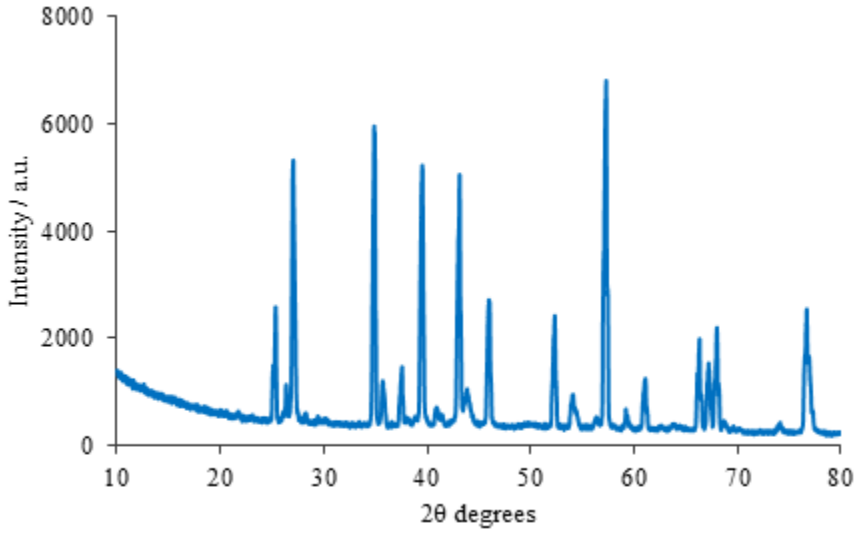

Figure 4.16: XRD spectrum of the fMWCNT-Au_{nano}/Pd_{nano} composite modified SPE.

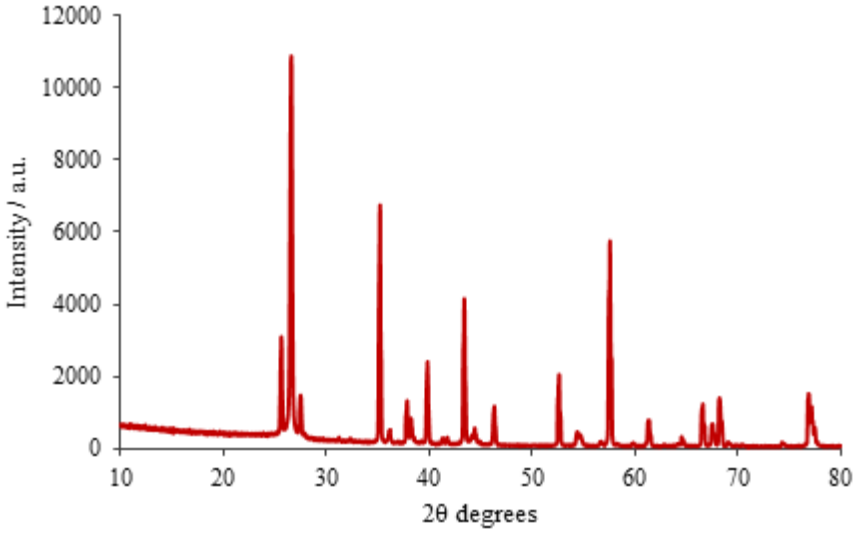

Figure 4.17: XRD spectrum of the fMWCNT-Au_{nano} composite modified SPE.

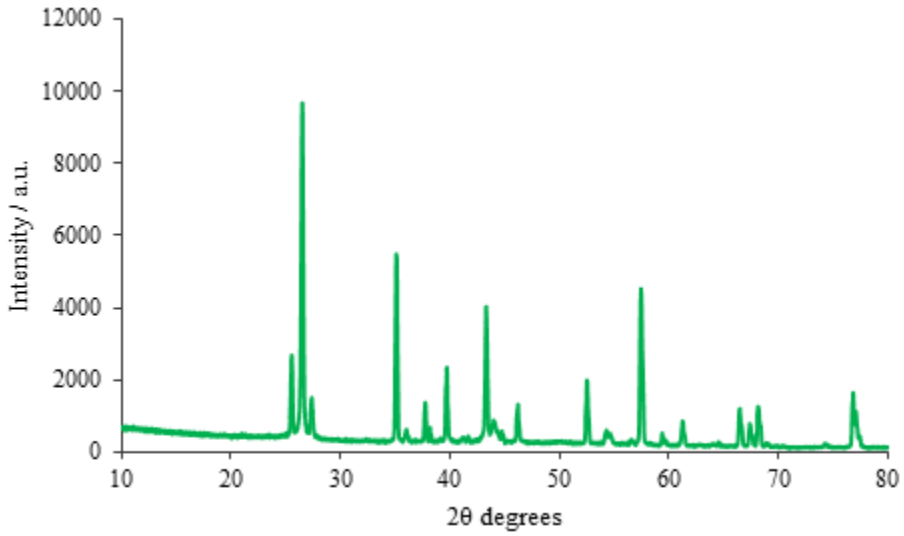

Figure 4.18: XRD spectrum of the fMWCNT-Pd_{nano} composite modified SPE.

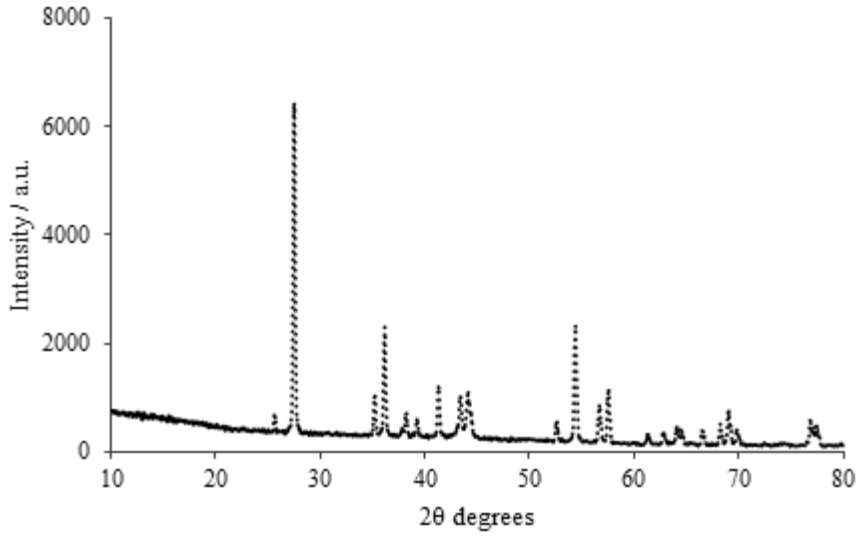

Figure 4.19: XRD spectrum of the SPE substrate.

Data obtained for all relevant species are displayed in Table 4.3. No data are included for either Al_2O_3 or TiO_2 and all unlisted peaks correspond to these species. It can be seen that graphitic peaks are obtained from analysis of all composites, which corresponds to the carbon nanotubes but may also be associated with the underlying carbon working electrode. Both Au and Pd are detected in the fMWCNT-Au_{nano}/Pd_{nano} composite film as expected. The presence of AuPd is also detected which indicates that an AuPd alloy or bi-metallic was formed in the composite. Representative peaks for this can be located at 39.31^0, 39.42^0 and 39.52^0 which represent the (111) plane of

AuPd [22]. At the fMWCNT-Au_{nano} composite film, peaks at 38.17^0, 44.41^0 and 64.52^0 correspond to the (111), (200) and (220) planes of Au [23, 24], respectively. Characteristic Pd peaks are also present at the fMWCNT-Pd_{nano} composite film. Peaks at both 39.61^0 and 39.73^0 represent the (111) crystalline plane [25, 26] and those at 46.10^0 and 46.22^0 represent the (200) plane of Pd [25, 26] although graphitic peaks are also present at these positions. The peak at 67.43^0 is associated with Pd (220) [25, 26]. Graphitic peaks are also identified in the spectra which can be associated with the carbon nanotubes. Non-graphitic carbon is also detected in the fMWCNT-Pd_{nano} sample which may result from the working electrode.

Table 4.3: XRD data for the fMWCNT-Au_{nano}/Pd_{nano}, fMWCNT-Au_{nano} and fMWCNT-Pd_{nano} composite modified SPE electrodes.

Peak Position / 2θ degrees	Height / counts	d-spacing / Å	Substance
fMWCNT-Au_{nano}/Pd_{nano}			
26.35	684.12	3.38	Graphite
39.31	2182.02	2.29	AuPd
39.42	4191.16	2.28	AuPd + Pd
39.52	4777.12	2.28	AuPd + Pd
43.84	603.41	2.06	Au
45.98	2278.90	1.97	Pd
54.07	596.01	1.69	Graphite
62.57	44.53	1.48	Graphite
67.19	1203.56	1.39	Pd
76.90	1373.96	1.24	Au
fMWCNT-Au_{nano}			
26.57	10484.70	3.35	Graphite
38.17	603.10	2.35	Au
43.29	2341.68	2.08	Graphite
43.40	3975.19	2.08	Graphite
44.41	439.48	2.04	Au
46.21	692.63	1.96	Graphite
46.31	1038.19	1.96	Graphite
54.65	280.35	1.67	Graphite
56.68	113.51	1.62	Graphite
64.52	249.56	1.44	Au
77.48	494.18	1.23	Au + Graphite
fMWCNT-Pd_{nano}			
26.53	9239.00	3.36	Graphite
39.62	1304.96	2.27	Pd
39.73	1997.46	2.26	Pd
43.32	3655.28	2.08	Graphite
46.10	679.47	1.96	Pd + Graphite
46.22	1014.87	1.96	Pd + Graphite
54.61	276.90	1.68	Graphite
56.61	111.40	1.62	Graphite
61.27	635.35	1.51	C
67.43	550.72	1.38	Pd
76.85	1498.73	1.24	C
77.43	312.25	1.23	Graphite

4.2.2.3 Scan Rate Analysis

Scan rate studies were carried out at both the fMWCNT-Au_{nano}/Pd_{nano} composite modified GC electrode and SPE for comparison. The same scan rate analysis discussed in Chapter 3, Section 3.2.9.10, was used at these films. As discussed previously, data obtained from scan rate studies can be applied to the Randles-Sevcik equation to estimate the electroactive surface areas (ESAs) of electrode surfaces, but only if the redox processes occurring are under semi-infinite diffusion-control (SID). ESAs may be estimated from the slope of the Randles-Sevcik plot described by Equation 4.4. In this equation, *n* is the number of electrons, *v* is the scan rate, *D* is the diffusion coefficient, *A* the area of the electrode and *C* is concentration [27-29].

$$i_p = 2.68 \times 10^5 n^{\frac{3}{2}} A D^{\frac{1}{2}} C v^{\frac{1}{2}} \qquad 4.4$$

The electrochemical probe used in this study and in previous scan rate studies was ferrocyanide. Unfortunately, in previous work, Chapter 3, Section 3.2.9.10, it was found that processes other than SID were occurring at the electrochemical interface and this was assumed to be thin layer diffusion, TLD. TLD commonly occurs at carbon nanotube films and porous carbon films [30-35], as discussed in Chapter 3. It would appear that TLD was occurring at these new fMWCNT-Au_{nano}/Pd_{nano} films. Although ESA estimations could not be carried out due to this, information could be obtained from the ferrocyanide redox peak separations. As in the previous scan rate studies, Chapter 3, Section 3.2.9.10, the redox peak separations (ΔE) for all scan rates applied were obtained from the resulting CVs. The values of ΔE can provided interesting information on the rates of the electron transfer at electrochemical films. The peak separations were obtained using Equation 4.5, where, *Ea* is the peak potential of the oxidation wave, *Ec* is peak potential of the reduction peak and *n* is the number of electrons transferred in the redox process[36]. ΔE can provide interesting information on the rate of the electron transfers at electrochemical films and when this system is under SID control, values of 59 mV/*n* signify a reversible redox couple, which is a fast electron transfer process [37]. Values higher than this represent a quasi-reversible process, which is a slower process [1, 36].

$$\Delta E = Ea - Ec = \frac{59\ \text{mV}}{n} \qquad 4.5$$

The resulting CVs of the fMWCNT-Au_{nano}/Pd_{nano} composite modified GC electrode and SPE cycled in a 1.0 mM ferrocyanide solution made in 0.1 M KCl are shown in Figures 4.20 (a) and (b). Before each scan rate was commenced, the films were cycled in a background electrolyte of 0.1 M KCl. As expected, an increase in the scan rate results in an increase in the currents obtained and these peak currents can be plotted as a function of the square root of the scan rate, Figures 4.20 (c) and (d). An almost linear relationship is seen in both of these plots, which may initially imply that a SID process is occurring at the electrode surface [28, 29], data shown in Table 4.4. Also, a large difference in slope values, calculated from the data fitting, is evident between the modified GC electrode and SPE, which can be due to the differences in surface areas, data shown in Table 4.4. Although an almost linear plot is obtained, an even better correlation between the data is evident when these data are applied to a plot of the current versus the scan rate, Figures 4.20 (e) and (f). Linearity in this plot implies that adsorption processes may be occurring at the surface of this electrode [28, 29]. To elucidate which processes were occurring, plots of the logarithm of current versus the logarithm of scan rate, 'log-log', were employed, Figure 4.21. As can be seen in the plots, the slopes obtained from the trendlines are much higher than a value 0.5 which corresponds to a SID process [1]. This implied that TLD is occurring in conjunction with SID, a common process at porous systems [30-35]. A slope of 0.8603 is obtained for the composite modified GC electrode and a slightly larger slope of 0.8891 is calculated for the modified SPE.

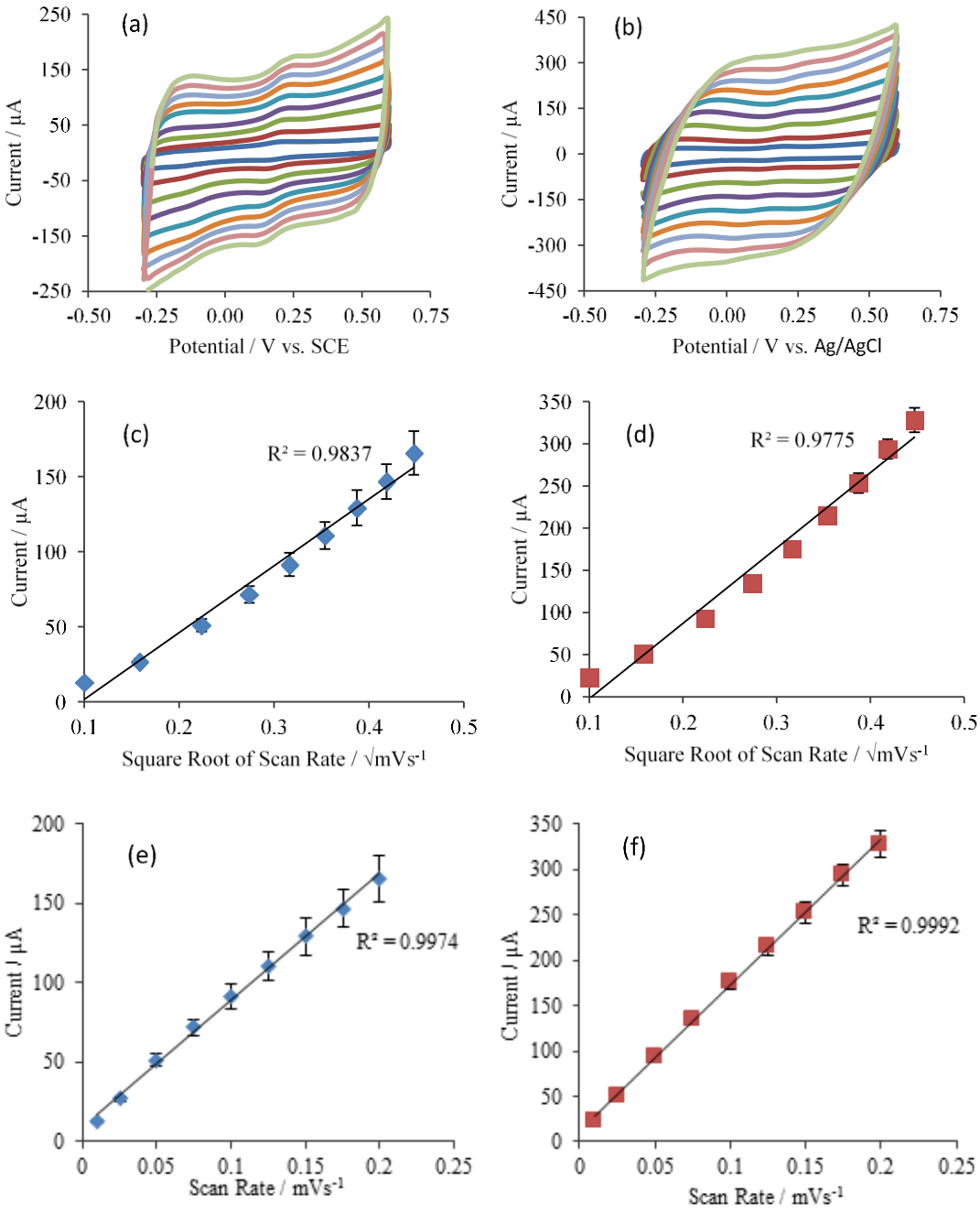

Figure 4.20: Cyclic voltammograms of the fMWCNT-Au_{nano}/Pd_{nano} modified **(a)** GC and **(b)** SPE cycled in a 1.0 mM ferrocyanide solution made in 0.1 M KCl at scan rates of 10, 25, 50, 75, 100, 125, 150, 175 and 200 mV s^{-1} and the resulting plots of current versus the square root of scan rate, Figures **(c)** and **(d)**, and versus the scan rate, Figures **(e)** and **(f)**, for both films, respectively, n = 3.

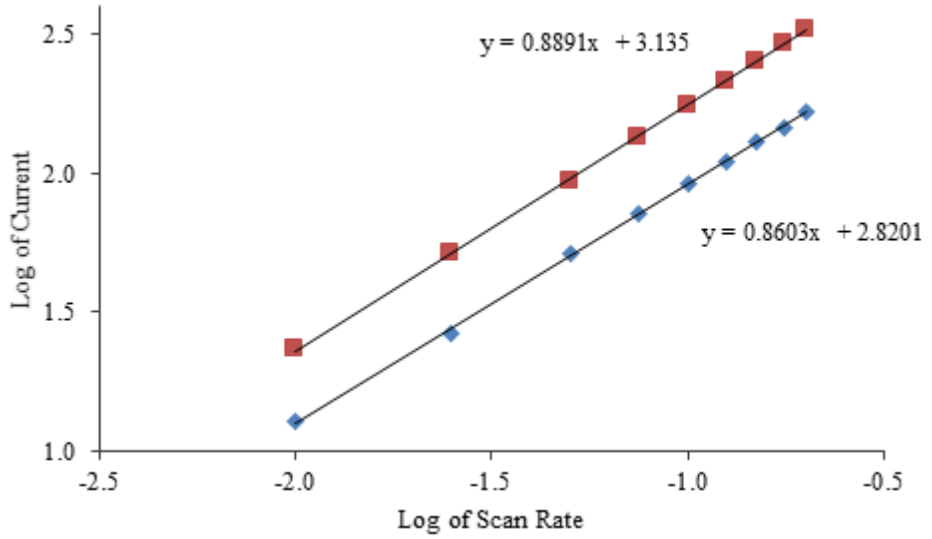

Figure 4.21: Plots of the logarithm of the peak current as a function of the logarithm of the scan rate for the fMWCNT-Au_{nano}/Pd_{nano} composite films formed on a GC electrode (blue points) and a SPE (DRP-150) (red points), n = 3.

Table 4.4 Table of the correlation coefficients, R^2 values, and slope values obtained from the diffusion plots of the peak current versus the square root of scan rate and slope values from the logarithm of peak current versus logarithm of scan rate plots for all composite films, n = 3.

Composite Film	R^2 Values of Diffusion Plots	Slope Values / $A/\sqrt{Vs^{-1}}$	Total ESA / cm^2	Slope Values of Log Plots	Diffusion Processes
GC/fMWCNT-Au_{nano}/Pd_{nano}	0.9837	4.449×10^{-4}	†	0.8991	SID + TLD
SPE/fMWCNT-Au_{nano}/Pd_{nano}	0.9775	8.925×10^{-4}	†	0.8603	SID + TLD

† Films not suitable for total ESA estimations using this technique.

As mentioned, additional information can be obtained from the CVs at each of the scan rates, from analysis of the redox peak separations, ΔE. Data are displayed in Figure 4.21 for both the composite modified GC electrodes and SPEs, along with ΔE values obtained from the optimised fMWCNT-Au_{nano} modified GC electrodes and SPEs, shown for comparison. As discussed in Chapter 3, Section 3.2.9.10, values

measured for ΔE may only be compared to the SID model of 59 mV, Equation 4.5, if SID is the exclusive process occurring at the electrode surface [30, 35]. And although ΔE can still be measured if TLD is occurring, data may only be used comparatively if the effects of TLD are equivalent at each surface [35]. As mentioned, the mass transfer processes can be calculated using a 'log-log' plot, shown in Figure 4.21. The slope value obtained from these plots for the fMWCNT-Au_{nano}/Pd_{nano} composite modified GC electrodes and SPEs, were 0.8991 and 0.8603, respectively, data displayed in Table 4.4. The slope values obtained for the fMWCNT-Au_{nano} modified GC electrode and SPEs, shown in Chapter 3, Section 3.2.9.10, were 0.8400 and 0.9000, respectively. Since these values are very similar, comparisons in electron transfer kinetics may be made.

It is clear from this plot that the calculated ΔE values differ greatly between the composite modified GC electrodes and the SPEs, with those arising from the SPEs being of much larger values. This finding is related to kinetic limitations at the modified SPEs and suggests that slower electron transfers may be occurring at these surfaces. This could be related to the screen printed nature of the SPEs. Another interesting finding was that ΔE values do not seem to differ greatly between the composites used. This means that the variations in ΔE may be a result of the electrode substrates used and not the composite films. The slower electron transfers at these modified SPEs could possibly explain why the current responses for glucose were not as high as expected at the fMWCNT-Au_{nano} modified SPEs, as discussed in Chapter 3, Section 3.2.8, even though a much larger surface area of Au was present, as found during the H_2SO_4 cycling, shown in Chapter 3, Section 3.2.9.10.

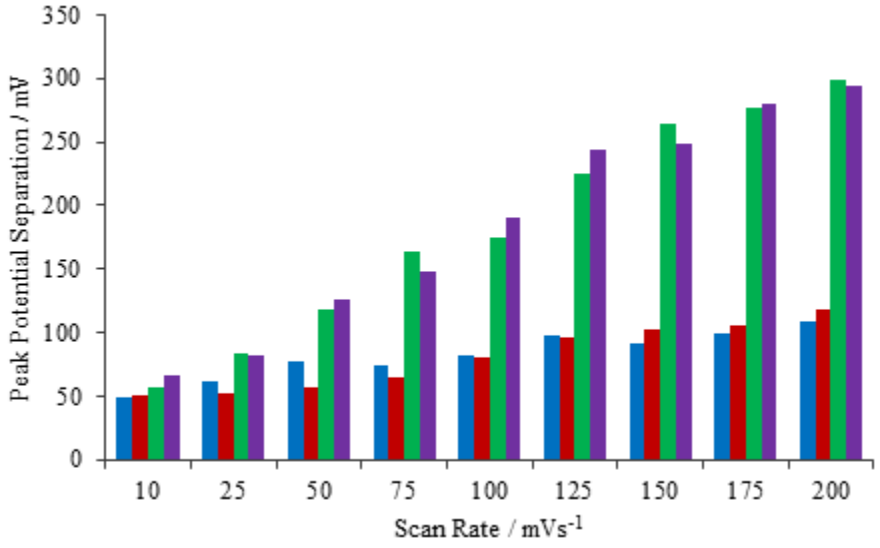

Figure 4.22: Plot of the ferrocyanide redox peak separations, ΔE, as a function of the scan rate for the — fMWCNT-Au_{nano} and — fMWCNT-Au_{nano}/Pd_{nano} modified GC electrode and for the — fMWCNT-Au_{nano} and — fMWCNT-Au_{nano}/Pd_{nano} modified SPE.

4.2.2.4 Electrochemical Impedance Spectroscopy

Electrochemical Impedance Spectroscopy (EIS) was carried out as a complementary study to measure and compare the changes in the capacitance and resistance at the fMWCNT-Au_{nano}/Pd_{nano} composite films over varying potentials and for comparison with EIS data obtained at the previous fMWCNT-Au_{nano} composite films, discussed in Chapter 3, Section 3.2.9.11. The same potentials, -0.10 V, 0.20 V and 0.50 V vs. SCE, frequency range, 65 mHz – 3 mHz, and perturbation, 5 mV, were used in this work. Again, the prepared films were initially held at the potentials under investigation prior to analysis for a period of 30 min, to reach steady states. EIS was carried out using a conventional three electrode set up with a GC working electrode and an SCE reference. The modified SPEs were not studied due to possible instabilities of the SPEs during analysis. The equivalent circuit, shown in Figure 4.23, was used during modelling, with a Rs component representing the solution resistance, R1 representing the charge-transfer resistance and a CPE1, constant phase element, and a C1 element representing a capacitor [38]. As with previous EIS studies reported in Chapter 3, Section 3.2.9.11, an improved fitting was apparent when the capacitor,

C1, was used in place of a CPE, CPE2, even though CPEs are frequently used in circuit modelling when surface inhomogeneities exist [38].

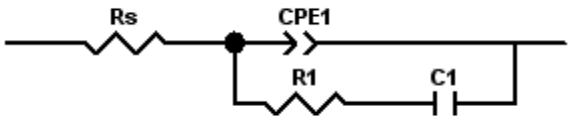

Figure 4.23: Equivalent circuit used to fit the impedance data.

Impedance data were presented as Complex plane or Nyquist plots and as Bode plots. As mentioned previously, the imaginary and real components of the impedance are plotted to give the Complex plane or Nyquist plots, while the modulus of the impedance and the phase angle are presented as a function of frequency to give the Bode plot. Bode plots are generally separated into two plots displaying the magnitude of the impedance and the phase angle as a function of the logarithm of frequency[39]. Plots obtained at 0.20 V vs. SCE for the fMWCNT-Au_{nano}/Pd_{nano} composite film are shown in Figures 4.24 (a), (b) and (c) with plots of the optimised fMWCNT-Au_{nano} modified film and of a GC electrode, shown for comparison. It is clear that EIS data obtained at the fMWCNT-Au_{nano}/Pd_{nano} composite film differ greatly from the non-modified GC and that more capacitive features are apparent. Differences in the plots is also evident between this composite film and the fMWCNT-Au_{nano} film, although the resulting capacitance and resistance data, calculated during circuit modelling using ZView® software, in general is quite similar, shown in Figures 4.25 – 4.27.

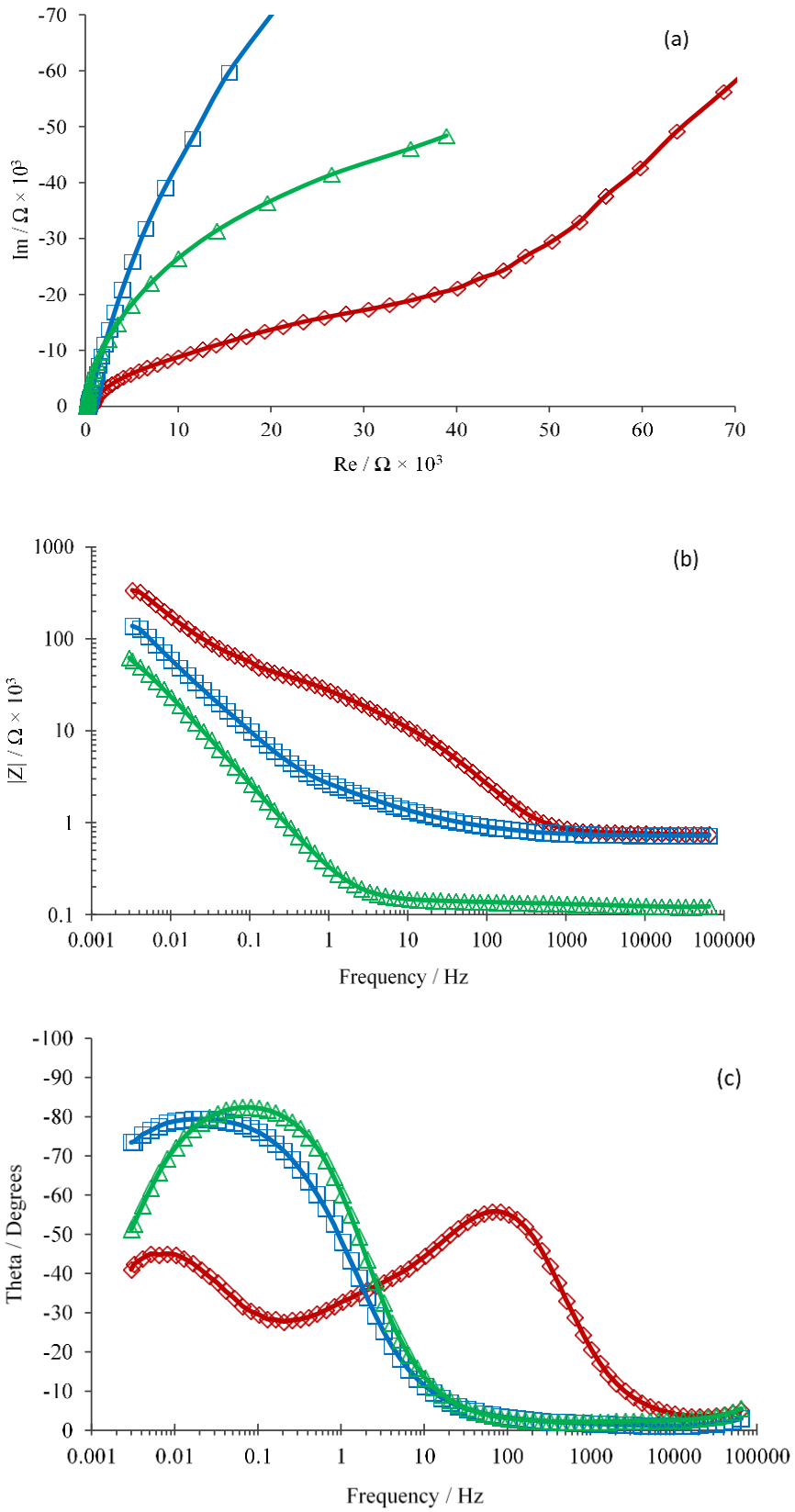

Figure 4.24: (a) Complex Plane (Nyquist) plot, **(b)** and **(c)** Bode plots recorded in 0.1 M PBS solution, pH 7.4 at 0.20 V vs. SCE of — the optimsed fMWCNT-Au_{nano}/Pd_{nano} composite film — the optimised fMWCNT-Au_{nano} composite film and — a GC electrode.

Figure 4.25 shows capacitance data obtained from the CPE1 elements during analysis conducted at the potentials of – 0.10 V, 0.20 V and 0.50 V vs. SCE at the optimised fMWCNT-Au_{nano}/Pd_{nano} and the fMWCNT-Au_{nano} composite films, for comparison. It was clear from previous EIS studies at the fMWCNT-Au_{nano} films, that the CPE1 capacitance varied with applied potential, with - 0.10 V vs. SCE yielding the largest capacitance. This finding correlated well with the CVs obtained in PBS in which more capacitive characteristics are evident at more negative potential ranges, an example seen in Section 4.2.1.1, Figure 4.3. The same trend occurs at the fMWCNT-Au_{nano}/Pd_{nano} composite film, which again corresponds with the obtained CVs in PBS, shown previously. Overall a slight increase in the CPE1 capacitance is observed at the fMWCNT-Au_{nano}/Pd_{nano} composite films in comparison to the fMWCNT-Au_{nano} films which may be due to an increase in surface area [2].

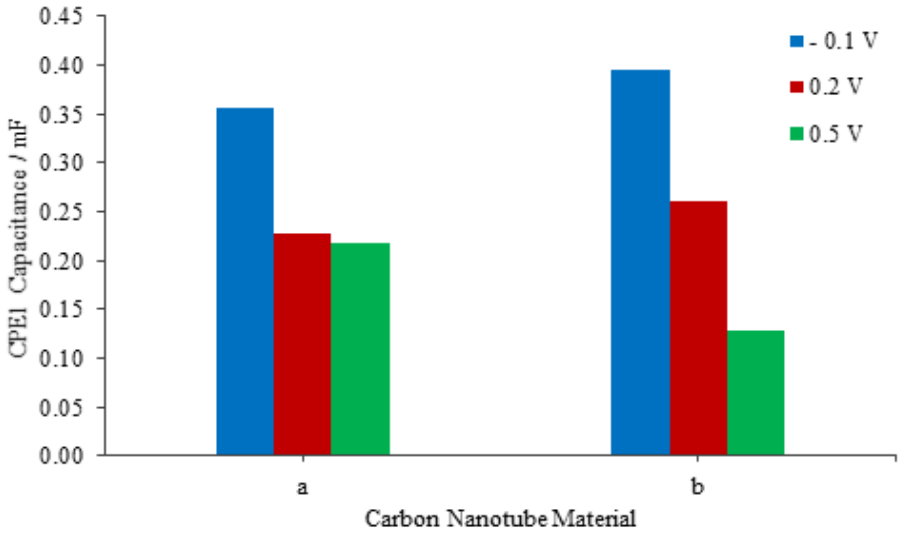

Figure 4.25: Plots of the CPE1 capacitance values obtained at potentials of -0.10 V, 0.20 V and 0.50 V vs. SCE for the H_2SO_4 optimised **(a)** fMWCNT-Au_{nano} and **(b)** the 24 h fMWCNT-Au_{nano}/Pd_{nano} composite film.

Having plotted capacitance data obtained from the C1 elements, again a trend is evident, with the C1 capacitance being most significant towards more negative potentials, Figure 4.26. Again this trend is apparent from CVs of the composites in PBS, Section 4.2.1.1, Figure 4.2. Overall the C1 capacitance values obtained at all applied potentials are larger at the fMWCNT-Au_{nano}/Pd_{nano} composite film than at the fMWCNT-Au_{nano} film, shown in Figure 4.26. These larger values could also be related

to an increased surface area due to the presence of the Pd_{nano}. The opposite trends are observed in relation to the resistance values obtained from the R1 components of the circuit model as expected, Figure 4.27 below. Resistance values are lower overall at the fMWCNT-Au_{nano}/Pd_{nano} composite films over all of the potentials used in comparison to the fMWCNT-Au_{nano} film and the applied potential of -0.10 V yields the lowest resistance response. These data corresponded well with the capacitance data obtained and this may be associated with an increased surface area.

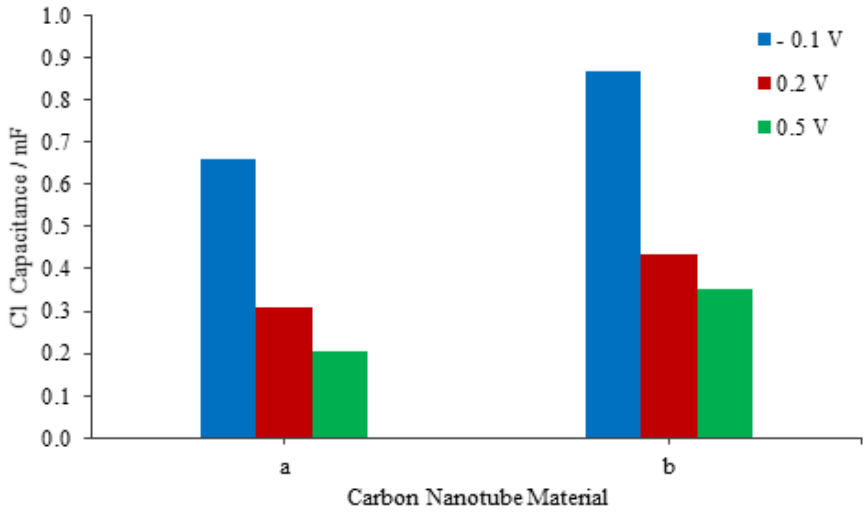

Figure 4.26: Plots of the C1 capacitance values obtained at potentials of -0.10 V, 0.20 V and 0.50 V vs. SCE for the H_2SO_4 optimised **(a)** fMWCNT-Au_{nano} and **(b)** the fMWCNT-Au_{nano}/Pd_{nano} composite film.

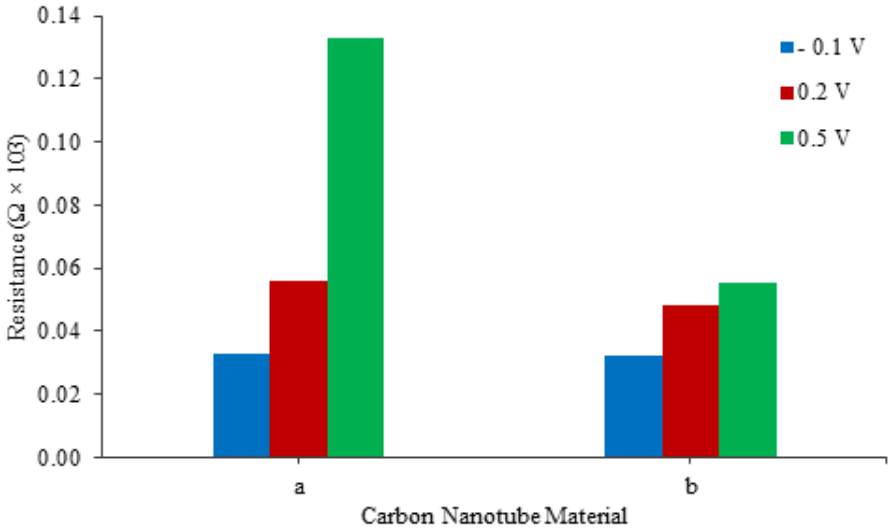

Figure 4.27: Plots of the R1 resistance values obtained at potentials of -0.10 V, 0.20 V and 0.50 V vs. SCE for the H_2SO_4 optimised **(a)** fMWCNT-Au_{nano} and **(b)** the fMWCNT-Au_{nano}/Pd_{nano} composite film.

4.3 Summary of Results

In this chapter results are presented on the synthesis and characterisation of the fMWCNT-Au_{nano}/Pd_{nano} composite films and their use as non-enzymatic glucose sensors. This bi-metallic composite film was produced through the electrodeposition of PdNPs onto the surface of pre-formed fMWCNT-Au_{nano} composite films. Initially experimentation was conducted on a GC electrode using a conventional three electrode setup and an optimum potential and duration for Pd deposition was determined. The electrodeposition of Pd at the potential of 0.45 V vs. SCE for the duration of 240 s yielded a sufficient coverage of PdNPs with a mode diameter of 95 nm. This resulting composite film, fMWCNT-Au_{nano}/Pd_{nano}, exhibited promising properties in relation to non-enzymatic glucose sensing and it was shown using control experiments that it was the presence of both Au_{nano} and Pd_{nano} that facilitated these improvements. Using CV the onset of glucose oxidation began at more negative potentials in comparison to the potentials of oxidation at the fMWCNT-Au_{nano} composite films. Because of this shift, it was hoped that glucose detection could be conducted in potential regions at which, AA and UA would not be detected, since the oxidation of the two interferants generally occurs at more positive potentials. Experimental work related to chemical interference at all composite films is discussed in Chapter 5.

Having discovered the general conditions necessary for the development of the fMWCNT-Au_{nano}/Pd_{nano} composite film on a GC electrode, the system was then miniaturised using SPEs (DRP-150). It was again evident that Pd electrodeposition for the duration of 240 s yielded optimum glucose sensitivity, although a potential of -0.10 V vs Ag/AgCl was used due to a change in the reference electrode type. Using the SPEs, PdNPs with a mode diameter of 95 nm were again formed on the composite film.

CPA experiments were then carried out using the modified SPEs at the constant potentials of -0.05 V and -0.45 V vs Ag/AgCl. The potential of -0.05 V vs. Ag/AgCl was chosen for comparisons with the detection at the fMWCNT-Au_{nano} modified SPE and due to its location just after the large forward oxidation wave for glucose. The more negative potential of -0.45 V vs Ag/AgCl was used for the possible avoidance

of certain interferants, results of which are discussed in the following Chapter 5. Glucose detection using CPA at -0.05 V vs. Ag/AgCl yielded a linear calibration curve, although overall sensitivity was less than that for the fMWCNT-Au_{nano} modified SPE. The use of the more negative potential of -0.45 V vs. Ag/AgCl was possible, although sensitivities were even further reduced along with non-linear trends in the data obtained. This non-linearity may have implications in future sensing work at this potential.

Morphological, qualitative and quantitative characterisations of the composite films were carried out using SEM, EDX and XRD. Electrochemical characterisations were conducted using scan rate analyses and EIS. It was confirmed through analysis of all films that PdNPs were present at significant concentrations. PdNPs existed mainly below 100 nm in diameter in all films, including in the controls, and at a concentration of ~ 3% wt. Au was also detected in the films, although at % weights slightly under the pre-calculated 2% wt.

Scan rate analyses of these films, formed on both GC electrodes and on SPEs yielded some valuable information. Unfortunately data obtained from these analyses could not be applied to the Randles-Sevcik equation for electroactive surface measurements due to the contribution of TLD. Nevertheless information on the electron transfer processes of the films could be determined using the redox peak separations (ΔE) of the resulting CVs. It was determined that sluggish electron transfer processes occurred when using the SPEs and there were no noticeable differences between data for the fMWCNT-Au_{nano}/Pd_{nano} and the fMWCNT-Au_{nano} composites. Limitations in electron transfer were largely due to the underlying carbon substrate of the SPEs. These limitations may explain why the current responses obtained for glucose at the composite modified films did not reach expected values.

Results obtained from EIS analyses of the fMWCNT-Au_{nano}/Pd_{nano} films, followed the same trends as those of the fMWCNT-Au_{nano} films. Measured capacitance values increased as more negative potentials were applied and the resistance values followed the opposite trend. These trends also occurred at the fMWCNT-Au_{nano} composite films and the only major difference was that results obtained for the fMWCNT-

Au_{nano}/Pd_{nano} modified composite may indicate the presence of slightly larger surface areas. This can be explained due to the presence of Pd_{nano}.

4.4 References

1. A. J. Bard and L. R. Faulkner, *Electrochemical Methods: Fundamentals and Applications*, John Wiley & Sons, New York, 2001.
2. M. Taketani and M. Baudry, *Advances in Network Electrophysiology: Using Multi-Electrode Arrays*, Springer, 2006.
3. J. Xu, C. Zhang, X. Wang, H. Ji, C. Zhao, Y. Wang and Z. Zhang, *Green Chemistry*, 2011, **13**, 1914-1922.
4. X. Chen, H. Pan, H. Liu and M. Du, *Electrochimica Acta*, 2010, **56**, 636-643.
5. T. L. Lomocso and E. A. Baranova, *Electrochimica Acta*, 2011, **56**, 8551-8558.
6. S. B. Aoun, Z. Dursun, T. Koga, G. S. Bang, T. Sotomura and I. Taniguchi, *Journal of Electroanalytical Chemistry*, 2004, **567**, 175-183.
7. K. Soliman, L. Kibler and D. Kolb, *Electrocatalysis*, 2012, **3**, 170-175.
8. Z. Dursun, S. B. Aoun and I. Taniguchi, *Turkish Journal of Chemistry*, 2008, **32**, 423 – 430.
9. Z. Liu, J. Y. Lee, W. Chen, M. Han and L. M. Gan, *Langmuir*, 2003, **20**, 181- 187.
10. V. Stamenkovic, M. Arenz, B. B. Blizanac, P. N. Ross and N. M. Markovic, *Journal of New Materials for Electrochemical Systems*, 2004, **7**, 125-132.
11. L. Y. Chen, X. Y. Lang, T. Fujita and M. W. Chen, *Scripta Materialia*, 2011, **65**, 17-20.
12. Y. Li, Y.-Y. Song, C. Yang and X.-H. Xia, *Electrochem. Commun.*, 2007, **9**, 981-988.
13. J. Leng, W.-M. Wang, L.-M. Lu, L. Bai and X.-L. Qiu, *Nanoscale Research Letters*, 2014, **9**, 99.
14. H. Gao, F. Xiao, C. B. Ching and H. Duan, *ACS Applied Materials & Interfaces*, 2011, **3**, 3049-3057.
15. S. Vashist, *Diagnostics*, 2013, **3**, 385-412.
16. R. Thangamuthu, Y.-C. Wu and S.-M. Chen, *Electroanalysis*, 2009, **21**, 165- 171.
17. L. Wang, P. Huang, J. Bai, H. Wang, X. Wu and Y. Zhao, *International Journal of Electrochemical Science*, 2006, **1**, 334-342.
18. C. Liao, M. Zhang, L. Niu, Z. Zheng and F. Yan, *J. Mater. Chem. B*, 2013, **1**, 3820-3829.
19. F. G. Banica, *Chemical Sensors and Biosensors: Fundamentals and Applications*, John Wiley & Sons, Chichester, West Sussex, 2012.
20. N. Kasai and M. Kakudo, *X-Ray Diffraction by Macromolecules*, 2005.
21. B. D. Cullity, *Elements Of X Ray Diffraction*, Addison-Wesley, 1956.
22. J.-J. Lv, S.-S. Li, A.-J. Wang, L.-P. Mei, J.-R. Chen and J.-J. Feng, *Electrochimica Acta*, 2014, **136**, 521-528.
23. X. Hou, L. Wang, X. Wang and Z. Li, *Diamond and Related Materials*, 2011, **20**, 1329-1332.
24. Y. Shi, R. Yang and P. K. Yuet, *Carbon*, 2009, **47**, 1146-1151.

25. Z. Wang, C. Xu, G. Gao and X. Li, *RSC Advances*, 2014, **4**, 13644-13651.
26. R. K. Petla, S. Vivekanandhan, M. Misra, A. K. Mohanty and N. Satyanarayana, *Journal of Biomaterials and Nanobiotechnology*, 2012, **3**, 14- 19.
27. F. G. Thomas and G. Henze, *Introduction to Voltammetric Analysis: Theory and Practice*, CSIRO Publishing 2001.
28. I. Svancara, K. Kalcher, A. Walcarius and K. Vytras, *Electroanalysis with Carbon Paste Electrodes*, CRC Press, 2012.
29. T. Ndlovu, O. A. Arotiba, S. Sampath, R. W. Krause and B. B. Mamba, *Int. J. Electrochem. Sci.*, 2012, **7**, 9441-9453.
30. G. P. Keeley and M. E. G. Lyons, *International Journal of Electrochemical Science*, 2009, **4**, 794 - 809
31. M. J. Sims, N. V. Rees, E. J. F. Dickinson and R. G. Compton, *Sensors and Actuators B: Chemical*, 2010, **144**, 153-158.
32. M. Gara and R. G. Compton, *New Journal of Chemistry*, 2011, **35**, 2647-2652.
33. M. C. Henstridge, E. J. F. Dickinson, M. Aslanoglu, C. Batchelor-McAuley and R. G. Compton, *Sensors and Actuators B: Chemical*, 2010, **145**, 417-427.
34. L. Xiao, G. G. Wildgoose and R. G. Compton, *Sensors and Actuators B: Chemical*, 2009, **138**, 524-531.
35. I. Streeter, G. G. Wildgoose, L. Shao and R. G. Compton, *Sensors and Actuators B: Chemical*, 2008, **133**, 462-466.
36. S. A. Wring and J. P. Hart, *Analyst (London)*, 1992, **117**, 1215-1229.
37. H. S. Nalwa, *Handbook of Surfaces and Interfaces of Materials, Five-Volume Set*, Academic Press, 2001.
38. E. Barsoukov and J. R. Mac Donald, *Impedance Spectroscopy: Theory, Experiment, and Applications*, John Wiley & Sons, New Jersey, 2005.
39. V. F. Lvovich, *Impedance Spectroscopy: Applications to Electrochemical and Dielectric Phenomena*, John Wiley & Sons, New Jersey, 2012.

Chapter 5

Chemical Interference at all Composite Modified Screen Printed Electrodes and Reusability and Shelf-Life Studies

5.1 Introduction

In this chapter the effect of chemical interference at each of the fMWCNT-Au_{nano}, fMWCNT-Au_{nano}/Nafion® and fMWCNT-Au_{nano}/Pd_{nano} composite modified SPEs is investigated using various chemical species which can be present in the blood. These composite films were produced using the same methods used in Chapter 2, Section and 2.2.6.4 for the fMWCNT-Au_{nano} and fMWCNT-Au_{nano}/Nafion® modified SPEs, respectively, and in Chapter 2, Section 2.2.7, for the fMWCNT-Au_{nano}/Pd_{nano} composite film. As discussed in Chapter 3 and 4, only the fMWCNT-Au_{nano}(NaBH4) composite, produced using the $NaBH_4$ reducing agent was used as that produced using trisodium citrate lacked stability. The name of the composite was shortened hereon to fMWCNT-Au_{nano} for clarity. Only the modified SPEs were used in this study as they provided better sensitivity towards glucose, in comparison to the modified GC electrodes, discussed in Chapter 3.

Ascorbic acid (AA) and uric acid (UA) are two electroactive species investigated, which exist in high concentrations physiologically and are known to cause significant problems in electrochemical sensors. The presence of the monosaccharides fructose and galactose is also studied, which are similar carbohydrates to glucose. The effect of chloride and serum albumins on glucose sensing is also investigated, along with the possible effects of the commonly used drug acetaminophen. Reusability and shelf-life studies are undertaken to determine the reproducibility of the sensors over use and time.

5.2 Results and Discussion

5.2.1 Interferences from Chemical Interferants

All of the fMWCNT-Au_{nano} modified SPEs were produced using the same method discussed in Chapter 2, Section 2.2.6.2, in which 10.0 µl of a 4.0 mg/ml fMWCNT-Au_{nano} dispersion in 1.0% SDS was cast onto a SPE (DRP-150). These films were then electrochemically pre-treated in 0.3 M NaOH and 1.0 M H_2SO_4 solutions. To produce the fMWCNT-Au_{nano}/Nafion® films, 3.0 µl of a 50:50 (vol/vol) Nafion 117® solution made in ethanol absolute was cast onto the prepared fMWCNT-Au_{nano} composite films, as discussed in Chapter 2, Section 2.2.6.4. The fMWCNT-Au_{nano}/Pd_{nano} composite films were formed using the same procedure discussed in Chapter 2, Section 2.2.7, in which Pd was electodeposited onto the surface of pre-existing fMWCNT-Au_{nano} films at -0.10 V vs. Ag/AgCl for 240 s in a 2.5 mM $PdSO_4$ solution made in 0.5 M H_2SO_4. Nafion® was not applied to these fMWCNT-Au_{nano}/Pd_{nano} composite films as it was hoped that selective glucose detection would be possible at these films in the response of interferants due to the negative potential of -0.45 V vs. Ag/AgCl being used during CPA analyses.

Cyclic voltammetry (CV) was employed initially to investigate the possible current responses arising from the oxidation and/or reduction of the chemical interferants being investigated. This analysis was useful for determining the onset potentials for the oxidation of the species which could help determine if they would be oxidisable at the potentials used during constant potential amperometry (CPA) experiments. Glucose detection in the presence of these interferants was not undertaken using CV. Using CPA the electrochemical response of each interferant was investigated in both the presence and absence of glucose. During CPA experiments in the presence of glucose an injection of 4.0 mM glucose was initially conducted as to observe its oxidation current response, this was followed by the chemical interferant as to observe any increase or decrease in the currents comparatively with that of glucose. Any increases in the currents would imply that oxidation of the interferant was occurring and a decrease would indicate a surface poisoning process. Aliquots of glucose were injected post-interferant as to determine if glucose detection remained possible. Also,

the detection of these interferants in the absence of glucose was undertaken as to eliminate any possibility of current masking by glucose.

5.2.1.1 Ascorbic Acid

Ascorbic acid (AA), also known as vitamin C, is a water soluble antioxidant compound needed in a number of metabolic reactions in animals and plants, including the synthesis of collagen and the maintenance of healthy teeth, gums and blood vessels [1]. Although the presence of AA is essential, it can be a problematic interfering compound in electrochemical sensing systems [2] and is present in the blood at high levels, up to 0.10 mM [3]. AA exists in its anionic form, ascorbate, at physiological pH, as shown in Scheme 5.1, and is an electroactive compound that can be easily oxidised at many electrode substrates and over broad potential ranges [4]. The electrooxidation of AA is irreversible and is believed to be a two electron step producing dehydro-l-ascorbic acid [5]. In addition, the products of AA oxidation can foul electrode surfaces thereby resulting in a decrease in the current responses at solid electrodes [6].

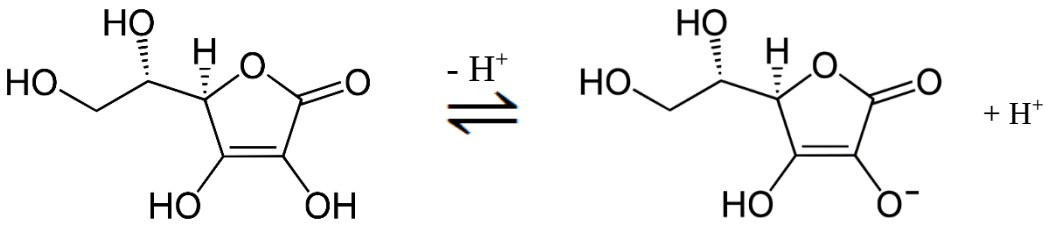

Scheme 5.1: Dissociation of Ascorbic Acid

To possibly overcome interference from AA and other anionic species present during electrochemical sensing, negatively charged membranes can be used, of which Nafion® proves useful [6]. Nafion® is a fluorosulfonated polyanion material which can be coated onto an electrode and it excludes anionic interferences through electrostatic repulsion [7]. Other useful materials for this purpose include overoxidised polypyrrole [8], anionic surfactants [9], chitosan [7] and poly(o-phenylenediamine) [10].

5.2.1.1.1 Interference from Ascorbic Acid at SPE/fMWCNT-Au_{nano} and SPE/fMWCNT-Au_{nano}/Nafion® Films

Cyclic voltammetry (CV) was the electrochemical technique used initially for the investigation of AA and other chemical interference at the composite modified films. Using CV, the current responses and the onset potentials for the oxidation of the chemical species could be visualised. This provided useful insight into the possibility of interference when using constant potential amperometry (CPA).

Two AA concentrations, 0.10 mM and 0.50 mM, were studied. AA exists at a maximum concentration of 0.10 mM in the blood and as such this is the most relevant concentration studied. The higher concentration of 0.50 mM was investigated for easier visualisation of the oxidation responses, which was less apparent at the lower concentration of 0.10 mM AA. It is clear that the detection of AA is possible at the fMWCNT-Au_{nano} modified SPE, shown in Figure 5.1 (a), although the current responses are not overly significant even at the maximum physiological blood concentration of 0.10 mM. The 0.50 mM AA yielded larger currents, as expected, with a peak current of 2.86×10^{-5} A (28.6 μA), resulting at -0.15 V vs. Ag/AgCl. It is also evident that AA oxidation occurs over a broad potential range, from -0.30 V to 0.20 V vs. Ag/AgCl, which may be problematic as it coincided with the potential of -0.05 V used for glucose detection during CPA. However, having applied the Nafion® membrane the interference of AA at both concentrations is greatly reduced, as seen in Figure 5.1 (b). Again the peak current for 0.10 mM AA is not measurable at the fMWCNT-Au_{nano}/Nafion® SPE, although that of the 0.50 mM AA at -0.15 V vs. Ag/AgCl is 1.04×10^{-5} A (10.4 μA). This corresponds to over a 60% reduction in interference using Nafion®.

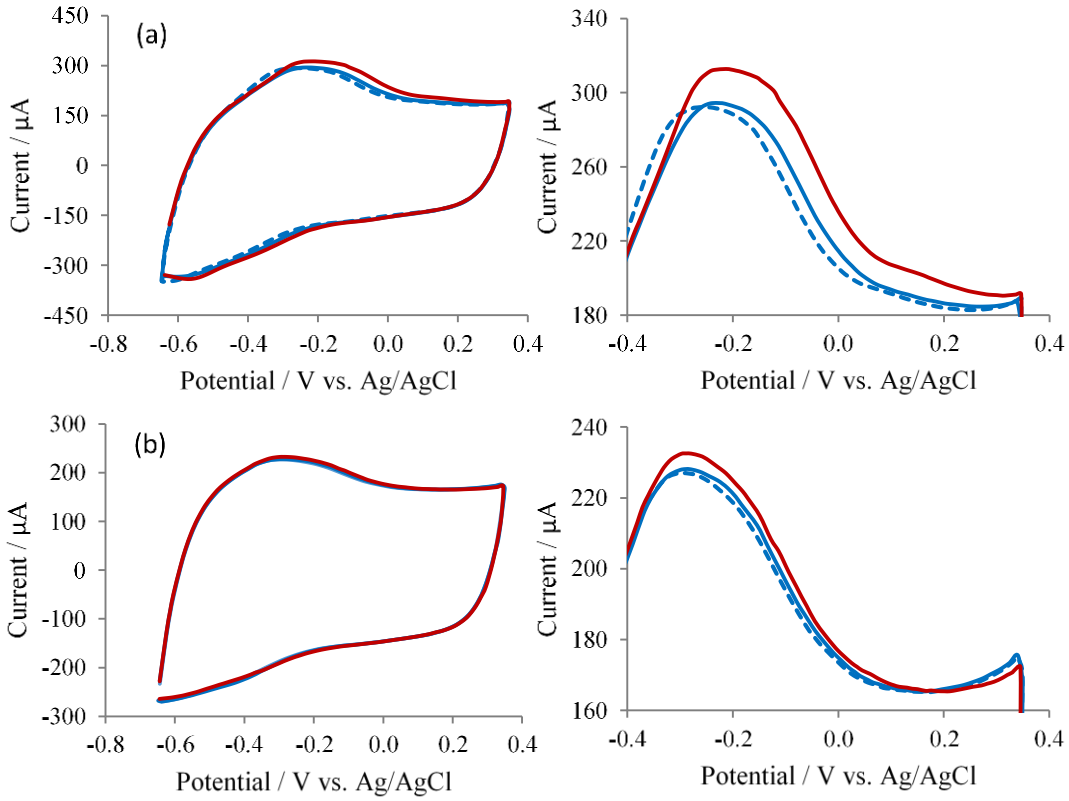

Figure 5.1: Cyclic voltammograms, recorded at 100 mV s^{-1}, of **(a)** the fMWCNT-Au_{nano} and **(b)** fMWCNT-Au_{nano}/Nafion® modified SPEs in a - - - 0.10 M PBS solution (pH 7.40) and PBS solutions containing — 0.10 mM and — 0.50 mM ascorbic acid. Magnified sections of the CVs showing the oxidation waves for AA are shown to the right.

After the CV experiments, AA interference at the composite films was investigated using CPA. Experiments were initially conducted in the presence of glucose to compare the current responses relative to glucose and to observe any possible surface fouling by AA. Aliquots of glucose were injected prior to and after AA injection. For all interference studies, the initial response for glucose was measured at 4.0 mM, then additions were made to give 8.0 mM and 12.0 mM glucose. Any significant reduction in the glucose currents during and after AA injection would indicate fouling from AA. As seen in Figures 5.2 (a) and (b) no interference from AA at 0.10 mM is apparent at either the fMWCNT-Au_{nano} or fMWCNT-Au_{nano}/Nafion® modified SPEs. This is not expected at the film without Nafion® as previous experiments using CV, Figure 5.1, indicate that slight current responses are possible at this concentration. However, when AA at 0.50 mM is present, a current response is evident, albeit small in

comparison to that of glucose. That of 0.50 mM AA yields a small current response of 0.25×10^{-5} A (2.5 μA), in comparison with that of 1.07×10^{-5} A (10.7 μA) for 4.0 mM glucose. The oxidation of 0.50 mM AA only causes over a 20% increase in the current relative to that of 4.0 mM glucose even at this excessively high concentration which is 5 times larger than that present in the blood. AA at this concentration is also detected at the Nafion® containing film, Figure 5.2 (b), although the currents are much less significant. The current for 0.50 mM AA is measured at 0.30×10^{-6} A (0.30 μA). This corresponds to a 90% decrease in interference in comparison to that at the fMWCNT-Au_{nano} films, shown in Figure 5.2 (a). Even though AA interference has been reduced using Nafion®, the films sensitivity towards glucose has been dramatically reduced also by almost 90%, as discussed in Chapter 3, Section 3.2.8. This Nafion® membrane equally reduced the detection of AA and glucose, although the stability of the glucose current responses in the presence of the Nafion® membrane have improved. No evidence of surface fouling by AA is apparent at this sensor even without Nafion® as the glucose responses post AA injection do not appear to be reduced and corresponded with the glucose calibration curves reported for these films in Chapter 3. It seems that the use of Nafion® is not necessary for the selective sensing of glucose at these films in the presence of this interferant at the concentrations studied.

Since no current responses were evident for 0.10 mM AA, it was thought that the currents from glucose may have been masking those of AA. CPA experiments with AA, in the absence of glucose were carried out to measure more accurate responses and this was also carried out for all of the interferants. Results and data are shown and discussed in Section 5.2.1.8.

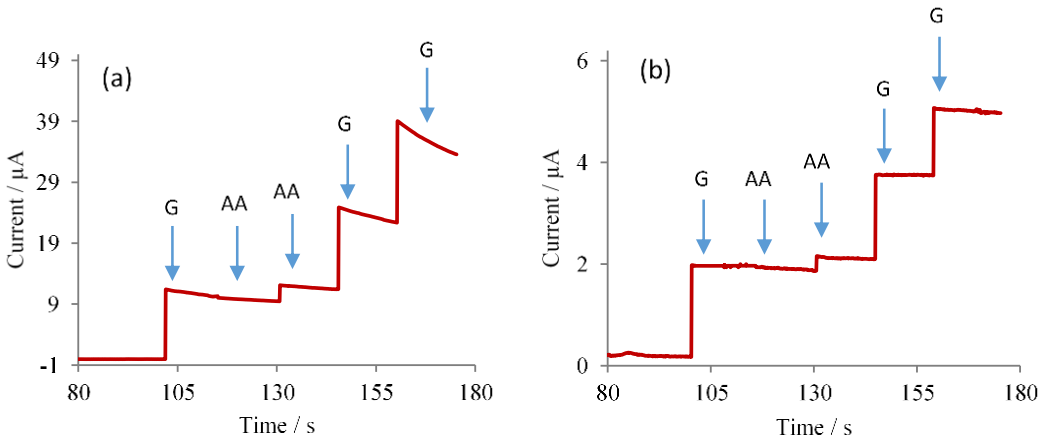

Figure 5.2: Current-time plots for the oxidation of glucose and ascorbic acid, recorded at -0.05 V vs. Ag/AgCl, at **(a)** the fMWCNT-Au_{nano} and **(b)** the fMWCNT-Au_{nano}/Nafion® modified SPEs in 0.10 M PBS (pH 7.40) with the successive additions of glucose (4.0, 8.0 and 12.0 mM) and ascorbic acid (0.10 and 0.50 mM) aliquots from stock solutions, made in 0.10 M PBS.

5.2.1.1.2 Interference from Ascorbic Acid at SPE/fMWCNT-Au_{nano}/Pd_{nano} Films

Interference from AA was also studied at the fMWCNT-Au_{nano}/Pd_{nano} modified SPE, using both CV and CPA. Results prove to be quite different in comparison to those of the previous fMWCNT-Au_{nano} films, as evident in Figures 5.3 (a) and (b). Although no measurable currents are again seen for 0.10 mM AA using CV and those of 0.50 mM are also small. The onset of interference begins at around -0.20 V vs. Ag/AgCl for the 0.50 mM AA and a peak current of 0.37×10^{-6} A (0.37 µA) can be measured at -0.15 V vs. Ag/AgCl. It is not entirely clear whether this increase in current is associated with the oxidation of AA or due to changes in the background currents due to fouling at the composite surface. This current is very similar to that obtained from a similar study at the fMWCNT-Au_{nano}/Nafion® sensor, Section 5.2.1.1.1. The onset for AA interference occurs at a much more positive potential than that used for glucose during CPA experiments, at -0.45 V vs. Ag/AgCl, and as such it was hoped that selective glucose detection would be possible using CPA in the presence of this interferant, even without Nafion®. Unfortunately this is not possible as surface fouling of the electrode occurs upon addition of AA, which can be seen during both CV and

CPA analyses, Figures 5.3 (a) and (b). The CV shown in Figure 5.3 (a) of the 0.50 mM AA shows a change in the large Pd oxide reduction peak, visible at -0.40 V vs. Ag/AgCl, whereby it decreases in intensity and shifts in potential to -0.22 V vs. Ag/AgCl. This may indicate that some surface AA adsorption is occurring. When CPA is employed, in the presence of glucose, no oxidation of AA is apparent, although a sharp decrease in the current occurs which again indicates a fouling process. The initial current obtained for 4.0 mM glucose is 0.45×10^{-5} A (4.5 μA), although this is reduced by 50% and 70%, to 0.23×10^{-5} A (2.3 μA) and 0.14×10^{-5} A (1.4 μA) in the presence of 0.10 mM and 0.50 mM AA, respectively. Further glucose detection post AA injection is severely affected and as such accurate detection of glucose is not possible at this film in the presence of AA. Again, detection of AA at this film in the absence of glucose is discussed in Section 5.2.1.8 as to examine any possible current masking by glucose. As mentioned previously, these sensors were not modified with Nafion®, as their actual purpose was to avoid its use.

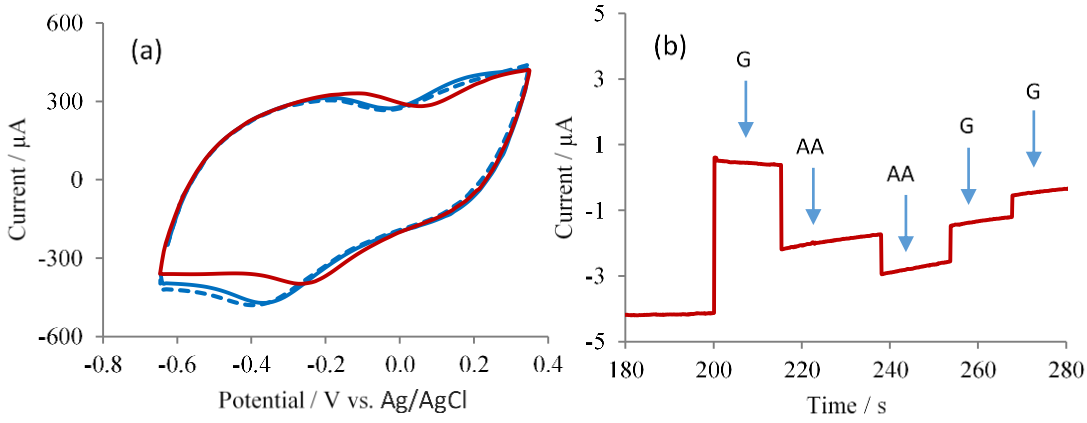

Figure 5.3: (a) Cyclic voltammogram, recorded at 100 mV s^{-1}, of the fMWCNT-Au_{nano}/Pd_{nano} modified SPE in a - - - 0.10 M PBS solution (pH 7.40) and PBS solutions containing — 0.10 mM and — 0.50 mM ascorbic acid. Figure 5.3 **(b)** shows the current-time plot for the oxidation of glucose and ascorbic acid, recorded at -0.45 V vs. Ag/AgCl, at the fMWCNT-Au_{nano}/Pd_{nano} modified SPE in 0.10 M PBS (pH 7.40) with the successive additions of glucose (4.0, 8.0 and 12.0 mM) and ascorbic acid (0.10 and 0.50 mM) aliquots from stock solutions, made in 0.10 M PBS.

5.2.1.2 Uric Acid

Uric acid (UA) is a naturally occurring compound found in the human body and is the primary end product of purine metabolism [11]. UA is known to possess antioxidant properties, although abnormally high concentrations, a condition known as hyperuricemia, can be associated with several diseases such as gout, insulin resistance, hypertension and cardiovascular disease [11]. Lower UA levels, known as hypouricemia, can be associated with Alzheimer's disease [12] and multiple sclerosis [13]. UA exists alongside glucose in the blood at normal-high concentrations ranging from 4.8 – 7.1 mg/dl (0.28 – 0.42 mM) in women and from 5.80 – 7.60mg/dl (0.34 – 0.45 mM) in men [14], with higher levels being hyperuricemic. Although these concentrations are much lower than those present for glucose, UA is an electroactive species and may be oxidised and cause surface fouling at electrode surfaces [15]. The electrooxidation of UA is reported to be an irreversible two electron process in which UA is oxidsed firstly to 4,5-dihydroxyluric acid, which is unstable and then into allantoin [16]. Its oxidation potentials usually overlap those of other species at conventional electrodes [17]. These problems make UA a very challenging interfering

compound in the selective detection of other analytes [17]. At physiological pH, UA exists primarily in its anionic form urate and its dissociation involves keto-enol tautomerism in which its deprotonation occurs at one of the monohydroxy tautomers [18], shown in Schematic 5.2. Due to its existence as urate, the use of Nafion® can be beneficial for reducing its interference [19].

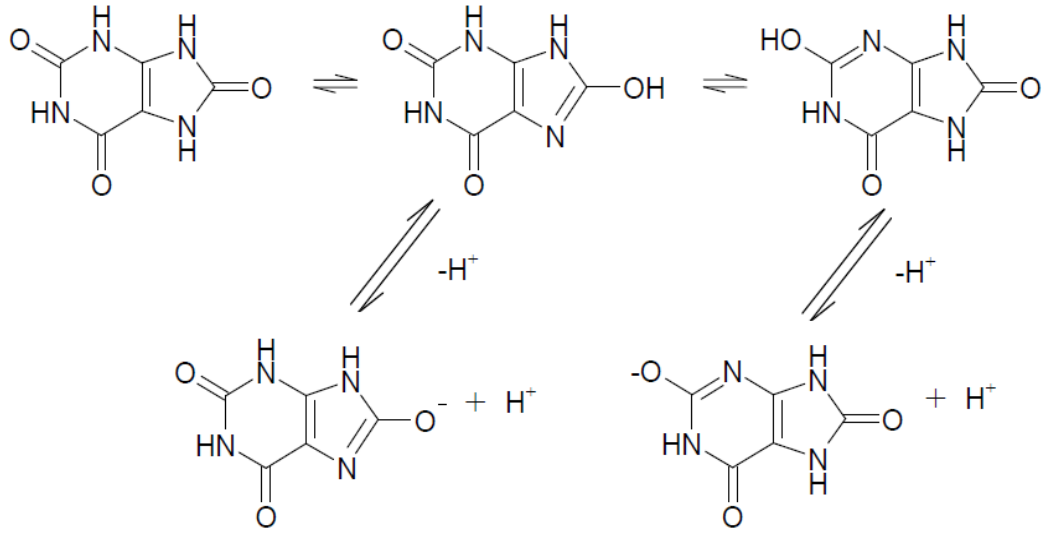

Scheme 5.2: Dissociation of Uric Acid

5.2.1.2.1 Interference from Uric Acid at SPE/fMWCNT-Au_{nano} and SPE/fMWCNT-Au_{nano}/Nafion® Films

Interference from UA was studied using both CV and CPA. Two concentrations of UA were studied, 0.37 mM and 0.45 mM UA, which correspond to the lower and upper levels of UA present in males, respectively. It is evident that UA causes interference at the fMWCNT-Au_{nano} modified SPE, as can be seen in the CVs displayed in Figure 5.4 (a), in which there are broad current responses ranging from -0.40 V to 0.30 V vs. Ag/AgCl. The 0.37 mM UA yields a peak current of 2.80×10^{-5} A (28.0 µA) at -0.07 V vs. Ag/AgCl and as expected, the higher concentration of 0.45 mM yields a higher peak current of 6.04×10^{-5} A (60.4 µA). The use of a Nafion® membrane proves very useful in reducing interference from this interferant, as seen in Figure 5.4 (b). Currents for 0.37 mM UA are not measurable using CV, although that of 0.45 mM are reduced and a peak current of 2.00×10^{-5} A (20.0 µA) can be measured

at -0.07 V vs. Ag/AgCl. The use of Nafion® reduces this signal for AA at 0.45 mM by almost 70%, although a signal is still apparent within a potential range below that used for the detection of glucose using CPA.

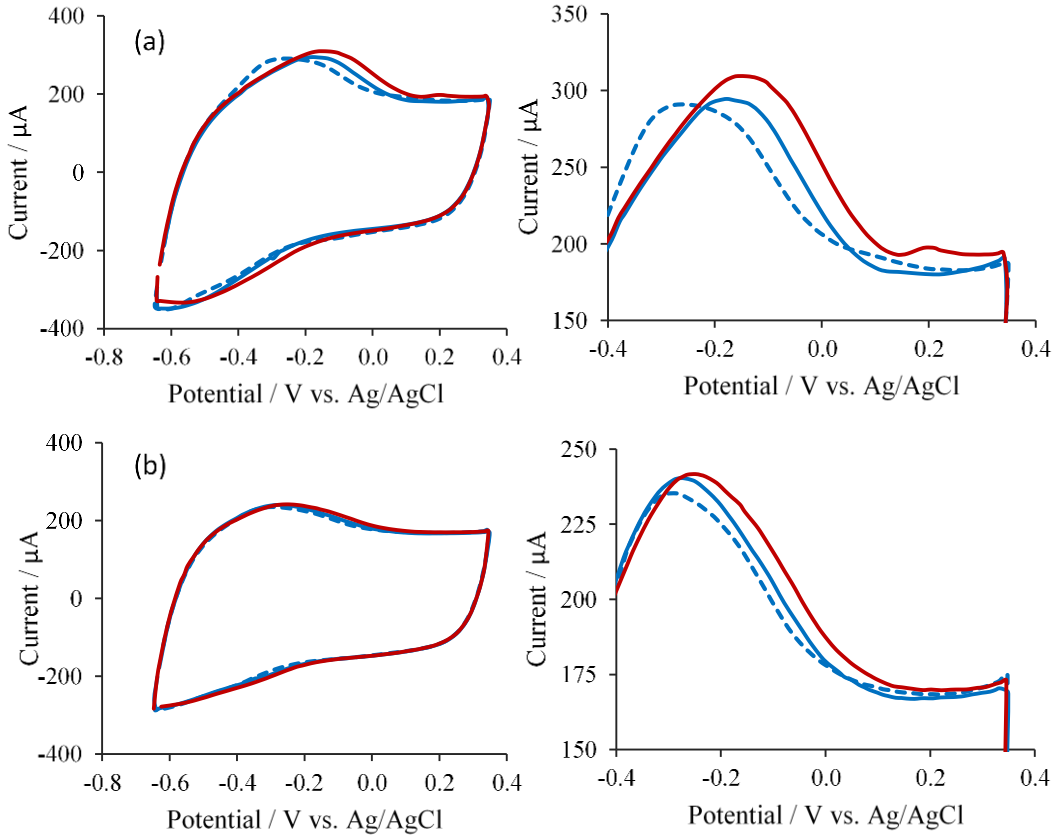

Figure 5.4: Cyclic voltammograms, recorded at 100 mV s^{-1}, of **(a)** the fMWCNT-Au_{nano} and **(b)** fMWCNT-Au_{nano}/Nafion® modified SPEs in a - - - 0.10 M PBS solution (pH 7.40) and PBS solutions containing — 0.37 mM and — 0.45 mM uric acid. Magnified sections of the CVs showing the oxidation waves for UA are shown to the right.

CPA studies were conducted similarly to those of the previous studies using AA. Again, glucose was injected initially, followed by UA for comparison of the currents and then by glucose to investigate any electrode fouling by UA. It is clear that without a Nafion® membrane, UA poses a serious problem at the fMWCNT-Au_{nano} film, as seen in Figure 5.5 (a). Currents for glucose have almost completely diminished upon the injection of UA and the currents obtained for the additional injections of glucose post-injection are severely reduced. Using Nafion®, interference from UA is greatly reduced, although not eliminated and glucose detection post UA injection is not as

severely hindered. The initial current for 4.0 mM glucose is 0.19×10^{-5} A (1.9 μA) at the fMWCNT-Au_{nano}/Nafion® film, although this is reduced by 20% to 0.15×10^{-5} A (1.5 μA) with the addition of UA. This reduction may indicate surface fouling by UA. To completely eliminate UA interference, an increased amount of Nafion® could be applied to the sensor, although this would reduce the sensitivity towards glucose even further and as such was not conducted. The present decrease in glucose sensitivity using this membrane is almost 90%, as discussed in Chapter 3, Section 3.2.8. No oxidation of UA is apparent at these films, although currents could be masked by those of glucose. Results shown in Section 5.2.1.8, discuss UA detection in the absence of glucose.

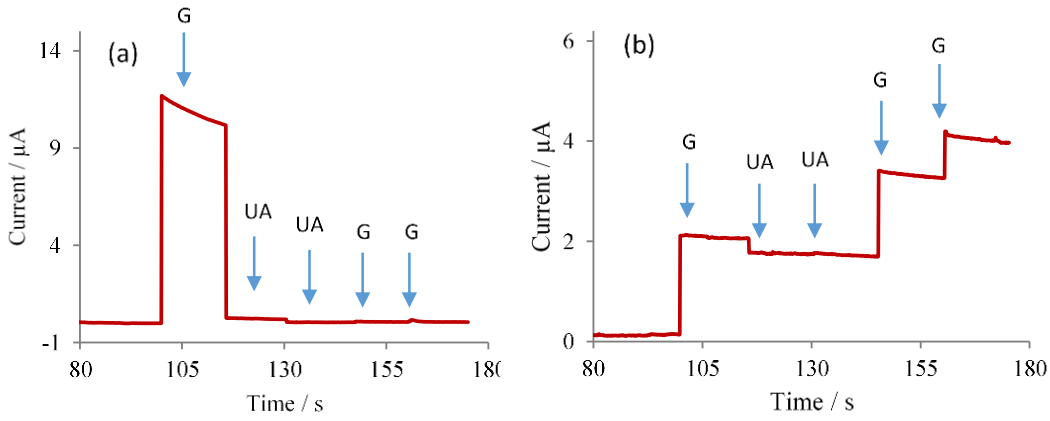

Figure 5.5: Current-time plots for the oxidation of glucose and uric acid, recorded at -0.05 V vs. Ag/AgCl, at **(a)** the fMWCNT-Au_{nano} and **(b)** the fMWCNT-Au_{nano}/Nafion® modified SPEs in 0.01 M PBS (pH 7.40) with the successive additions of glucose (4.0, 8.0 and 12.0 mM) and uric acid (0.37 and 0.45 mM) aliquots from stock solutions, made in 0.10 M PBS.

5.2.1.2.2 Interference from Uric Acid at SPE/fMWCNT-Au_{nano}/Pd_{nano} Films

As with the previous studies with AA at the fMWCNT-Au_{nano}/Pd_{nano} modified SPE, Section 5.2.1.1.2, UA also appeared to be a significant source of interference at this composite film. It can be seen in the CVs in Figure 5.6 (a) that current responses for UA occurs over a wide potential range, from about -0.40 V to 0.30 V vs. Ag/AgCl. As in Section 5.2.1.1.2, it is not entirely clear if oxidation of UA is occurring at this film, or if a surface fouling process is causing changes in the background currents. As such peak currents for UA were not assigned using CV analysis. Also, a decrease and shift in the Pd oxide reduction peak, at -0.40 V vs. Ag/AgCl, is noticeable and this change is most apparent with the higher concentration of UA at 0.42 mM. These results indicate that UA has a fouling effect at the composite surface. When CPA is used for the detection of both glucose and UA, Figure 5.6 (b), again evidence of surface fouling is apparent due to the decrease in the currents for glucose during and after UA injection. The initial currents achieved for 4.0 mM glucose, are decreased by about 35% and by almost 100% in the presence of 0.37 mM and 0.45 mM UA, respectively. It was hoped that UA would not have any effect on glucose detection during CPA at such a negative potential, due to its more positive onset of oxidation. Although oxidation of UA is not apparent in this study UA fouled the sensing surface

and almost eliminated glucose detection. As such, this sensor would not be suitable for accurate glucose sensing in the presence of UA. As in other studies, UA detection in the absence of glucose is carried out, data shown in Section 5.2.1.8.

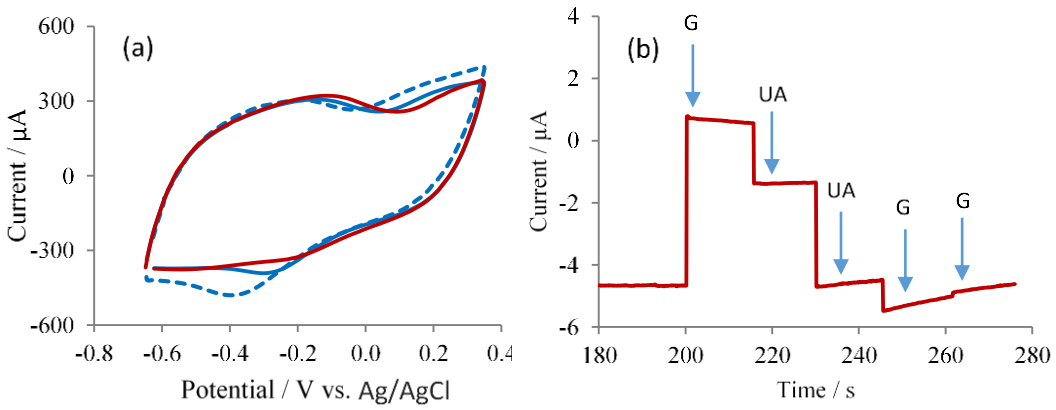

Figure 5.6: (a) Cyclic voltammogram, recorded at 100 mV s^{-1}, of the fMWCNT-Au_{nano}/Pd_{nano} modified SPE in a - - - 0.10 M PBS solution (pH 7.40) and PBS solutions containing ▬ 0.37 mM and ▬ 0.45 mM uric acid. Figure 5.6 **(b)** shows the current-time plot for the oxidation of glucose and uric acid, recorded at -0.45 V vs. Ag/AgCl, at the fMWCNT-Au_{nano}/Pd_{nano} modified SPE in 0.10 M PBS (pH 7.40) with the successive additions of glucose (4.0, 8.0 and 12.0 mM) and uric acid (0.37 and 0.45 mM) aliquots from stock solutions, made in 0.10 M PBS.

5.2.1.3 Galactose

Galactose (Gal) is a monosaccharide sugar and a C-4 epimer of glucose and is one of two products of lactose digestion, the other being glucose [20]. At equilibrium, galactose predominately exists as four isomers, α-D-galactopyranose (33.3%), β-D-galactopyranose (62.5%), α-D-galactofurnose (1.4%) and β-D-galactofuranose (2.8%) [21], as shown in Scheme 5.3. Normal physiological concentrations typically exist below 6 mg/dl (0.33 mM) [22] although they may be as high as 10 mg/dl (0.55 mM) [23]. Abnormally high levels of galactose in the blood is known as galactosemia and is a metabolic disorder primarily arising in the neonatal period. Galactocemia is caused by deficiencies in either galactokinase (galactosemia type II), galactose-1-phosphate uridyltransferase (GALT, galactosemia type I) or uridine diphosphate

galactose-4-epimerase (galactosemia type III). GALT is the most severe of these three and results in the accumulation of galactose in the blood to toxic levels [22]. Other than its possible effects on health, galactose has shown to be a source of interference at electrochemical glucose sensors in which it can be oxidised along with glucose [24-27]. Electrochemical oxidation of galactose predominantly yields galactonic acid after prolonged electrolyses along with traces of other species, according to HPLC analysis [28]. As such, interference from galactose has been studied at the composite modified electrode using both CV and CPA.

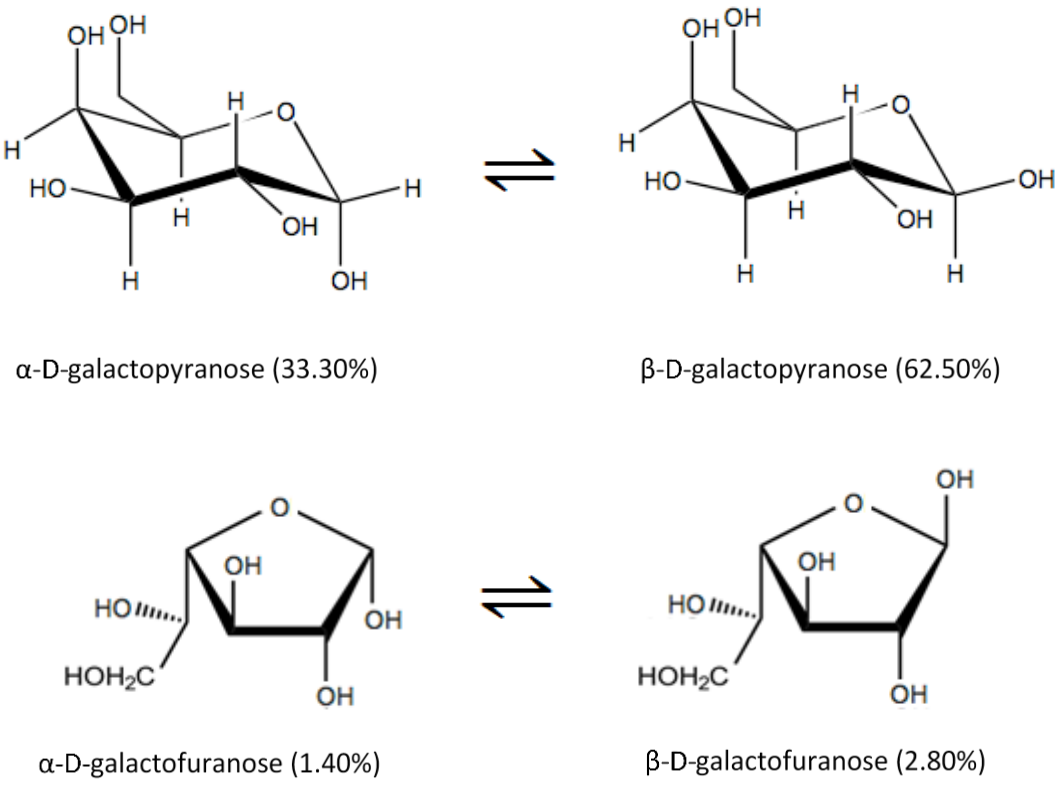

Scheme 5.3: Mutarotation of Galactose

5.2.1.3.1 Interference from Galactose at SPE/fMWCNT-Au$_{nano}$ and SPE/fMWCNT-Au$_{nano}$/Nafion® Films

CV was employed initially, followed by CPA using three galactose concentrations of 0.25 mM, 0.55 mM and 1.00 mM, representing low, high and excessively high concentrations. On the basis of the CV analyses, little evidence of interference is seen

at the fMWCNT-Au_{nano} and fMWCNT-Au_{nano}/Nafion® composite films, Figures 5.7 (a) and (b). No measurable currents occur for all the concentrations used at either films using CV analysis. Because of this, interference during CPA experiments were expected to be minimal.

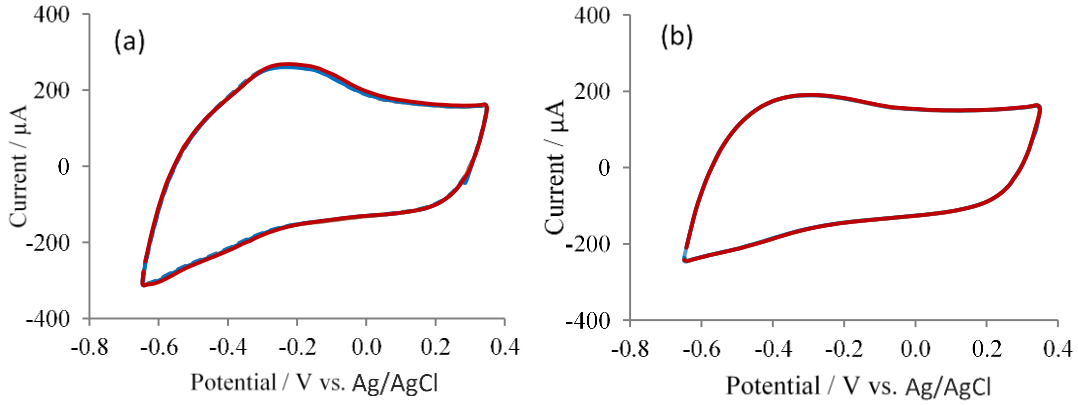

Figure 5.7: Cyclic voltammograms, recorded at 100 mV s^{-1}, of **(a)** the fMWCNT-Au_{nano} and **(b)** fMWCNT-Au_{nano}/Nafion® modified SPEs in a - - - 0.10 M PBS solution (pH 7.40) and PBS solutions containing — 0.25 mM, — 0.55 mM and —1.00 mM galactose.

CPA analyses were conducted using the three concentrations of galactose. Oxidation of galactose occurred at these concentrations, as can be seen in Figures 5.8 (a) and (b), although the currents are small in comparison to those of glucose. At the fMWCNT-Au_{nano} film a current of 1.05×10^{-5} A (10.5 µA) is measured for the initial 4.0 mM glucose addition. No current increase is apparent upon the first injection of galactose, which corresponds to 0.25 mM galactose. Although currents increase by 3% and 10% to 1.08×10^{-5} A (10.8 µA) and 1.15×10^{-5} A (11.5 µA) in the presence of 0.55 mM and 1.00 mM galactose, respectively. At the fMWCNT-Au_{nano}/Nafion® film a current of 0.18×10^{-5} A (1.8 µA) is measured for the initial 4.0 mM glucose addition. This current increases by 6%, 12% and 25%, to 0.19×10^{-5} A (1.9 µA), 0.20×10^{-5} A (2.0 µA) and 0.22×10^{-5} A (2.2 µA) in the presence of 0.25 mM, 0.55 mM and 1.00 mM galactose, respectively. At both systems, glucose detection post galactose addition do not appear affected. The oxidation of galactose in the absence of glucose at these films is discussed in Section 5.2.1.8. Overall glucose detection appears unaffected which indicates that no poisoning of the electrode surface is occurring. These results indicate

that accurate and selective detection of physiological glucose in the presence of physiological concentrations of galactose is possible using these sensing films.

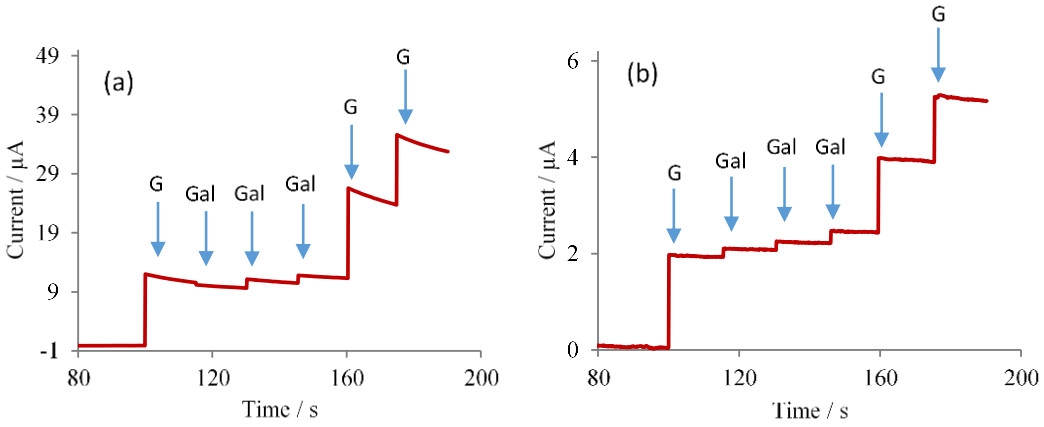

Figure 5.8: Current-time plots for the oxidation of glucose and galactose, recorded at -0.05 V vs. Ag/AgCl, at **(a)** the fMWCNT-Au_{nano} and **(b)** the fMWCNT-Au_{nano}/Nafion® modified SPEs in 0.10 M PBS (pH 7.40) with the successive additions of glucose (4.0, 8.0 and 12.0 mM) and galactose (0.25, 0.55 and 1.00 mM) aliquots from stock solutions, made in 0.10 M PBS.

5.2.1.3.2 Interference from Galactose at SPE/fMWCNT-Au_{nano}/Pd_{nano} Films

Using CV, no evidence of galactose oxidation is evident, Figure 5.9 (a). CPA results initially followed the same trend, as seen in Figure 5.9 (b), in which the first two injections of 0.25 mM and 0.55 mM galactose did not result in an increase in the current. However the third injection, corresponding to 1.00 mM galactose did yield a slight increase, although this is not accurately measureable. As in previous interference studies with AA and UA, Sections 5.2.1.1.2 and 5.2.1.2.2, it appears that galactose causes some surface fouling as the currents arising from the initial 4.0 mM glucose injection are reduced. The initial 4.0 mM glucose yields a current of 0.42×10^{-5} A (4.2 µA), although this decreases by about 20% in each instance to 0.34×10^{-5} A (3.4 µA), 0.32×10^{-5} A (3.2 µA) and 0.34×10^{-5} A (3.4 µA) in the presence of 0.25 mM, 0.55 mM and 1.00 mM galactose, respectively.

No oxidation of galactose is observed initially and a significant decrease in the initial glucose current occurred post injection. This also occurs with the second galactose

injection although a slight increase in the current occurs with the third injection. The currents for glucose post galactose also appear to be reduced. These findings indicate that galactose is reducing the films sensitivity towards glucose possibly due to a surface poisoning effect. Oxidation of galactose is indeed possible at this film at high concentrations, as seen during the third injection. It is possible that peaks from the lower concentrations have been masked by glucose. As such, CPA analysis using solely galactose is investigated, as discussed in Section 5.2.1.8.

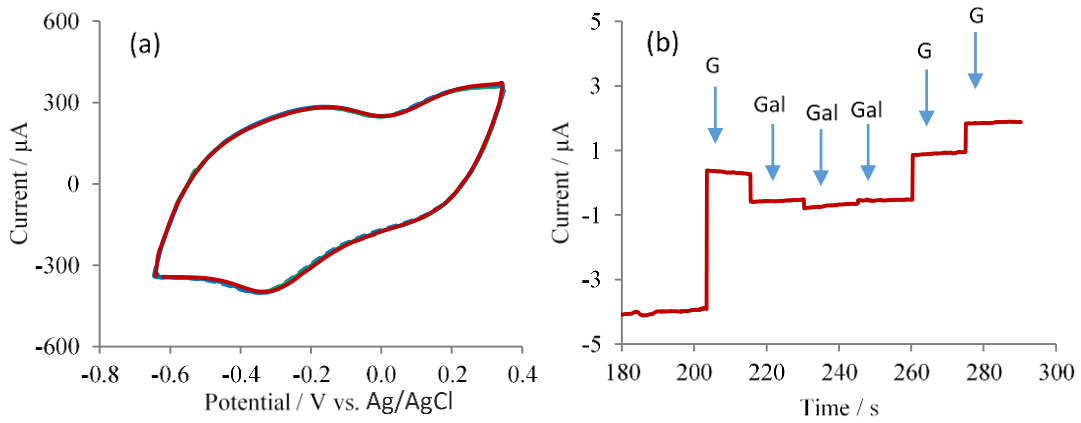

Figure 5.9: (a) Cyclic voltammogram, recorded at 100 mV s^{-1}, of the fMWCNT-Au_{nano}/Pd_{nano} modified SPE in a - - - 0.10 M PBS solution (pH 7.40) and PBS solutions containing — 0.25 mM, — 0.55 mM and —1.00 mM galactose. Figure 5.9 **(b)** shows the current-time plot for the oxidation of glucose and galactose, recorded at -0.45 V vs. Ag/AgCl, at the fMWCNT-Au_{nano}/Pd_{nano} modified SPE in 0.10 M PBS (pH 7.40) with the successive additions of glucose (4.0, 8.0 and 12.0 mM) and galactose (0.25, 0.55 and 1.00 mM) aliquots from stock solutions, made in 0.10 M PBS.

5.2.1.4 Fructose

Fructose is a simple carbohydrate found in many plants. It is an important dietary monosaccharide, along with glucose and galactose, which is absorbed into the bloodstream during digestion [29]. At equilibrium, fructose predominately exists as four isomers, α-D-fructopyranose (3%), β-D-fructopyranose (72%), α-D-fructofuranose (5%) and β-D-fructofuranose (20%) [30], shown in Scheme 5.4. Serum fructose concentrations in healthy (non-diabetic) individuals exist at 7.7 ± 1.6 μM and significantly higher levels are present in diabetic patients, 12.0 ± 3.8 μM [31]. Higher levels of fructose in the body can be associated with various conditions including hypertriglyceridemia and insulin resistance [32] and obesity [33]. In electrochemical sensing systems, fructose is often regarded as a potential interferant due to its coexistence in the blood, although as shown in recent works, it does not cause significant interference at some electrochemical sensors [34, 35]. Nonetheless, its potential effects on glucose sensing was investigated in this work at levels present in diabetic patients and at exaggerated levels, a hundred times higher.

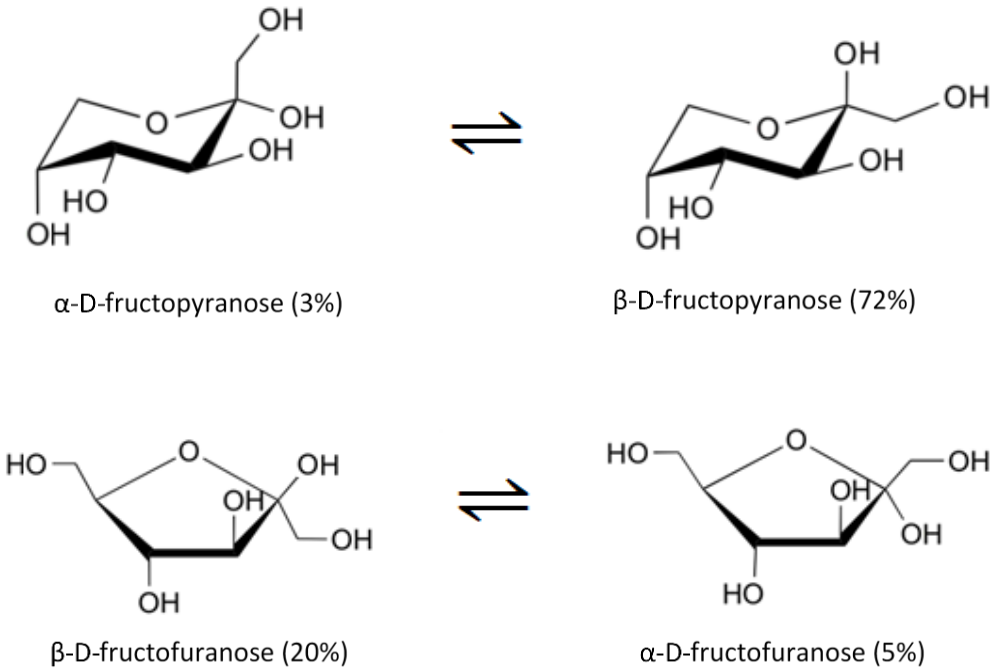

Scheme 5.4: Mutarotation of Fructose

5.2.1.4.1 Interference from Fructose at SPE/fMWCNT-Au_{nano} and SPE/fMWCNT-Au_{nano}/Nafion® Films

As with previous interference studies, CV was initially employed to investigate the position and intensity of the possible oxidation currents for fructose at the composite films. CPA was then employed in each case to examine the effects of fructose interference in the presence of glucose. From CV analyses, shown in Figures 5.10 (a) and (b), it seems as if fructose is not a source of interference at the fMWCNT-Au_{nano} films with or without Nafion®. No oxidation responses or any changes in current are observed, even at excessively high concentrations. Using CPA this same trend is initially apparent, although a slight increase in the current is visible at the fMWCNT-Au_{nano} film at the higher fructose concentration of 2.75 mM, shown in Figures 5.11 (a) and (b). The presence of the excessively high 2.75 mM fructose results in a current of 0.10×10^{-5} A (1.0 μA). This corresponds to a 10% increase relative to that of 4.0 mM glucose. There is no effect on the glucose responses post-fructose injection. At the fMWCNT-Au_{nano}/Nafion® film, no fructose interference occurs and the currents for glucose are not affected. These results indicate that the detection of physiological concentrations of fructose is not possible at these films, although it may be possible that currents for glucose may have a masking effect during CPA. As such, CPA experiments investigating fructose interference in the absence of glucose is shown in Section 5.2.1.8.

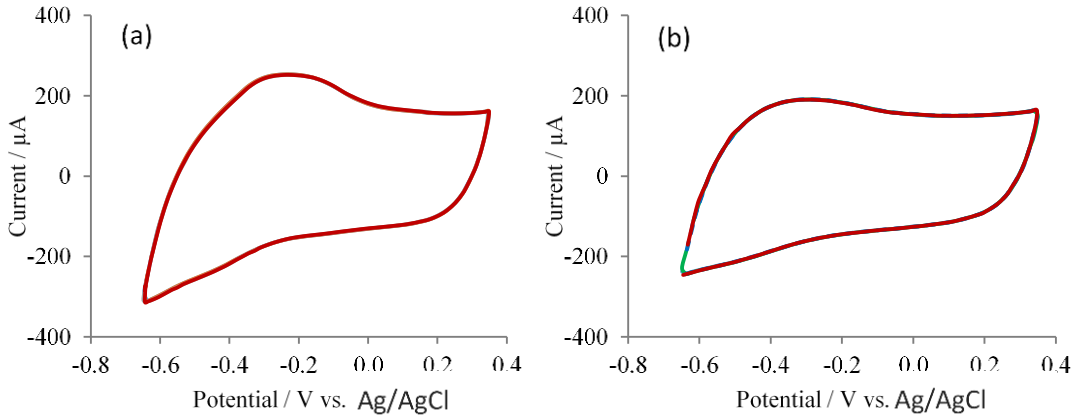

Figure 5.10: Cyclic voltammograms, recorded at 100 mV s^{-1}, of **(a)** the fMWCNT-Au_{nano} and **(b)** fMWCNT-Au_{nano}/Nafion® modified SPEs in a - - - 0.10 M PBS solution (pH 7.40) and PBS solutions containing — 6. 33 µM, — 27.75 µM and — 2.75 mM fructose.

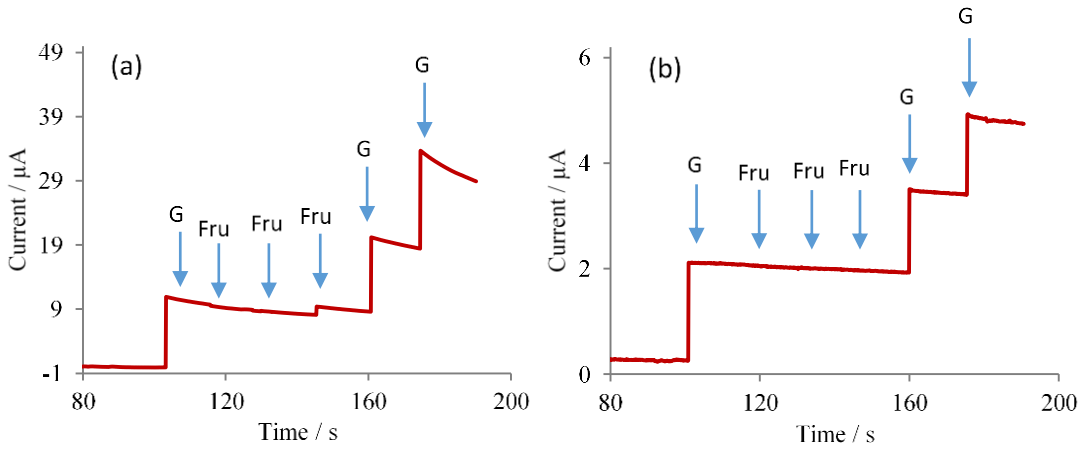

Figure 5.11: Current-time plots for the oxidation of glucose and fructose, recorded at -0.05 V vs. Ag/AgCl, at **(a)** the fMWCNT-Au_{nano} and **(b)** the fMWCNT-Au_{nano}/Nafion® modified SPEs in 0.10 M PBS (pH 7.40) with the successive additions of glucose (4.0, 8.0 and 12.0 mM) and fructose (6.33 µM, 27.75 µM and 2.75 mM) aliquots from stock solutions, made in 0.10 M PBS.

5.2.1.4.2 Interference from Fructose at SPE/fMWCNT-Au_{nano}/Pd_{nano} Films

Using CV, no oxidation of fructose or any changes in the overall current responses is observed, Figures 5.12 (a). In previous studies using AA and UA, Sections 5.2.1.1.2

and 5.2.1.2.2, changes in the Pd oxide reduction peak are evident upon addition of the interferant, which suggests a surface adsorption process is occurring. This is not the case with fructose using CV. Although upon addition of fructose during CPA analysis, albeit at extremely small concentrations, the initial current for 4.0 mM glucose decreases significantly. This trend follows with the successive fructose injections and no oxidation of fructose is apparent. The initial 4.0 mM glucose yields a current of 0.45×10^{-5} A (4.5 µA), although this decreases by 20%, 30% and 50% to 0.36×10^{-5} A (3.6 µA), 0.31×10^{-5} A (3.1 µA) and 0.23×10^{-5} A (2.3 µA) in the presence of 6.33 µM, 27.55 µM and 2.75 mM fructose, respectively. Glucose detection post-fructose injection is again investigated, although current responses are also affected. These occurrences suggest that fructose has a poisoning effect at this sensing film and that accurate glucose detection is not possible. CPA analysis of fructose in the absence of glucose is shown in Section 5.2.1.8 to again investigate the possibility of current asking by glucose.

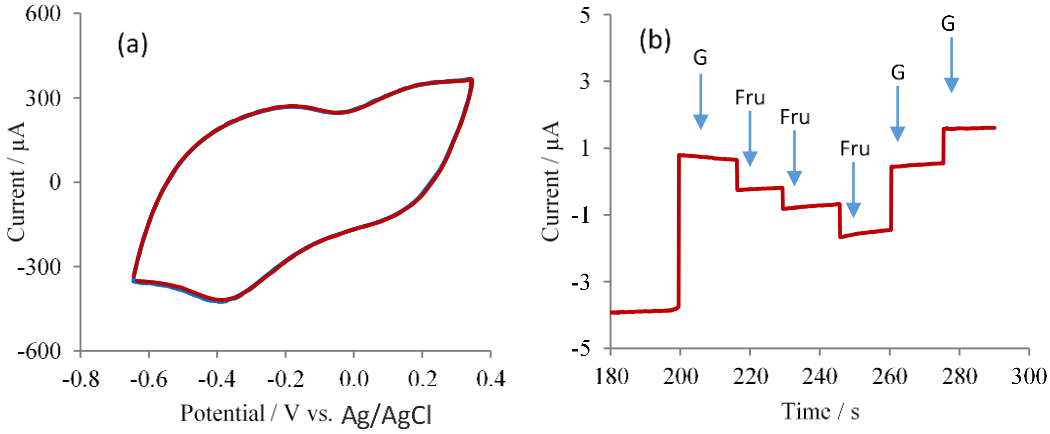

Figure 5.12: (a) Cyclic voltammogram, recorded at 100 mV s^{-1}, of the fMWCNT-Au_{nano}/Pd_{nano} modified SPE in a - - - 0.10 M PBS solution (pH 7.40) and PBS solution containing — 6. 33 µM, — 27.75 µM and — 2.75 mM fructose. Figure 5.12 **(b)** shows the current-time plot for the oxidation of glucose and fructose, recorded at -0.45 V vs. Ag/AgCl, at the fMWCNT-Au_{nano}/Pd_{nano} modified SPE in 0.10 M PBS (pH 7.40) with the successive additions of glucose (4.0, 8.0 and 12.0 mM) and fructose (6.33 µM, 27.75 µM and 2.75 mM) aliquots from stock solutions, made in 0.10 M PBS.

5.2.1.5 Acetaminophen

Acetaminophen, more commonly known as paracetamol, is a widely used over-the-counter analgesic and antipyretic that is absorbed into the blood from the upper intestinal tract post-ingestion [36]. The therapeutic range of acetaminophen in the blood ranges from 10 – 20 mg/l (0.066 – 0.132 mM) [37]. When used in the therapeutic range it has low toxicity, although high levels of acetaminophen within the body can produce serious health effects including liver failure and death [38].

Acetaminophen is an external influence and does not exist naturally in the blood, but when ingested its presence can cause interference at electrochemical blood sensors. Acetaminophen is an electroactive substance and can strongly adhere to and poison sensing surfaces [39]. It is oxidised to N-acetyl-p-quinoneimine via a two electron step [40]. Although it is neutrally charged at physiological pH [36], the use of Nafion® has shown to be useful for reducing its interference at electrochemical glucose sensors [41]. Interference from acetaminophen was investigated at the highest therapeutic level of 20 mg/L (0.13 mM) and at a significantly higher concentration of 100 mg/l (0.66 mM), which was deemed to be a relevant level in a study by Weidemaier K. *et al*. on glucose sensing [23].

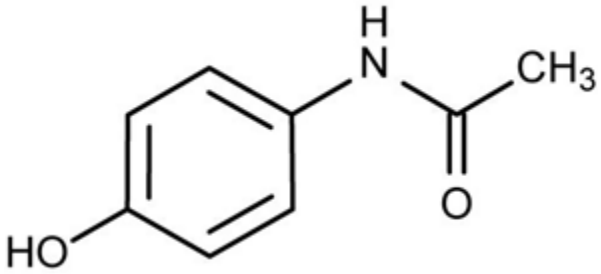

Figure 5.13: Structure of Acetaminophen

5.2.1.5.1 Interference from Acetaminophen at SPE/fMWCNT-Au_{nano} and SPE/fMWCNT-Au_{nano}/Nafion® Films

As with previous studies, both CV and CPA were used to investigate acetaminophen interference. Using CV, clearly defined peaks are seen for the acetaminophen to N-acetyl-p-quinoneimine redox couple at 0.20 V and -0.05 V, respectively, Figures 5.14

(a) and (b). At the fMWCNT-Au_{nano} films, the peak currents for the oxidation of 0.13 mM and 0.66 mM acetaminophen are measured to be 3.24×10^{-5} A (32.4 μA) and 14.97×10^{-5} A (149.7 μA) at the potentials of 0.21 V and 0.27 V vs. Ag/AgCl, respectively. Nafion® reduces the intensity of peaks by 25% and 50% to 2.47×10^{-5} A (24.7 μA) and 7.75×10^{-5} A (77.5 μA), measured at the potentials of 0.19 V and 0.23 V vs. Ag/AgCl, respectively, Figure 5.14 (b). Since the oxidation of acetaminophen occurs at a potential more positive than that of glucose, it was hoped that it would not pose any problems during glucose sensing using CPA.

Interference from acetaminophen during CPA is shown in Figures 5.15 (a) and (b). Again glucose was injected initially followed by acetaminophen and again by glucose. It is clear that acetaminophen oxidation does not occur at either sensors, which was expected, although the currents arising from the initial oxidation of glucose are severely reduced. As mentioned, acetaminophen can pose issues in electrochemical sensing due to its poisoning of electrode surfaces. This may occur at these films and the exceptional decrease in glucose detection post injection may support this. The initial current for the oxidation of 4.0 mM glucose is measured to be 1.12×10^{-5} A (11.2 μA) at the fMWCNT-Au_{nano} film during CPA, Figure 5.15 (a). This peak decreases in intensity by almost 40% and 70% to 0.70×10^{-5} A (7.0 μA) and 0.31×10^{-5} A (3.1 μA), in the presence of 0.13 mM and 0.66 mM acetaminophen, respectively. The oxidation of glucose post-acetaminophen injection has also been severely affected. Nafion® does not eliminate the poisoning effects of acetaminophen, although it reduces its severity, as seen in Figure 5.15 (b). The initial oxidation of 4.0 mM glucose at the fMWCNT-Au_{nano} film results in a current of 0.19×10^{-5} A (1.9 μA). This decreases by a lesser extent of 10% and 30% to 0.17×10^{-5} A (1.76 μA) and 0.13×10^{-5} A (1.3 μA) in the presence of 0.13 mM and 0.66 mM acetaminophen, respectively. Glucose detection post-injection of acetaminophen is affected, although not to the same extent as the previous fMWCNT-Au_{nano} sensor in Figure 5.15 (a). Overall the use of Nafion® reduces the detection of acetaminophen by over 50% during CPA, as measured from the redox peaks in Figure 5.14.

It can be seen that Nafion® does indeed reduce acetaminophen interference, although in this study it was shown to not eliminate it fully. Due to this, it can be concluded that these films are not suitable for glucose detection in the presence of this interferant.

As in the previous interferant studies, the detection of acetaminophen in the absence of glucose is discussed in Section 5.2.1.8.

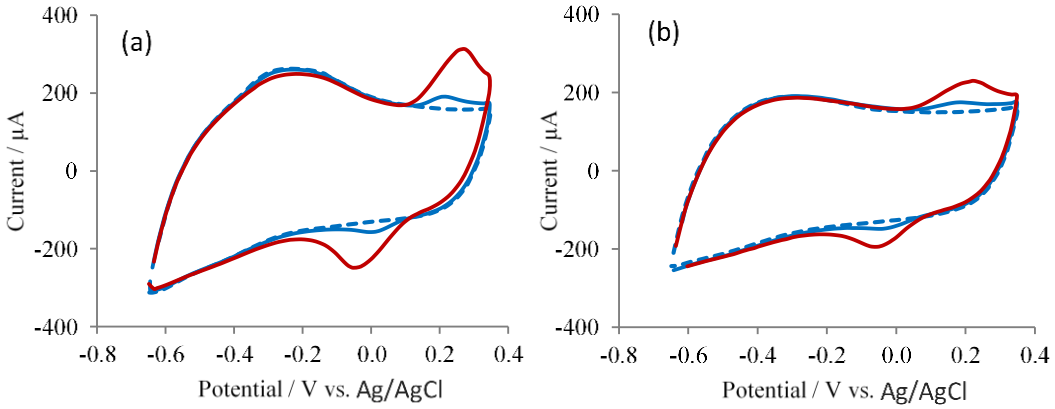

Figure 5.14: Cyclic voltammograms, recorded at 100 mV s^{-1}, of **(a)** the fMWCNT-Au_{nano} and **(b)** fMWCNT-Au_{nano}/Nafion® modified SPEs in a - - - 0.10 M PBS solution (pH 7.40) and PBS solutions containing — 0.13 mM and — 0.66 mM acetaminophen.

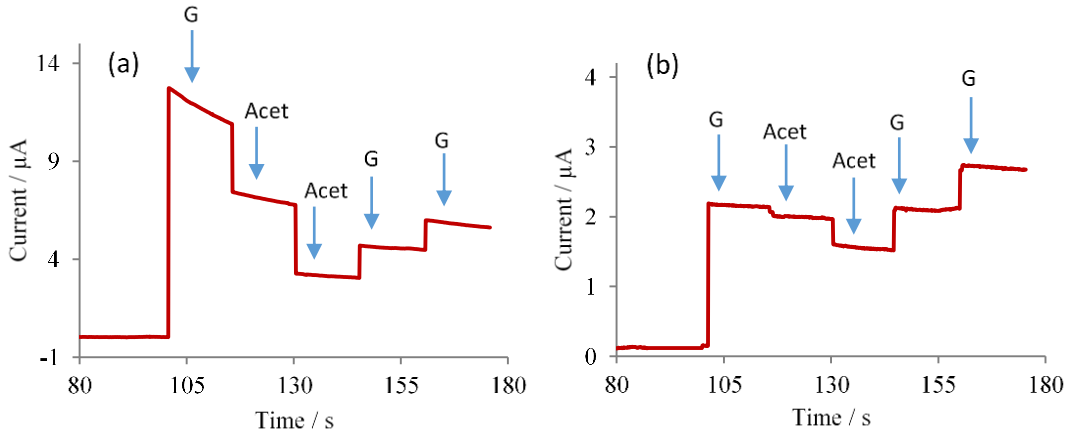

Figure 5.15: Current-time plots for the oxidation of glucose and acetaminophen, recorded at -0.05 V vs. Ag/AgCl, at **(a)** the fMWCNT-Au_{nano} and **(b)** the fMWCNT-Au_{nano}/Nafion® modified SPEs in 0.10 M PBS (pH 7.40) with the successive additions of glucose (4.0, 8.0 and 12.0 mM) and acetaminophen (0.13 and 0.66 mM) aliquots from stock solutions, made in 0.10 M PBS.

5.2.1.5.2 Interference from Acetaminophen at SPE/fMWCNT-Au_{nano}/Pd_{nano} Films

The CVs showing acetaminophen interference at the fMWCNT-Au_{nano}/Pd_{nano} composite film, shown in Figure 5.16 (a), appear quite different to those of the previous fMWCNT-Au_{nano} and fMWCNT-Au_{nano}/Nafion® films. At lower concentrations of 0.13 mM, no clear redox peaks can be seen for acetaminophen, although a slight decrease and shift in the Pd oxide reduction peak, at about -0.40 V vs. Ag/AgCl, is clear. As with AA and UA, it was assumed that this was caused by surface poisoning. When the higher concentration of 0.66 mM is investigated, redox peaks for acetaminophen are apparent, at approximately 0.25 V and at 0.00 V vs. Ag/AgCl and the Pd oxide reduction peak almost disappears. This may indicate a surface fouling process.

From CPA analysis in the presence of glucose it is clear that the current response for glucose is drastically affected by acetaminophen. Shown in Figure 5.16 (b), it can be seen that no oxidation responses are present, as expected, although the current arising from the initial response for 4.0 mM glucose is completely diminished upon injection of acetaminophen. Further addition of this interferant gives rise to lower currents. Also, glucose detection post acetaminophen addition is not possible. Of all the interferants studied, it seems as if acetaminophen poses the biggest problem at these sensing films. As such, it can be concluded that these films are not suitable for glucose detection in the presence of this interferant.

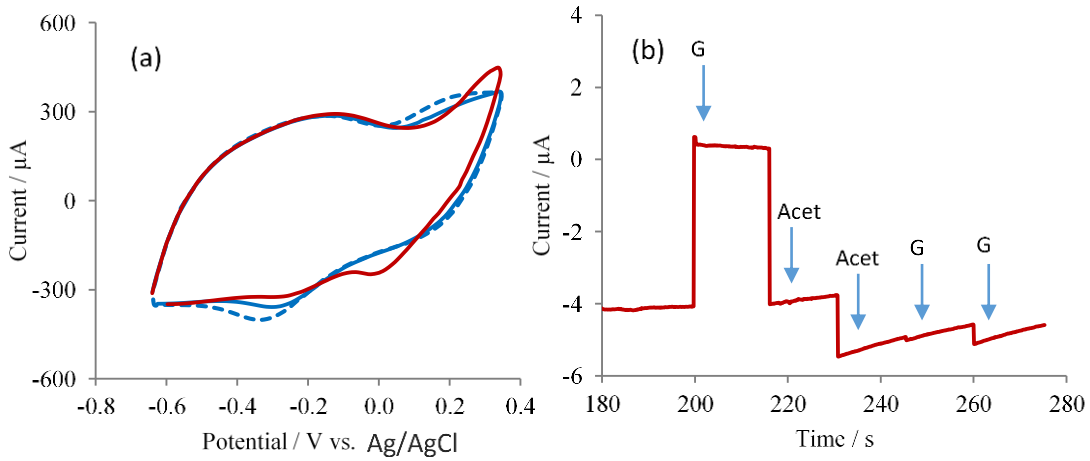

Figure 5.16: (a) Cyclic voltammogram, recorded at 100 mV s^{-1}, of the fMWCNT-Au_{nano}/Pd_{nano} modified SPE in a - - - 0.10 M PBS solution (pH 7.40) and PBS solution containing — 0.13 mM and — 0.66 mM acetaminophen. Figure 5.16 **(b)** shows the current-time plot for the oxidation of glucose and acetaminophen, recorded at -0.45 V vs. Ag/AgCl, at the fMWCNT-Au_{nano}/Pd_{nano} modified SPE in 0.10 M PBS (pH 7.40) with the successive additions of glucose (4.0, 8.0 and 12.0 mM) and acetaminophen (0.13 and 0.66 mM) aliquots from stock solutions, made in 0.10 M PBS.

5.2.1.6 Serum Albumins

Serum albumins are globular soluble proteins formed in the liver and are essential constituents of blood plasma where they have roles in transportation of nutrients, blood and hormones through the vascular system and in maintaining osmotic pressure [42]. Human serum albumin (HSA) concentrations in the blood are significant with normal levels ranging from 3.5 to 5.0 g/dl. Levels below 3.5 g/dl are abnormal and can be a result of malnutrition and/or kidney disease [42]. Over 50% of human plasma content is composed of serum albumins [43]. These proteins possess a heart-shaped tertiary structure, of which 67% is composed of α-helices and they have three homologous domains containing two sub domains. Overall these proteins are negatively charged [43].

Although HSAs are present in human blood, they were not studied in this work. Instead, bovine serum albumin (BSA) were used in these interference studies, the structure of which is displayed in Figure 5.17 [44]. BSA is a commonly used albumin

which has a high degree of homology to HSA [45]. Like HSA its tertiary structure exists as a heart shape, 67% is composed of alpha helices and it also consists of three homologous domains which are composed of two sub domains [46].

Studies show that BSA can bind to and aggregate on the surface of MWCNTs [47]. Interactions between nanoparticles and proteins typically include Van der Waals and electrostatic forces, hydrogen bonds and hydrophobic interactions [47]. Work by Chen *et al.* showed that BSA can bind to AuNPs on electrochemical films which result in a decrease in current responses and electron transfer [48]. It was expected that these possible interactions would negatively affect glucose sensing when albumins were present.

Figure 5.17: Structure of Serum Albumin [44].

5.2.1.6.1 Interference from Serum Albumins at SPE/fMWCNT-Au_{nano} and SPE/fMWCNT-Au_{nano}/Nafion® Films

As with the previous interference studies, CV and CPA were used. Initially using CV analysis, the fMWCNT-Au_{nano} films with and without Nafion®, were cycled in 0.10 M PBS to obtain stable background responses. These sensors were then cycled in a 0.10 M PBS solution containing BSA, at a concentration of 4.125 g/dl, as to investigate any changes caused by BSA. This was followed by 10.0 mM glucose detection in PBS with the presence of BSA. As seen in the CVs of the fMWCNT-Au_{nano} film without

Nafion®, Figure 5.18 (a), the presence of BSA has an effect on the background current response. Also, glucose oxidation does not occur. It is assumed that the BSA may be adsorbing onto the composite surface and thus impeding glucose detection. The results from the fMWCNT-Au_{nano}/Nafion® sensor prove to be quite different, as seen in Figure 5.18 (b). With the use of Nafion® it appears that glucose detection is possible in the presence of BSA, as a broad oxidation response can be observed from -0.40 V to 0.20 V vs. Ag/AgCl in the forwards scan.

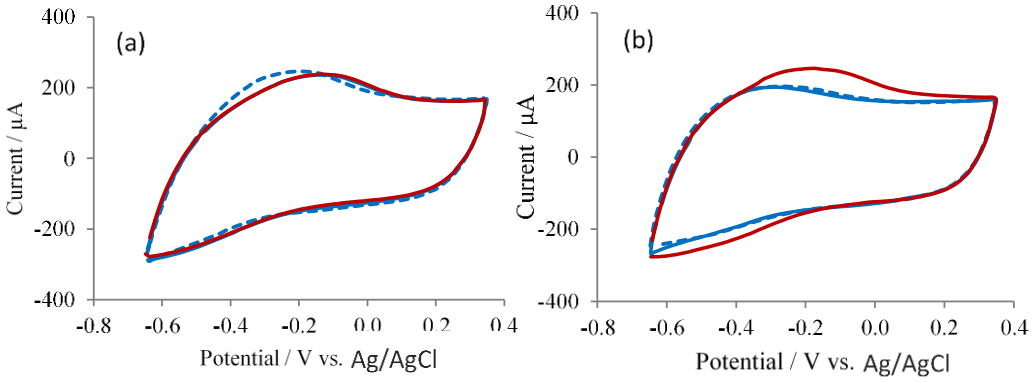

Figure 5.18: Cyclic voltammograms, recorded at 100 mV s^{-1}, of **(a)** the fMWCNT-Au_{nano} and **(b)** fMWCNT-Au_{nano}/Nafion® modified SPEs in a - - - 0.10 M PBS solution (pH 7.40), a — PBS solution containing serum albumin (4.125 g/dl) and — this solution containing 10.0 mM glucose.

Since glucose detection was only possible at the Nafion® containing film, CPA was only conducted at this sensor and the results are shown in Figure 5.19. As observed, typical step-like current responses are achieved upon injection of glucose. In the presence of albumins it can be seen that the films sensitivity towards glucose has decreased at this fMWCNT-Au_{nano}/Nafion® film, in comparison to results obtained in the absence of BSA, data shown in Chapter 3, Section 3.2.8. The resulting calibration curve is shown in Figure 5.20 in which a non-linear trend occurs over the various glucose concentrations. As such, the sensitivity value was not calculated and the % decrease in sensitivity in the presence of BSA was not calculated. Overall, glucose detection is possible in the presence of physiologically relevant levels of albumins using the Nafion® coated film, although the sensitivity is reduced. A LOD of 0.043 µM can be calculated from the background currents obtained during CPA.

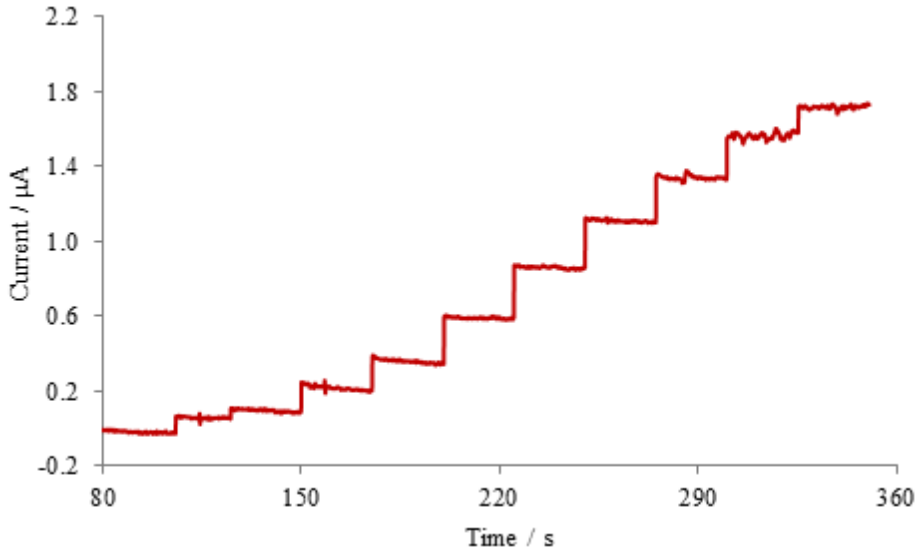

Figure 5.19: Current-time plots for the oxidation of glucose, recorded at -0.05 V vs. Ag/AgCl at the fMWCNT-Au_{nano}/Nafion® modified SPEs in 0.10 M PBS (pH 7.40) containing serum albumins (4.125 g/dl) with the successive additions of glucose aliquots from stock solutions, made in 0.10 M PBS.

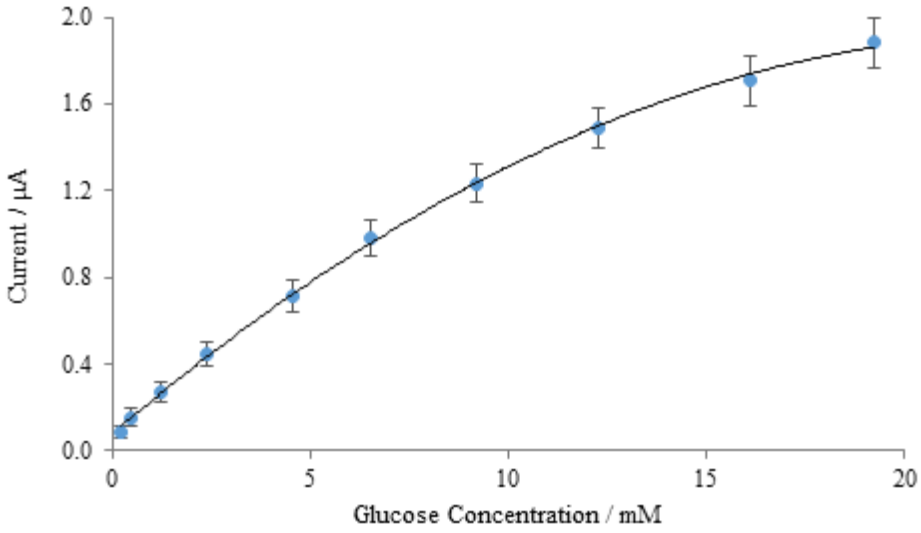

Figure 5.20: Calibration curve for the oxidation of glucose in 0.10 M PBS (pH 7.40) at the fMWCNT-Au_{nano}/Nafion® modified SPEs, n = 3.

5.2.1.6.2 Interference from Serum Albumins at SPE/fMWCNT-Au_{nano}/Pd_{nano} Films

CV analysis of BSA interference at the fMWCNT-Au_{nano}/Pd_{nano} film, data shown in Figure 5.21, resulted in similar results to the previous fMWCNT-Au_{nano} film without Nafion®, Section 5.2.1.6.1. Again, the film was cycled in 0.10 M PBS, followed by 0.10 M PBS containing BSA with and without 10.0 mM glucose. Upon cycling in the BSA solution, it is clear that the previously defined Pd oxide reduction peaks are almost eliminated. It is assumed that the BSA has again adsorbed on the surface. Glucose detection is also not possible in the presence of BSA at this film, as with the previous composite film, displayed in Section 5.2.1.6.1, Figure 5.18 (a). As such, CPA work was not carried out at this film.

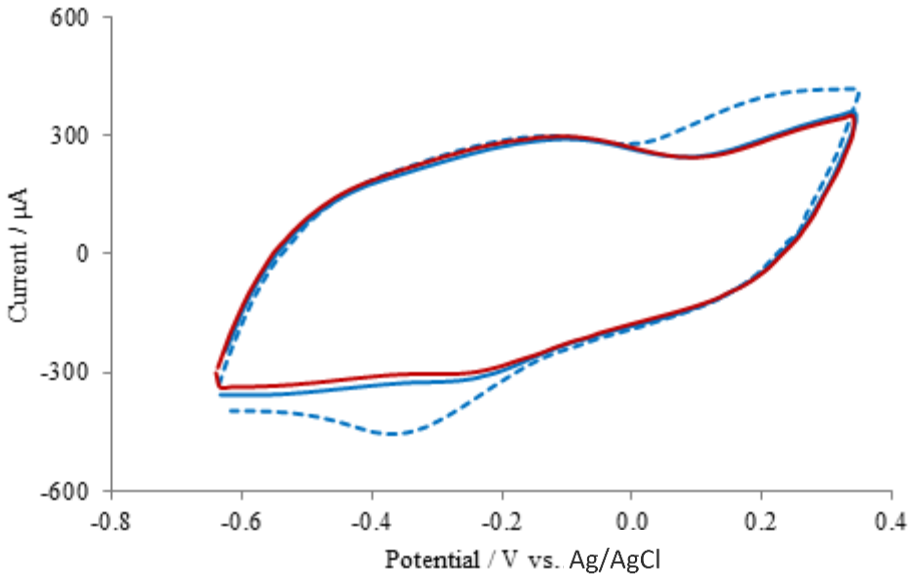

Figure 5.21: Cyclic voltammogram, recorded at 100 mV s^{-1}, of the **(a)** fMWCNT-Au_{nano}/Pd_{nano} modified SPE in a - - - 0.10 M PBS solution (pH 7.40), a — PBS solution containing serum albumin (4.125 g/dL) and — this solution containing 10.0 mM glucose.

5.2.1.7 Chloride

Chloride is one of the most important electrolytes in the blood where it is present at concentrations ranging from 96-106 mM [49]. It is essential in maintaining many

physical and chemical properties within the body, including normal blood volume, pressure, and pH [49]. Sodium chloride provides the main source of chloride in the body, which when absorbed into the blood is regulated by the kidneys. Excess chloride is excreted from the body in the urine, but persistently high levels may indicate kidney damage [49].

The presence of chloride during electrochemical sensing of glucose at non-enzymatic sensors can cause significant problems. Chloride ions strongly chemisorb onto the surface of noble metals, including Au and Pt, thus reducing the adsorption of glucose and its detection [39, 50, 51]. The current responses for the electrooxidation of glucose at Au are proportional to the concentrations of chlorides present [39]. In contrast, work by Meng *et al.* which investigated the use of PdNP/CNT composites, demonstrated significant anti-chloride poisoning properties of Pd and no effects on glucose sensing [52].

5.2.1.7.1 Interference from Chloride at SPE/fMWCNT-Au$_{nano}$ and SPE/fMWCNT-Au$_{nano}$/Nafion® Films

As with the previous BSA study, the effect of chloride on glucose detection was investigated initially using CV followed by CPA. NaCl at a concentration of 0.10 M was used as a source of chloride. For CV analysis, the prepared electrodes were firstly cycled in the background solution of 0.10 M PBS. They were then cycled in a PBS solution containing 0.10 M NaCl with and without 10.0 mM glucose. Data is shown in Figures 5.22 (a) and (b). As can be seen, the presence of chloride results in a change of the background currents, in comparison to those not containing chloride. Also, glucose detection is severely reduced, in comparison to detection without chloride, shown in Chapter 3, Section 3.28, as expected at both films with or without Nafion®. These glucose currents are not measurable from the resulting CVs. Nafion® may not reduce the extent of interference due to the small size of the chloride anions and their high concentration.

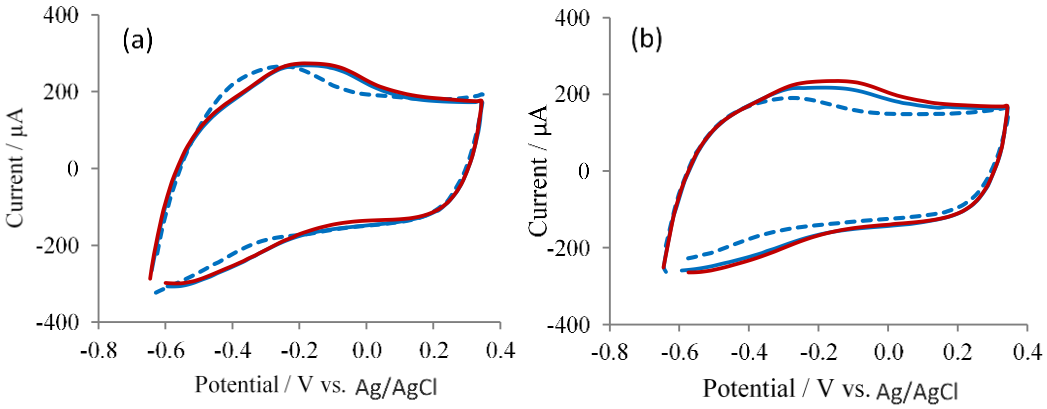

Figure 5.22: Cyclic voltammograms, recorded at 100 mV s^{-1}, of **(a)** the fMWCNT-Au_{nano} and **(b)** fMWCNT-Au_{nano}/Nafion® modified SPEs in a - - - 0.10 M PBS solution (pH 7.40), a — PBS solution containing 0.10 M NaCl and — this solution containing 10.0 mM glucose.

This poor sensitivity towards glucose in the presence of 0.10 NaCl is reflected in CPA studies, shown in Figures 5.23 (a) and (b) and in the resulting calibration curves, Figures 5.24 (a) and (b). An almost linear correlation between data is seen with the fMWCNT-Au_{nano} film, although this is not the case with the Nafion® coated composite, which has significant errors. As such, a sensitivity value could not be calculated for the Nafion® coated film. LODs and sensitivity values are displayed in Table 5.1. A sensitivity value of 0.088 µA/mM is calculated for the fMWCNT-Au_{nano} film. Results obtained in the absence of chloride are shown in Chapter 3, Section 3.2.8, in which a sensitivity of 2.766 µA/mM is obtained. In the presence of 0.10 M NaCl it can be estimated that the sensors sensitivity for glucose has been reduced by over 95%. This reduction in sensitivity may be due to the adsorption of chloride on the metal surfaces, thereby hindering the adsorption of glucose. These results are consistent with the issues with glucose detection in the presence of chloride at noble metal non-enzymatic sensors [39, 50, 51]. A low LOD value of 0.150 µM was obtained for the fMWCNT-Au_{nano} film, which is lower than the levels of glucose found in the blood. This can be compared to a LOD of 0.049 µM obtained at this film in the absence of chloride, Chapter 3, Section 3.2.8, which is almost 70% lower. An even lower LOD value of 0.027 µM was calculated for the Nafion® containing film.

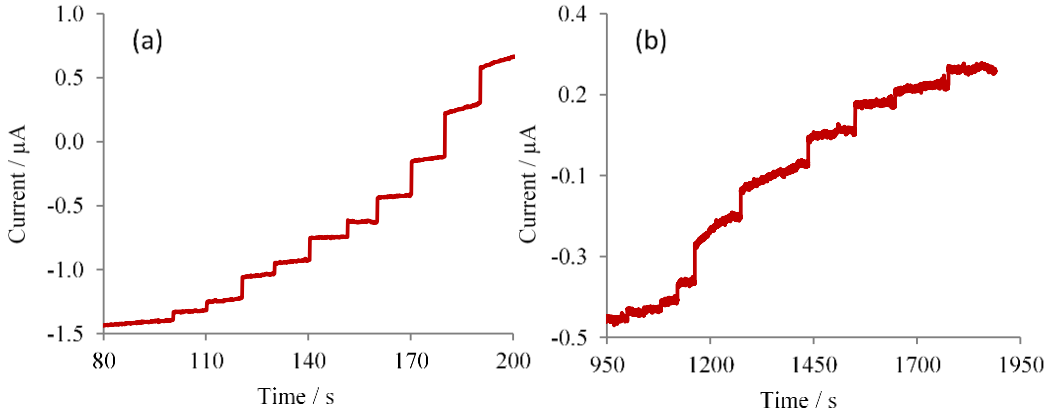

Figure 5.23: Current-time plots for the oxidation of glucose, recorded at -0.05 V vs. Ag/AgCl, at **(a)** the fMWCNT-Au_{nano} and **(b)** the fMWCNT-Au_{nano}/Nafion® modified SPEs in 0.10 M PBS (pH 7.40) containing 0.10 M sodium chloride with the successive additions of glucose aliquots from stock solutions, made in 0.01 M PBS.

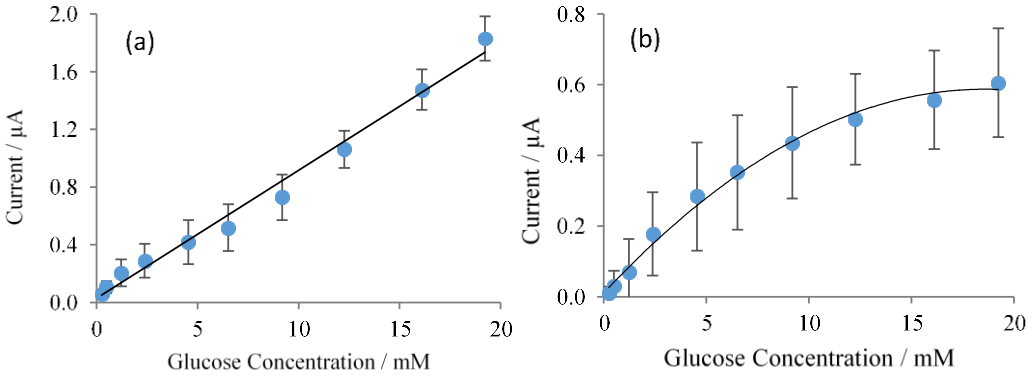

Figure 5.24: Calibration curve for the oxidation of glucose in 0.10 M PBS (pH 7.40) containing 0.10 M sodium chloride at the **(a)** fMWCNT-Au_{nano} and **(b)** fMWCNT-Au_{nano}/Nafion® modified SPEs, n = 3.

Table 5.1: Limits of detection and film sensitivity values towards the oxidation of glucose at the fMWCNT-Au_{nano} and fMWCNT-Au_{nano}/Nafion® composite modified SPEs in the presence of chlorides, n = 3.

Without Nafion®				With Nafion®		
Potential / V vs. SCE	**LOD /µM**	**Sensitivity / µA/mM**	**Error / µA/mM**	**LOD / µM**	**Sensitivity / µA/mM**	**Error / µA/mM**
-0.05	0.150	0.088	± 0.005	0.027	†	†

† LOD and sensitivity values not calculated.

5.2.1.7.2 Interference from Chloride at SPE/fMWCNT-Au_{nano}/Pd_{nano} Films

Although it was hoped that the presence of Pd would reduce the anti-fouling effects of chloride, chlorides also had a negative effect on glucose detection at this fMWCNT-Au_{nano}/Pd_{nano} film. As can be seen in Figure 2.25, with the presence of 0.10 M NaCl, the characteristic Pd oxide reduction peak is essentially eliminated. This is assumed to be a result of surface fouling, in which the chloride may be causing a surface passivation. Also, no glucose detection is possible. To add to this negative result, glucose detection using CPA is also not possible. These results further demonstrate the negative effects that chlorides pose to some non-enzymatic glucose sensors.

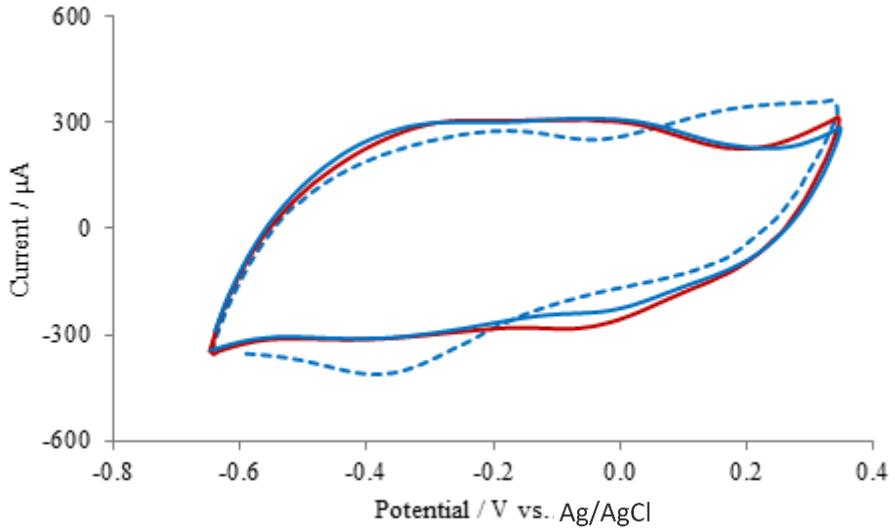

Figure 5.25: Cyclic voltammogram, recorded at 100 mV s^{-1}, of the fMWCNT-Au_{nano}/Pd_{nano} modified SPE in a - - - 0.10 M PBS solution (pH 7.40), a —— 0.10 M PBS solution (pH 7.40) containing 0.10 M sodium chloride and —— this solution containing 10.0 mM glucose.

5.2.1.8 Oxidation of Interferants in the Absence of Glucose at all Composite Films

The oxidation of each interferant using CPA in the absence of glucose was investigated at the fMWCNT-Au_{nano}, fMWCNT-Au_{nano}/Nafion® and the fMWCNT-Au_{nano}/Pd_{nano} modified SPEs. This was conducted due to the possibility that the current responses obtained during previous CPA analyses in the presence of glucose may be underestimated. Physiological levels of each interferant were analysed and data are displayed in Figure 5.26 and Figure 5.27 for the fMWCNT-Au_{nano} films and the fMWCNT-Au_{nano}/Pd_{nano} film, respectively.

As with previous findings, no evidence of UA, fructose or acetaminophen oxidation is apparent at either the fMWCNT-Au_{nano} or fMWCNT-Au_{nano}/Nafion® films. Oxidation of AA and galactose is possible, albeit not significant. At the fMWCNT-Au_{nano} and fMWCNT-Au_{nano}/Nafion® film, currents of 0.81×10^{-6} A (0.81 µA) and 0.45×10^{-7} A (0.045 µA) are obtained for 0.10 mM AA in the absence of glucose, respectively. With previous CPA experiments in the presence of glucose, Section 5.2.1.1.1, no oxidation responses is visible for 0.10 mM AA at the fMWCNT-Au_{nano}

or fMWCNT-Au_{nano}/Nafion® films, respectively. This indicates that masking of the AA currents is occurring. Nonetheless the currents for AA are not significant in comparison to those obtained for glucose, as shown in Section 5.2.1.1.1. Currents of 1.34×10^{-6} A (1.34 μA) and 0.24×10^{-6} A (0.24 μA) are obtained for 0.55 mM galactose in the absence of glucose at the fMWCNT-Au_{nano} and fMWCNT-Au_{nano}/Nafion® films, respectively. In comparison to the CPA experiments in the presence of glucose, Section 5.2.1.3.1, a much smaller current of 0.30×10^{-6} A (0.30 μA) is obtained for 0.55 mM galactose at the fMWCNT-Au_{nano} film, although a similar current response of 0.23×10^{-6} A (0.23 μA) is measured at the fMWCNT-Au_{nano}/Nafion® film. This indicates that some current masking by glucose is occurring at the fMWCNT-Au_{nano} films during CPA. Nonetheless interference from galactose is not deemed to be significant as currents are small in comparison to those of glucose, shown in Section 5.2.1.3.1. It can be seen that the use of Nafion® greatly limits interference from both AA and galactose, although as discussed this membrane equally hinders the extent of glucose detection. In this study, shown in Figure 5.26, interference from 0.10 mM AA has been reduced by over 90% and 80% for 0.55 mM galactose with the use of Nafion®. Although AA, galactose and fructose are not major sources of interference at these films, it has been shown in Sections 5.2.1.2.1 and 5.2.1.5.1 that acetaminophen and UA cause interference.

Current data obtained at the fMWCNT-Au_{nano}/Pd_{nano} is shown in Figure 5.27. As expected, no oxidation currents are obtained for most interferants at this film. A slight oxidation response for 0.55 mM galactose is achieved which is very small in comparison to those obtained during glucose oxidation, as seen in Section 5.2.1.3.2. As discussed in Section 5.2.1.3.2, no oxidation of 0.55 mM galactose is apparent in the presence of glucose. This indicates again that current masking by glucose is also occurring during CPA at the fMWCNT-Au_{nano}/Pd_{nano} film. Although these interference results seem promising, most interferants appear to possess poisoning properties at this bi-metallic system and as such it is not suitable for selective non-enzymatic glucose sensing.

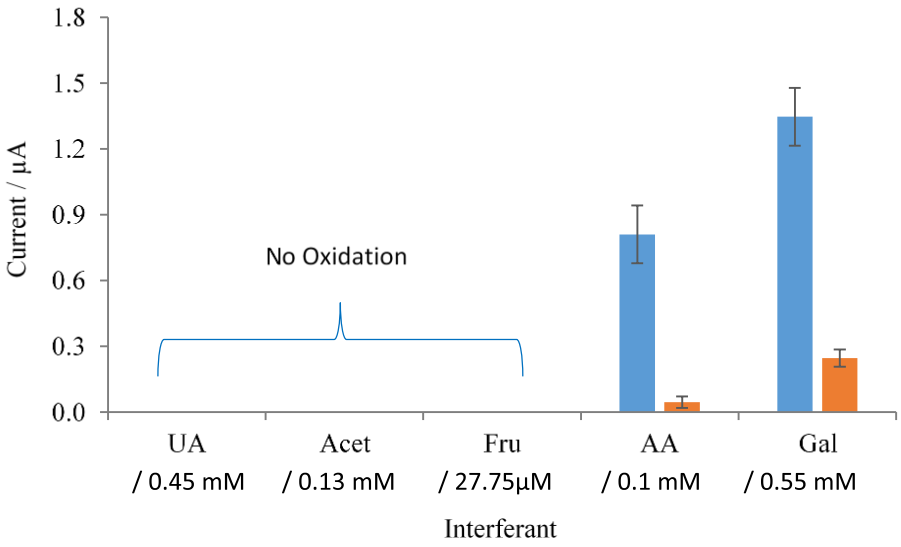

Figure 5.26: Current responses measured using CPA at -0.05 V vs. Ag/AgCl for the oxidation of all interferants at physiological concentrations in 0.10 M PBS (pH 7.40) at the —— fMWCNT-Au_{nano} and —— fMWCNT-Au_{nano}/Nafion® modified SPEs, n = 3.

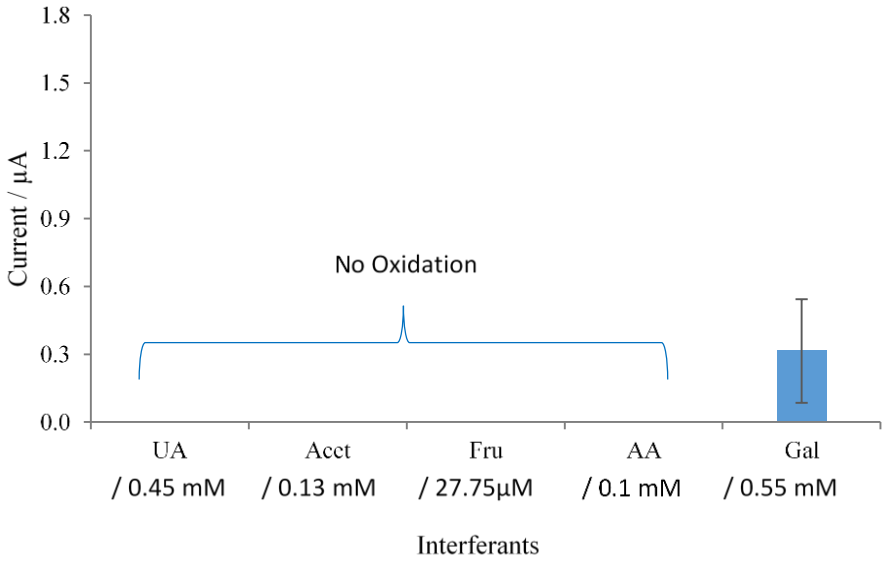

Figure 5.27: Current responses measured using CPA at -0.45 V vs. Ag/AgCl for the oxidation of all interferants at physiological concentrations in 0.10 M PBS (pH 7.40) at the —— fMWCNT-Au_{nano}/Pd_{nano} modified SPEs, n = 3.

5.2.2 Reusability of all Composite Modified SPEs

5.2.2.1 fMWCNT-Au_{nano} and fMWCNT-Au_{nano}/Nafion® Modified SPEs

As with all chemical sensors, the prospect of sensor reusability is an attractive attribute. As such, the reusability of each sensor was investigated using CPA. Prior to each glucose measurement, the electrodes were cycled in a 0.10 M PBS solution using CV to remove any adsorbed glucose and were then held at the relevant applied potentials during CPA to yield steady-state current responses. Re-measurements were carried out quickly and sensors were not stored for periods of time between measurements. Results are displayed in Figure 5.28 (a) and (b) for the fMWCNT-Au_{nano} and fMWCNT-Au_{nano}/Nafion® composite films, respectively. Overall it is clear that the currents obtained remain quite constant over the various uses for both sensors. These results indicate that both sensors retain accuracy over successive use.

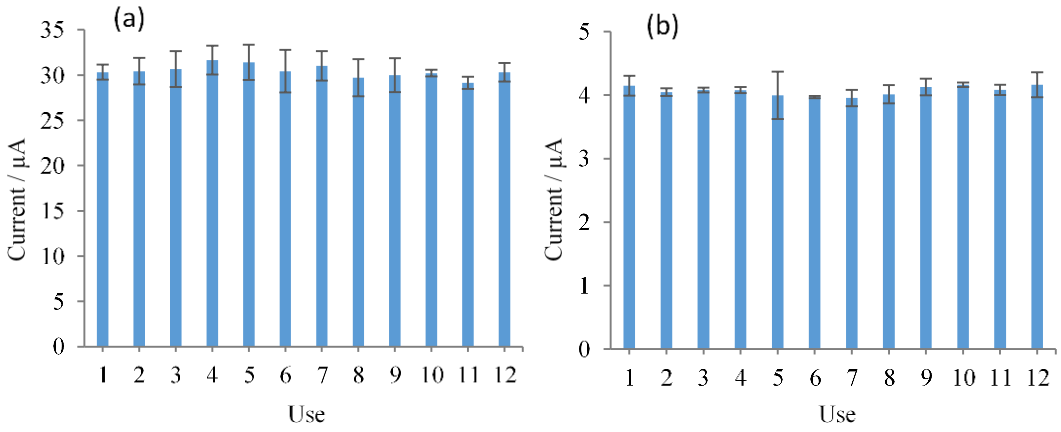

Figure 5.28: Current responses for the oxidation of 10.0 mM glucose in 0.10 M PBS (pH 7.40) at the (a) fMWCNT-Au_{nano} and (b) fMWCNT-Au_{nano}/Nafion® modified SPEs over various uses, n = 3.

5.2.2.2 fMWCNT-Au_{nano}/Pd_{nano} Modified SPEs

Following the same trend as the previous sensors, the fMWCNT-Au_{nano}/Pd_{nano} modified SPE also displayed a good degree of reusability. Current responses for glucose were relatively stable over use. Again, these results indicate that accuracy can

be retained over successive use which is an ideal quality to have for electrochemical sensing.

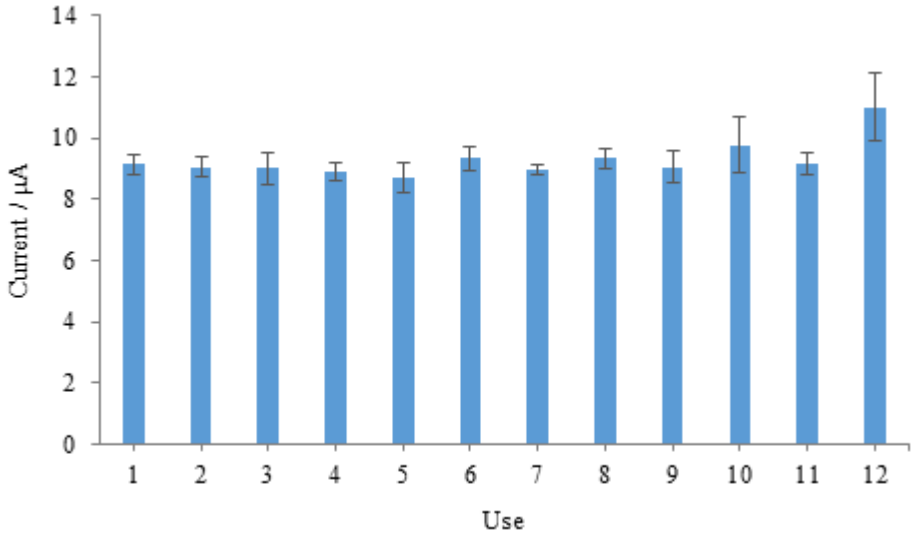

Figure 5.29: Current responses for the oxidation of 10.0 mM glucose in 0.10 M PBS (pH 7.40) at the fMWCNT-Au_{nano}/Pd_{nano} modified SPE over various uses, n = 3.

5.2.3 Shelf-Life Studies of all Composite Modified SPEs

5.2.3.1 fMWCNT-Au_{nano} and fMWCNT-Au_{nano}/Nafion® Modified SPEs

As with reusability, it was important to investigate the shelf-life and to ascertain the ideal storage conditions for the chemical sensors. In this study, each sensor was tested over a period of time, from days to weeks. Between testing, the sensors were stored in either 0.10 M PBS solution of pH 7.40 or in air. This was to determine the most appropriate means of storage for each sensor.

Results for the fMWCNT-Au_{nano} modified SPEs are displayed in Figure 5.30. It is clear that the current responses for 10.0 mM glucose are initially the same, as expected and they agree with the responses obtained previously for this sensor, data shown in Chapter 3. However, having been stored for more than 24 h (Day 2) their effectiveness decreases substantially. Over this period, the sensitivities of the fMWCNT-Au_{nano} sensors stored in PBS and in air decrease by over 30% in each instance. This trend is seen for this sensor stored both in air and PBS and is proportional to storage time. The

storage conditions play a significant role in the sensors sensitivity over time. It can be seen that storage in air provides the best results as the decreases in the current responses for glucose are not as significant over time, in comparison to those stored in PBS. All of these sensors stored in PBS cease to work completely at Day 14, although those stored in air remain responsive to at least Day 28, but with significantly decreased sensitivities. It was thought that storage in PBS may have resulted in damaging reactions between both the composite films and the other electrical components of the SPE and species in the storage solution. It is possible that surface oxides may be impeding the glucose oxidation. To remove these possible oxides, the sensors may have been scanned towards negative 'reduction' potentials in a medium such a H_2SO_4. This however was not investigated. Overall, these results are not promising and indicate limitations in stability of these sensors over time

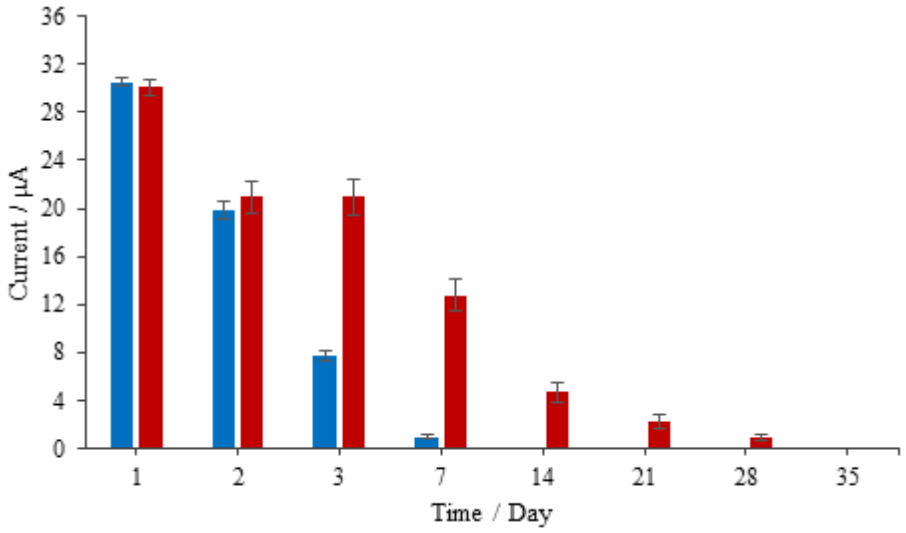

Figure 5.30: Current responses for the oxidation of 10.0 mM glucose in 0.10 M PBS (pH 7.40) at the fMWCNT-Au_{nano} modified SPEs, that were stored in —— PBS and in —— air, over time, n = 3.

With the fMWCNT-Au_{nano}/Nafion® modified SPEs results were slightly different. The sensors stored in both PBS and in air retain their stability and sensitivity towards glucose after 24 h (Day 2), unlike those without the Nafion® membrane. On Day 3 the sensors stored in air again retain the sensitivity although those stored in PBS do not. On Day 3 the sensitivity of the fMWCNT-Au_{nano}/Nafion® sensors stored in PBS

decreases by 30%. After Day 3, the sensitivities of all sensors declines, regardless of storage conditions. From Day 14 onwards the sensors stored in PBS do not work, similar to the previous fMWCNT-Au_{nano} sensor. Those stored in air also perform for longer periods of time, over 28 days, although with decreased sensitivities.

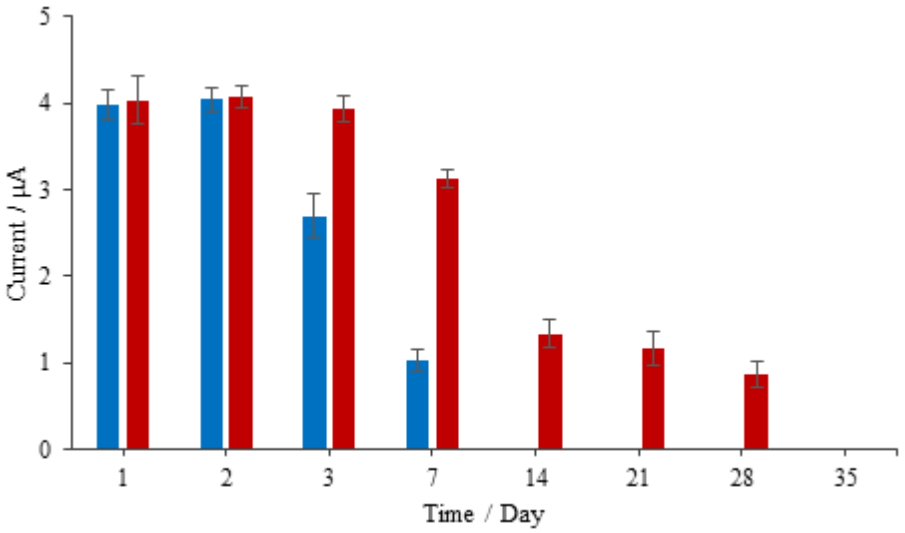

Figure 5.31: Current responses for the oxidation of 10.0 mM glucose in 0.10 M PBS (pH 7.40) at the fMWCNT-Au_{nano}/Nafion® modified SPEs, that were stored in —— PBS and in - - air, over time, n = 3.

5.2.3.2 fMWCNT-Au_{nano}/Pd_{nano} Modified SPEs

Again with the fMWCNT-Au_{nano}/Pd_{nano} modified SPE, a similar overall trend in shelf-life is observed, Figure 5.32. Initially, the sensitivity for glucose drops after 24 h for all sensors stored in both PBS and air and this trend is proportional to storage time. On Day 2 the fMWCNT-Au_{nano}/Pd_{nano} sensors stored in PBS and air have decreased by almost 20% and 30%, respectively. Similarly to the other sensors, from Day 14 onwards the sensors stored in PBS cease to work, although those in air remain responsive, albeit at reduced sensitivities. This outcome from PBS storage is not expected to be as significant with this sensor as the current response shows an almost predictable trend with a gradual decrease seen over time. The sensor stored in air is capable of detecting glucose for a much extended period of time, over 28 days, although as with previous sensors the sensitivities have decreased substantially.

Overall, none of the three sensors show long term stability in either PBS or air, and as such they are not deemed appropriate for storage. Indeed this may not be a promising conclusion but it can be mentioned that these sensors possess an excellent degree of reusability, as discussed previously in Section 5.2.2. As mentioned, there is a possibility that oxides may surface oxides may have been formed on the sensing surfaces and this may have effected glucose detection. The use of electrochemical cycling towards reduction potentials in an acidic medium may have been sufficient to remove these oxides and to regenerate the electroactive film, although this theory was not investigated.

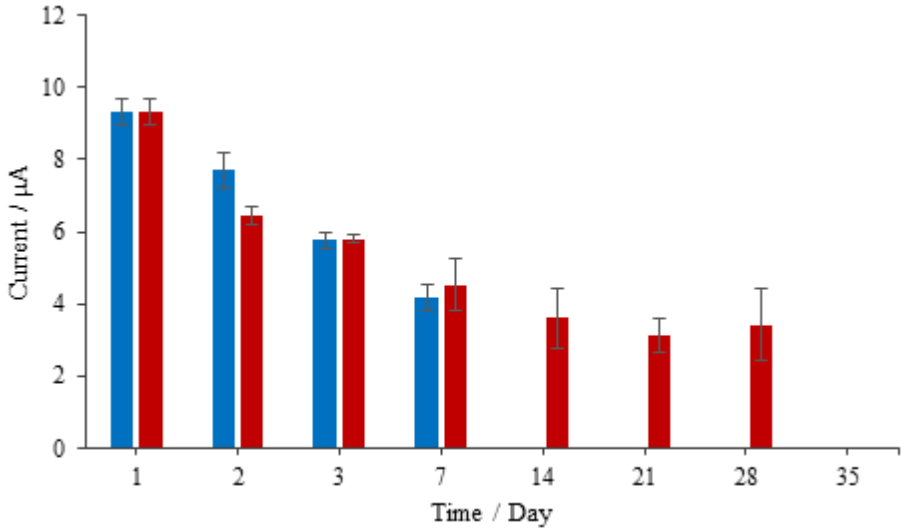

Figure 5.32: Current responses for the oxidation of 10.0 mM glucose in 0.10 M PBS (pH 7.40) at the fMWCNT-Au_{nano}/Pd_{nano} modified SPE, that were stored in ▬ PBS and in ▬ air, over time, n = 3.

5.3 Summary of Results

In this chapter results are presented on the effects of common chemical interferences at the fMWCNT-Au_{nano}, fMWCNT-Au_{nano}/Nafion® and fMWCNT-Au_{nano}/Pd_{nano} composite modified SPEs. Interference from two naturally occurring electroactive substances, AA and UA is investigated, along with the commonly used external influence acetaminophen. Two carbohydrates, fructose and galactose were also tested and the effect of chloride and serum albumins on glucose detection was also examined. Other than the effects of chemical interference, sensor reusability and shelf-life and storage studies were carried out.

In relation to chemical interference it was found that many of the interferants posed significant problems at the sensing films. It was found that interference from AA at the fMWCNT-Au_{nano} films was not that problematic at physiological concentrations. This may be due to the negative potential used for glucose detection, which may have not been ideal to oxidise AA. As expected the use of Nafion® decreased the interference from AA even further, although the use of this membrane also greatly reduced the sensors response towards glucose. Even though the sensitivity was reduced, the stability of the current responses for glucose in the presence of the Nafion® membrane were improved. Overall it may be said that the use of Nafion® was not essential for selective detection of glucose in the presence of 0.10 mM AA at the fMWCNT-Au_{nano} modified SPEs. The same outcome was not apparent at the fMWCNT-Au_{nano}/Pd_{nano} films. The presence of AA at these films caused significant poisoning of the surface which effected the films and impeded glucose detection.

Although AA was not a source of interference at the fMWCNT-Au_{nano} films, the other electroactive species UA posed many problems. Upon injection of UA during CPA the current responses for glucose immediately decreased to the baseline. The addition of further aliquots of glucose yielded no measurable current responses which suggest that UA caused significant surface poisoning. As expected, the use of Nafion® greatly reduced the extent of its interference, although it did not eliminate it fully. These results indicate that accurate glucose detection is not possible in the presence of hyperuricemic concentrations of UA. Unfortunately, it was found that UA also

exhibited negative effects at the fMWCNT-Au_{nano}/Pd_{nano} films. Again, it was clear that UA caused surface poisoning and reduced glucose detection.

The electroactive substance acetaminophen was also found to be problematic during glucose sensing. This interferant caused surface poisoning at all of the composite films but the use of Nafion® did reduce this slightly. Neither of the carbohydrates, fructose or galactose, posed any significant issues at the fMWCNT-Au_{nano} and fMWCNT-Au_{nano}/Nafion® films. It was found that galactose was oxidisable at these films, although the currents were relatively insignificant in comparison to those obtained for glucose. Fructose was not a source of interference, even at very high concentrations. From these results it can be concluded that accurate glucose detection in the presence of both fructose and galactose is possible at the fMWCNT-Au_{nano} and fMWCNT-Au_{nano}/Nafion® films. This same conclusion could not be said for the fMWCNT-Au_{nano}/Pd_{nano} film. Interference from either fructose or galactose was not expected at this film although results showed a drop in the currents for glucose when galactose was present and significant decrease when fructose was present. This again indicates that surface poisoning is occurring and as such accurate glucose detection is not possible at fMWCNT-Au_{nano}/Pd_{nano} film in the presence of these interferants.

Glucose detection at these composite films in the presence of relevant levels of chloride and serum albumins also yielded interesting results. In regards to serum albumins, it was found that glucose detection was only possible at the fMWCNT-Au_{nano}/Nafion® modified SPE due to protection from Nafion®. Chloride also proved to be a major source of interference at the sensing films. Sensitivities for glucose were significantly reduced by over 95% at the fMWCNT-Au_{nano} films when physiological concentrations of chloride were present, which is in keeping with other studies using Au in non-enzymatic glucose sensors. Although studies show that Pd can possess anti-poisoning properties towards chloride, this was not the case at this fMWCNT-Au_{nano}/Pd_{nano} sensor and glucose detection was not possible.

Reusability studies of the sensors showed very promising results. It was observed that accurate glucose detection was possible over the subsequent uses of each sensor. Shelf-life studies did not follow the same trend and it was found that the sensors responses for glucose decreased over time. Even when stored for the short period of

24 h a sufficient decrease in the currents were observed. It was found that storage in air was superior and that storage in PBS was not suitable.

5.4 References

1. K. Iqbal, A. Khan and M. Muzaffar Ali Khan Khattak, *Pakistan Journal of Nutrition*, 2004, **3**, 5-13.
2. X. Zhang, H. Ju and J. Wang, *Electrochemical Sensors, Biosensors and their Biomedical Applications*, Academic Press, 2011.
3. M. D. Rubianes and G. A. Rivas, *Electrochemistry Communications*, 2003, **5**, 689-694.
4. S. Vaddiraju, PhD, University of Connecticut, 2009.
5. J. Jose Ruiz, A. Aldaz and M. Dominguez, Canadian Journal of Chemistry, 1977, 55, 2799-2806.
6. Z. Zhang, J. Zheng, Y. Zhang, W. Zhang, L. Li, Z. Cao, H. Wang, C. Li, Y. Gao and J. Liu, *International Journal of Electrochemical Science*, 2013, **8**, 4183 - 4193.
7. R. E. Özel, K. N. Wallace and S. Andreescu, *Analytica Chimica Acta*, 2011, **695**, 89-95.
8. K. Pihel, Q. D. Walker and R. M. Wightman, *Analytical Chemistry*, 1996, **68**, 2084-2089.
9. N. F. Atta, A. Galal and R. A. Ahmed, *Journal of The Electrochemical Society*, 2011, **158**, F52-F60.
10. X. Liu, H. Zhu and X. Yang, *RSC Advances*, 2014, **4**, 3706-3712.
11. A. So and B. Thorens, *The Journal of Clinical Investigation*, 2010, **120**, 1791- 1799.
12. T.-S. Kim, C.-U. Pae, S.-J. Yoon, W.-Y. Jang, N. J. Lee, J.-J. Kim, S.-J. Lee, C. Lee, I.-H. Paik and C.-U. Lee, *International Journal of Geriatric Psychiatry*, 2006, **21**, 344-348.
13. C. M. Knapp, C. S. Constantinescu, J. H. Tan, R. McLean, G. R. Cherryman and I. Gottlob, *Multiple Sclerosis*, 2004, **10**, 278-280.
14. D. J. Schretlen, A. B. Inscore, H. A. Jinnah, V. Rao, B. Gordon and G. D. Pearlson, *Neuropsychology*, 2007, **21**, 136-140.
15. S. Thirumalairajan, K. Girija, V. Ganesh, D. Mangalaraj, C. Viswanathan and N. Ponpandian, *Crystal Growth & Design*, 2012, **13**, 291-302.
16. M. Chao, X. Ma and X. Li, International Journal of Electrochemical Science, 2012, 7, 2201-2213.
17. J. Jiang and X. Du, *Nanoscale*, 2014, 6, 11303-11309.
18. V. Jiménez and J. B. Alderete, *Journal of Molecular Structure: THEOCHEM*, 2005, **755**, 209-214.
19. M. Vidotti, L. H. Dall'Antonia, E. P. Cintra and S. I. Córdoba de Torresi, *Electrochimica Acta*, 2004, **49**, 3665-3670.
20. M. Campbell and S. Farrell, *Biochemistry*, Cengage Learning, 2011.
21. J. Pazourek, *Journal of Separation Science*, 2010, **33**, 974-981.
22. J.-S. Jeong, H.-R. Yoon and S.-P. Hong, *Journal of Chromatography A*, 2007, **1140**, 157-162.

23. K. Weidemaier, A. Lastovich, S. Keith, J. B. Pitner, M. Sistare, R. Jacobson and D. Kurisko, *Biosensors and Bioelectronics*, 2011, **26**, 4117-4123.
24. D. Rathod, C. Dickinson, D. Egan and E. Dempsey, *Sensors and Actuators B: Chemical*, 2010, **143**, 547-554.
25. L. L. E. Salins, R. A. Ware, C. M. Ensor and S. Daunert, *Analytical Biochemistry*, 2001, **294**, 19-26.
26. S. A. Kumar, H.-W. Cheng, S.-M. Chen and S.-F. Wang, *Materials Science and Engineering: C*, 2010, **30**, 86-91.
27. Z. Zhuang, X. Su, H. Yuan, Q. Sun, D. Xiao and M. M. F. Choi, *Analyst*, 2008, **133**, 126-132.
28. P. Parpot, S. G. Pires and A. P. Bettencourt, *Journal of Electroanalytical Chemistry*, 2004, **566**, 401-408.
29. R. Roth, *Nutrition & Diet Therapy*, Cengage Learning, 2010.
30. S. Köpper and S. Freimund, *Helvetica Chimica Acta*, 2003, **86**, 827-843.
31. T. Kawasaki, H. Akanuma and T. Yamanouchi, *Diabetes Care*, 2002, **25**, 353- 357.
32. D. Faeh, K. Minehira, J.-M. Schwarz, R. Periasamy, S. Park and L. Tappy, *Diabetes*, 2005, **54**, 1907-1913.
33. M. E. Bocarsly, E. S. Powell, N. M. Avena and B. G. Hoebel, *Pharmacology Biochemistry and Behavior*, 2010, **97**, 101-106.
34. Z. Ibupoto, K. Khun, V. Beni, X. Liu and M. Willander, *Sensors*, 2013, **13**, 7926-7938.
35. Y. Xing, G. Gao, G. Zhu, J. Gao, Z. Ge and H. Yang, *Journal of The Electrochemical Society*, 2014, **161**, B106-B110.
36. G. S. N. Lau, *Metabolic Activation of Drugs and Other Xenobiotics in Hepatocellular Carcinoma*, Chinese University Press, 1997.
37. K. J. S. Anand, B. J. Stevens and P. J. McGrath, *Pain in Neonates and Infants*, Elsevier Health Sciences, 2007.
38. R. J. Fontana, *Medical Clinics of North America*, 2008, **92**, 761-794.
39. K. E. Toghill and a. R. G. Compton, *International Journal of Electrochemical Science*, 2010, **5**, 1246-1301
40. H. Shafiei, M. Haqgu, D. Nematollahi and R. M. Gholami, *International Journal of Electrochemical Science*, 2008, **3**, 1092-1107.
41. D. Moatti-Sirat, V. Poitout, V. Thomé, M. N. Gangnerau, Y. Zhang, Y. Hu, G. S. Wilson, F. Lemonnier, J. C. Klein and G. Reach, *Diabetologia*, 1994, **37**, 610-616.
42. M. E. Z. Estes, *Health Assessment & Physical Examination*, Thomson Delmar Learning, 2006.
43. G. J. Quinlan, G. S. Martin and T. W. Evans, *Hepatology*, 2005, **41**, 1211- 1219.
44. G. Li, D. Magana and R. B. Dyer, *Nature Communications*, 2014, **5**.
45. B. X. Huang, H.-Y. Kim and C. Dass, *Journal of the American Society for Mass Spectrometry*, 2004, **15**, 1237-1247.

46. S. Jana, S. Ghosh, S. Dalapati and N. Guchhait, *Photochemical & Photobiological Sciences*, 2012, **11**, 323-332.
47. X. Zhao, R. Liu, Z. Chi, Y. Teng and P. Qin, *The Journal of Physical Chemistry B*, 2010, **114**, 5625-5631.
48. S. Chen, R. Yuan, Y. Chai, L. Min, W. Li and Y. Xu, *Electrochimica Acta*, 2009, **54**, 7242-7247.
49. W. H. K., H. W. D. and H. J. W., *Clinical Methods: The History, Physical, and Laboratory Examinations*, Boston: Butterworths, 1990.
50. S. Park, H. Boo and T. D. Chung, *Analytica Chimica Acta*, 2006, **556**, 46-57.
51. M. Tominaga, M. Nagashima, K. Nishiyama and I. Taniguchi, *Electrochemistry Communications*, 2007, **9**, 1892-1898.
52. L. Meng, J. Jin, G. Yang, T. Lu, H. Zhang and C. Cai, *Analytical Chemistry*, 2009, **81**, 7271-7280.

Chapter 6

General Conclusions

6.1 Conclusions

In this work, composite materials comprising of pristine (MWCNTs) and acid-functionalised multiwalled carbon nanotubes (fMWCNTs) with gold nanoparticles (AuNPs), palladium nanoparticles (PdNPs) and a combination of both Au and Pd were synthesised and characterised and used in electrochemical sensors for the non-enzymatic detection of glucose at physiological pH.

Initial work was focused on synthetically reducing AuNPs onto the surface of non-functionalised MWCNTs using the reducing agent sodium borohydride ($NaBH_4$). The composite was named MWCNT-Au_{nano}($NaBH_4$). Due to the hydrophobic nature of the MWCNTs, they were dispersed in a 1.0% sodium dodecyl sulfate (SDS) solution to create a homogeneous black suspension to which the reduction of the Au salt could be undertaken in. The mixture was left for 5 min to react and the composite was then isolated and washed over a 0.45 µm membrane using vacuum filtration. This isolation and purification step was carried out for all composite materials produced using the synthetic reduction method. It was confirmed through EDX analysis that Au was present in the MWCNT-Au_{nano}($NaBH_4$) composite and using AAS an Au loading of 1% wt. was calculated. This composite was then cast onto a GC electrode, from a dispersion produced in SDS, to form the electrochemical sensing surface. A pre-treatment step in 0.30 M NaOH was undertaken before each analysis. In this step, the composite-modified GC electrode was cycled in the 0.30 M NaOH solution until redox peaks assigned to the redox activity of Au appeared and stabilised in the resulting CVs. This step was an essential step to remove the adsorbed SDS from the drop cast films and enabled glucose detection. Glucose detection was carried out by cycling the sensor in a 0.10 M PBS solution (pH 7.40) containing concentrations of glucose ranging from 1 – 10 mM. The resulting CVs exhibited glucose oxidation peaks in both the forward and reverse scans, although that in the reverse scan, at 0.25 V vs. SCE, provided the largest current response and was therefore used to construct a calibration curve. From the linear plot, a sensitivity value of 0.504 µA/mM was determined from the slope and using the currents of the blank responses in just 0.10 M PBS, a LOD value of 1.348 µM was calculated.

To try to improve the composite's sensitivity towards glucose, the Au loading within the composite material was increased. This was achieved through the use of the same synthetic procedure previously mentioned, although fMWCNTs were employed in place of pristine MWCNTs. The defects sites formed on the surface of the carbon nanotubes during the acid functionalisation are beneficial for the deposition of AuNPs, as AuNPs tend to form around these sites. Various fMWCNTs, formed from concentrated HNO_3 reflux for 18 h, 24 h and 48 h were used during syntheses. All of these composite materials provided films with improved sensitivity towards glucose, although the composite formed using the 24 h fMWCNTs provided optimum sensitivity. This composite was named 24 h fMWCNT-$Au_{nano}(NaBH_4)$ and was initially cast onto a GC electrode to form the composite-modified film. A sensitivity value of 2.102 µA/mM was calculated from the linear calibration plot, which is a value over 300% higher than that measured using the MWCNT-$Au_{nano}(NaBH_4)$ composite film. The 24 h fMWCNT-$Au_{nano}(NaBH_4)$ composite was fully characterised using techniques including SEM, TEM, EDX, AAS and XRD. The composite contained crystalline face centered cubic (fcc) (111) AuNPs on the surface of the fMWCNTs with a mode diameter of 7.5 nm. The Au loading was calculated to be 2.0 wt. from both EDX and AAS analysis. The presence of AuNPs on the fMWCNTs was also suggested during Raman spectroscopy, as the characteristic G and D bands of the graphitic fMWCNTs were increased in intensity. This occurrence is known as surface enhanced Raman scattering (SERs).

To even further increase the films sensitivity towards glucose, an electrochemical cycling step in 0.5 M and 1.0 M H_2SO_4 was employed. This step was used as a cleaning step to remove any adsorbed species remaining in the composite film, namely SDS and also to help remove oxides from the Au surfaces so that a maximum amount of Au metal could be exposed. During this analyses, a large reduction peak at 0.90 V vs. SCE appeared, which corresponded to the reduction of Au oxide, which was produced in the forward cycles in H_2SO_4, and the intensity of these reduction peaks corresponded to the surface area of Au metal exposed in the film. By cycling the modified GC electrodes in 0.5 M and 1.0 M H_2SO_4, the Au surface area could be increased to 0.2874 cm^2 and 0.4562cm^2, respectively. This is much larger than the Au surface area of 0.0549 cm^2 calculated at the MWCNT-$Au_{nano}(NaBH_4)$ composite film. An overall increase in the capacitance was also evident in the CVs, which can be

related to a larger surface area. As such, the 1.0 M H_2SO_4 pre-treatment step was used to 'optimise' the sensitivities of all prepared films. The sensitivity of the 1.0 M H_2SO_4 optimised film towards glucose was increased to 2.430 µA/mM, in comparison to that of 2.102 µA/mM obtained at the film without acid treatment. Electrochemical Impedance Spectroscopy (EIS) was undertaken to investigate the changes in the capacitance and resistance at acid-treated and non-treated composite films. It was found that the 1.0 M H_2SO_4 optimised film provided the highest capacitance values and lowest resistance values during EIS, which may be associated with an increase in surface area. Using these optimised composite films, CPA analysis was then employed to detect glucose. A constant potential of 0.30 V vs. SCE was used during CPA, which was deemed to be the optimum potential as it provided the largest current responses for glucose during analyses.

In an attempt to further increase the sensors sensitivity, a new fMWCNT-Au_{nano} composite was produced using different synthesis conditions and the reducing agent trisodium citrate (TriSodCit). This new composite was named fMWCNT-Au_{nano}(TriSodCit). Through characterisation studies it was found that the fMWCNT-Au_{nano}(TriSodCit) composite contained an increased Au loading at 5.0% wt. and that fcc (111) AuNPs were formed with a mode diameter of 23 nm. From high resolution TEM work, lattice fringes were visible on the AuNPs and by measuring the distance between these fringes, the inter-atomic distance, it was also determined that fcc AuNPs were produced. The composite film formed provided a higher sensitivity towards glucose due to its higher loading of Au and larger Au exposed surface area. A sensitivity value of 4.070 µA/mM was calculated from the glucose calibration curve. Although the sensitivity was improved, the use of this composite material was not continued due to stability reasons. When this material was dispersed in a SDS solution for casting onto the GC electrodes, the resulting dispersions only produced sensitive films for one or two days. It was assumed that AuNP aggregation was occurring in the concentrated dispersions, possibly due to their larger size and closer proximity to one another. As such, further work was only undertaken using the fMWCNT-Au_{nano}($NaBH_4$) composite material.

Having optimised the detection system on the GC electrodes, the system was then miniaturised through the use of carbon screen-printed electrodes (SPEs). Two types

of SPEs were used, one containing a planar-type carbon working electrode and the other with an ordered macroporous carbon working electrode. The macroporous SPEs were used to investigate possible improvements in glucose sensitivity, as they reportedly contained a higher surface area. Although, no improvements in sensitivity were seen and as such only the planar SPEs were further used. CPA was again employed for glucose detection at the modified SPEs, although the applied potential was modified to -0.05 V vs. Ag/AgCl, due to the different reference electrode used. These modified SPEs, provided an improved sensitivity towards glucose, measured to be 2.766 µA/mM. A lower LOD of 0.049 µM was also calculated from the background currents during CPA analysis. Another benefit of these much smaller systems was that steady-state baseline currents could be achieved much faster during CPA, in comparison to the previous GC electrochemical systems.

The application of Nafion® on the modified SPEs was investigated for the purpose of improved selectivity for glucose in the presence of possible interferants. Chemical interferants studied included, AA, UA, Fructose, Galactose, Acetaminophen, BSA and Chloride. Although it was found that Nafion® did in fact reduce interference and increase selectivity, it also acted as a diffusion barrier towards glucose and as such decreased the sensors sensitivity. Because of this, the next approach was to attempt to eliminate the use of Nafion®, through the use of a different type of composite. A new bi-metallic composite was produced by electrodepositing PdNPs onto the surface of pre-prepared and optimised fMWCNT-$Au_{nano}(NaBH_4)$ modified SPEs. These composite films were named fMWCNT-Au_{nano}/Pd_{nano} and consisted of PdNPs with a mode diameter of 95 nm and contained an estimated Pd loading of about 3% wt., from EDX analysis.

Using these bi-metallic films, it was possible to detect glucose at a more negative potential of -0.45 V vs. Ag/AgCl, in comparison to the -0.05 V vs. Ag/AgCl previously used. This shift in the onset of oxidation may have been due to a change in the work function of the bi-metallic composite. A more positive film may have been formed which could have shifted the potential of zero charge towards a more negative potential, thus resulting in the formation of the catalytically active $Au(OH)_{ads}$ at more negative potentials. It was hoped that the use of this negative potential would not facilitate the oxidation of interferant species, such as AA and UA, which commonly

oxidise towards more positive potentials and would also reduce their interference at the films surface. Although these films could facilitate glucose detection at more negative potentials, it was found that they were not useful for selective sensing as interference was significant using all of the interferants studied. Overall the fMWCNT-Au_{nano} and fMWCNT-Au_{nano}/Nafion® modified sensors were far superior in regards to anti-interference and also sensitivity.

Reusability studies and storage studies were carried out with the optimised fMWCNT-Au_{nano}, fMWCNT-Au_{nano}/Nafion® and fMWCNT-Au_{nano}/Pd_{nano} composite modified SPEs. It was found that all sensors were capable of accurately detecting glucose over twelve successive uses, although they were found not to be suitable for storage in either air or PBS as their sensitivity towards glucose decreased significantly after a very short time in storage. This reduction in sensitivity may be a result of oxides being formed on the exposed Au and Pd surfaces over time and also due to oxidative damage of the SPE circuits. A more appropriate study may have involved their storage in air/oxygen free environments, those commonly used for storage of commercial glucose sensors.

6.2 Future Work

There are a number of potential applications that could be associated with the composite sensors produced. The detection of glucose non-enzymatically could be continued and research could be focused on improving the sensors selectivity towards glucose and on reducing poisoning by coexisting substances present in the blood. This may be possible through further use of a negatively charged membrane such as Nafion®, although the problem of chloride poisoning would still exist. Investigation into the use of other bi-metallic or alloy composites that may be resistant to chloride poisoning could be carried out. The fMWCNT-Au_{nano} material could be used as a base material to create such alloys. In recent work by Wang *et al.*[1] it has been reported that platinum (Pt) metal also suffers from chloride poisoning during glucose detection, although when combined with lead (Pb) in varying ratios to form the bi-metallic alloy (Pt-Pb), the sensors were capable of detecting glucose while being highly resistant to chloride poisoning. However, in this current thesis work, the bi-metallic system studied, Au-Pd, did not possess such qualities. If both the selectivity was optimised and the poisoning by substances was eliminated, a next step could be focussed on

selectively testing for glucose in real blood samples. Although, due to the issues present in non-enzymatic glucose sensing, the composite sensors may find more suitable applications in other electrochemical detection systems. For example, during the interference studies it was found that acetaminophen could be detected at the composite films, as faradaic redox processes were visible in the CVs. Other potentially detectable molecules at carbon and gold based electrodes may include DNA [2], hydrogen peroxide [3] and various neurotransmitters such as cortisol [4], androsterone [4] and dopamine [5] and the neurotransmitter precursor L-DOPA [6].

Due to the large surface areas of Au present in the prepared composite films, these films may also find applications in heterogenous catalysis. Recent work by Shanahan *et al.*[7], reports the use of AuNP-single walled carbon nanotube composites for a solvent-less aerobic oxidation of a secondary alcohol. The use of AuNPs within fuel cells has also been reported. In a study by Matsuoka *et al.* [8] it has been shown that films containing AuNPs can be used in direct methanol fuel cells. A recent report by Kulesza [9] *et al.* also discusses the use of AuNPs and their alloys in carbon monoxide and alcohol fuel cells.

6.3 Conference Presentations

David Branagan and Carmel Breslin, "The Formation of Metal-Carbon Nanotube Composites for Applications in Non-Enzymatic Glucose Sensing", 66th Irish Universities Chemistry Research Colloquium, National University of Ireland, Galway, 19/06/14 – 20/06/14, [Oral presentation] – WINNER.

David Branagan and Carmel Breslin, "Non-Enzymatic Selective Detection of Glucose Based on a Gold-Decorated Multi-Walled Carbon Nanotube Composite", 224th Electrochemical Society Meeting, San Francisco, California, 27/10/2013 – 01/11/2013, [Poster presentation].

David Branagan and Carmel Breslin, "Formation and Characterisation of Three-dimensional Macroporous Copper Structures", Electrochemical Horizons 2012, Trinity College Dublin, Ireland, 02/09/2012 – 04/09/2012, [Poster presentation].

6.4 Papers in Preparation/Submitted

Non-enzymatic Glucose Sensor Based on a Gold Nanoparticle-Multiwalled Carbon Nanotube-Nafion® Modified Screen Printed Electrode, [Preparation].

A Gold Nanoparticle-Carbon Nanotube Composite Material and its Application in Chromium Sensing, [Submitted].

David Branagan and Carmel B. Breslin. Non-Enzymatic Selective Detection of Glucose Based on a Gold Nanoparticle-Carbon Nanotube Composite Film. *ECS Transactions*, 2014, 58 (25), 59-65, [Published].

6.5 References

1. J. Wang, D. F. Thomas and A. Chen, *Analytical Chemistry*, 2008, **80**, 997- 1004.
2. L. Li, S. Wang, T. Yang, S. Huang and J. Wang, *Biosensors and Bioelectronics*, 2012, **33**, 279-283.
3. J. Narang, N. Chauhan and C. S. Pundir, *Analyst*, 2011, **136**, 4460-4466.
4. M. Moreno-Guzmán, L. Agüí, A. González-Cortés, P. Yáñez-Sedeño and J. M. Pingarrón, *Journal of Solid State Electrochemistry*, 2013, **17**, 1591-1599.
5. S. Yang, Y. Yin, G. Li, R. Yang, J. Li and L. Qu, *Sensors and Actuators B: Chemical*, 2013, **178**, 217–221.
6. G.-Z. Hu, L. Chen, Y. Guo, X.-L. Wang and S.-J. Shao, *Electrochimica Acta*, 2010, **55**, 4711-4716.
7. A. E. Shanahan, J. A. Sullivan, M. McNamara and H. J. Byrne, *New Carbon Materials*, 2011, **26**, 347-355.
8. K. Matsuoka, K. Miyazaki, Y. Iriyama, K. Kikuchi, T. Abe and Z. Ogumi, *The Journal of Physical Chemistry C*, 2007, **111**, 3171-3174.
9. P. J. Kulesza, I. S. Pieta, I. A. Rutkowska, A. Wadas, D. Marks, K. Klak, L. Stobinski and J. A. Cox, *Electrochimica Acta*, 2013, **110**, 474-483.

Appendix

MATERIALS & SURFACE SCIENCE INSTITUTE

UNIVERSITY *of* LIMERICK

David Branagan

National University of Ireland Maynooth
Department of Chemistry
Maynooth
Co. Kildare

Re: **Quotation No. MSSI14Q112XRD**

SAMPLE: 3 Samples for XRD

DATE REPORTED: 30th July 2014

INTRODUCTION

Three multi-walled carbon nanotube samples were received for XRD scan.

TECHNICAL DETAILS

SAMPLE PREPARATION: Samples were on Chi-Phi stage. All run under same conditions.

ANALYSIS TYPE: X-Ray Diffraction

INSTRUMENT: PANalytical Empyrean

RESULTS As seen in the following pages

ATTACHMENTS .XRDML ; .csv

Dr. Wynette Redington

Research Fellow, MSSI

Anchor Scan Parameters: Sample 1-Au_CNT
Dataset Name Sample 1-Au_CNT
File name C:\XRD Data\Wynette\NUI Maynooth\2014-July24\July28\Sample 1-Au_CNT.xrdml
Comment Configuration=Chi-Phi-z Stage, Owner=User-1, Creation date=2/20/2012 9:05:27 AM
Goniometer=Theta/Theta; Minimum step size 2Theta:0.0001; Minimum step size Omega:0.0001
Sample stage=Chi-Phi-z stage 240 mm (reflection); Minimum step size Phi:0.01; Minimum step size Chi:0.01; Minimum step size Z:0.001
Diffractometer system=EMPYREAN
Measurement program=C:\PANalytical\Data Collector\Programs\Wynette\ChiPhi-GonioProgs\Chi-Phi--Focus-gonio.xrdmp, Identifier=67C559EF-52C2-4C84-BB9C-415BF3647818
Measurement Date / Time 7/28/2014 12:08:13 PM
Operator User
Raw Data Origin XRD measurement (*.XRDML)
Scan Axis Gonio
Start Position [°2Th.] 10.0091
End Position [°2Th.] 79.9881
Step Size [°2Th.] 0.0130
Scan Step Time [s] 58.3950
Scan Type Continuous
PSD Mode Scanning
PSD Length [°2Th.] 3.35
Offset [°2Th.] 0.0000
Divergence Slit Type Fixed
Divergence Slit Size [°] 0.2177
Specimen Length [mm] 10.00
Measurement Temperature [°C] 25.00
Anode Material Cu
K-Alpha1 [Å] 1.54060
K-Alpha2 [Å] 1.54443
K-Beta [Å] 1.39225

K-A2 / K-A1 Ratio 0.50000
Generator Settings 40 mA, 40 kV
Diffractometer Type 0000000011121830
Diffractometer Number 0
Goniometer Radius [mm] 240.00
Dist. Focus-Diverg. Slit [mm] 100.00
Incident Beam Monochromator No
Spinning No

Graphics: Sample 1-Au_CNT

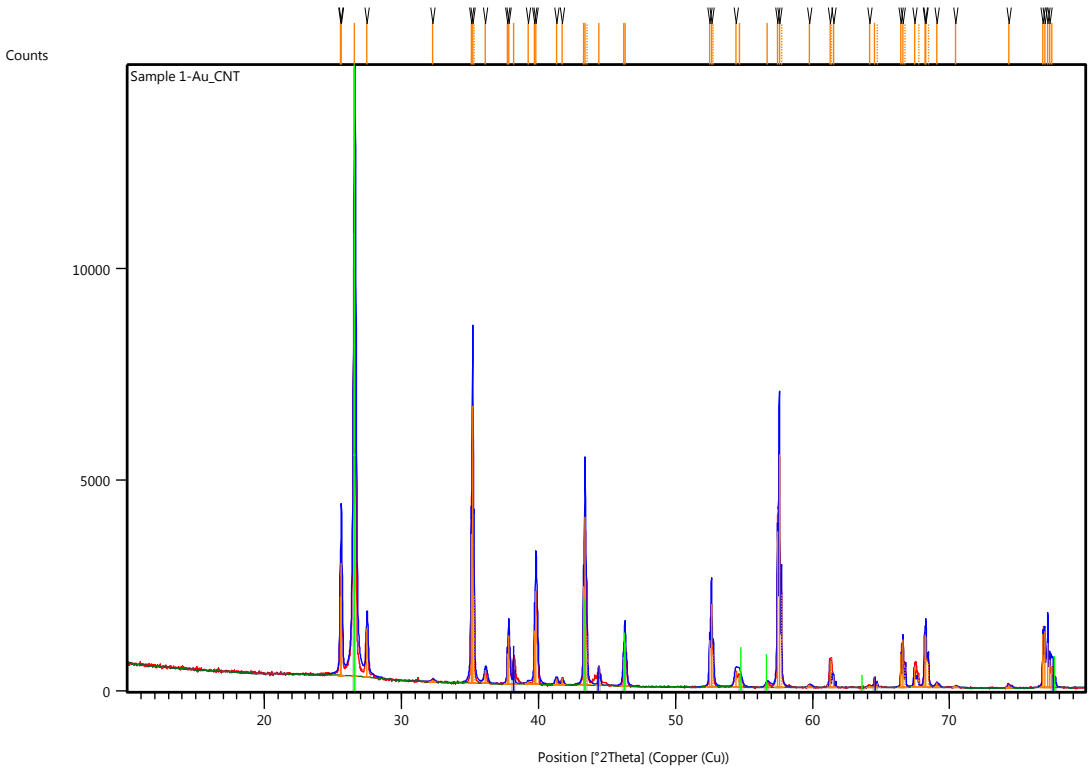

Peak List: Sample 1-Au_CNT

Pos. [°2Th.]	Height [cts]	FWHM Left [°2Th.]	d-spacing [Å]	Rel. Int. [%]	Tip Width	Matched by
25.5398	1869.51	0.0780	3.48494	17.83	0.0936	
25.6228	2646.01	0.0895	3.47673	25.24	0.1075	
26.5774	10484.70	0.2047	3.35397	100.00	0.2456	98-001-7197
27.4861	1156.05	0.1407	3.24512	11.03	0.1689	
32.2745	46.91	0.3070	2.77376	0.45	0.3684	
35.0937	3517.36	0.0936	2.55501	33.55	0.1123	
35.2101	6554.40	0.0780	2.54683	62.51	0.0936	
35.3268	2069.07	0.0468	2.54499	19.73	0.0562	
36.1359	318.06	0.2184	2.48367	3.03	0.2621	
37.7221	720.10	0.0624	2.38280	6.87	0.0749	
37.8392	1139.80	0.1092	2.37570	10.87	0.1310	
38.1717	603.10	0.0468	2.35577	5.75	0.0562	98-005-1004
39.2489	45.76	0.1872	2.29355	0.44	0.2246	
39.7153	1276.07	0.0780	2.26769	12.17	0.0936	
39.8270	2207.91	0.1404	2.26158	21.06	0.1685	
41.3001	152.27	0.2184	2.18426	1.45	0.2621	
41.7370	164.12	0.0936	2.16240	1.57	0.1123	
43.2893	2341.68	0.0624	2.08838	22.33	0.0749	98-001-7197
43.4031	3975.19	0.1092	2.08317	37.91	0.1310	98-001-7197
43.5485	1165.82	0.0624	2.08171	11.12	0.0749	
44.4130	439.48	0.0780	2.03812	4.19	0.0936	98-005-1004
46.2122	692.63	0.1248	1.96287	6.61	0.1498	98-001-7197
46.3141	1038.19	0.1092	1.95879	9.90	0.1310	98-001-7197

52.4851	1102.63	0.0780	1.74208	10.52	0.0936	
52.6196	1950.55	0.1092	1.73794	18.60	0.1310	
52.7618	793.70	0.0780	1.73790	7.57	0.0936	
54.3923	368.39	0.2184	1.68542	3.51	0.2621	
54.6571	280.35	0.2496	1.67787	2.67	0.2995	98-001-7197
56.6836	113.51	0.3120	1.62260	1.08	0.3744	98-001-7197
57.4409	3697.18	0.0936	1.60300	35.26	0.1123	
57.5704	5516.70	0.0624	1.59970	52.62	0.0749	
57.7324	2233.73	0.0624	1.59956	21.30	0.0749	
59.7674	64.84	0.2496	1.54604	0.62	0.2995	
61.2740	646.00	0.0780	1.51158	6.16	0.0936	
61.3734	701.02	0.0468	1.51313	6.69	0.0562	
61.5423	282.18	0.0624	1.50564	2.69	0.0749	
64.1445	47.42	0.1872	1.45069	0.45	0.2246	
64.5243	249.56	0.0936	1.44306	2.38	0.1123	98-005-1004
64.7241	132.92	0.0936	1.44267	1.27	0.1123	
66.4588	797.99	0.0780	1.40567	7.61	0.0936	
66.5910	1120.14	0.0624	1.40321	10.68	0.0749	
66.7647	523.08	0.0780	1.40345	4.99	0.0936	
67.4391	477.17	0.1248	1.38760	4.55	0.1498	
67.7410	281.42	0.0936	1.38559	2.68	0.1123	
68.1934	1241.03	0.1092	1.37408	11.84	0.1310	
68.2733	1188.74	0.0780	1.37267	11.34	0.0936	
68.4737	577.82	0.0780	1.37254	5.51	0.0936	
69.0485	106.35	0.2184	1.35914	1.01	0.2621	
70.4417	36.94	0.2496	1.33563	0.35	0.2995	
74.3108	85.70	0.1872	1.27537	0.82	0.2246	
76.8170	1275.76	0.0780	1.23989	12.17	0.0936	
76.9298	1340.49	0.0780	1.23835	12.79	0.0936	

77.1674	1061.26	0.0936	1.23513	10.12	0.1123	
77.2986	655.35	0.0624	1.23336	6.25	0.0749	
77.4785	494.18	0.1248	1.23095	4.71	0.1498	98-005-1004; 98-001-7197

Identified Patterns List: Sample 1-Au_CNT

Visible	Ref. Code	Score	Compound Name	Displacement [°2Th.]	Scale Factor	Chemical Formula
*	98-005-1004	48	Gold	0.002	0.061	Au1
*	98-001-7197	38	Graphite 3R	-0.048	1.016	C1

Plot of Identified Phases: Sample 1-Au_CNT

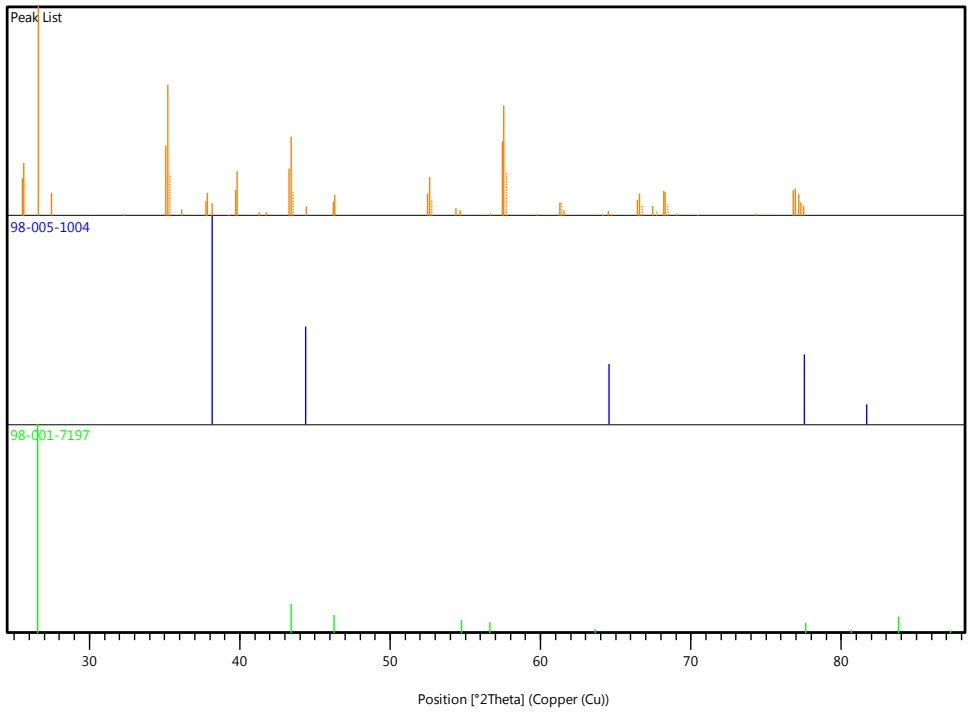

Document History: Sample 1-Au_CNT
Insert Measurement:
- File name = "Sample 1-Au_CNT.xrdml"
- Modification time = "7/29/2014 9:45:51 AM"

- Modification editor = "User"

Default properties:
- Measurement step axis = "None"
- Internal wavelengths used from anode material: Copper (Cu)
- Original K-Alpha1 wavelength = "1.54060"
- Used K-Alpha1 wavelength = "1.54060"
- Original K-Alpha2 wavelength = "1.54443"
- Used K-Alpha2 wavelength = "1.54443"
- Original K-Beta wavelength = "1.39225"
- Used K-Beta wavelength = "1.39225"
- Irradiated length = "10.00000"
- Spinner used = "No"
- Receiving slit size = "0.10000"
- Step axis value = "0.00000"
- Offset = "0.00000"
- Sample length = "10.00000"
- Modification time = "7/29/2014 9:45:51 AM"
- Modification editor = "User"

Interpolate Step Size:
- Derived = "Yes"
- Step Size = "0.01"
- Modification time = "7/29/2014 9:45:51 AM"
- Modification editor = "PANalytical"

Determine Background:
- Add to net scan = "Nothing"
- User defined intensity = "-5"
- Correction method = "Automatic"
- Bending factor = "1"
- Minimum significance = "0.7"
- Minimum tip width = "0"
- Maximum tip width = "1"
- Peak base width = "2"
- Use smoothed input data = "Yes"
- Granularity = "20"
- Modification time = "7/28/2014 3:14:26 PM"
- Modification editor = "User"

Search Peaks:
- Minimum significance = "2"
- Minimum tip width = "0.01"
- Maximum tip width = "1"

- Peak base width = "2"
- Method = "Top of smoothed peak"
- Modification time = "7/28/2014 3:14:36 PM"
- Modification editor = "User"

Search & Match:
- Allow pattern shift = "Yes"
- Auto residue = "Yes"
- Data source = "Profile and peak list"
- Demote unmatched strong = "No"
- Multi phase = "Yes"
- Restriction set = "Untitled"
- Restriction = "Restriction set"
- Subset name = ""
- Match intensity = "Yes"
- Two theta shift = "0"
- Identify = "Yes"
- Max. no. of accepted patterns = "5"
- Minimum score = "5"
- Min. new lines / total lines = "60"
- Search depth = "10"
- Minimum new lines = "5"
- Minimum scale factor = "0.1"
- Intensity threshold = "0"
- Use line clustering = "Yes"
- Line cluster range = "1.5"
- Search sensitivity = "1.8"
- Use adaptive smoothing = "Yes"
- Smoothing range = "1.5"
- Threshold factor = "3"
- Modification time = "7/29/2014 9:46:31 AM"
- Modification editor = "User"

Search & Match:
- Allow pattern shift = "Yes"
- Auto residue = "Yes"
- Data source = "Profile and peak list"
- Demote unmatched strong = "No"
- Multi phase = "Yes"
- Restriction set = "Untitled"
- Restriction = "Restriction set"
- Subset name = ""
- Match intensity = "Yes"
- Two theta shift = "0"

- Identify = "Yes"
- Max. no. of accepted patterns = "5"
- Minimum score = "5"
- Min. new lines / total lines = "60"
- Search depth = "10"
- Minimum new lines = "5"
- Minimum scale factor = "0.1"
- Intensity threshold = "0"
- Use line clustering = "Yes"
- Line cluster range = "1.5"
- Search sensitivity = "1.8"
- Use adaptive smoothing = "Yes"
- Smoothing range = "1.5"
- Threshold factor = "3"
- Modification time = "7/29/2014 9:46:48 AM"
- Modification editor = "User"

Anchor Scan Parameters: Sample 2_PdCNT-2
Dataset Name Sample 2_PdCNT-2
File name C:\XRD Data\Wynette\NUI Maynooth\2014-July24\July28\Sample 2_PdCNT-2.xrdml
Comment Configuration=Chi-Phi-z Stage, Owner=User-1, Creation date=2/20/2012 9:05:27 AM
Goniometer=Theta/Theta; Minimum step size 2Theta:0.0001; Minimum step size Omega:0.0001
Sample stage=Chi-Phi-z stage 240 mm (reflection); Minimum step size Phi:0.01; Minimum step size Chi:0.01; Minimum step size Z:0.001
Diffractometer system=EMPYREAN
Measurement program=C:\PANalytical\Data Collector\Programs\Wynette\ChiPhi-GonioProgs\Chi-Phi--Focus-gonio.xrdmp, Identifier=67C559EF-52C2-4C84-BB9C-415BF3647818
Measurement Date / Time 7/28/2014 3:28:01 PM
Operator User
Raw Data Origin XRD measurement (*.XRDML)
Scan Axis Gonio
Start Position [°2Th.] 10.0091
End Position [°2Th.] 79.9881
Step Size [°2Th.] 0.0130
Scan Step Time [s] 58.3950
Scan Type Continuous
PSD Mode Scanning
PSD Length [°2Th.] 3.35
Offset [°2Th.] 0.0000
Divergence Slit Type Fixed

Divergence Slit Size [°] 0.2177
Specimen Length [mm] 10.00
Measurement Temperature [°C] 25.00
Anode Material Cu
K-Alpha1 [Å] 1.54060
K-Alpha2 [Å] 1.54443
K-Beta [Å] 1.39225
K-A2 / K-A1 Ratio 0.50000
Generator Settings 40 mA, 40 kV
Diffractometer Type 0000000011121830
Diffractometer Number 0
Goniometer Radius [mm] 240.00
Dist. Focus-Diverg. Slit [mm] 100.00
Incident Beam Monochromator No
Spinning No

Graphics: Sample 2_PdCNT-2

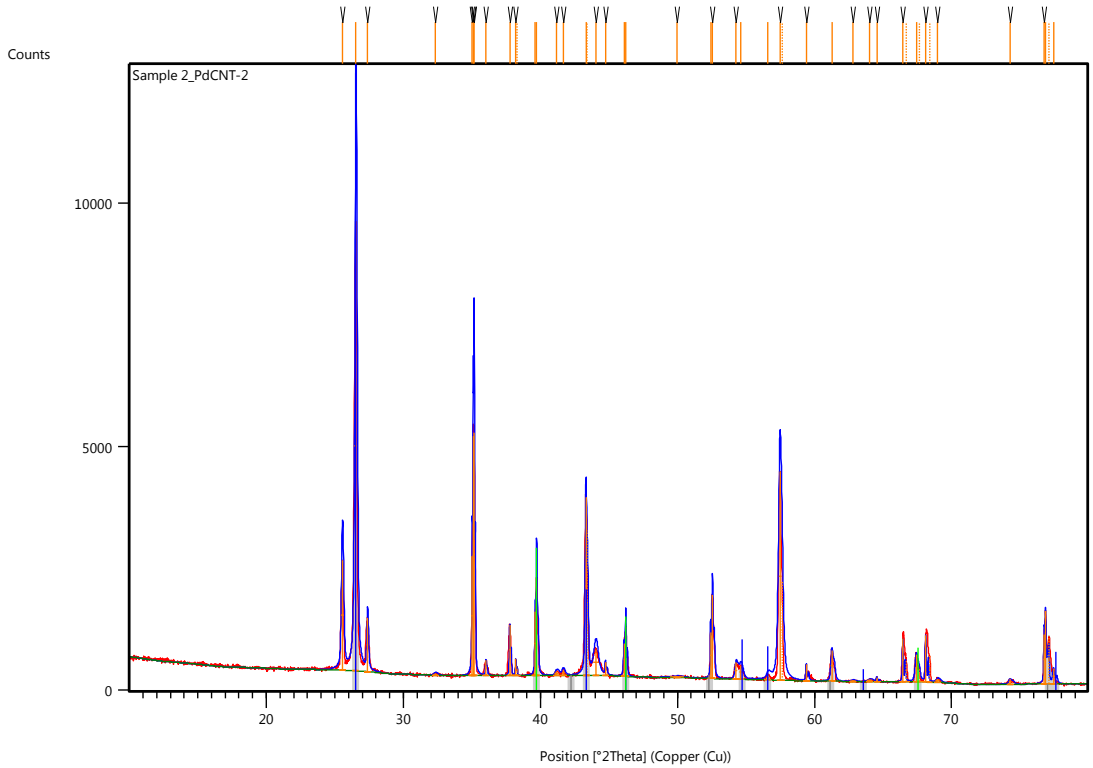

Peak List: Sample 2_PdCNT-2

Pos. [°2Th.]	Height [cts]	FWHM Left [°2Th.]	d-spacing [Å]	Rel. Int. [%]	Tip Width	Matched by
25.5497	2261.01	0.1663	3.48650	24.47	0.1996	
26.5297	9239.00	0.1791	3.35990	100.00	0.2149	98-001-7197
27.3765	1099.89	0.1023	3.25786	11.90	0.1228	
32.3395	43.39	0.3070	2.76834	0.47	0.3684	
35.0172	2444.88	0.0468	2.56042	26.46	0.0562	
35.0935	4917.07	0.0780	2.55503	53.22	0.0936	
35.1659	4976.41	0.0512	2.55205	53.86	0.0614	
36.0239	313.33	0.0895	2.49321	3.39	0.1075	
37.7623	1042.09	0.0768	2.38233	11.28	0.0921	
38.1992	342.10	0.0624	2.35413	3.70	0.0749	
38.2984	185.88	0.0468	2.35410	2.01	0.0562	
39.6270	1304.96	0.0780	2.27254	14.12	0.0936	98-002-2010
39.7279	1997.46	0.0936	2.26700	21.62	0.1123	98-002-2010
41.1932	90.98	0.3120	2.18968	0.98	0.3744	
41.6584	116.78	0.2184	2.16630	1.26	0.2621	
43.3258	3655.28	0.1404	2.08671	39.56	0.1685	98-001-7197
43.3947	2974.31	0.0624	2.08873	32.19	0.0749	
44.0277	526.42	0.3744	2.05506	5.70	0.4493	
44.7481	279.62	0.0780	2.02363	3.03	0.0936	
46.1075	679.47	0.1092	1.96708	7.35	0.1310	98-001-7197; 98-002-2010
46.2193	1014.87	0.0624	1.96258	10.98	0.0749	98-001-7197; 98-002-2010
49.9887	24.18	0.9984	1.82307	0.26	1.1981	

52.4204	949.47	0.0468	1.74408	10.28	0.0562	98-005-4402
52.5372	1720.16	0.1248	1.74048	18.62	0.1498	
54.2769	342.01	0.1872	1.68872	3.70	0.2246	
54.6142	276.90	0.2496	1.67909	3.00	0.2995	98-001-7197
56.6070	111.40	0.2496	1.62462	1.21	0.2995	98-001-7197
57.4692	4288.83	0.2496	1.60228	46.42	0.2995	
57.6436	2031.80	0.0780	1.60181	21.99	0.0936	
59.3959	336.23	0.0936	1.55482	3.64	0.1123	
61.2712	635.35	0.1872	1.51165	6.88	0.2246	98-005-4402
62.7840	24.74	0.3744	1.47881	0.27	0.4493	
64.0372	46.51	0.3744	1.45286	0.50	0.4493	
64.5458	92.63	0.0936	1.44264	1.00	0.1123	
66.4326	886.78	0.0780	1.40617	9.60	0.0936	
66.6998	444.15	0.0936	1.40466	4.81	0.1123	
67.4298	550.72	0.2184	1.38777	5.96	0.2621	98-002-2010
67.6369	270.54	0.0936	1.38747	2.93	0.1123	
68.1074	964.93	0.0780	1.37561	10.44	0.0936	
68.3992	553.33	0.0780	1.37385	5.99	0.0936	
68.9740	76.49	0.3120	1.36043	0.83	0.3744	
74.2689	102.16	0.2496	1.27599	1.11	0.2995	
76.7534	1007.40	0.0780	1.24076	10.90	0.0936	
76.8512	1498.73	0.0936	1.23942	16.22	0.1123	98-005-4402
77.1007	981.63	0.0780	1.23910	10.62	0.0936	
77.4326	312.25	0.1560	1.23156	3.38	0.1872	98-001-7197

Identified Patterns List: Sample 2_PdCNT-2

Visible	Ref. Code	Score	Compound Name	Displacement [°2Th.]	Scale Factor	Chemical Formula
*	98-001-7197	40	Graphite 3R	-0.100	1.005	C1
*	98-002-2010	49	Palladium	-0.199	0.204	Pd1
*	98-005-4402	12	Carbon	0.153	0.006	C1

Plot of Identified Phases: Sample 2_PdCNT-

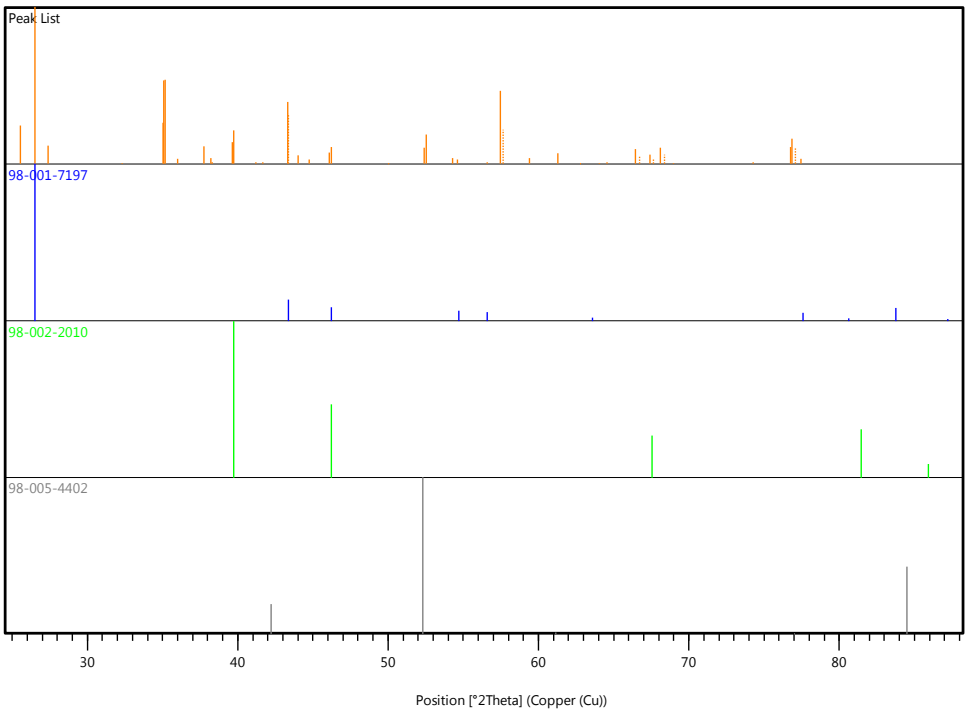

Anchor Scan Parameters: Sample 3-Au_PdCNT

Dataset Name Sample 3-Au_PdCNT
File name C:\XRD Data\Wynette\NUI Maynooth\2014-July24\July28\Sample 3-Au_PdCNT.xrdml
Comment Configuration=Chi-Phi-z Stage, Owner=User-1, Creation date=2/20/2012 9:05:27 AM

Goniometer=Theta/Theta; Minimum step size 2Theta:0.0001; Minimum step size Omega:0.0001

Sample stage=Chi-Phi-z stage 240 mm (reflection); Minimum step size Phi:0.01; Minimum step size Chi:0.01; Minimum step size Z:0.001

Diffractometer system=EMPYREAN

Measurement program=C:\PANalytical\Data Collector\Programs\Wynette\ChiPhi-GonioProgs\Chi-Phi--Focus-gonio.xrdmp, Identifier=19D4F285-6384-4008-A611-83E2414CC55F

Measurement Date / Time	7/28/2014 10:15:07 AM
Operator	User
Raw Data Origin	XRD measurement (*.XRDML)
Scan Axis	Gonio
Start Position [°2Th.]	10.0091
End Position [°2Th.]	79.9881
Step Size [°2Th.]	0.0130
Scan Step Time [s]	58.3950
Scan Type	Continuous
PSD Mode	Scanning
PSD Length [°2Th.]	3.35
Offset [°2Th.]	0.0000
Divergence Slit Type	Fixed
Divergence Slit Size [°]	0.2177
Specimen Length [mm]	10.00
Measurement Temperature [°C]	25.00
Anode Material	Cu
K-Alpha1 [Å]	1.54060
K-Alpha2 [Å]	1.54443
K-Beta [Å]	1.39225
K-A2 / K-A1 Ratio	0.50000
Generator Settings	40 mA, 40 kV
Diffractometer Type	0000000011121830
Diffractometer Number	0
Goniometer Radius [mm]	240.00
Dist. Focus-Diverg. Slit [mm]	100.00
Incident Beam Monochromator	No
Spinning	No

Graphics: Sample 3-Au_PdCNT

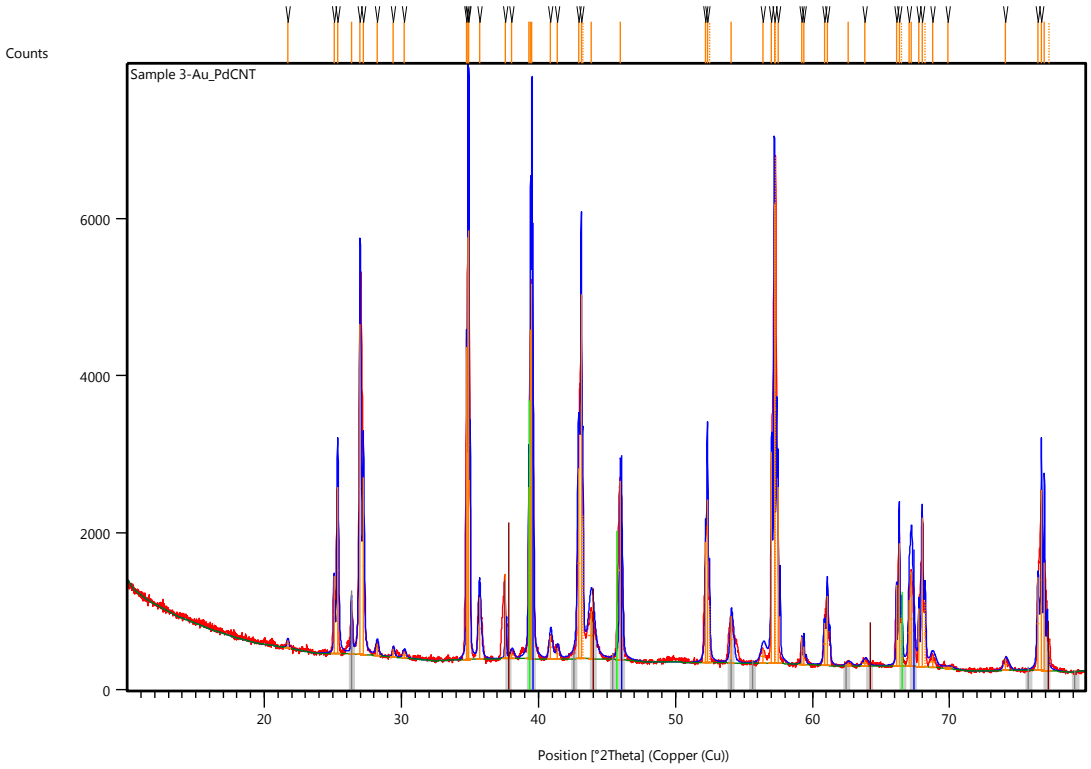

Peak List: Sample 3-Au_PdCNT

Pos. [°2Th.]	Height [cts]	FWHM Left [°2Th.]	d-spacing [Å]	Rel. Int. [%]	Tip Width	Matched by
21.7061	94.04	0.1535	4.09440	1.46	0.1842	
25.0885	993.06	0.0384	3.54954	15.37	0.0461	
25.3372	2119.05	0.1407	3.51525	32.79	0.1689	
26.3548	684.12	0.0640	3.38180	10.59	0.0768	98-006-2959
26.9741	4209.04	0.1279	3.30555	65.13	0.1535	
27.2206	2259.27	0.1023	3.27617	34.96	0.1228	
28.2289	151.21	0.2047	3.16139	2.34	0.2456	
29.4125	108.80	0.1535	3.03682	1.68	0.1842	
30.2048	81.59	0.2558	2.95894	1.26	0.3070	
34.7632	3980.45	0.0624	2.57854	61.59	0.0749	

34.8561	5378.22	0.0468	2.57188	83.22	0.0562	
34.9298	5463.22	0.0512	2.56875	84.54	0.0614	
35.6899	790.31	0.2047	2.51577	12.23	0.2456	
37.5647	1068.78	0.0468	2.39242	16.54	0.0562	
38.0581	93.85	0.3070	2.36449	1.45	0.3684	
39.3103	2182.02	0.0936	2.29011	33.77	0.1123	98-007-0933
39.4223	4191.16	0.0780	2.28387	64.86	0.0936	98-002-2010; 98-007-0933
39.5263	4777.12	0.1023	2.27998	73.92	0.1228	98-002-2010; 98-007-0933
40.8742	305.61	0.2303	2.20786	4.73	0.2763	
41.3859	139.31	0.2047	2.18173	2.16	0.2456	
42.9185	2424.89	0.1872	2.10557	37.52	0.2246	
43.1240	4641.86	0.0936	2.09601	71.83	0.1123	
43.2627	1845.02	0.0624	2.09480	28.55	0.0749	
43.8458	603.41	0.4992	2.06316	9.34	0.5990	98-007-0764
45.9840	2278.90	0.1560	1.97208	35.26	0.1872	98-002-2010
52.2015	1542.36	0.1248	1.75088	23.87	0.1498	
52.3321	2076.57	0.1092	1.74681	32.13	0.1310	
52.4977	724.66	0.0780	1.74602	11.21	0.0936	
54.0734	596.01	0.2184	1.69460	9.22	0.2621	98-006-2959
56.3778	181.75	0.4368	1.63068	2.81	0.5242	
57.0127	2698.39	0.1092	1.61402	41.76	0.1310	
57.2214	5861.58	0.0936	1.60862	90.70	0.1123	
57.3040	6462.34	0.0624	1.61049	100.00	0.0749	
57.4779	2247.14	0.0780	1.60205	34.77	0.0936	
59.2065	352.27	0.0780	1.55934	5.45	0.0936	

59.3595	227.90	0.0936	1.55568	3.53	0.1123	
60.8656	536.57	0.1560	1.52074	8.30	0.1872	
61.0845	886.36	0.1248	1.51582	13.72	0.1498	
62.5757	44.53	0.4368	1.48323	0.69	0.5242	98-006-2959
63.8219	76.02	0.3744	1.45724	1.18	0.4493	
66.1232	1034.98	0.0624	1.41199	16.02	0.0749	
66.3229	1565.40	0.1248	1.40823	24.22	0.1498	
66.5033	643.44	0.0936	1.40833	9.96	0.1123	
67.0595	841.00	0.1560	1.39453	13.01	0.1872	
67.1967	1203.56	0.2184	1.39202	18.62	0.2621	98-002-2010
67.7505	742.92	0.0780	1.38198	11.50	0.0936	
68.0106	1899.79	0.1404	1.37733	29.40	0.1685	
68.1825	825.02	0.1248	1.37769	12.77	0.1498	
68.7407	151.65	0.3744	1.36447	2.35	0.4493	
69.8621	23.43	0.7488	1.34529	0.36	0.8986	
74.0788	149.59	0.3120	1.27879	2.31	0.3744	
76.4526	1183.91	0.1716	1.24489	18.32	0.2059	
76.6976	2300.45	0.0780	1.24152	35.60	0.0936	
76.9031	1373.96	0.1248	1.23872	21.26	0.1498	98-007-0764
77.2646	397.43	0.1248	1.23689	6.15	0.1498	

Identified Patterns List: Sample 3-Au_PdCNT

Visible	Ref. Code	Score	Compound Name	Displacement [°2Th.]	Scale Factor	Chemical Formula
*	98-002-2010	38	Palladium	-0.344	0.695	Pd1
*	98-007-0933	28	Gold Palladium (1/1)	0.181	0.412	Au1 Pd1
*	98-006-2959	27	Graphite 3R	0.202	0.102	C1
*	98-007-0764	9	Gold	-0.359	0.217	Au1

Plot of Identified Phases: Sample 3-Au_PdCNT

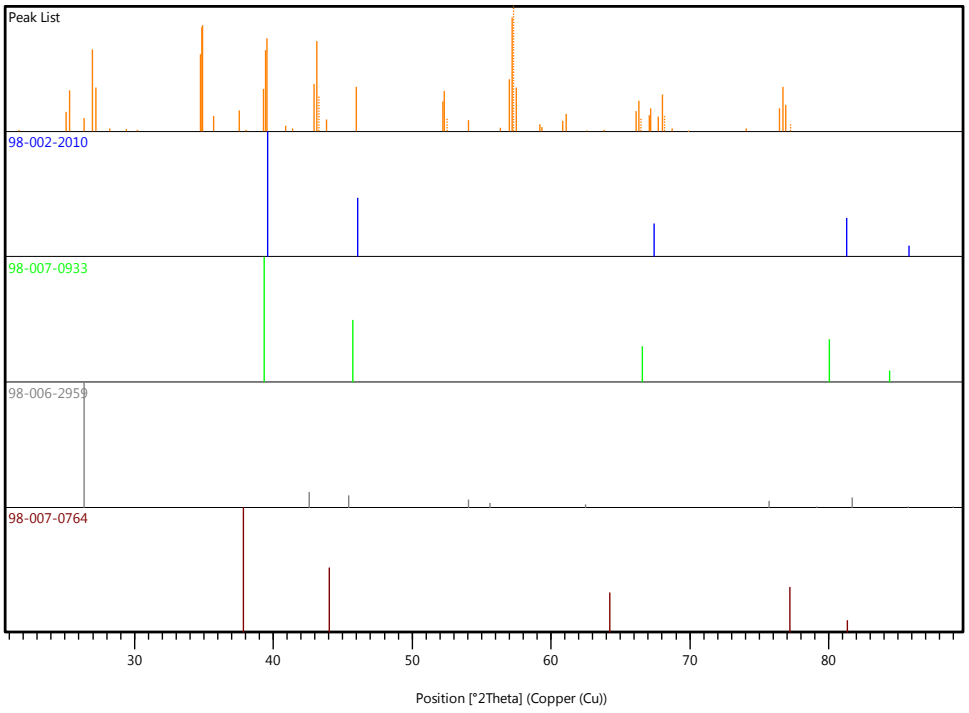

Anchor Scan Parameters: BlueSurface-fullscan

Dataset Name BlueSurface-fullscan
File name C:\XRD Data\Wynette\NUI Maynooth\2014-July24\July28\BlueSurface-fullscan.xrdml
Comment Configuration=Chi-Phi-z Stage, Owner=User-1, Creation date=2/20/2012 9:05:27 AM
Goniometer=Theta/Theta; Minimum step size 2Theta:0.0001; Minimum step size Omega:0.0001
Sample stage=Chi-Phi-z stage 240 mm (reflection); Minimum step size Phi:0.01; Minimum step size Chi:0.01; Minimum step size Z:0.001
Diffractometer system=EMPYREAN
Measurement program=C:\PANalytical\Data Collector\Programs\Wynette\ChiPhi-GonioProgs\Chi-Phi--Focus-gonio.xrdmp, Identifier=2921A34B-335F-4979-80AA-2E64430E0F31
Measurement Date / Time 7/29/2014 10:12:53 AM
Operator User
Raw Data Origin XRD measurement (*.XRDML)
Scan Axis Gonio
Start Position [°2Th.] 10.0091
End Position [°2Th.] 79.9881
Step Size [°2Th.] 0.0130
Scan Step Time [s] 58.3950
Scan Type Continuous
PSD Mode Scanning
PSD Length [°2Th.] 3.35
Offset [°2Th.] 0.0000
Divergence Slit Type Fixed
Divergence Slit Size [°] 0.2177
Specimen Length [mm] 10.00
Measurement Temperature [°C] 25.00
Anode Material Cu
K-Alpha1 [Å] 1.54060
K-Alpha2 [Å] 1.54443
K-Beta [Å] 1.39225
K-A2 / K-A1 Ratio 0.50000
Generator Settings 40 mA, 40 kV
Diffractometer Type 0000000011121830
Diffractometer Number 0
Goniometer Radius [mm] 240.00
Dist. Focus-Diverg. Slit [mm] 100.00
Incident Beam Monochromator No
Spinning No

Graphics: BlueSurface-fullscan

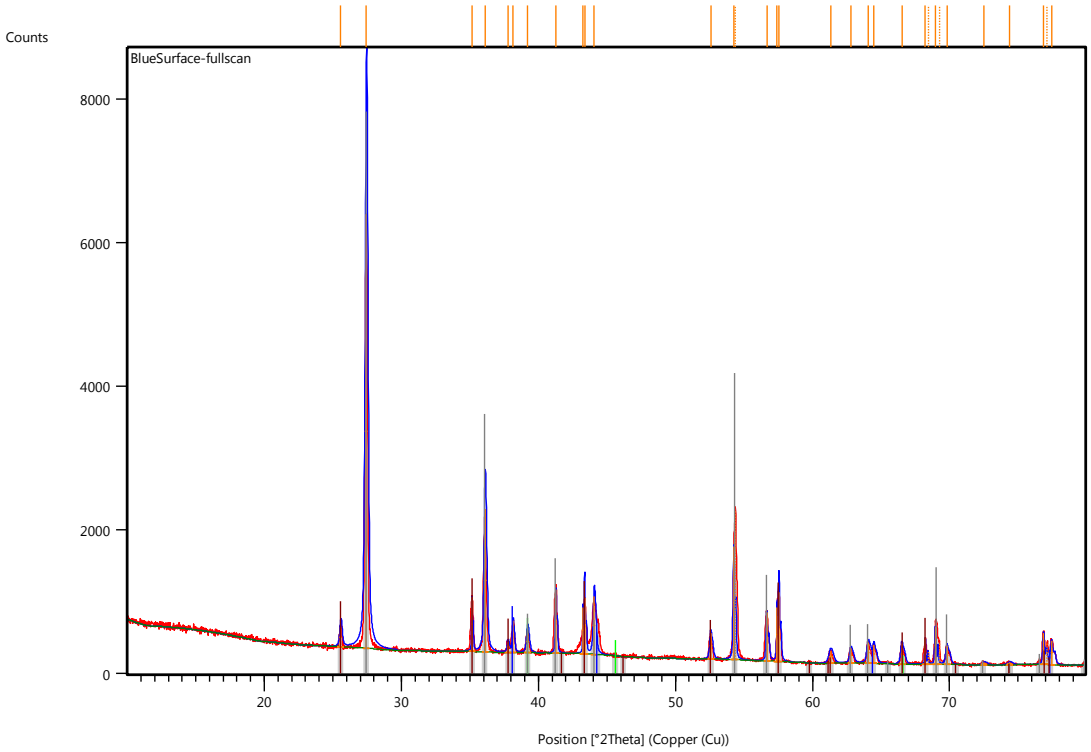

Peak List: Graphics: BlueSurface-fullscan

Pos. [°2Th.]	Height [cts]	FWHM Left [°2Th.]	d-spacing [Å]	Rel. Int. [%]	Tip Width	Matched by
25.5807	279.56	0.1791	3.48235	4.63	0.2149	98-006-0930
27.4444	6039.25	0.2175	3.24996	100.00	0.2610	98-000-6062
35.1571	754.17	0.0640	2.55266	12.49	0.0768	98-006-0930
36.1100	1988.84	0.1919	2.48746	32.93	0.2303	98-000-6062
37.7707	148.12	0.1535	2.38182	2.45	0.1842	98-006-0930
38.1555	439.19	0.1151	2.35868	7.27	0.1382	98-006-2944
39.2066	307.07	0.2047	2.29784	5.08	0.2456	98-002-2008; 98-000-6062
41.2772	889.16	0.0895	2.18723	14.72	0.1075	98-000-6062
43.2620	639.38	0.0624	2.08964	10.59	0.0749	98-006-0930
43.3818	783.09	0.0895	2.08587	12.97	0.1075	98-006-0930
44.0724	811.78	0.1791	2.05478	13.44	0.2149	98-000-6062
52.5675	364.02	0.1791	1.74098	6.03	0.2149	98-006-0930
54.2549	1576.96	0.1092	1.68936	26.11	0.1310	98-000-6062
54.3681	2090.22	0.0780	1.69030	34.61	0.0936	
56.6630	674.85	0.1248	1.62314	11.17	0.1498	98-000-6062
57.4150	748.97	0.0780	1.60366	12.40	0.0936	98-006-0930

57.5357	967.05	0.1092	1.60058	16.01	0.1310	98-006-0930
61.3093	167.90	0.3120	1.51080	2.78	0.3744	98-006-0930
62.7969	207.01	0.2184	1.47854	3.43	0.2621	98-000-6062
64.0646	279.66	0.2496	1.45230	4.63	0.2995	98-000-6062
64.4832	253.94	0.1872	1.44389	4.20	0.2246	98-006-2944
66.5172	291.67	0.2184	1.40458	4.83	0.2621	98-002-2008; 98-006-0930
68.2244	367.97	0.0780	1.37353	6.09	0.0936	98-006-0930
68.4397	170.09	0.0936	1.37314	2.82	0.1123	
68.9510	522.42	0.0936	1.36082	8.65	0.1123	98-000-6062
69.2487	304.61	0.0936	1.35907	5.04	0.1123	
69.8082	262.05	0.2184	1.34619	4.34	0.2621	98-000-6062
72.5039	37.56	0.3744	1.30264	0.62	0.4493	98-000-6062
74.3575	34.14	0.3744	1.27469	0.57	0.4493	98-000-6062; 98-006-0930
76.8595	441.62	0.1404	1.23931	7.31	0.1685	98-006-0930
77.1247	310.13	0.0936	1.23878	5.14	0.1123	
77.4428	336.26	0.1872	1.23143	5.57	0.2246	98-006-2944; 98-006-0930

Identified Patterns List: Graphics: BlueSurface-fullscan

Visible	Ref. Code	Score	Compound Name	Displacement [°2Th.]	Scale Factor	Chemical Formula
*	98-006-2944	38	Gold	0.004	0.074	Au1
*	98-002-2008	24	Palladium	-0.214	0.055	Pd1
*	98-000-6062	69	Rutile	-0.008	0.856	O2 Ti1
*	98-006-0930	66	Corundum	-0.017	0.126	Al2 O3

Plot of Identified Phases: BlueSurface-fullscan